KOMUNIKÁCIE

COMMUNICATIONS

SCIENTIFIC LETTERS OF THE UNIVERSITY OF ŽILINA

Volume 28

MULTIDISCIPLINARY JOURNAL FOR SCIENCES IN TRANSPORT

UNIVERSITY
OF ŽILINA

ISSN 1335-4205
9 771335 420009

1/2026

UNIVERSITY OF ŽILINA
EDIS-Publishing House
UNIZA

EDIS-Publishing House of the University of Žilina (UZ) is one of the University of Žilina‘s consituents. The beginning of its existence dates back to 1990. In the course of its work, the publishing house has published more than 5 100 titles of book publications, especially university textbooks, scientific monographs, scripts, prose, but also enriched the book market with titles of regional, children‘s and popular literature.

Students and professional public have the opportunity to purchase published titles in the „Selling Study Literature“ directly on the premises of the University of Žilina, in the EDIS shop or upon order on a „cash on delivery“ basis. All published titles are available at: www.edis.uniza.sk.

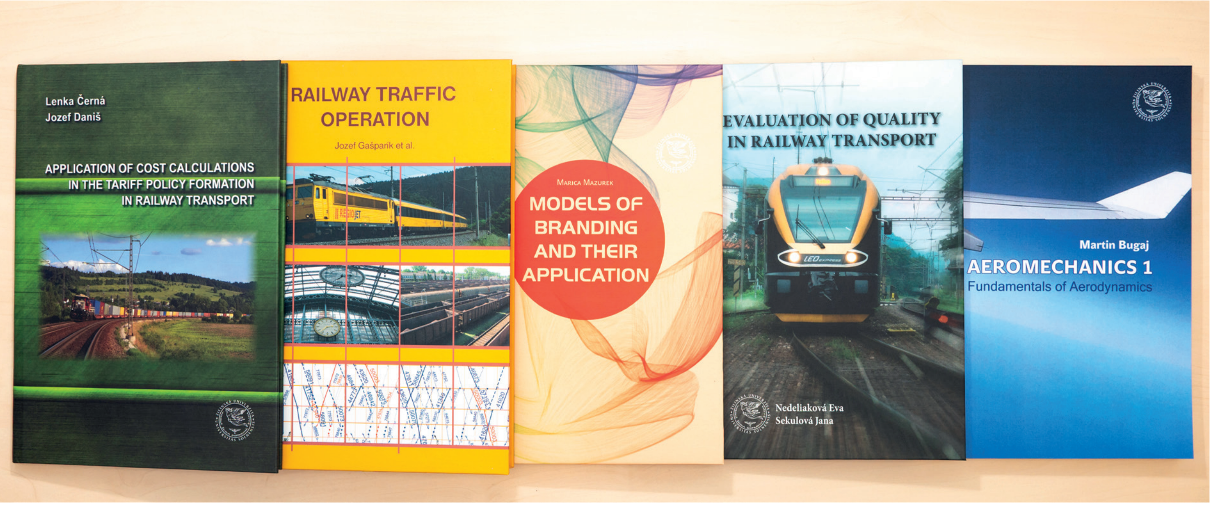

EDIS-Publishing House of the University of Žilina offers book titles in English

Eva Nedeliaková, Jana Sekulová
EVALUATION OF QUALITY IN RAILWAY TRANSPORT
ISBN 978-554-1272-6 Price 8.00 €

Martin Bugaj
AEROMECHANICS 1
ISBN 978-80-554-1675-5 Price 14.50 €

Marica Mazurek
MODELS OF BRANDING AND THEIR APPLICATION
ISBN 978-80-554-1705-9 Price 9.00 €

Jozef Melcer
DYNAMICS OF STRUCTURES
ISBN 978-80-554-1698-4 Price 19.00 €

Jozef Gašparík et al.
RAILWAY TRAFFIC OPERATION
ISBN 978-80-554-1281-8 Price 15.80 €

Lenka Černá, Jozef Daniš
APPLICATION OF COST ALCULATIONS IN THE TARIFF POLICY FORMATION IN RAILWAY TRANSPORT
ISBN 978-80-554-1391-4 Price 7.61 €

Tetiana Hovorushchenko et.al.
CD - INTELLIGENT INFORMATION-ANALYTICAL TECHNOLOGIES...
ISBN 978-80-554-1729-5 Price 3.50 €

Karol Matiaško, Michal Kvet, Marek Kvet
CD - PRACTICES FOR DATABASE SYSTEMS
ISBN 978-80-554-1397-6 Price 2.20 €

Veronika Valašková, Daniela Kucharová
USB - STATICS OF STRUCTURES 3
ISBN 978-80-554-1826-1 Price: 8,90 €

Michal Kvet, Karol Matiaško, Štefan Toth
USB - PRACTICAL SQL FOR ORACLE CLOUD
ISBN 978-80-554-1880-3 Price: 11,30 €

Michal Kvet, Karol Matiaško, Marek Kvet
USB - BECOME EXPERT IN MYSQL PRACTICES FOR DATABASE SYSTEMS IN MYSQL
ISBN 978-80-554-1786-8 Price 13.50 €

Michal Kvet, Alenka Baggia, Monika Borkovcová, Diana Mudrinić, Frane Urem
E-book - Environmental Data Analysis
ISBN 978-80-554-2145-2 Price 0,00 €

Michal Kvet
E-book – Become master in SQL
ISBN 978-80-554-2132-2 Price 0,00 €

EDIS-Publishing House UNIZA

Univerzitná 8215/1,
010 26 Žilina,
Slovakia

e-mail: edis_objednavky@uniza.sk, edis@uniza.sk
www.edis.uniza.sk

KOMUNIKÁCIE
COMMUNICATIONS

VEDECKÉ LISTY ŽILINSKEJ UNIVERZITY
SCIENTIFIC LETTERS OF THE UNIVERSITY OF ZILINA
multidisciplinary journal for sciences in transport

A - OPERATION AND ECONOMICS IN TRANSPORT

B - MECHANICAL ENGINEERING IN TRANSPORT

C - ELECTRICAL ENGINEERING IN TRANSPORT

D - CIVIL ENGINEERING IN TRANSPORT

E - MANAGEMENT SCIENCE AND INFORMATICS IN TRANSPORT

F - SAFETY AND SECURITY ENGINEERING IN TRANSPORT

EVALUATING PORT PERFORMANCE IN EU COUNTRIES WITH FUZZY AND GREY LOGIC

Gül Alışar Kayar[1,*], **İlker İbrahim Avşar**[2]

[1]Toros University, Mersin, Turkey
[2]Osmaniye Korkut Ata University, Osmaniye, Turkey

*E-mail of corresponding author: gul.alisar@toros.edu.tr

Gül Alışar Kayar 0009-0009-1675-6877, İlker İbrahim Avşar 0000-0003-2991-380X

Resume

Ports are fundamental components of global supply chains, and their performance is critical to sustaining international trade and economic activity. Recognizing that existing studies often focus on individual ports rather than broader regional patterns, a new hybrid Multi-Criteria Decision-Making (MCDM) model is proposed to provide a more comprehensive assessment framework. Based on expert judgments, the Fuzzy Analytic Hierarchy Process (AHP) results indicate that cargo type is the most influential determinant, followed by cargo direction and container volume. Using Evaluation based on Distance from Average Solution - Grey (EDAS-G) and Additive Ratio Assessment - Grey (ARAS-G), the port performance across 24 EU countries for the period 2014-2023, incorporating a temporal dimension that enables multi-year trend analysis. The hybrid grey-based ranking shows that Italy, Spain, the Netherlands, and Germany rank the highest, while Slovenia, Bulgaria, Malta, and Cyprus consistently rank at the lower end.

Available online: https://doi.org/10.26552/com.C.2026.011

Article info
Received 13 September 2025
Accepted 9 December 2025
Online 16 January 2026

Keywords:
logistics
port
fuzzy AHP
EDAS-G
ARAS-G

ISSN 1335-4205 (print version)
ISSN 2585-7878 (online version)

1 Introduction

Ports are among the most crucial components of global trade. They play a vital role in maritime trade [1-2]. The efficiency of ports directly impacts a country's export performance and, consequently, its economic development [3]. Therefore, accurate predictions of port performance require comprehensive research, and such studies are crucial for the sector [4]. However, significant gaps remain in the existing literature on ports in certain areas [5]. Closing these gaps is crucial because improving port efficiency directly impacts global trade and the global supply chain by increasing efficiency [6].

Research into improving the port efficiency is highly valuable for the industry [7]. Some ports are known to increase their efficiency levels by effectively utilizing their resources. However, not all the ports exhibit this characteristics; some fail to utilise their resources effectively [8]. Therefore, it is essential to compare ports to assess the sector's overall situation and identify the efficient and inefficient ones.

The existing literature on ports is generally dominated by studies focusing on a single port. Conversely, comparative studies are limited, leaving a significant gap in this field [9]. In this regard, a comprehensive approach is adopted in this study, similar to that used by Moros-Daza et al. (2025) [2]. This study is based on findings from an MCDM analysis of port performance across 24 EU countries. The primary objective of the study was to shed light on the dynamics of EU port performance by addressing the following research questions:

RQ1: What are the relative weights of the criteria affecting the performance of ports in EU member states?

RQ2: How do countries' performance rankings change according to the identified criteria?

In this study is adopted a new hybrid MCDM model. The primary reason for choosing this approach was the multidimensional nature of port performance and the inadequacy of existing single method approaches to encompass all these dimensions. The study provides a comprehensive analysis of a 10-year dataset. Criteria weights were determined using the Fuzzy AHP method, which reveals the relative importance of indicators affecting the port performance. Subsequently, the port performance of EU countries was evaluated using the

EDAS-G and ARAS-G methods together, revealing how their rankings changed across different reference points. Combining effective analytical logic for addressing uncertainty with grey system theory, which can handle missing and insufficient data, increases the reliability of the evaluation process. Furthermore, the proposed hybrid model is tested through sensitivity analyses to enhance its robustness.

2 Literature research

2.1 Port

Ports play a strategic role in ensuring the effective operation of the global supply chain. Therefore, analyzing port efficiency levels and identifying the most suitable alternatives is vital for decision-makers. In this context, the MCDM methods are powerful tools that facilitate the rational, systematic selection of alternatives. The MCDM methods are widely used in literature to select the best option from among various alternatives (e.g., [10-14]. There is extensive literature on the use of MCDM methods in port-related decision-making processes. The section presents various recent studies from the literature that address the application of MCDM methods in port analysis.

For example, Ilyas et al. (2024), [15] and Ur Rehman and Ali (2021), [16] evaluated China's energy supply route options using transport corridors and ports, applying MCDM methods. Similarly, Bagocius et al. (2014) used an MCDM approach to determine the optimal location for an LNG port in the Baltic Sea [17]. Furthermore, researchers from various disciplines have employed these methods for port selection, comparative port analysis, and regional port functionality, taking into account various geographic, economic, and operational criteria.

Kine et al. (2025) used the geographic information systems and MCDM methods together to determine suitable locations for dry cargo ports. The study's findings reveal that the two most decisive criteria in port location selection are distance to the highway and distance to the railroad. On the other hand, the distance to an existing port was identified as the least important factor [18].

Kolakowski et al. (2024) analyzed Polish ports regarding bunkering. Their research was focused on determining the most suitable port and fuel type for this process. The research data were obtained using the Delphi technique and analysed using MCDM. Based on expert opinions, three main factors were identified: access to market supply and demand, supply chain reliability, and delivery security. According to the analysis, the Port of Swinoujscie is the leading port for refueling [19].

Wang and Li (2023) addressed sustainability issues in ports. In the first stage, nine sustainability-related criteria were evaluated using the MCDM method. The Step-wise Weight Assessment Ratio Analysis (SWARA) and Weighted Aggregated Sum and Product Assessment (WASPAS) methods were employed in this evaluation process. In the second stage, cities that could minimise economic, environmental, and social costs were identified as suitable locations for dry ports. The analysis revealed that the key regions for dry ports were Suzhou, Chongqing, Chengdu, Wuhan, Changsha, Wuxi, and Hefei. It also showed that shippers operating in regions close to ports prefer road transportation, whereas those in more distant regions prefer rail [20].

Garg et al. (2023) evaluated Chinese ports using the fuzzy AHP model, an MCDM method. Of the six factors identified for measuring port sustainability performance, environmental considerations, digitalisation, automation, and strategy were deemed the most significant. The researcher emphasises that the results of the MCDM can inform the strategic decision-making processes of sector managers and policymakers [21].

Ighravwe and Mashao (2023) evaluated Nigerian ports within the framework of the security criterion. In the analysis, the Technique for Order Preference by Similarity to Ideal Solution (TOPSIS) and WASPAS methods from MCDM were used in conjunction. The evaluation was based on five key criteria: human security; property security and monitoring capabilities; resilience and flexibility against regular and irregular threats; and measures to address physical security breaches. The analysis reveals that human security is the most critical criterion. According to the TOPSIS ranking, Apapa Port was identified as the highest-performing port, while Onne Port ranked lowest in the evaluation [22].

Pamucar and Gorcun (2022) used a hybrid Fuzzy LBWA-CoCoSo'B method to evaluate European ports. According to the research findings, the port cost stands out as the most effective criterion. According to the port performance ranking, the Port of Antwerp ranked first, achieving the highest score. At the same time, the Port of Barcelona ranked the lowest in line with the evaluated criteria [23].

Lamii et al. (2022) analyzed risk factors in ports. In the research process, literature review, Delphi technique, and MCDM method were used, respectively. AHP, a MCDM technique, was used to reveal the complex structure of port systems. The risk factors were then prioritized according to the identified criteria. The findings show that human and economic-based risk factors are critical for ports. Such risk factors can disrupt port business processes. Gorcun (2021) analyzed the efficiency of Black Sea container ports through MCDM methods. Two different models were used in the research. The first model combines Entropy and Operational Competitiveness Rating Analysis (OCRA) methods, whereas the second model combines Entropy with the Technique for Order Preference by Similarity to Ideal Solution (EATWIOS) method. The study has two main objectives. The first one is to determine whether the MCDM methods used are effective evaluation tools in the maritime sector. The second one is to analyze the comparative performance of the Black Sea ports. Nine input and four output criteria were used in the performance evaluation. According to the final ranking, Constanza Port is the highest-performing port among the nine ports analyzed [24-25].

Kannika et al. (2019) evaluated Thailand's port system from a sustainability perspective. In the analysis process, BWM and MCDM methods were used together. The evaluation criteria are grouped under three main headings: economic, environmental, and social. The study's results reveal that cost efficiency is the most important criterion. High-quality service and infrastructure investments follow this criterion [26].

Clearly, the MCDM methods are widely favoured in both academic and practical contexts of port management and strategic planning. A review of the relevant literature reveals that MCDM approaches have become increasingly important in port analyses, providing a systematic basis for decision-making processes.

2.2 EU, Port and MCDM

Various studies have evaluated European countries using different MCDM approaches. For instance, Burhan (2024), [27] assessed EU member states with VIKOR (VlseKriterijumska Optimizacija I Kompromisno Resenje) and Multi-Attribute Ideal-Real Comparative Analysis (MAIRCA) based on nine criteria, including air emissions, RandD investment, high-speed internet accessibility, patent applications, the number of RandD personnel, modal split in transport, and education levels. The 2023 VIKOR results ranked Sweden, Germany, and France as the top performers, while the MAIRCA results identified Sweden, Germany, and Denmark as the top performers.

As this example illustrates, both the selection of criteria and the choice of the MCDM techniques vary substantially across studies. Due to this methodological diversity, it is rare to encounter research that uses the same dataset and model configuration. Accordingly, no directly comparable study was identified in existing literature.

3 Methodology

In this study, a new hybrid MCDM model is proposed to evaluate the port performance of the EU countries. In this context, the criterion weights were calculated using the Fuzzy AHP method. The ranking of alternatives was performed using both the EDAS-G and ARAS-G methods. The steps of the methods used in this study are presented below.

3.1 Fuzzy AHP

The AHP has been utilized in numerous studies for years to address MCDM problems. However, a decision maker's evaluation may often be fuzzy and uncertain. In such cases, it may not be possible to obtain the decision maker's assessment unambiguously through the AHP's traditional pairwise comparison method [28]. The fuzzy AHP enables decision-makers to express their evaluations using fuzzy numbers rather than relying on precise numerical values [29]. Fuzzy AHP addresses these challenges by structuring the decision-making process within a hierarchical framework and identifying a compromise solution among competing criteria [30]. Given the uncertainty and imprecision inherent in expert judgments on port performance criteria, this approach provides a more realistic and reliable weighting structure; therefore, the Fuzzy AHP method was preferred in this study. Triangular Fuzzy Numbers (TFNs) are preferred for representing linguistic variables, and this method facilitates comparisons.

The fuzzy AHP method is implemented in the following steps [31]:

Step 1. Definition of Object and Goal Sets with Degree Analysis Initialization

Let $X = \{x_1, x_2, \ldots, x_n\}$ be an object set and $U = \{u_1, u_2, \ldots, u_n\}$ be a goal set. Degree analysis (g_i) is applied for each target with respect to each criterion. The TFN M_1 are used to express the M degree analysis value associated with the targets.

$$S_i = \sum_{j=1}^{m} M_{gi}^{j} \otimes \left[\sum_{i=1}^{n} \sum_{j=1}^{m} v M_{gi}^{j} \right]^{\{-1\}}, \tag{1}$$

g_i provides the TFN associated with the j-th target based on the i-th criterion.

Step 2. Calculation of the Degree of Possibility Between Triangular Fuzzy Numbers

M_1, shown with (l_1, m_1, u_1) parameters and M_2, (l_2, m_2, u_2). The degree of possibility is defined as,

$$V(M_2 \geq M_1) = \sup_{y \geq x} \left[\min\left(\mu_{M_1}(x), \mu_{M_2}(y) \right) \right], \tag{2}$$

$$V(M_2 \geq M_1) = hgt(M_1 \cap M_2) = \mu_{M_2}(d) = \\ = \begin{cases} 1, \ if\ m_2 \geq m_1 \\ 0, \ if\ l_1 \geq u_2 \\ \dfrac{l_1 - u_2}{(m_2 - u_2) - (m_1 - l_1)}, otherwise, \end{cases} \tag{3}$$

where d is the ordinate of the point D where μ_{M_1} and μ_{M_2} cross.

Step 3. Computation and Normalization of the Fuzzy Significance Vector

Significance vector is calculated indicated as $W' = (d'(A_1), d'(A_2), \ldots, d'(A_{nT}))^T \ i = \{1, 2, \ldots, n\}$ and vector normalized applied. $W' = (d(A_1), d(A_2), \ldots, d(A_n))^T \ i = \{1, 2, \ldots, n\}$ vector is calculated as significance vector where $d'(A_i) = \min V(S_i \geq S_k)$.

***Table 1** Statement and TFN, [32]*

Statement	TFN
Equal Importance (EI)	(1,1,1)
Moderate importance (MI)	(1,3,5)
Strong Importance (SI)	(3,5,7)
Very Strong Importance (VSI)	(5,7,9)
Extreme Importance (EXI)	(7,9,11)

Table 1 presents the linguistic statements and their corresponding TFNs used in the analysis.

3.2 EDAS-G

The EDAS method is a reliable and versatile tool for decision-making processes that require systematic evaluation [33]. The main feature of the EDAS method is its two distance measures: Positive Distance from Mean (PDA) and Negative Distance from Mean (NDA). The EDAS-G was developed by Stanujkic et al. (2017) [34]. Grey numbers represent the minimum and maximum expected performance ratings of the alternative against each criterion. The EDAS-G method provides more consistent and reliable results by evaluating alternatives against both positive and negative ideal solutions in MCDM problems involving uncertainty. Since the port performance data often contain incomplete, imprecise, or fluctuating values across years and countries, the grey extension of EDAS offers a more robust structure for handling uncertainty; therefore, the EDAS-G method was preferred in this study**.**

The steps of EDAS-G are implemented in the following stages [34]:

Step 1. Forming The Matrix for Grey Decision-Making (Y)

$$\otimes Y=\begin{bmatrix}[\underline{y}_{11},\bar{y}_{11}] & [\underline{y}_{12},\bar{y}_{12}] & \cdots & [\underline{y}_{1n},\bar{y}_{1n}]\\ [\underline{y}_{11},\bar{y}_{11}] & [\underline{y}_{22},\bar{y}_{22}] & \cdots & [\underline{y}_{2n},\bar{y}_{2n}]\\ \cdots & \cdots & \cdots & \cdots\\ [\underline{y}_{m1},\bar{y}_{m1}] & [\underline{y}_{m2},\bar{y}_{m2}] & \cdots & [\underline{y}_{mn},\bar{y}_{mn}]\end{bmatrix}. \tag{4}$$

Step 2. Determine The Grey Average Answer

$$\otimes Y_j^{\circ}=([\underline{y}^{\circ}_{1},\bar{y}_1^{\circ}],[\underline{y}^{\circ}_{2},\bar{y}_2^{\circ}],\cdots[\underline{y}^{\circ}_{n},\bar{y}_n^{\circ}]). \tag{5}$$

Step 3. Determination of the Grey Distances from the Average Solution. The Grey positive distance from the mean is obtained using the formula, $\otimes d_{ij}^{+}=[\underline{d}_{ij}^{+},\bar{d}_{ij}^{+}]$ and the Grey negative distance from average $\otimes d_{ij}^{-}=[\underline{d}_{ij}^{-},\bar{d}_{ij}^{-}]$,

$$\underline{d}_{ij}^{+}=\begin{cases}\dfrac{\max(0,(\underline{y}_{ij}-\bar{y}_j^{\circ}))}{0.5(\underline{y}^{\circ}_{j}+\bar{y}_j^{\circ})}; & j\in \Omega_{\max}\text{ and}\\ \dfrac{\max(0,(\underline{y}^{\circ}_{j}-\bar{y}_{ij}))}{0.5(\underline{y}^{\circ}_{j}+\bar{y}_j^{\circ})}; & j\in \Omega_{\min}\end{cases}, \tag{6}$$

$$\bar{d}_{ij}^{+}=\begin{cases}\dfrac{\max(0,(\underline{y}_{ij}-\bar{y}_j^{\circ}))}{0.5(\underline{y}^{\circ}_{j}+\bar{y}_j^{\circ})}; & j\in \Omega_{\max}\text{ and}\\ \dfrac{\max(0,(\underline{y}^{\circ}_{j}-\bar{y}_{ij}))}{0.5(\underline{y}^{\circ}_{j}+\bar{y}_j^{\circ})}; & j\in \Omega_{min}\end{cases}, \tag{7}$$

$$\underline{d}_{ij}^{-}=\begin{cases}\dfrac{\max(0,(\underline{y}^{\circ}_{j}-\underline{y}_{ij}))}{0.5(\underline{y}^{\circ}_{j}+\bar{y}_j^{\circ})}; & j\in \Omega_{\max}\text{ and}\\ \dfrac{\max(0,(\underline{y}_{ij}-\bar{y}_j^{\circ}))}{0.5(\underline{y}^{\circ}_{j}+\bar{y}_j^{\circ})}; & j\in \Omega_{min}\end{cases}, \tag{8}$$

$$\bar{d}_{ij}^{-}=\begin{cases}\dfrac{\max(0,(\underline{y}^{\circ}_{j}-\underline{y}_{ij}))}{0.5(\underline{y}^{\circ}_{j}+\bar{y}_j^{\circ})}; & j\in \Omega_{\max}\text{ and}\\ \dfrac{\max(0,(\bar{y}_{ij}-\underline{y}^{\circ}_{j}))}{0.5(\underline{y}^{\circ}_{j}+\bar{y}_j^{\circ})}; & j\in \Omega_{\min}\end{cases}, \tag{9}$$

Step 4. Determine the Weighted Grey Distances for PDA and NDA. The grey PDA's weighted sum by using the formula $\otimes Q_i^{+}=[\underline{Q}_i^{+},\overline{Q}_i^{+}]$ and the grey NDA's weighted sum, $\otimes Q_i^{-}=[\underline{Q}_i^{-},\overline{Q}_i^{-}]$

$$\underline{Q}_i^{+}=\sum_{j=1}^{n} w_j\underline{d}_{ij}^{+}, \tag{10}$$

$$\overline{Q}_i^{+}=\sum_{j=1}^{n} w_j\overline{d}_{ij}^{+}, \tag{11}$$

$$\underline{Q}_i^{-}=\sum_{j=1}^{n} w_j\underline{d}_{ij}^{-}, \tag{12}$$

$$\overline{Q}_i^{-}=\sum_{j=1}^{n} w_j\overline{d}_{ij}^{-}. \tag{13}$$

Step 5. Determine the Representative (Typical) Scores of Alternatives. Each alternative's weighted sums of the Grey PDA and Grey NDA should be set to their typical values.

$$\underline{S}_i^{+}=\frac{\underline{Q}_i^{+}}{\max_k \overline{Q}_k^{+}}, \tag{14}$$

$$\overline{S}_i^{+}=\frac{\overline{Q}_i^{+}}{\max_k \overline{Q}_k^{+}}, \tag{15}$$

$$\underline{S}_i^{-}=1-\frac{\overline{Q}_i^{-}}{\max_k \overline{Q}_k^{+}},, \tag{16}$$

$$\underline{S}_i^- = 1 - \frac{\underline{Q}_i^-}{\max\limits_k \overline{Q}_k^+}, \tag{17}$$

Step 6. Determine the Appraisal Score S_i

$$S_i = \frac{1}{2}\left[(1-\alpha)\left(\underline{S}_i^- + \underline{S}_i^+\right) + \alpha\left(\overline{S}_i^- + \overline{S}_i^+\right)\right]. \tag{18}$$

Step 7. Determination of the Best Alternative Based on S_i Scores. Rank the options based on the evaluation score's declining values. The best option is the one with the highest S_i.

3.3 ARAS-G

In the ARAS methodology, a utility function is employed to evaluate the intricate relative efficiency of a prospective alternative. This utility function directly quantifies the efficacy of the alternatives by contemplating the cumulative impact of the values and weights assigned to the pivotal criteria within the dilemma [35]. The ARAS methodology, conceived by Turskis and Zavadskas (2010), is predicated on juxtaposing the utility function values of the alternatives against the utility function value of the optimal alternative, in contrast to other MCDM approaches [36-37]. Since the ARAS-G can effectively handle uncertainty and provides stable rankings through its utility-based structure, it was preferred in this study.

The stages of the ARAS-G methodology proposed by Turskis and Zavadskas (2010) are elucidated below [36]:

Step 1. Formulation of the Grey Decision-Making Matrix

$$\otimes X = \llbracket \otimes x_{ij} \rrbracket_{mxn} = \begin{bmatrix} [\otimes x_{01}] & [\otimes x_{02}] & \dots & [\otimes x_{0n}] \\ [\otimes x_{11}] & [\otimes x_{12}] & \dots & [\otimes x_{1n}] \\ [\otimes x_{21}] & [\otimes x_{22}] & \dots & [\otimes x_{2n}] \\ \vdots & \vdots & \ddots & \vdots \\ [\otimes x_{m1}] & [\otimes x_{m2}] & & [\otimes x_{mn}] \end{bmatrix}; \tag{19}$$

$i = 0, 1, \dots m;$

$j = 1, 2 \dots n;$

where m is the number of alternatives, n number of criteria, $\otimes x_{ij}$ is the grey number, which represents the performance value of the i_{th} alternative in terms of the j_{th} criterion, finally $\otimes x_{0j}$ is the optimal value of j_{th} criterion. If the optimal value of j_{th} criterion is unknown, then optimal value of j calculated as follows:

If the preferred values of the criterion are the maxima (benefit)

$$\otimes x_{0j} = \max_i \otimes x_{ij}. \tag{20}$$

If the preferred values of the criterion are the minima (cost)

$$\otimes x_{0j} = \min_i \otimes x_{ij}. \tag{21}$$

Step 2. Construction of the Normalized Grey Decision-Making Matrix

$$\otimes \overline{X} = \llbracket \otimes \bar{x}_{ij} \rrbracket_{mxn} = \begin{bmatrix} [\otimes \bar{x}_{01}] & [\otimes \bar{x}_{02}] & \dots & [\otimes \bar{x}_{0n}] \\ [\otimes \bar{x}_{11}] & [\otimes \bar{x}_{12}] & \dots & [\otimes \bar{x}_{1n}] \\ [\otimes \bar{x}_{21}] & [\otimes \bar{x}_{22}] & \dots & [\otimes \bar{x}_{2n}] \\ \vdots & \vdots & \ddots & \vdots \\ [\otimes \bar{x}_{m1}] & [\otimes \bar{x}_{m2}] & & [\otimes \bar{x}_{mn}] \end{bmatrix}; \tag{22}$$

$i = 0, 1, \dots m;$

$j = 1, 2 \dots n.$

The criteria, whose preferred values are the maxima, are normalized as follows

$$\otimes \bar{x}_{ij} = \frac{\otimes x_{ij}}{\sum_{i=0}^{m} \otimes x_{ij}}. \tag{23}$$

The criteria, whose preferred values are the minima, are normalized as follows

$$\otimes x_{ij} = \frac{1}{\otimes x_{ij}^*}, \ \otimes \bar{x}_{ij} = \frac{\otimes x_{ij}}{\sum_{i=0}^{m} \otimes x_{ij}}. \tag{24}$$

Step 3. Formulation of the Normalized-Weighted Grey Decision Matrix

$$\otimes \hat{X} = \llbracket \otimes \hat{x}_{ij} \rrbracket_{mxn} = \begin{bmatrix} [\otimes \hat{x}_{01}] & [\otimes \hat{x}_{02}] & \dots & [\otimes \hat{x}_{0n}] \\ [\otimes \hat{x}_{11}] & [\otimes \hat{x}_{12}] & \dots & [\otimes \hat{x}_{1n}] \\ [\otimes \hat{x}_{21}] & [\otimes \hat{x}_{22}] & \dots & [\otimes \hat{x}_{2n}] \\ \vdots & \vdots & \ddots & \vdots \\ [\otimes \hat{x}_{m1}] & [\otimes \hat{x}_{m2}] & & [\otimes \hat{x}_{mn}] \end{bmatrix}; \tag{25}$$

$i = 0, 1, \dots m;$

$j = 1, 2 \dots n;$

$\otimes \hat{x}_{ij} = \otimes \bar{x}_{ij} \cdot \otimes w_j, \quad i = 0, 1, \dots, m.$

Step 4. Determination of the Values of the Optimality Function

$$\otimes S_i = \sum_{j=1}^{n} \otimes \hat{x}_{ij}, \tag{26}$$

where $\otimes S_i$ is the grey value of the optimality function of i-th alternative. The performance degree of alternatives can be assessed according to this $\otimes S_i$ value.

$\otimes S_i$ remains a grey number; to convert a grey value to a crisp value, several methodologies exist. In this manuscript, the centre-of-area method is employed for transforming a grey value to a crisp value.

$$S_i \frac{1}{2}\left(\otimes S_i\left(\underline{l}, \overline{u}\right)\right), i = 0, 1, \dots, m. \tag{27}$$

Step 5. Calculation of the Utility Degree

$$K_i = \frac{S_i}{S_0}, i = 1, 2, \dots, m, \tag{28}$$

where S_i and S_0 represent the optimality criteria values, derived from Equation (28).

The intricate relative efficiency of the reasonable alternative can be assessed in accordance with the utility function values.

***Table 2** Summary of mathematical symbols and notation used in the study*

Symbol	Description
(l,m,u)	Triangular fuzzy number: lower-middle-upper values
M_j^i	Fuzzy pairwise comparison value between criteria *i* and *j*
$V(M_1 \geq M_2)$	Degree of possibility that one fuzzy number is greater than another
S_i	Significance value of criterion *i* (before normalization)
w_i	Normalized weight of criterion *i*
$\underline{y}^{\circ}_{ij} + \bar{y}^{\circ}_{ij}$	Grey performance interval of alternative *i* under criterion *j*
$\underline{A}_j + \overline{A}_j$	Grey average value for criterion *j*
SP_i	Weighted grey PDA value for alternative *i*
SN_i	Weighted grey NDA value for alternative *i*
TSO_i, TSN_i	Typical (crisp) values of weighted PDA and NDA
AS_i	Appraisal score of alternative *i*
x_i	Optimal value of criterion *j* (benefit/cost)
n_{ij}	Normalized grey value in ARAS-G
S_i	Optimality function value (grey)
S_j^*	Crisp optimality value (center-of-area)
K_i	Utility degree of alternative *i*

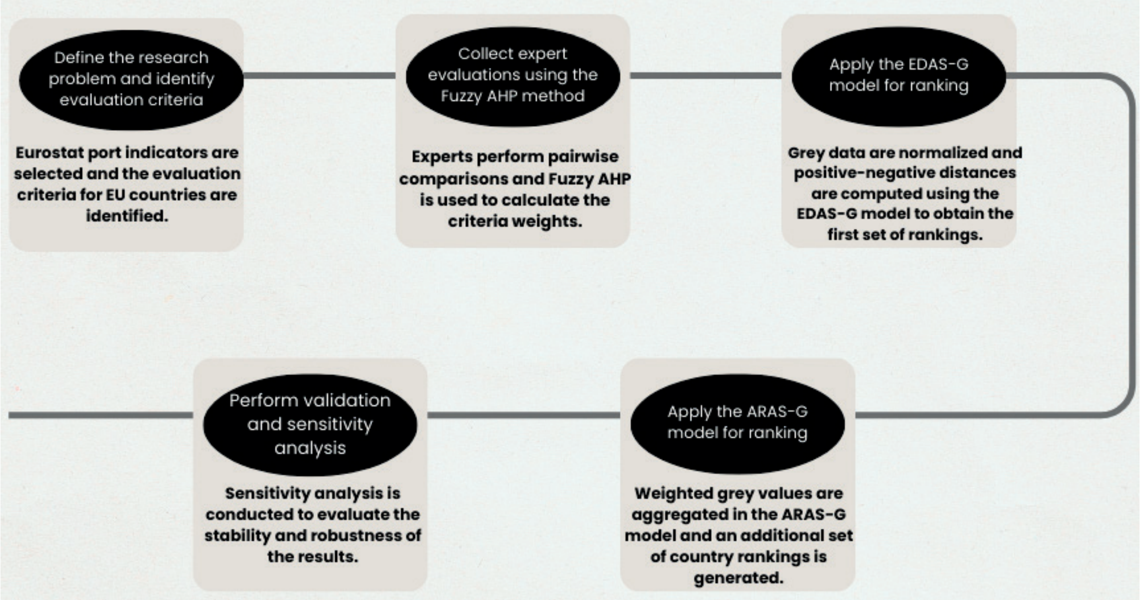

***Figure 1** Flow chart of the proposed model*

The mathematical symbols and notation employed within the Fuzzy AHP, EDAS-G, and ARAS-G procedures are systematically presented in Table 2.

4 Dataset and the application

Eurostat published its data 10 times: for the years 2014, 2015, 2016, 2017, 2018, 2019, 2020, 2021, 2022, and 2023 [38]. These data are published in two categories: quarterly and annually. In this study, the port performance is assessed through a multidimensional set of operational, economic, and environmental indicators. Since the data for some EU countries is not consistent from year to year, 24 countries were considered as alternatives. The fuzzy AHP method was used to weight the criteria. Among various MCDM methods, fuzzy AHP is the most widely used for addressing complex problems [39]. Fuzzy logic is compelling in solving complex problems that involve predictive thinking and decision-making processes [40]. Decision makers can flexibly express their opinions across different value ranges and represent their indecision numerically [41].

The flowchart of the proposed model is presented in Figure 1. The definitions of the criteria used in this study are shown in Table 3. These criteria encompass the

Table 3 *Criteria list, [38]*

Criteria	Definitions	Type
C1-Number of ship arrivals and departures	Vessels arriving at main ports by type	Benefit
C2-Container volume	Containers handled in main ports by loading status	Benefit
C3-Passenger traffic	Passengers embarked and disembarked in all ports	Benefit
C4-Cargo direction	Gross weight of goods by inwards and outwards movements	Benefit
C5-Cargo type	Gross weight of goods handled in main ports by cargo type	Benefit
C6-GDP	Gross domestic product (GDP) at current market prices	Benefit
C7-Air pollutants	Air pollutants by source sector	Cost
C8-Municipal waste management	Municipal waste by waste management operations	Benefit
C9-Share of renewable energy	Share of energy from renewable sources	Benefit

Table 4 *Fuzzy AHP-Based aggregated pairwise evaluation of criteria*

	C1	C2	C3	C4	C5	C6	C7	C8	C9
C1	(1.000, 1.000, 1.000)	(0.723, 0.433, 0.336)	(2.853, 5.078, 7.164)	(0.815, 0.695, 0.653)	(0.373, 0.206, 0.143)	(1.332, 1.442, 1.533)	(2.141, 4.360, 6.434)	(2.853, 5.078, 7.164)	(2.141, 4.360, 6.434)
C2	(1.377, 2.290, 2.942)	(1.000, 1.000, 1.000)	(4.076, 6.119, 8.139)	(0.903, 0.744, 0.688)	(0.465, 0.228, 0.154)	(1.549, 1.525, 1.572)	(2.408, 4.514, 6.544)	(3.000, 5.000, 7.000)	(3.000, 5.000, 7.000)
C3	(0.347, 0.196, 0.138)	(0.244, 0.161, 0.121)	(1.000, 1.000, 1.000)	(0.292, 0.174, 0.126)	(0.186, 0.133, 0.106)	(0.541, 0.373, 0.302)	(1.000, 0.641, 0.525)	(1.000, 0.642, 0.525)	(1.000, 0.330, 0.200)
C4	(1.222, 1.425, 1.513)	(1.105, 1.330, 1.445)	(3.380, 5.711, 7.841)	(1.000, 1.000, 1.000)	(0.581, 0.391, 0.315)	(1.715, 2.537, 3.147)	(2.141, 4.360, 6.434)	(2.954, 5.165, 7.237)	(2.667, 4.829, 6.882)
C5	(2.954, 5.165, 7.237)	(2.141, 4.360, 6.434)	(5.348, 7.361, 9.369)	(1.719, 2.531, 3.160)	(1.000, 1.000, 1.000)	(1.835, 2.667, 3.276)	(2.408, 4.514, 6.544)	(3.323, 5.348, 7.361)	(3.323, 5.348, 7.361)
C6	(0.746, 0.686, 0.647)	(0.641, 0.654, 0.626)	(1.838, 2.662, 3.289)	(0.579, 0.392, 0.313)	(0.540, 0.373, 0.301)	(1.000, 1.000, 1.000)	(1.243, 2.141, 2.798)	(1.552, 3.680, 5.720)	(1.243, 2.141, 2.798)
C7	(0.465, 0.228, 0.154)	(0.412, 0.221, 0.150)	(1.000, 1.549, 1.904)	(0.465, 0.228, 0.154)	(0.412, 0.221, 0.150)	(0.800, 0.465, 0.353)	(1.000, 1.000, 1.000)	(1.000, 1.933, 2.627)	(0.801, 0.464, 0.355)
C8	(0.347, 0.196, 0.138)	(0.330, 0.200, 0.140)	(1.000, 1.552, 1.904)	(0.337, 0.192, 0.137)	(0.299, 0.186, 0.133)	(0.642, 0.270, 0.173)	(1.000, 0.514, 0.381)	(1.000, 1.000, 1.000)	(0.801, 0.299, 0.186)
C9	(0.465, 0.228, 0.154)	(0.330, 0.200, 0.140)	(1.000, 3.000, 5.000)	(0.373, 0.206, 0.143)	(0.299, 0.186, 0.133)	(0.800, 0.465, 0.353)	(1.246, 2.137, 2.809)	(1.246, 3.323, 5.348)	(1.000, 1.000, 1.000)

key environmental, economic, and operational aspects of port activity to the extent permitted by data availability and comparability across EU countries.

4.1 Results obtained from the Fuzzy AHP

The importance levels of the criteria were determined by a group of five port experts (two academics from the Department of International Trade and Logistics, a Professor in Marketing, a Manager of an International Logistics Firm, and a Director of an International Port). There are studies in the literature that suggest the five decision makers are sufficient, and these studies were conducted with this number [42-44]. The linguistic expressions used by the decision makers were converted into triangular fuzzy numbers, and the evaluations were combined using geometric averaging to create a joint decision matrix. The resulting fuzzy AHP-based aggregated pairwise evaluation of the criteria is presented in Table 4. After applying the fuzzy AHP steps to the data, the weights of the Port Performance indicators are determined. The results are presented in Table 5.

According to the analysis results, the most important criterion is "Cargo Type," with a weight of 29%. This is followed by "Cargo Direction" (22%), "Container Volume" (21%), and "Number of Ship Arrivals and

***Table 5** Fuzzy AHP weight results for port performance indicators*

Criteria	W	%
C1	0.183	0.18
C2	0.214	0.21
C3	0.000	0.00
C4	0.217	0.22
C5	0.293	0.29
C6	0.063	0.06
C7	0.000	0.00
C8	0.000	0.00
C9	0.030	0.03

***Table 6** Grey decision matrix, criteria C_1 to C_3*

	C1	C2	C3
Belgium	(69, 1270)	(9726, 13192)	(22303, 25886)
Bulgaria	(1, 6)	(195, 282)	(2855, 3451)
Denmark	(30859, 44226)	(750, 1080)	(268047, 361601)
Germany	(16373, 31412)	(12680, 15918)	(104925, 117120)
Estonia	(8213, 15057)	(204, 288)	(28730, 32091)
Ireland	(814, 2867)	(797, 1176)	(11428, 12587)
Greece	(40895, 74956)	(3983, 6329)	(362036, 515899)
Spain	(14283, 34324)	(14358, 17663)	(136661, 204514)
France	(10445, 26638)	(4572, 6387)	(41967, 64092)
Croatia	(18779, 34142)	(138, 442)	(195657, 285456)
Italy	(55147, 86530)	(10247, 13080)	(381820, 505968)
Cyprus	(5, 76)	(300, 417)	(1818, 3179)
Latvia	(249, 1072)	(359, 479)	(5025, 6680)
Lithuania	(280, 368)	(350, 1051)	(4211, 5123)
Malta	(7955, 14622)	(77, 134)	(23288, 45967)
Netherlands	(857, 2010)	(11719, 15539)	(34997, 42488)
Poland	(1905, 2787)	(1793, 3107)	(14543, 18678)
Portugal	(551, 2147)	(2649, 3309)	(12002, 14189)
Romania	(0, 1)	(643, 830)	(3968, 5356)
Slovenia	(0, 34)	(676, 1048)	(1397, 2138)
Finland	(7089, 19514)	(1199, 1441)	(23997, 32175)
Sweden	(14020, 30523)	(1451, 1639)	(66785, 82191)
Norway	(1724, 6640)	(727, 915)	(54942, 71354)
Turkey	(289, 2233)	(8146, 12591)	(48685, 65846)

Departures" (18%), reflecting their substantial influence on operational and logistical performance. The GDP plays a moderate role with a weight of 6%, while the Share of Renewable Energy contributes minimally (3%). The Passenger Traffic, Air Pollutants, and Municipal Waste Management receive zero weight, indicating no significant effect within this evaluation structure. These zero-weight outcomes are common in fuzzy AHP studies and have similarly been reported in previous research [45-48]. Grey numbers were generated from data published over 10 years periods (2014-2023). For each country in the alternative list, the maximum and minimum values constituted the lower and upper values. The generated decision matrix was evaluated using both the EDAS-G and ARAS-G methods to obtain robust performance rankings.

4.2 Results obtained from the EDAS-G

After determining the criterion weights, grey numbers representing each country's performance during the specified time period were calculated for each criterion. The application of grey numbers

Table 7 *Grey decision matrix, criteria C_4 to C_6*

	C4	C5	C6
Belgium	(237852, 288827)	(237359, 288827)	(403003, 596321)
Bulgaria	(25258, 30997)	(25258, 30997)	(43024, 94709)
Denmark	(91382, 98230)	(76402, 87880)	(265635, 382309)
Germany	(267837, 303742)	(267837, 303742)	(2927430, 4185550)
Estonia	(23010, 43578)	(22040, 40172)	(20365, 38188)
Ireland	(47483, 55120)	(46325, 52636)	(200818, 520935)
Greece	(167036, 194468)	(145928, 180296)	(167539, 225197)
Spain	(427672, 497812)	(427672, 497812)	(1038949, 1498324)
France	(271964, 308629)	(266859, 303757)	(2153733, 2822455)
Croatia	(18551, 23607)	(14529, 21435)	(44284, 78048)
Italy	(443141, 509397)	(433598, 499193)	(1627405, 2128001)
Cyprus	(6948, 10268)	(6948, 10259)	(17482, 31340)
Latvia	(36153, 71836)	(33974, 70261)	(22790, 39072)
Lithuania	(37237, 52462)	(37237, 52462)	(36410, 73793)
Malta	(3370, 7211)	(3370, 7211)	(8948, 20542)
Netherlands	(545105, 607527)	(545105, 607525)	(678627, 1067599)
Poland	(68744, 136410)	(68107, 135977)	(408714, 748923)
Portugal	(79371, 93356)	(78956, 91916)	(173053, 267384)
Romania	(43753, 69250)	(42598, 68654)	(150528, 324369)
Slovenia	(18012, 23127)	(18012, 23127)	(37270, 63951)
Finland	(95640, 120488)	(93606, 118143)	(205855, 273318)
Sweden	(159611, 179949)	(159611, 179949)	(435641, 551781)
Norway	(193605, 225781)	(180267, 199621)	(322823, 425446)
Turkey	(378688, 535825)	(378688, 535825)	(626785, 1030514)

Table 8 *Grey decision matrix, criteria C_7 to C_9*

	C7	C8	C9
Belgium	(5860, 9770)	(406, 755)	(8, 15)
Bulgaria	(13450, 27410)	(334, 467)	(18, 23)
Denmark	(9740, 11660)	(759, 844)	(29, 44)
Germany	(168100, 278210)	(606, 648)	(14, 22)
Estonia	(5500, 12320)	(303, 389)	(26, 41)
Ireland	(4320, 9810)	(531, 631)	(9, 15)
Greece	(50700, 85860)	(488, 524)	(15, 25)
Spain	(31170, 161230)	(448, 482)	(16, 25)
France	(23370, 35440)	(497, 558)	(14, 22)
Croatia	(2450, 5320)	(377, 430)	(27, 31)
Italy	(20360, 37060)	(423, 462)	(17, 20)
Cyprus	(2790, 6960)	(488, 596)	(9, 20)
Latvia	(3270, 4440)	(351, 461)	(37, 44)
Lithuania	(4790, 6980)	(412, 467)	(24, 32)
Malta	(290, 2800)	(565, 748)	(5, 15)
Netherlands	(10510, 20450)	(468, 533)	(5, 17)
Poland	(90050, 206210)	(272, 370)	(11, 17)
Portugal	(11630, 22350)	(442, 545)	(30, 35)
Romania	(11980, 44290)	(216, 288)	(24, 26)
Slovenia	(2720, 6690)	(257, 429)	(21, 25)
Finland	(14330, 29150)	(468, 630)	(39, 51)
Sweden	(10630, 13150)	(390, 452)	(51, 66)
Norway	(1980, 2260)	(414, 799)	(68, 77)
Turkey	(266430, 368670)	(352, 398)	(13, 18)

***Table 9** The result of the EDAS-G*

	$\otimes Q_i^{+}$	$\otimes Q_i^{-}$	$\otimes S_i^{+}$	$\otimes S_i^{-}$	Rank
Belgium	(0.393, 1.520)	(1.241, 4.792)	(0.109, 0.221)	(0.930, 0.965)	6
Bulgaria	(0.000, 0.001)	(0.000, 0.003)	(0.716, 0.999)	(0.683, 0.773)	22
Denmark	(0.322, 0.587)	(1.014, 1.850)	(0.318, 0.561)	(0.822, 0.899)	9
Germany	(0.844, 2.307)	(2.662, 7.275)	(0.000, 0.019)	(0.994, 1.000)	4
Estonia	(0.000, 0.022)	(0.000, 0.068)	(0.632, 0.949)	(0.699, 0.799)	17
Ireland	(0.000, 0.002)	(0.000, 0.006)	(0.554, 0.882)	(0.720, 0.824)	19
Greece	(0.507, 1.281)	(1.599, 4.040)	(0.027, 0.210)	(0.933, 0.991)	7
Spain	(1.288, 3.009)	(4.062, 9.488)	(0.000, 0.016)	(0.995, 1.000)	2
France	(0.393, 1.007)	(1.240, 3.175)	(0.026, 0.161)	(0.949, 0.992)	8
Croatia	(0.179, 0.421)	(0.563, 1.329)	(0.590, 0.816)	(0.741, 0.813)	10
Italy	(1.659, 3.153)	(5.230, 9.942)	(0.002, 0.015)	(0.995, 0.999)	1
Cyprus	(0.000, 0.000)	(0.000, 0.000)	(0.781, 1.064)	(0.663, 0.752)	24
Latvia	(0.008, 0.025)	(0.024, 0.079)	(0.584, 0.945)	(0.700, 0.815)	16
Lithuania	(0.000, 0.011)	(0.000, 0.036)	(0.612, 0.946)	(0.700, 0.806)	20
Malta	(0.000, 0.000)	(0.000, 0.000)	(0.727, 1.048)	(0.667, 0.770)	23
Netherlands	(1.422, 2.800)	(4.484, 8.830)	(0.074, 0.172)	(0.945, 0.976)	3
Poland	(0.000, 0.024)	(0.000, 0.076)	(0.196, 0.739)	(0.766, 0.938)	14
Portugal	(0.000, 0.015)	(0.000, 0.047)	(0.344, 0.671)	(0.787, 0.891)	15
Romania	(0.000, 0.004)	(0.000, 0.014)	(0.548, 0.903)	(0.714, 0.826)	18
Slovenia	(0.000, 0.003)	(0.000, 0.011)	(0.708, 0.997)	(0.684, 0.775)	21
Finland	(0.010, 0.033)	(0.032, 0.105)	(0.318, 0.668)	(0.788, 0.899)	13
Sweden	(0.024, 0.150)	(0.075, 0.474)	(0.099, 0.352)	(0.888, 0.969)	12
Norway	(0.052, 0.242)	(0.163, 0.762)	(0.153, 0.350)	(0.889, 0.952)	11
Turkey	(0.743, 2.241)	(2.344, 7.066)	(0.027, 0.141)	(0.955, 0.991)	5

facilitates performance assessment of alternatives and incorporates a temporal dimension into the evaluation process [49]. Interval series containing upper and lower limits can be interpreted as grey numbers. Representing uncertain data with upper and lower bounds provides more information than the traditional real numbers [50]. The Grey decision matrix is shown in Table 6.

The weighted and normalized weighted grey aggregates of PDA and NDA, derived from the application of Equation (10) to (17), are presented in Table 9. The subsequent phase involves ranking the options. Values of the criteria functions for the alternatives S_i were computed using Equation (18). Values S_i and the ultimate ranking of the alternatives are likewise illustrated in Table 9.

4.3 Results obtained from the ARAS-G

The ranking of the alternatives was obtained directly from the decision matrix in Tables 6-8 using the obtained criterion weights, and the calculation procedure outlined in Equations (19) - (28) was applied. As presented in Table 10, the ARAS-G results provide the final ranking of the alternatives.

5 Sensitivity analysis

The sensitivity analysis can be performed by changing the criterion weights [51]. In this study, the sensitivity analysis, approach widely used in the literature, was adopted, and the model's stability was tested through the two alternative scenarios: equalizing the criterion weights and interchanging the highest and lowest weights [52-53]. The first scenario assumes the criteria weights are equal. The second is the scenario in which the criterion weights for the highest and lowest weights are interchanged. The results obtained from the two different scenarios are shown in Table 11.

The sensitivity analysis results indicate only limited changes in rankings between the two scenarios. While equalizing and redistributing the criteria weights may result in small shifts in the positions of some countries, the overall structure of the rankings is largely preserved, confirming the model's stability. For instance, Italy, Spain, and Germany consistently appeared among the highest-performing countries across both Scenario 1 and Scenario 2 in both EDAS-G and ARAS-G results. Turkey, Sweden, and the Netherlands also showed steady performance patterns, maintaining similar rank intervals under both weighting schemes.

Similarly, the lowest-performing countries exhibited

***Table 10** The result of the ARAS-G*

	S_s	K_s	Ranking
Optimal	0.1608		
Belgium	0.0611	0.3800	8
Bulgaria	0.0055	0.0345	22
Denmark	0.0419	0.2606	9
Germany	0.0901	0.5602	4
Estonia	0.0087	0.0541	20
Ireland	0.0113	0.0704	16
Greece	0.0697	0.4331	6
Spain	0.1114	0.6928	2
France	0.0629	0.3912	7
Croatia	0.0243	0.1512	12
Italy	0.1286	0.7996	1
Cyprus	0.0028	0.0172	24
Latvia	0.0099	0.0618	18
Lithuania	0.0089	0.0554	19
Malta	0.0041	0.0257	23
Netherlands	0.1081	0.6720	3
Poland	0.0218	0.1358	13
Portugal	0.0205	0.1275	15
Romania	0.0110	0.0685	17
Slovenia	0.0058	0.0360	21
Finland	0.0216	0.1344	14
Sweden	0.0357	0.2220	11
Norway	0.0371	0.2304	10
Turkey	0.0870	0.5407	5

***Table 11** The result of the sensitivity analysis*

	Proposed Model		Scenario 1		Scenario 2	
	EDAS-G	ARAS-G	EDAS-G	ARAS-G	EDAS-G	ARAS-G
Belgium	6	8	9	11	5	9
Bulgaria	22	22	24	24	22	24
Denmark	9	9	8	7	8	11
Germany	4	4	2	2	4	5
Estonia	17	20	16	18	18	22
Ireland	19	16	18	19	17	18
Greece	7	6	5	4	6	6
Spain	2	2	3	3	2	2
France	8	7	6	6	9	10
Croatia	10	12	11	13	10	12
Italy	1	1	1	1	1	1
Cyprus	24	24	20	22	19	21
Latvia	16	18	14	16	13	14
Lithuania	20	19	19	20	15	19
Malta	23	23	15	12	14	3
Netherlands	3	3	4	5	3	4
Poland	14	13	23	17	24	20
Portugal	15	15	17	15	20	15
Romania	18	17	22	23	23	23
Slovenia	21	21	21	21	16	16
Finland	13	14	13	14	21	17
Sweden	12	11	12	10	12	13
Norway	11	10	10	9	11	8
Turkey	5	5	7	8	7	7

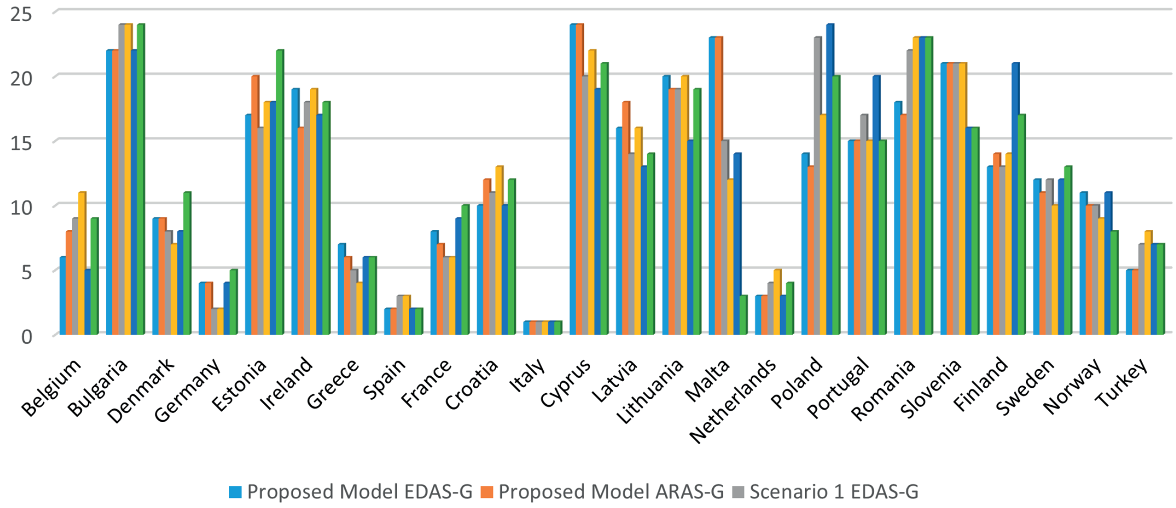

***Figure 2** The line chart of the sensitivity analysis*

strong stability. Cyprus, Malta, Bulgaria, Lithuania, and Slovenia remained in the bottom segment in both scenarios, confirming that the model's outputs do not fluctuate significantly with changes in the criteria weights. Figure 2 presents the line chart of the sensitivity analysis, clearly illustrating the stability of country rankings across the different weighting scenarios.

Overall, the sensitivity analysis demonstrates that the proposed Fuzzy AHP-based EDAS-G and ARAS-G model is robust and reliable. The rankings are not substantially affected by modifications in the weighting structure, indicating that the evaluation framework provides consistent and credible assessments of EU countries' port performance.

6 Discussion

In this section are summarised the elements discussed in previous sections and presents the framework of the key findings obtained from MCDM analyses. The article aim was to provide a systematic comparison of EU countries' port performance using selected criteria, creating a readily accessible reference for further scientific study.

6.1 Research design and findings

Ports are essential components of international trade networks, and their performance has significant implications for the competitiveness and resilience of national and regional economies. The findings of this study provide the new comparative insights into EU port performance by combining the fuzzy and grey-based MCDM approaches. Using expert-derived fuzzy judgments, the criterion weights obtained through the Fuzzy AHP highlight the relative influence of operational, economic, and environmental factors on port performance. The subsequent EDAS-G and ARAS-G analyses reveal consistent country rankings, offering a more nuanced interpretation of performance differences across the EU.

The results indicate that the proposed hybrid model can effectively differentiate between the higher and lower-performing ports, addressing the need for broader comparative assessments identified in the literature. Unlike the majority of existing studies-which typically focus on individual ports-this research provides a multi-country, multi-criteria perspective. This broader analytical scope contributes to a more comprehensive understanding of regional performance patterns and highlights areas where ports underperform relative to their peers.

Moreover, the sensitivity analysis confirms that the rankings remain largely stable under varying weight scenarios, underscoring the robustness of the model. These findings reinforce the value of holistic decision-making tools in port performance evaluation and support their wider adoption in both academic research and strategic industry applications.

The results of the hybrid MCDM analysis reveal that the "Cargo Type" (29%) is the most influential criterion affecting port performance. This indicates that the composition and diversity of cargo handled, such as bulk, liquid, and containerized goods, play a decisive role in shaping operational efficiency and competitiveness. Cargo diversity reflects the adaptability and functional complexity of ports, making it a key determinant of performance.

The second major determinant is the "Cargo Direction" (22%), showing that the balance and volume of inbound and outbound cargo movements are critical for assessing the strategic relevance and throughput efficiency of ports. Closely following, "Container Volume" (21%) emerges as another central indicator, highlighting the importance of containerized trade as a core driver of port activity in the EU.

"Number of Ship Arrivals and Departures" (18%) contributes substantially as well, emphasizing that the frequency of vessel calls remains a significant indicator of operational intensity and port utilization.

In contrast, several indicators have minimal or no impact on overall performance. Passenger Traffic, Air Pollutants, and Municipal Waste Management have weights of 0, suggesting that these variables do not meaningfully differentiate port performance within the EU context. GDP (6%) and Share of Renewable Energy (3%) carry relatively small weights, indicating that broader macroeconomic or sustainability-related factors play a limited role in shaping port efficiency compared to operational cargo-handling attributes.

Overall, the findings underscore that the EU ports are primarily evaluated based on their operational capacity, particularly their ability to handle diverse cargo types, maintain balanced cargo flows, and manage container volumes efficiently. These insights highlight the need for ports to strengthen the cargo-handling infrastructure, diversify operational capabilities, and optimize throughput to maintain and enhance their strategic position within the global supply chains.

6.2 Countries

The results of the EDAS-G and ARAS-G analyses suggest that Italy is the best performer. A review of the literature confirms that various academic studies support this finding. For example, Ruocco and Mazzarino (2026) investigated innovation in the Italian port sector and proposed strategies to improve port performance [54]. Barbagallo et al. (2026), on the other hand, examined ports from a sustainability perspective [55]. Thirdly, de Luca and Valentinuz (2024) assessed social sustainability [56]. These examples demonstrate that academic publications on the Italian port sector corroborate and lay the groundwork for the current findings.

Lupi et al. (2021) argued that Italian ports are well-positioned in terms of cost for cargo originating in North America and the Far East. They also stated that unloading Far Eastern cargo at Italian ports would provide additional benefits for many European countries. Together, these factors make Italian ports strategically important for Europe and could contribute to the development of the Italian port sector [57]. In a separate study, Danielis and Gregori (2013) examined Italian ports and found that they had advantages over Belgian ports [58]. Although the ports compared in this study are limited, the results obtained are consistent with those of the present study for both countries.

Pascual (2016) emphasises that Italy and Spain have a long history of maritime trade. This study shows that these two countries rank first and second, respectively, in terms of port performance. Just as geographical location can, a historical background in ports can give countries an advantage. Similarly, the Netherlands is renowned for its extensive maritime history and favourable geographical location for maritime activities. However, historical processes and geographical location alone are insufficient to determine a country's port performance [59]. As Caballini and Benzi (2023) stated, the efficiency of port processes is paramount. Reducing costs and expediting procedures, particularly customs clearance, are fundamental to overall performance. In this regard, countries would benefit from adopting a holistic approach to port operations and improving all stages of foreign trade [60]. Similarly, Belcore et al. (2024) emphasised the importance of speed in port processes [61].

As shown here, port performance can be evaluated from multiple perspectives. In this context, the countries in question were in this study examined using various criteria, thereby making a valuable addition to the existing body of literature on the subject. However, the evaluation is limited to data from accessible countries. Countries for which data could not be accessed, along with the relevant criteria, were excluded.

7 Conclusion

This study fills a gap in existing literature by evaluating the port performance of EU countries using an integrated approach based on fuzzy and grey logic. The fuzzy AHP was employed to determine the weights of the criteria, and the EDAS-G and ARAS-G method was used for the analysis. The results revealed that container volume and cargo diversity are particularly important performance factors. Italy, Spain, and the Netherlands stand out thanks to their strong infrastructure and high transaction volumes, whereas Malta, Bulgaria, and Cyprus could improve their capacity and efficiency. Furthermore, the sensitivity analysis results confirm that the method provides stable and reliable rankings. Overall, in the study is clearly demonstrated that EU ports must increase their container-handling capacities, adapt to cargo diversity, and improve operational efficiency if they are to remain competitive. In this respect, this research should serve as a strategic guide for policymakers and industry stakeholders alike.

7.1 Policy recommendations

Based on the findings of this study, several strategic recommendations can be made for business leaders and policymakers. Countries like Italy, Spain, and the Netherlands, which rank among the top in port performance, should continue investing in infrastructure to strengthen their role as regional logistics hubs. Businesses operating in these countries can leverage port efficiency to create more flexible and cost-effective supply chains. Policymakers should capitalize on this advantage by promoting green port technologies, digitalization, and sustainable infrastructure development. In contrast, countries, such as Malta, Bulgaria, and Cyprus, which rank lower, should prioritize modernizing their ports' infrastructure, increasing capacity, and attracting private sector investment. Transforming those ports into integrated logistics hubs can significantly increase their competitiveness and enable them to play a more active role in regional trade.

Furthermore, the port performance is influenced not only by physical capacity but by customs procedures, digital integration, and management efficiency, as well. Therefore, strengthening public-private partnerships and establishing transparent, data-driven decision-making processes in port governance are crucial. As a general recommendation for all the countries, regular monitoring of performance metrics and conducting benchmarking can provide a solid foundation for evidence-based policy development. Through such strategic initiatives, ports across Europe can transform from mere transit points into vital economic factors that contribute significantly to regional growth and global trade competitiveness.

7.2 Limitations of the study

From a country perspective, the study's focus on EU countries means global comparisons and comparisons of the performance dynamics of major non-European ports are not possible. Furthermore, the natural geographic and operational differences between island and continental countries, or between Mediterranean and Northern European ports, can structurally affect comparative analyses.

One of the main limitations of this study is its reliance on Eurostat data alone. Another significant limitation is that the analysis only included countries for which the data were available. From a methodological perspective, the assessment was based on expert judgements, and it was found that the ranking results were sensitive to the weighting of the criteria. Therefore, the two different methods were employed and a sensitivity analysis was performed.

7.3 Future research

Given limitations, it is recommended that the future studies comparatively use different fuzzy and grey-based MCDM methods and adopt multi-layered analysis approach that reduces the assessment to port and terminal levels. Adding new criteria to the analysis would broaden the scope of performance measurement. Significant contributions to literature could also be made by conducting the global comparisons that include major non-European trading ports, and by applying scenario analyses to examine the port performance in the context of economic shocks, supply chain crises, and geopolitical developments. Integrating MCDM methods with time series models or machine learning techniques would also be beneficial. It is believed that more comprehensive, multidimensional approaches developed in this direction would enable the port performance to be evaluated more comprehensively from academic and sectoral perspectives.

Acknowledgment

The authors received no financial support for the research, authorship and/or publication of this article.

Conflicts of interest

The authors declare that they have no known competing financial interests or personal relationships that could have appeared to influence the work reported in this paper.

Author Contributions

The first author was responsible for conducting the analyses, developing the overall framework of the paper, supervising the writing process, and performing the final proofreading. The second author contributed by writing the introduction, literature review, and conclusion sections, and assisted in shaping the overall structure of the manuscript. Both authors reviewed and approved the final version of the manuscript.

References

[1] ISSA-ZADEH, S. B., GARAY-RONDERO, C. L. Decarbonizing seaport maritime traffic: finding hope. *World* [online]. 2025, **6**(2), 47. eISSN 2673-4060. Available from: https://doi.org/10.3390/world6020047

[2] MOROS-DAZA, A., MOROS-MARCILLO, A., PACHECO-BUSTOS, C. A. Greening seaports: Evaluating impacts and policies for renewable energy systems. *Renewable and Sustainable Energy Reviews* [online]. 2025, **213**, 115475. ISSN 1364-0321, eISSN 1879-0690. Available from: https://doi.org/10.1016/j.rser.2025.115475

[3] BUI, T. U., CHO, G. S. Efficiency analysis of container ports in Vietnam using stochastic frontier analysis. *Journal of Ocean Engineering and Technology* [online]. 2025, **39**(1), p. 56-62. eISSN 2287-6715. Available from: https://doi.org/10.26748/KSOE.2024.100

[4] LU, Z., QIU, W. Resilience analysis of seaport-dry-port network in container transport: multi-stage load redistribution dynamics following cascade failure. *Systems* [online]. 2025, **13**(4), 299. eISSN 2079-8954. Available from: https://doi.org/10.3390/systems13040299

[5] GONCALVES, M., SALGADO, C., DE SOUSA, A., TEIXEIRA, L. Data storytelling and decision-making in seaport operations: a new approach based on business intelligence. *Sustainability* [online]. 2025, **17**(1), 337. eISSN 2071-1050. Available from: https://doi.org/10.3390/su17010337

[6] PEREIRA, M. T., ROCHA, N., SILVA, F. G., MOREIRA, M. A. L., ALTINKAYA, Y. O., PEREIRA, M. J. Process optimization in sea ports: integrating sustainability and efficiency through a novel mathematical model. *Journal of Marine Science and Engineering* [online]. 2025, **13**(1), 119. eISSN 2077-1312. Available from: https://doi.org/10.3390/jmse13010119

[7] NEUGEBAUER, J., HEILIG, L., VOSS, S. Dynamic driving in seaports: current and future applications. *Cleaner Logistics and Supply Chain* [online]. 2025, **14**, 100203. eISSN 2772-3909. Available from: https://doi.org/10.1016/j.clscn.2025.100203

[8] LOCAITIENE, V., CIZIUNIENE, K. Assessing the logistics efficiency of Baltic region seaports through DEA-BCC and spatial analysis. *Journal of Marine Science and Engineering* [online]. 2024, **13**(1), 50. eISSN 2077-1312. Available from: https://doi.org/10.3390/jmse13010050

[9] MOHSENDOKHT, M., KONTOVAS, C., CHANG, C.-H., QU, Z., LI, H., YANG, Z. Resilience analysis of seaports: a critical review of development and research directions. *Maritime Policy and Management* [online]. 2025, latest articles, p. 1-36. ISSN 0308-8839, eISSN 1464-5254. Available from: https://doi.org/10.1080/03088839.2025.2483410

[10] OZEKENCI, E. K. Financial and environmental performance analysis of logistics company on the Fortune 500 by MEREC-based AROMAN methods. *Politik Ekonomik Kuram/Political Economic Theory* [online]. 2024, **8**(3), p. 709-724. eISSN 2587-2567. Available from: https://doi.org/10.30586/pek.1517266

[11] OZEKENCI, E. K. A hybrid MPSI-Extended AROMAN decision-making model for assessing green logistics performance: the case of Asia-Pacific countries. *Logforum* [online]. 2025, **21**(1), 7. ISSN 1895-2038, eISSN 1734-459X. Available from: https://doi.org/10.17270/J.LOG.001154

[12] LU, W., CHOI, S.-B., YEO, G.-T. Resilient route selection of oversized cargo transport: the case of South Korea-Kazakhstan. *The International Journal of Logistics Management* [online]. 2022, **33**(2), p. 410-430. ISSN 0957-4093, eISSN 1758-6550. Available from: https://doi.org/10.1108/IJLM-11-2020-0445

[13] KIEU, P. T., NGUYEN, V. T., NGUYEN, V. T., HO, T. P. A spherical fuzzy analytic hierarchy process (SF-AHP) and combined compromise solution (CoCoSo) algorithm in distribution center location selection: a case study in agricultural supply chain. *Axioms* [online]. 2021, **10**(2), 53. eISSN 2075-1680. Available from: https://doi.org/10.3390/axioms10020053

[14] ZHOU, Y., LI, Z., DUAN, W. Exploring the dynamic impact of the Northern Sea Route on China-Europe multimodal transportation competition in the context of the Belt and Road Initiative. *Ocean and Coastal Management* [online]. 2024, **257**, 107346. ISSN 0964-5691, eISSN 0964-5691. Available from: https://doi.org/10.1016/j.ocecoaman.2024.107346

[15] ILYAS, M., JIN, Z., ULLAH, I., ALMUJIBAH, H. A fuzzy logic-based risk assessment framework for the crude oil transportation supply chain. *Ocean Engineering* [online]. 2024, **311**(2), 118997. ISSN 0029-8018, eISSN 1873-5258. Available from: https://doi.org/10.1016/j.oceaneng.2024.118997

[16] UR REHMAN, O., ALI, Y. Optimality study of China's crude oil imports through China Pakistan economic corridor using fuzzy TOPSIS and cost-benefit analysis. *Transportation Research Part E: Logistics and Transportation Review* [online]. 2021, **148**, 102246. ISSN 1366-5545, eISSN 1878-5794. Available from: https://doi.org/10.1016/j.tre.2021.102246

[17] BAGOCIUS, V., ZAVADSKAS, E. K., TURSKIS, Z. Selecting a location for a liquefied natural gas terminal in the Eastern Baltic Sea. *Transport* [online]. 2014, **29**(1), p. 69-74. ISSN 1648-4142, eISSN 1648-3480. Available from: https://doi.org/10.3846/16484142.2014.897996

[18] KINE, H. Z., SHIFERAW, Z., GEBRESENBET, G., TAVASSZY, L., LJUNGBERG, D. GIS-based multi-criteria decision-making approach for dry port location analysis: the case of Ethiopia. *Research in Transportation Business and Management* [online]. 2025, **60**, 101370. ISSN 2210-5395, eISSN 2210-5409. Available from: https://doi.org/10.1016/j.rtbm.2025.101370

[19] KOLAKOWSKI, P., GIL, M., WROBEL, K. Stakeholders' view on selecting a prospective location for marine alternative fuels bunkering station. *Marine Policy* [online]. 2024, **164**, 106164. ISSN 0308-597X, eISSN 1872-9460. Available from: https://doi.org/10.1016/j.marpol.2024.106164

[20] WANG, C., LI, L. A two-phase model for sustainable location of dry ports: a case of Ningbo-Zhoushan Port in China. *Transportation Planning and Technology* [online]. 2023, **46**(3), p. 304-334. ISSN 0308-1060, eISSN 1029-0354. Available from: https://doi.org/10.1080/03081060.2023.2184818

[21] GARG, C. P., KASHAV, V., WANG, X. Evaluating sustainability factors of green ports in China under fuzzy environment. *Environment, Development and Sustainability* [online]. 2023, **25**(8), p. 7795-7821. eISSN 1573-2975. Available from: https://doi.org/10.1007/s10668-022-02375-7

[22] IGHRAVWE, D. E., MASHAO, D. Application of a fuzzy multi-criteria decision framework for safety-critical maritime infrastructure evaluation. *Heliyon* [online]. 2023, **9**(7), e17782. eISSN 2405-8440. Available from: https://doi.org/10.1016/j.heliyon.2023.e17782

[23] PAMUCAR, D., GORCUN, O. F. Evaluation of the European container ports using a new hybrid fuzzy LBWA-CoCoSo'B techniques. *Expert Systems with Applications* [online]. 2022, **203**, 117463. ISSN 0957-4174, eISSN 1873-6793. Available from: https://doi.org/10.1016/j.eswa.2022.117463

[24] LAMII, N., BENTALEB, F., FRI, M., MABROUKI, C., SEMMA, E. A. Use of DELPHI-AHP method to identify and analyze risks in seaport dry port system. *Transactions on Maritime Science* [online]. 2022, **11**(1), p. 185-206. ISSN 1848-3305, eISSN 1848-3313. Available from: https://doi.org/10.7225/toms.v11.n01.w12

[25] GORCUN, O. F. Efficiency analysis of Black Sea container seaports: application of an integrated MCDM approach. *Maritime Policy and Management* [online]. 2021, **48**(5), p. 672-699. ISSN 0308-8839, eISSN 1464-5254. Available from: https://doi.org/10.1080/03088839.2020.1783467

[26] KANNIKA, N., HUA TAN, P. K., PAWAR, P. K. Enhancing the competitiveness of container seaports through sustainability: a case study of Thailand. *Procedia Manufacturing* [online]. 2019, **39**, p. 1587-1596. ISSN 2351-9789. Available from: https://doi.org/10.1016/j.promfg.2020.01.283

[27] BURHAN, H. A. Sustainability in industry, innovation and infrastructure: a MCDM based performance evaluation of European Union and Turkey for sustainable development goal 9 (SDG 9). *Verimlilik Dergisi Journal of Productivity* [online]. 2024, **year 2024**, p. 21-38. ISSN 1013-1388, eISSN 2757-6973. Available from: https://doi.org/10.51551/verimlilik.1333767

[28] AGYEKUM, E. B., VELKIN, V. I. Multi-criteria decision-making approach in assessing the key barriers to the adoption and use of SWH in West Africa - combination of modified Delphi and Fuzzy AHP. *International Journal of Thermofluids* [online]. 2024, **23**, 100795. eISSN 2666-2027. Available from: https://doi.org/10.1016/j.ijft.2024.100795

[29] NADEEM, R., SINGH, R., PATIDAR, A., YUSLIZA, M. Y., RAMAYAH, T., AZMI, F. T. Prioritizing determinants of employees' green behavior in the Indian hotel industry: an analytic hierarchy process (AHP) and fuzzy AHP approach. *Journal of Hospitality and Tourism Insights* [online]. 2025, **8**(8), p. 2900-2919. ISSN 2514-9792, eISSN 2514-9806. Available from: https://doi.org/10.1108/JHTI-07-2024-0737

[30] RAJA, S., PRAVEENKUMAR, V. Optimizing additive manufacturing parameters for graphene-reinforced PETG impeller production: a fuzzy AHP-TOPSIS approach. *Results in Engineering* [online]. 2024, **24**, 103018. eISSN 2590-1230. Available from: https://doi.org/10.1016/j.rineng.2024.103018

[31] CHANG, D. Y. Applications of the extent analysis method on fuzzy AHP. *European Journal of Operational Research* [online]. 1996, **95**(3), p. 649-655. ISSN 0377-2217, eISSN 1872-6860. Available from: https://doi.org/10.1016/0377-2217(95)00300-2

[32] VAN LAARHOVEN, P. J. M., PEDRYCZ, W. A fuzzy extension of Saaty's priority theory. *Fuzzy Sets and Systems* [online]. 1983, **11**(1-3), p. 229-241. ISSN 0165-0114, eISSN 1872-6801. Available from: https://doi.org/10.1016/S0165-0114(83)80082-7

[33] IMRAN, R., ULLAH, K. Circular intuitionistic fuzzy EDAS approach: a new paradigm for decision-making in the automotive industry sector. *Spectrum of Engineering and Management Sciences* [online]. 2025, **3**(1), 76-92. eISSN 3009-3309. Available from: https://doi.org/10.31181/sems31202537i

[34] STANUJKIC, D., ZAVADSKAS, E. K., GHORABAEE, M. K., TURSKIS, Z. An extension of the EDAS method based on the use of interval grey numbers. *Studies in Informatics and Control* [online]. 2017, **26**(1), p. 5-12. ISSN 1220-1766, eISSN 1841-429X. Available from: https://doi.org/10.24846/v26i1y201701

[35] SUMRIT, D., KEERATIBHUBORDEE, J. Risk assessment framework for reverse logistics in waste plastic recycle industry: a hybrid approach incorporating FMEA decision model with AHP-LOPCOW-ARAS under trapezoidal fuzzy set. *Decision Making: Applications in Management and Engineering* [online]. 2025, **8**(1), p. 42-81. ISSN 2560-6018, eISSN 2620-0104. Available from: https://doi.org/10.31181/dmame812025984

[36] TURSKIS, Z., ZAVADSKAS, E. K. A novel method for multiple criteria analysis: grey additive ratio assessment (ARAS-G) method. *Informatica* [online]. 2010, **21**(4), p. 597-610. ISSN 0868-4952, eISSN 1822-8844. Available from: https://doi.org/10.15388/Informatica.2010.307

[37] KARADAG AK, O., HAZAR, A., BABUSCU, S. Evaluation of the financial performance of development and investment banks with entropy-based ARAS method. *Macroeconomics and Finance in Emerging Market Economies* [online]. 2025, **18**(2), p. 441-461. ISSN 1752-0843, eISSN 1752-0851. Available from: https://doi.org/10.1080/17520843.2022.2035523

[38] EUROSTAT - European statistics database [online]. 2024. Available from: https://ec.europa.eu/eurostat

[39] NAZIM, M., MOHAMMAD, C. W., SADIQ, M. A comparison between fuzzy AHP and fuzzy TOPSIS methods to software requirements selection. *Alexandria Engineering Journal* [online]. 2022, **61**(12), p. 10851-10870. ISSN 1110-0168, eISSN 2090-2670. Available from: https://doi.org/10.1016/j.aej.2022.04.005

[40] YU, D., KOU, G., XU, Z., SHI, S. Analysis of collaboration evolution in AHP research: 1982-2018. *International Journal of Information Technology and Decision Making* [online]. 2021, **20**(1), p. 7-36. ISSN 0219-6220, eISSN 1793-6845. Available from: https://doi.org/10.1142/S0219622020500406

[41] HASELI, G., SHEIKH, R., WANG, J., TOMASKOVA, H., TIRKOLAEE, E. B. A novel approach for group decision making based on the best-worst method (G-BWM): application to supply chain management. *Mathematics* [online]. 2021, **9**(16), 1881. eISSN 2227-7390. Available from: https://doi.org/10.3390/math9161881

[42] BOONMEE, C., TANPRUTTIANUNT, N. A fuzzy multi-criteria decision framework for community isolation center site selection to enhance public health resilience. *Journal of Safety Science and Resilience* [online]. 2025, **7**(1), p. 1-24. eISSN 2666-4496. Available from: https://doi.org/10.1016/j.jnlssr.2025.100227

[43] HASHMI, N., SHANKARANARAYANAN, G., MALONE, T. W. Is bigger better? A study of the effect of group size on collective intelligence in online groups. *Decision Support Systems* [online]. 2023, **167**, 113914. ISSN 0167-9236, eISSN 1873-5797. Available from: https://doi.org/10.1016/j.dss.2022.113914

[44] PUSKA, A., STILIC, A., STEVIC, Z. A comprehensive decision framework for selecting distribution center locations: a hybrid improved fuzzy SWARA and fuzzy CRADIS approach. *Computation* [online]. 2023, **11**(4), 73. eISSN 2079-3197. Available from: https://doi.org/10.3390/computation11040073

[45] LIMA-JUNIOR, F. R., CARPINETTI, L. C. R. Dealing with the problem of null weights and scores in fuzzy analytic hierarchy process. *Soft Computing* [online]. 2020, **24**(13), p. 9557-9573. ISSN 1432-7643, eISSN 1433-7479. Available from: https://doi.org/10.1007/s00500-019-04464-8

[46] SEQUEIRA, M., HILLETOFTH, P. Applying fuzzy analytical hierarchy process to reshoring decisions with complexity and uncertainty. In: 9th International Conference on Operations and Supply Chain Management: proceedings. 2019. ISBN 9786027060470, p. 1-13.

[47] SEQUEIRA, M., ADLEMO, A., HILLETOFTH, P. A hybrid fuzzy-AHP-TOPSIS model for evaluation of manufacturing relocation decisions. *Operations Management Research* [online]. 2023, **16**(1), p. 164-191. ISSN 1936-9735, eISSN 1936-9743. Available from: https://doi.org/10.1007/s12063-022-00284-6

[48] VINOGRADOVA-ZINKEVIC, I. Comparative sensitivity analysis of some fuzzy AHP methods. *Mathematics* [online]. 2023, **11**(24), 4984. eISSN 2227-7390. Available from: https://doi.org/10.3390/math11244984

[49] YILDIRIM, B. F., ADIGUZEL MERCANGOZ, B. Evaluating the logistics performance of OECD countries by using fuzzy AHP and ARAS-G. *Eurasian Economic Review* [online]. 2020, **10**(1), p. 27-45. eISSN 2147-429X. Available from: https://doi.org/10.1007/s40822-019-00131-3

[50] YE, J., MA, Z., XIONG, P., GUO, X. An interval feature discrete Grey-Markov model based on data distributions and applications. *Applied Mathematical Modelling* [online]. 2023, **117**, p. 802-819. ISSN 0307-904X, eISSN 1872-8480. Available from: https://doi.org/10.1016/j.apm.2023.01.017

[51] ROY, P. K., SHAW, K. A multicriteria credit scoring model for SMEs using hybrid BWM and TOPSIS. *Financial Innovation* [online]. 2021, **7**(1), 77. eISSN 2199-4730. Available from: https://doi.org/10.1186/s40854-021-00295-5

[52] DEMIR, H., ARSLAN, C. A sensitivity analysis on a MCDM problem evaluated by ARAS method. *Journal of Mechanical Engineering: Prakash* [online]. 2022, **1**(1), p. 27-38. ISSN 0974-6846. Available from: https://doi.org/10.56697/JMEP.2022.1104

[53] OZAYTURK, I., OZEKENCI, E. K. Analysis of trade competitiveness of the world's leading textiles exporters by hybrid MCDM methods. *Isletme Arastırmaları Dergisi/Journal of Business Research* [online]. 2024, **16**(1), p. 166-186. ISSN 1309-0712. Available from: https://doi.org/10.20491/isarder.2024.1784

[54] RUOCCO D., MAZZARINO M. Port-system-innovation: a comprehensive model for freight railway digital automation. A case study of Trieste Port, Italy [online]. In: *Computational Science and its Applications - ICCSA 2025 workshops. ICCSA 2025. Lecture Notes in Computer Science. Vol 15897.* GERVASI, O., MURGANTE, B., GARAU, CH., KARACA, Y., FAGINAS LAGO, M. N., SCORZA, F., BRAGA, A. C. (Eds.). Cham: Springer, 2026. ISBN 978-3-031-97659-9, eISBN 978-3-031-97660-5. Available from: https://doi.org/10.1007/978-3-031-97648-3_9

[55] BARBAGALLO, A., TORRISI, V., RICCI, S., TWRDY, E., IGNACCOLO, M. Assessing ship emissions: an estimation approach applied to the Port of Catania (Italy) [online]. In: *Computational Science and its Applications - ICCSA 2025 workshops. ICCSA 2025. Lecture Notes in Computer Science. Vol 15897.* GERVASI, O., MURGANTE, B., GARAU, CH., KARACA, Y., FAGINAS LAGO, M. N., SCORZA, F., BRAGA, A. C. (Eds.). Cham: Springer, 2026. ISBN 978-3-031-97659-9, eISBN 978-3-031-97660-5. Available from: https://doi.org/10.1007/978-3-031-97660-5_9

[56] DE LUCA, P., VALENTINUZ, G. Social sustainability for health and well-being in port areas: a general framework proposal with a social value approach. *Corporate Social Responsibility and Environmental Management* [online]. 2024, **31**(6), p. 6234-6245. ISSN 1535-3958, eISSN 1535-3966. Available from: https://doi.org/10.1002/csr.2920

[57] LUPI, M., PRATELLI, A., CAMPI, F., CECCOTTI, A., FARINA, A. The “Island Formation” within the hinterland of a port system: the case of the padan plain in Italy. *Sustainability* [online]. 2021, **13**(9), 4819. eISSN 2071-1050. Available from: https://doi.org/10.3390/su13094819

[58] DANIELIS, R., GREGORI, T. An input-output-based methodology to estimate the economic role of a port: the case of the port system of the Friuli Venezia Giulia Region, Italy. *Maritime Economics and Logistics* [online]. 2013, **15**, p. 222-255. ISSN 1479-2931, eISSN 1479-294X. Available from: https://doi.org/10.1057/mel.2013.1

[59] PASCUAL, R. M. G., ACEROS, C. The sword trade between Spain and Italy in the 16th and 17th centuries/ El comercio de espadas entre Espana e Italia en los siglos XVI y XVII (in Spanish). *Gladius* [online]. 2016, **36**, p. 161-179. eISSN 1988-4168. Available from: https://doi.org/10.3989/gladius.2016.0008

[60] CABALLINI, C., BENZI, M. Fast corridors: innovative customs processes and technology to increase supply chain competitiveness. The case of IKEA Italy. *Transportation Research Interdisciplinary Perspectives* [online]. 2023, **21**, 100909. eISSN 2590-1982. Available from: https://doi.org/10.1016/j.trip.2023.100909

[61] BELCORE, O. M., POLIMENI, A., DI GANGI, M. Performance analysis for a maritime port with high-frequency services: an Italian case study. *Case Studies on Transport Policy* [online]. 2024, **17**, 101263. ISSN 2213-624X, eISSN 2213-6258. Available from: https://doi.org/10.1016/j.cstp.2024.101263

AN ANALYTICAL MODEL FOR CALCULATING THE ACTIVE INTERACTION FORCES OF THE WORKING BODY OF EARTH-MOVING MACHINES WITH STICKY SOILS

Nurbol Kamzanov[1], **Shynbolat Tynybekov**[1], **Nursat Baikenzhe**[1], **Guldariya Naimanova**[2], **Bakytzhan Kyrgyzbay**[2], **Rustem Kozbagarov** [2,*]

[1]Satbayev University, Almaty, Republic of Kazakhstan
[2]Mukhametzhan Tynyshbayev ALT University, Almaty, Republic of Kazakhstan

*E-mail of corresponding author: r.kozbagarov@alt.edu.kz

Nurbol Kamzanov 0000-0002-2420-8362,
Nursat Baikenzhe 0009-0000-0290-9056,
Bakytzhan Kyrgyzbay 0009-0004-0317-7917,
Shynbolat Tynybekov 0009-0002-6146-2076,
Guldariya Naimanova 0000-0003-4619-7243,
Rustem Kozbagarov 0000-0002-7258-0775

Resume

In this study is presented an analytical mathematical model developed to determine the forces arising during the active penetration of machine working bodies into sticky rocks. The methodology is based on the method of element-by-element calculation of resistances, where the contact zone is divided into discrete prisms of material. As a result of the analysis, a final formula for the total penetration force is derived. This formula shows the dependence of the resistance force on the dimensions of the tool (thickness, depth, angle of sharpening) and the physical characteristics of the rock (internal friction, adhesion, stickiness). The model serves as a reliable engineering tool for the design and optimization of working bodies of earthmoving and mining equipment.

Article info
Received 31 July 2025
Accepted 30 October 2025
Online 10 November 2025

Keywords:
sticky rock
working body
earth-moving machine
angle of attack
penetration depth

Available online: https://doi.org/10.26552/com.C.2026.002

ISSN 1335-4205 (print version)
ISSN 2585-7878 (online version)

1 Introduction

The development and operation of earthmoving and mining machines, such as bulldozers, excavators, scrapers, and loaders, is inextricably linked to the problem of interaction between their working parts and the environment being processed. The efficiency, energy consumption, and service life of these machines directly depend on the resistance forces that arise during cutting, digging, and moving soil and rock [1-3]. The so-called sticky rocks pose a particular challenge for mechanized mining. These include wet clayey and loamy soils, oil-bituminous sands, and other materials with high adhesion (stickiness) to the surfaces of working bodies [4-5].

Working with sticky soils involves a number of technological difficulties [4-7]. First, high adhesive forces, combined with internal friction and cohesive forces, lead to a significant increase in overall digging resistance. This requires increased machine power, leads to fuel overconsumption, and reduces the overall productivity. Secondly, material sticking to blades, buckets, and knives distorts their working geometry, effectively "dulling" the cutting edges, which further exacerbates the first problem. Thirdly, difficulties arise with the complete unloading of buckets and bodies, which requires additional time and the use of special cleaning systems [8-9].

To solve these problems, engineers and researchers are pursuing two main approaches: developing the new materials and coatings for working parts that reduce adhesion, and optimizing the geometry of the working parts themselves. The second approach requires reliable calculation methods that allow interaction forces to be predicted at the design stage. Mathematical modelling becomes an indispensable tool in this context. It allows for a systematic study of the influence of each design parameter (e.g., cutting angle, blade thickness) on the forces that arise and finding their optimal combination [10-11].

The processes of interaction between the working bodies and material can be divided into active and passive. Passive interaction is mainly caused by the pressure of the environment on the working body (for example, soil pressure on a blade), while active interaction is associated with the forced penetration of the working body into the mass with the supply of external energy. It is precisely the active interaction at the cutting edge of the tool that is the key and most energy-intensive process determining the cutting resistance [12-14].

The purpose of this article is to present a detailed mathematical model describing the active interaction under normal (perpendicular) impact of the working body on an array of sticky rock. This model allows us to obtain an analytical formula for calculating the penetration force, which enables design engineers to quantitatively assess the effectiveness of various design solutions.

2 Materials and methods

2.1 General approach and assumptions

The proposed mathematical model of active interaction is based on the method of element-by-element calculation of resistances. The essence of the method is that the continuous medium in the zone in front of the working body is mentally divided into several separate elements (prisms) bounded by the assumed planes of sliding. Next, the equilibrium conditions are considered for each of these prisms, which allows to construct a system of equations and find the desired forces [13-14].

The model considers two interaction options depending on the angle of the working body: with and without the formation of a compacted core in front of it. This article presents a more general case-with the presence of a compacted core, which effectively becomes an extension of the working body and changes the conditions of its interaction with the environment.

The following fundamental assumptions were made when constructing the model:

1. Prisms of material bounded by planes of slip do not compact during interaction, but move as single, “solidified” bodies. This assumption is generally accepted in classical soil cutting theories and significantly simplifies the mathematical apparatus [15-16];
2. The planes of sliding along which the material prisms shift are straight lines and emerge onto the free surface at an angle equal to the angle of internal friction of the sticky rock (φ) [15-16].

2.2 Physical model and force system

The physical model of the process is shown in Figure 1 in the source document. A working body with a thickness of a and a width of b with a sharpening angle of α is inserted to a depth of h into the sticky rock mass. A compacted core is formed in front of it, and then the mass is divided into three main sliding prisms [17-19].

Here is considered the general case of normal impact of the working body on the material surface, when the compacted core complements the working body. The equilibrium conditions of the material prisms, bounded by sliding planes, are analyzed sequentially [11, 13]:

- for a prism of material with cross-section *bdec*:

$$\begin{aligned}&\sum x = -N_3 - N_4\sin\varphi - (N_4 tg\varphi + tg\varphi K_{v2}p_2S_4)\\&\cos\psi + N_3\sin\varphi + (N_5 tg\varphi + tg\varphi K_{v2}p_2S_5)\cos\psi = 0;\\&\sum y = -N_3 tg\varphi - tg\varphi K_{v2}p_2S_3 + N_4\cos\psi -\\&-(N_4 tg\varphi + tg\varphi K_{v2}p_2S_4)\times\sin\psi - N_5\cos\psi -\\&-N_5\cos\psi + (N_5 tg\varphi + tg\varphi K_{v2}p_2S_5)\sin\psi - G_2 = 0;\end{aligned}\tag{1}$$

- for a prism of material with a cross section *bfd:*

$$\begin{aligned}&\sum x = -N_5\sin\psi - (N_5 tg\varphi + tg\varphi K_{v2}p_2S_5)\\&\cos\psi + N_6 = 0,\\&\sum y = -N_5\cos\psi - (N_5 tg\varphi + tg\varphi K_{v2}p_2S_5)\\&\sin\psi - N_6 tg\rho K_{v1} - tg\rho K_{v1}p_1S_6 - G_3 = 0;\end{aligned}\tag{2}$$

- for a prism of material with cross section *abc*:

$$\begin{aligned}&\sum x = N_1\cos\varepsilon - (N_1 tg\varphi + tg\varphi K_{v2}p_2S_1)\sin\varepsilon +\\&+N_2\cos\varepsilon + (N_2 tg\varphi + tg\varphi K_{v2}p_2S_2)\sin\varepsilon - N_3 = 0;\\&\sum y = -N_1\sin\varepsilon - (N_1 tg\varphi + tg\varphi K_{v2}p_2S_1)\cos\varepsilon +\\&+N_2\sin\varepsilon - (N_2 tg\varphi + tg\varphi K_{v2}p_2S_2)\cos\varepsilon +\\&+N_3 tg\varphi + tg\varphi K_v p_2S_3 - G_1,\end{aligned}\tag{3}$$

where N_1, N_2, N_3, N_4, N_5 and N_6, - normal reaction forces acting perpendicular to the corresponding sliding surfaces and working body surfaces; G_1, G_2 and G_3 - the gravitational forces (weight) of the corresponding soil prisms involved in the interaction; S_1, S_2, S_3, S_4, S_5, S_6 - the areas of the corresponding sliding surfaces on which the forces act; K_{v1}, K_{v2} - coefficients of the influence of speed on stickiness and adhesion indicators; φ - angle of internal friction; ψ - angle of inclination of rock slip (shear) planes relative to the horizontal; ρ - angle of external friction; p_1 - specific adhesion; p_2 - traction.

For each of the three prisms, two equilibrium equations are formulated (the sums of the projections of all the forces on the horizontal and vertical axes are zero). This leads to a system of six linear algebraic equations with six unknown reaction forces.

The values of the sliding plane area S_1, S_2, … , S_5, S_6 and the weight of the material volume G_1, G_2 and G_3 at a penetration depth h, working body thickness a, width b with a sharpening angle $2\alpha\left(\alpha \geq \frac{\pi}{4} + \frac{\varphi}{2}\right)$ are as follows:

$$S_1 = S_2 = \frac{ab}{2\sin\varepsilon};\tag{4}$$

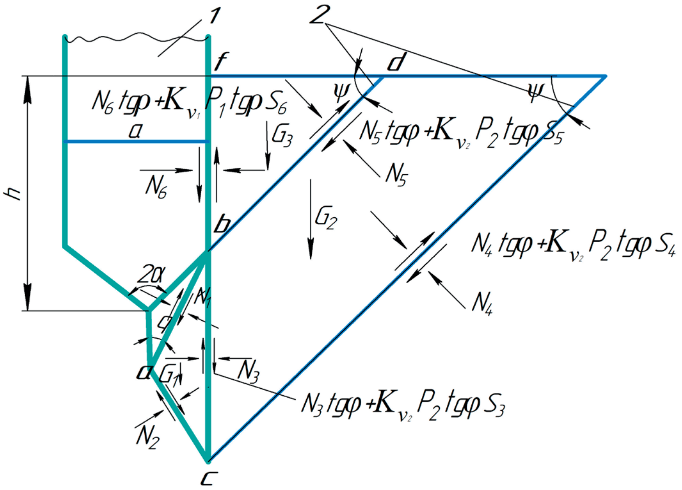

Figure 1 *Physical model of active interaction under normal impact of the working body on the rock mass: 1 - working body; 2 - sliding surface*

$$S_3 = \frac{ab}{tg\varepsilon}; \tag{5}$$

$$S_4 = \frac{a\left(h - \frac{a}{2tg\alpha} + \frac{a}{tg\varepsilon}\right)}{\sin\psi}; \tag{6}$$

$$S_5 = b\left(h - \frac{a}{2tg\alpha}\right)\frac{1}{\sin\psi}; \tag{7}$$

$$S_6 = b\left(h - \frac{a}{2tg\alpha}\right); \tag{8}$$

$$G_1 = \frac{1}{4}\frac{a^2 b}{tg\varepsilon}\gamma; \tag{9}$$

$$G_3 = \frac{1}{2}b\left(h - \frac{a}{2tg\alpha}\right)^2 ctg\psi\gamma; \tag{10}$$

$$G_2 = \frac{1}{2}bctg\psi\gamma\left[h - \left(\frac{a}{2tg\alpha} + \frac{a}{tg\varepsilon}\right)^2 - \left(h - \frac{a}{2tg\alpha}\right)^2\right] = \frac{1}{2}\gamma bctg\psi\left[\left(2h - \frac{a}{tg\alpha} + \frac{a}{tg\varepsilon}\right)\frac{a}{tg\varepsilon}\right]; \tag{11}$$

where h - depth of penetration; a - working body thickness; b - working width; α - angle of sharpening of the working body; ε - angle of the filled core; γ - material density.

2.2.1 Assumption about the shear angle

When considering the equilibrium of material prisms, bounded by the sliding planes, a relationship is established between the cutting angle of the working body α, the core filling angle ε, and the angle of inclination of the sliding planes.

In accordance with the classical principles of soil mechanics, when the compacted core acts as a continuation of the working body, the angle of inclination of the shear plane ψ to the horizon at the contact boundary is often taken according to the formula:

$$\psi = \frac{\pi}{4} + \frac{\varphi}{2}, \tag{12}$$

where φ - angle of internal friction of the material.

Since, in this general case, the compacted core complements the working body, its geometry (determined by the angle ε) directly affects the conditions for the formation of sliding planes.

The core filling angle ε is replaced by a classical expression that determines the most probable shear angle:

$$\varepsilon \approx \psi = \frac{\pi}{4} + \frac{\varphi}{2}. \tag{13}$$

This assumption allows for all the coefficients A_i to be expressed exclusively in terms of the fundamental physical properties of the material (φ, ρ) and the key geometric parameter α, which greatly simplifies engineering calculations. Further verification of the influence of this assumption is part of the required model validation.

3 Results and discussions

The main result of the work is obtaining an analytical solution for the system of equilibrium equations and deriving the final formula for calculating the insertion force of the working body.

Applying trigonometric transformations, one transforms Equations (1) - (3) and obtains an algebraic system of equations, linear with respect to unknowns N_1 to N_6 in the form:

$$\begin{gathered}
N_1 \frac{\cos(\varepsilon+\varphi)}{\cos\varphi} + N_2 \frac{\cos(\varepsilon-\varphi)}{\cos\varphi} - N_3 = 0; \\
-N_1 \frac{\sin(\varepsilon+\varphi)}{\cos\varphi} + N_2 \frac{\sin(\varepsilon-\varphi)}{\cos\varphi} + N_3 tg\varphi = \\
K_{v2} p_2 (2S_1 \cos\varepsilon - S_5) tg\varphi + G_1; \\
N_3 - N_4 \frac{\sin(\psi-\varphi)}{\cos\varphi} + N_6 \frac{\sin(\psi+\varphi)}{\cos\varphi} = \\
K_{v2} p_2 (S_4 - S_3) tg\varphi \cos\psi; \\
-N_3 tg + N_4 \frac{\cos(\psi+\varphi)}{\cos\varphi} - N_5 \frac{\cos(\psi+\varphi)}{\cos\varphi} = \\
K_{v2} p_2 [(S_3 - S_5)\sin\psi] tg\varphi + G_2; \\
N_5 \frac{\sin(\psi+\varphi)}{\cos\varphi} + N_6 = K_{v2} p_2 S_5 tg\varphi \cos\psi; \\
N_5 \frac{\sin(\psi+\varphi)}{\cos\varphi} - N_6 = K_{v1} p_1 S_6 tg\rho + \\
+ K_{v2} p_2 S_5 tg\varphi \sin\psi + G_3.
\end{gathered} \tag{14}$$

The system of six Equations (14) can be conveniently divided into three independent subsystems, each containing two equations. The solution is performed sequentially, starting with the last one, which is furthest from the working body of the prism.

This system can be divided into three subsystems: I - Equations (1) and (2), II - Equations (3) and (4), III - Equations (5) and (6). Solving the subsystem III one finds the value of force N_6. To do that, one multiplies its first equation by $\cos(\psi+\varphi)$ and, adding it term by term to the second equation multiplied by $\sin(\psi+\varphi)$, one gets:

$$\begin{gathered}
N_6[\cos(\psi+\varphi) - tg\rho \sin(\psi+\varphi)] = \\
K_{v2} p_2 S_5 tg\varphi [\cos\psi \cos(\psi+\varphi) \sin\psi + \\
+ \sin\psi \sin(\psi+\varphi)] + tg\rho K_{v1} p_1 S_6 \sin \\
(\psi+\varphi) + G_3 \sin(\psi+\varphi)
\end{gathered} \tag{15}$$

or

$$\begin{gathered}
N_6 = K_{v1} p_1 S_6 \frac{\sin\rho \sin(\psi+\varphi)}{\cos(\psi+\varphi+\rho)} + K_{v2} p_2 S_5 \\
\frac{\sin\varphi \cos\rho}{\cos(\psi+\varphi+\rho)} + G_3 \frac{\cos\rho \sin(\psi+\varphi)}{\cos(\psi+\varphi+\rho)}.
\end{gathered} \tag{16}$$

From the subsystem II, one determines the value of force N_3. The first equation of the system is multiplied by $\cos(\psi+\varphi)$, and the second by $\sin(\psi+\varphi)$, and, adding them term by term, one will find:

$$\begin{gathered}
N_3 \frac{\cos(\psi+2\varphi)}{\cos\varphi} = K_{v2} p_2 tg\varphi [(S_4 - S_5)\cos\varphi + \\
+ S_3 \sin(\psi+\varphi)] + G_2 \sin(\psi+\varphi)
\end{gathered} \tag{17}$$

or

$$\begin{gathered}
N_3 = \\
K_{v2} p_2 \frac{[(S_4 - S_5)]\cos\varphi + S_3 \sin(\psi+\varphi)\sin\varphi}{\cos(\psi+2\varphi)} + \\
+ G_2 \frac{\cos\varphi \sin(\psi+\varphi)}{\cos(\psi+2\varphi)}.
\end{gathered} \tag{18}$$

From system I, one determines the value of force N_1. Its first equation is multiplied by $\sin(\varepsilon-\varphi)$ and its second equation by $-\cos(\varepsilon-\varphi)$, and then, after adding them together term by term, one finds:

$$\begin{gathered}
N_1 \frac{\sin 2\varepsilon}{\cos\varphi} = N_3 \frac{\sin\varepsilon}{\cos\varphi} - K_{v2} p_2 (2S_1 \cos\varepsilon - S_3) \\
tg\varphi \cos(\varepsilon-\varphi) - G_1 \cos(\varepsilon-\varphi)
\end{gathered} \tag{19}$$

or

$$\begin{gathered}
N_1 = N_3 \frac{\sin\varepsilon}{\sin 2\varepsilon} - K_{v2} p_2 (2S_1 \cos\varepsilon - S_3) \\
\frac{\sin\varphi \cos(\varepsilon-\varphi)}{\sin 2\varepsilon} - G_1 \frac{\cos(\varepsilon-\varphi)\cos\varphi}{\sin 2\varepsilon}.
\end{gathered} \tag{20}$$

Substituting Equation (18) from (16), one calculates:

$$\begin{gathered}
N_1 = \\
K_{v2} p_2 \frac{[(S_4 - S_5\cos\varphi + S_3 \sin(\psi+\varphi))\sin\psi]}{2\cos\varepsilon \cos(\psi+2\varphi)} + \\
+ G_2 \frac{\cos\varphi \sin(\psi+\varphi)\cos\varphi}{2\cos\varepsilon \cos(\psi+2\varphi)} - \\
- G_1 \frac{\cos(\varepsilon+\varphi)\cos\varphi}{\sin 2\varepsilon}.
\end{gathered} \tag{21}$$

The force required to drive the working body into the sticky rock mass is determined by the formula:

$$\begin{gathered}
P_{kp} = N_1 \sin\varepsilon + (N_1 tg\varphi + tg\varphi K_{v2} p_2 S_1)\cos\varepsilon + \\
+ N_6 tg\rho + tg\rho K_{v1} p_1 S_6
\end{gathered} \tag{22}$$

or

$$\begin{gathered}
P_{kp} = N_1 \frac{\sin(\varepsilon+\varphi)}{\cos\varphi} + N_6 tg\rho + K_{v1} p_1 S_6 tg\rho + \\
+ K_{v2} p_2 S_{61} tg\varphi \cos\varepsilon.
\end{gathered} \tag{23}$$

Substituting the values of forces N_1 and N_2 into Equation (23), one obtains:

$$\begin{gathered}
P_{kp} = \left\{ K_{v2} p_2 \frac{(S_4 - S_5)\cos\varphi + S_3 \sin(\psi+\varphi)}{2\cos\varepsilon \cos(\psi+2\varphi)} \right. \\
\sin\varphi + G_2 \frac{\cos\varphi \sin(\psi+\varphi)}{2\cos\varepsilon \cos(\psi+2\varphi)} - \\
\left. - G_1 \frac{\cos(\varepsilon-\varphi)\cos\varphi}{\sin 2\varepsilon} \right\} \times \frac{\sin(\varepsilon+\varphi)}{\cos\varphi} + \\
+ \left\{ K_{v1} p_1 S_6 \frac{\sin\rho \sin(\psi-\varphi)}{\cos(\psi+\varphi+\rho)} + K_{v2} p_2 S_5 \right. \\
\left. \frac{\sin\varphi \cos\rho}{\cos(\psi+\varphi+\rho)} + G_3 \frac{\cos\rho \sin(\psi+\varphi)}{\cos(\psi+\varphi+\rho)} \right\} tg\rho + \\
+ K_{v1} p_1 S_6 tg\rho + K_{v1} p_1 S_1 tg\varphi \cos\varepsilon.
\end{gathered} \tag{24}$$

After reducing these terms and making the appropriate notations, one finds:

$$\begin{gathered}
P_{kp} = K_{v1} p_1 b\Big(h - \frac{a}{2tg\alpha}\Big) A_1 + K_{v2} p_2 \Big[\frac{ab}{2} A_2 + \\
+ b\Big(h - \frac{a}{2tg\alpha}\Big) A_3\Big] - \frac{\gamma a^2 b}{4} A_4 + \frac{\gamma b}{2} \\
\Big(h - \frac{a}{2tg\alpha} + \frac{a}{tg\varepsilon}\Big)^2 A_5 + \frac{\gamma b}{2}\Big(h - \frac{a}{2tg\alpha}\Big)^2 A_6,
\end{gathered} \tag{25}$$

where

$$A_1 = \frac{\sin\rho\cos(\psi+\varphi)}{\cos(\psi+\varphi+\upsilon)} = \frac{\sin\rho\cos\left(\frac{\pi}{4}+\frac{\varphi}{2}\right)}{\cos\left(\frac{\pi}{4}+\frac{\varphi}{2}+\rho\right)}; \quad (26)$$

$$A_2 = \frac{\sin\varphi}{\sin\varepsilon}\left(\frac{\cos\varphi+\sin\varphi+\sin(\psi+\varphi)}{\sin\psi\cos(\psi+2\varphi)} + \right. \\ \left. + \frac{\cos\varepsilon}{\cos\varphi}\right) = \frac{3tg\varphi}{\cos\left(\frac{\pi}{4}+\frac{3}{2}\varphi\right)} + \frac{tg\varphi(1-\sin\varphi)}{\cos\varphi}; \quad (27)$$

***Table 1** The values of the coefficients A_1, A_2, A_3, A_4, A_5, A_6*

Internal friction angle φ, degree	External friction angle ρ, degree	The value of the coefficients					
		A_1	A_2	A_3	A_4	A_5	A_6
5	3	0.06	0.51	0.01	0.54	0.78	-0.64
	5	0.10	0.51	0.02	0.54	0.78	-0.60
	10	0.22	0.51	0.04	0.54	0.78	-0.45
	15	0.38	0.51	0.07	0.54	0.78	-0.26
	20	0.60	0.51	0.12	0.54	0.78	0.01
	25	0.95	0.51	0.16	0.54	0.78	0.42
	30	1.56	0.51	0.30	0.54	0.78	1.15
10	3	0.06	1.21	0.02	0.57	1.23	-0.95
	5	0.10	1.21	0.04	0.57	1.23	0.89
	10	0.22	1.21	0.09	0.57	1.23	-0.72
	15	0.39	1.21	0.17	0.57	1.23	-0.47
	20	0.64	1.21	0.27	0.57	1.23	-0.12
	25	1.05	1.21	0.44	0.57	1.23	0.46
	30	1.85	1.21	0.78	0.57	1.23	1.60
15	3	0.06	2.31	0.04	0.58	2.05	-1.48
	5	0.10	2.31	0.07	0.58	2.05	-1.41
	10	0.23	2.31	0.16	0.58	2.05	-1.10
	15	0.41	2.31	0.29	0.58	2.05	-0.87
	20	0.69	2.31	0.48	0.58	2.05	-0.40
	25	1.19	2.31	0.83	0.58	2.05	0.45
	30	2.33	2.31	1.63	0.58	2.05	2.39
20	3	0.06	4.47	0.06	0.59	3.81	-2.55
	5	0.10	4.47	0.10	0.59	3.81	-2.46
	10	0.24	4.47	0.25	0.59	3.81	-2.18
	15	0.43	4.47	0.45	0.59	3.81	-1.78
	20	0.96	4.47	0.79	0.59	3.81	-1.12
	25	1.40	4.47	1.45	0.59	3.81	0.18
	30	3.29	4.47	3.42	0.59	3.81	4.05
25	3	0.06	11.01	0.08	0.59	9.36	-5.82
	5	0.10	11.01	0.15	0.59	9.36	-5.71
	10	0.24	11.01	0.36	0.59	9.36	-5.36
	15	0.46	11.01	0.68	0.59	9.36	-4.82
	20	0.85	11.01	1.24	0.59	9.36	-3.87
	25	1.74	11.01	2.55	0.59	9.36	-1.68
	30	6.16	11.01	9.02	0.59	9.36	9.21
28	3	0.06	30.80	0.10	0.58	26.43	-15.72
	5	0.10	30.80	0.18	0.58	26.43	-15.59
	10	0.23	30.80	0.44	0.58	26.43	-15.19
	15	0.48	30.80	0.86	0.58	26.43	-14.54
	20	0.92	30.80	1.63	0.58	26.43	13.32
	25	2.06	30.80	3.49	0.58	26.43	10.11
	30	14.74	30.80	26.11	0.58	26.43	24.99

$$A_3=\frac{\sin\varphi\sin\rho}{\sin\psi\cos(\psi+\varphi+\rho)}=\frac{\sin\varphi\sin\rho}{\cos\left(\frac{\pi}{4}+\frac{\varphi}{2}\right)\cos\left(\frac{\pi}{4}+\frac{\varphi}{2}+\rho\right)};\tag{28}$$

$$A_4=\frac{\cos(\varepsilon-\varphi)\sin(\varepsilon+\varphi)}{2\sin^2\varepsilon}=\frac{\sin\left(\frac{\pi}{4}+\frac{\varphi}{2}\right)\sin\left(\frac{\pi}{4}+\frac{3}{2}\varphi\right)}{1+\sin\varphi};\tag{29}$$

$$A_5=\frac{ctg\psi\sin(\psi+\varphi)\sin(\varepsilon+\varphi)}{2\cos\varepsilon\cos(\psi+2\varphi)}=\frac{1}{2}tg^2\left(\frac{\pi}{4}+\frac{\varphi}{2}\right)tg\left(\frac{\pi}{4}+\frac{3\varphi}{2}\right);\tag{30}$$

$$A_6=\frac{\begin{array}{c}2ctg\rho\cos\varepsilon\cos(\psi+2\varphi)-\\-\sin(\varepsilon+\varphi)\cos(\psi+\varphi+\rho)\end{array}}{2\cos\varepsilon\cos(\psi+2\varphi)\cos(\psi+\varphi+\rho)}ctg\psi\sin(\psi+\varphi)=\frac{\sin\rho\sin^2\left(\frac{\pi}{4}+\frac{\varphi}{2}\right)}{\cos\left(\frac{\pi}{4}+\frac{\varphi}{2}\right)\cos\left(\frac{\pi}{4}+\frac{\varphi}{2}+\rho\right)}-\frac{1}{2}tg^2\left(\frac{\pi}{4}+\frac{\varphi}{2}\right)tg\left(\frac{\pi}{4}+\frac{3}{2}\varphi\right),\tag{31}$$

where A_1, A_2, A_3, A_4, A_5, A_6 -are the dimensionless coefficients that depend only on the angular characteristics of the system: the angle of sharpening of the working body α, the angle of internal friction of the rock φ, and the angle of friction of the rock against the surface of the working body ρ. The formulas for calculating these coefficients are given in Equations (26)-(31) in the original work [4, 13]. The coefficients A_1 to A_6 obtained from the calculations, intended for practical use, are given in Table 1.

Table 1 shows how each coefficient changes as the external friction angle increases.

The coefficients A_1 and A_3 show a clear increase with an increase in both the internal friction angle (φ) and the external friction angle (ρ).

The coefficients A_2 and A_4 remain constant for a fixed value of φ and do not depend on the external friction angle ρ.

Coefficients A_5 and A_6 show a more complex relationship, where A_5 mainly increases, while A_6 changes its sign and also increases with increasing friction angles. This data helps to better understand the relationships between the physical properties of the material (friction angles) and the calculated coefficients.

The remaining coefficients have a more complex but analytically defined structure. Thus, the resulting formula is the final result of modelling and allows calculations of active resistance forces during the normal penetration.

3.1 Sensitivity analysis of formula P_{kp}

To assess the engineering significance of the developed model and quantitatively evaluate the influence of various input data on the final resistance force, a sensitivity analysis of the final formula P_{kp} in Equation (24) was performed.

The analysis focuses on four key parameters that have the greatest direct impact on the penetration force: h penetration depth; a working body thickness; p_1 specific adhesion; γ material density.

Sensitivity analysis was performed by sequentially varying each of the key parameters within ± 20% of their nominal value, while the other parameters remained fixed (ceteris paribus). The change in resistance force P_{kp} during this parameter change allows to determine the sensitivity coefficient of the model to this parameter.

The analysis results show that formula P_{kp} has varying degrees of sensitivity to each of the input parameters:

- High sensitivity to geometric parameters (h and a): The force demonstrates a strong, almost linear dependence on the penetration depth and thickness of the working body. A 10% increase in h or a leads to a disproportionately greater increase of P_{kp} due to an increase in the volume of material prisms and sliding surface areas. This analytically confirms the hypothesis that optimizing the geometry of the tool is the most effective way to reduce the energy intensity of the process.
- Moderate sensitivity to adhesion p_1: The specific adhesion parameter p_1 has a significant but more predictable effect, as it directly enters the adhesion terms of Equation (24). Effect of p_1 is particularly pronounced in the case of materials with high clay and moisture content.
- Low sensitivity to density γ: Force P_{kp} is the least sensitive to the density of a material γ. This is because the members dependent on the weight of the prisms account for a smaller proportion of the total resistance force compared to the forces caused by friction and adhesion, especially at shallow penetration depths.

The data obtained allows to quantitatively assess that, to minimize the resistance force P_{kp}, the greatest engineering attention should be paid to reducing the geometric parameters and applying coatings that reduce adhesion p_1.

4 Model validation

4.1 Model limitations and justification for validation

A significant limitation of the current study is its reliance solely on the analytical derivation of the formula for determining the force of penetration P_{kp}

in Equation (24). Although the method of element-by-element calculation of resistances provides a reliable theoretical basis, the accuracy and practical applicability of the analytical expression obtained depend entirely on the simplifying assumptions made in Section 2.1 (e.g., incompressibility of prisms, straightness of the slip planes).

Therefore, the external validation is extremely important for confirming the practical reliability of the developed model.

4.2 Model validation strategy

To ensure the engineering value and reliability of the derived formula for P_{kp}, the analytical results must be quantitatively compared to the data obtained by independent methods. The following two approaches are recommended for the future work:

Experimental validation:

- Comparison of the calculated strength P_{kp} to the measured data obtained during laboratory tests (e.g., direct shear tests or miniature cutting experiments) using typical viscous or sticky soils (e.g., wet clay or loam).

This comparison should cover a range of key parameters, such as different penetration depths h, working body thickness a, and speed, to evaluate the accuracy of the model under different operating conditions

Numerical validation:

- Comparison of the calculated force P_{kp} to the results obtained by numerical methods, in particular the finite element method.

The numerical model would allow for the nonlinear behavior of the material (plasticity, compaction) and the complex geometry of the compacted core to be taken into account, providing a reliable benchmark for comparison to the simplified linear assumptions of the analytical model.

Successful validation demonstrating a close correlation between the analytical results and independent data will confirm the applicability of the model for engineering design and optimization of working bodies in sticky rock conditions. Conversely, any significant deviation would indicate the need for further refinement of the initial assumptions, especially regarding the behavior of the material under load.

5 Conclusions

In this paper is presented and described in detail a mathematical model of active interaction between the working body and an array of sticky rock during normal penetration. Based on the method of element-by-element calculation of resistances and a number of physically justified assumptions, a final analytical formula for calculating the penetration force is derived.

Key findings:

1. The developed model allows quantitative determination of resistance force as a function of the geometric parameters of the tool (thickness, width, sharpening angle) and the physical and mechanical properties of the rock (weight, friction, adhesion);
2. The formula clearly divides the total resistance into components determined by the weight of the rock, its internal strength (cohesion), and adhesive forces (adhesion), which allows for analysis of the energy expenditure structure;
3. The model analytically confirms the practical importance of optimizing the geometry of the working body, in particular, it shows the effectiveness of reducing the thickness and sharpening angle of the cutting edge to reduce the energy intensity of the cutting process.

The presented model is a ready-made engineering tool that can be used in the design of working parts for bulldozers, scrapers, excavators, and other equipment to increase their efficiency when working in difficult conditions with sticky and hard rocks. It provides a theoretical basis for making informed design decisions aimed at reducing energy consumption and increasing machine productivity.

Acknowledgements

The authors received no financial support for the research, authorship and/or publication of this article.

Conflicts of interest

The authors declare that they have no known competing financial interests or personal relationships that could have appeared to influence the work reported in this paper.

References

[1] BALOVNEV, V. I. *Modelling of interaction processes with the environment of working bodies of road construction machines*. Moscow: Higher School, 1981, ISBN 5-217-02343-0.

[2] VOLKOV, D. P., KRIKUN, V. Y., TOTOLIN, P. E., GAEVSKAYA, K. S. *Machines for earthworks.* Moscow: Mechanical Engineering, 1992. ISBN 5-217-01973-5.

[3] DOTSENKO, A. I., KARASEV, G. N., KUSTAREV, G. V., SHESTOPALOV, K. K. *Machines for earthworks.* Moscow: Bastet, 2012. ISBN 978-5-903178-28-5.

[4] BOCHAROV, V. S. *Interaction of machine tools with bitumen-containing rocks*. Moscow: Transportation, 1992. ISBN 5-277-01382-2.

[5] LUKASHUK, O. A., KOMISSAROV, A. P., LETNEV, K. Y. *Machines for soil development. Design and calculation*. Ekaterinburg: Ural University Publishing House, 2018. ISBN 978-5-7996-2386-9.

[6] FEDOROV, D. I. *Working bodies of earth-moving machines*. Moscow: Mechanical Engineering, 1977. ISBN 5-217-00490-8.

[7] DOVGYALO, V. A., BOCHKAREV, D. I. *Road construction machines. Part I: Machines for earthworks.* Gomel: Belarusian State University of Transport, 2010. ISBN 978-985-468-741-4.

[8] QING-HUA, H., DA-QING, Z., PENG, H., HAI-TAO, Z. Modelling and control of hydraulic excavator arm. *Journal of Central South University of Technology* [online]. 2006, **13**(4), p. 422-427. ISSN 1005-9784, eISSN 2227-5223. Available from: https://doi.org/10.1007/s11771-006-0061-1

[9] YANG, CH., HUANG, K., LI, Y., WANG, J., ZHOU, M. Review for development of hydraulic excavator attachment. *Energy Science and Technology* [online]. 2012, **3**(2), p. 93-97. ISSN 1923-8460, eISSN 1923-8479. Available from: https://doi.org/10.3968/j.est.1923847920120302.386

[10] KOZBAGAROV, R. A., KAMZANOV, N. S., AKHMETOVA, S. D., ZHUSSUPOV, K. A., DAINOVA, Z. K. Determination of energy consumption of high-speed rock digging. *News of the National Academy of Sciences of the Republic of Kazakhstan, Series of Geology and Technical Sciences* [online]. 2021, **6**(450), p.85-92. ISSN 2224-5278, eISSN 2518-170X. Available from: https://doi.org/10.32014/2021.2518-170X.123

[11] KOZBAGAROV, R. A., SHALBAYEV, K. K., ZHIYENKOZHAYEV, M. S., KAMZANOV, N. S., NAIMANOVA, G. T. Design of cutting elements of reusable motor graders in mining. *News of the National Academy of Sciences of the Republic of Kazakhstan, Series of Geology and Technical Sciences* [online]. 2022, **3**(453) p.128-141. ISSN 2224-5278, eISSN 2518-170X. Available from: https://doi.org/10.32014/2022.2518-170X.185

[12] GUO, Z., DU, G., LI, Z., LI, X. Orthogonal experiment on resistance reduction by soil-engaging surfaces of bulldozer blade. *Nongye Jixie Xuebao / Transactions of the Chinese Society of Agricultural Machinery* [online]. 2015, **46**(7), p. 372-378. ISSN 1000-1298. Available from: https://doi.org/10.6041/j.issn.1000-1298.2015.07.053

[13] KOZBAGAROV, R., KAMZANOV, N., AMANOVA, M. BAIKENZHEYEVA, A., NAIMANOVA, G. Justification of the cam roller parameters for destruction of the road coatings for obtaining the lumpy asphalt scrap. *Communications - Scientific Letters of the University of Zilina* [online]. 2023, **25**(2), p. 103-1097. ISSN 2585-7878, eISSN 1335-4205. Available from: https://doi.org/10.26552/com.C.2023.028

[14] KOZBAGAROV, R. A., ZHIYENKOZHAYEV, M. S., KAMZANOV, N. S., TSYGANKOV, S. G., BAIKENZHEYEVA, A. S. Design of hydraulic excavator working members for development of mudslides. *News of the National Academy of Sciences of the Republic of Kazakhstan, Series of Geology and Technical Sciences* [online]. 2023, **2**(458), p. 134-141. ISSN 2224-5278, eISSN 2518-170X. Available from: https://doi.org/10.32014/2023.2518-170X.288

[15] TROYANOVSKAYA, I., GREBENSHCHIKOVA, O. Optimization of technical productivity of a bulldozer unit in terms of traction and speed parameter. *The Russian Automobile and Highway Industry Journal* [online]. 2025, **21**(6), p. 844-851. ISSN 2071-7296, eISSN 2658-5626. Available from: https://doi.org/10.26518/2071-7296-2024-21-6-844-8517

[16] MIAO, CH. Modeling and simulation research on the hydraulic system of the blade of an unmanned bulldozer. *Frontiers in Computing and Intelligent Systems* [online]. 2025, **11**(2), p.78-82. ISSN 2832-6024. Available from: https://doi.org/10.54097/n8pphn83

[17] YULIUS, M., NURBAITI, SARMIDI, MUHAMMAD, I. G. Usage procedure of Liebherr 756 bulldozer unit in live stockpile OPB 4 PT Bukit Asam Tbk/Prosedur penggunaan unit bulldozer Liebherr 756 di live stockpile OPB 4 PT. Bukit Asam, Tbk (in Indonesian). *Scientific Journal of Engineering and Science* [online]. 2025, **2**(1), p. 117-123. eISSN 3025-8871. Available from: https://doi.org/10.62278/jits.v2i1.50

[18] SHARMA, D., BARAKAT, N. Evolutionary bi-objective optimization for bulldozer and its blade in soil cutting. *Journal of The Institution of Engineers (India): Series C* [online]. 2019, **100**(2), p. 295-310. ISSN 2250-0545, eISSN 2250-0553. Available from: https://doi.org/10.1007/s40032-017-0437-z

[19] AKANKSHA, M., VIKAS, K. S., SHIVAM, VIPUL, C. A comprehensive review of bulldozers in modern construction. *Journal of Scientific Research and Reports* [online]. 2024, **30**(5), p. 337-342. ISSN 2320-0227. Available from: https://doi.org/10.9734/JSRR/2024/v30i51949

DETERMINING THE EFFICIENCY OF CLEANING VEHICLE EXHAUST GASES WITH AN ULTRASONIC MUFFLER DEPENDING ON THE ENGINE OPERATING MODE AND ULTRASOUND POWER

Igor Pak

Abylkas Saginov Karaganda Technical University, Kazakhstan

E-mail of corresponding author: i.pak@mail.ru

Igor Pak 0000-0002-6492-1525

Resume

The dependence has been obtained that links the degree of coagulation of soot particles, the parameters of the ultrasonic equipment, the geometric dimensions of the ultrasonic muffler, the frequency characteristics of ultrasound, and the parameters of the engine operating mode. In the paper is presented solving of a problem of determining the number of particles in 1 cm3 of exhaust gas depending on the smoke index. An example of calculating the required ultrasound power for a full-size ultrasonic vehicle muffler bench has been given.

Available online: https://doi.org/10.26552/com.C.2026.006

Article info

Received 24 July 2025
Accepted 8 December 2025
Online 18 December 2025

Keywords:

vehicle
engine
exhaust gas
ultrasonic muffler
ultrasonic cleaning
coagulation

ISSN 1335-4205 (print version)
ISSN 2585-7878 (online version)

1 Introduction

Present-day environmental safety standards for vehicles make it necessary to develop effective methods for reducing the toxicity of internal combustion engine exhaust gases. One of the most dangerous components of exhaust gases are the soot particles, especially fractions smaller than 10 microns (PM10). They easily penetrate the human respiratory system and cause diseases of the respiratory system and cardiovascular system. Long-term exposure to such particles can contribute to the development of chronic pathologies and negatively affect the environment, settling in the soil and water bodies [1-7]

Study in the field of developing the exhaust gas cleaning systems represents an urgent task aimed at reducing the content of soot particles and the other harmful substances in the exhaust gases of internal combustion engines. One of the promising areas for reducing the harmful emissions is the use of ultrasonic technologies in the exhaust gas neutralization system [8-14].

Works [8-9, 14] present the results of studies of the ultrasonic muffler operation that is a device in the form of a pipe with a built-in emitter of ultrasonic waves. In this case, the high-frequency acoustic vibrations contribute to the intensification of the processes of coagulation and sedimentation of solid particles. The set of parameters of the muffler mode and design determine the specific modes of its operation. The hypothesis of the study is an assumption of the existence of an optimal cleaning mode for specific designs of mufflers of different sizes and operating modes.

The aim of the study was to determine the optimal parameters of ultrasonic equipment for the most effective cleaning of exhaust gas during operation.

The scientific novelty of the study is establishing the dependence of the coagulation degree on the engine crankshaft speed, muffler characteristics and ultrasonic equipment.

The practical usefulness lies in the use of the established dependence in the design of exhaust gas cleaning systems to determine the characteristics of ultrasonic equipment and its operating mode.

Coagulation of particles in the exhaust gas of an internal combustion engine occurs almost constantly due to the chaotic movement of particles, their collisions and adhesion in the gas volume [15-17].

When exposed to ultrasound, the coagulation process is intensified, not only due to increasing orthokinetic

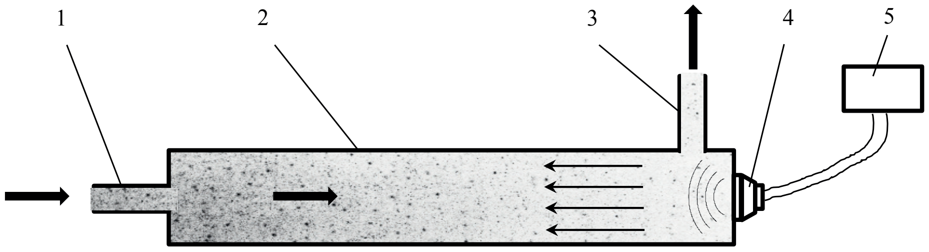

→ - the exhaust gas movement direction;
← - the ultrasound action direction;

1 - inlet pipe; 2 - muffler body; 3 - outlet pipe; 4 - ultrasonic wave emitter; 5 - ultrasonic pulse generator

***Figure 1** Ultrasonic muffler schematics*

coagulation, but due to the occurrence of hydrodynamic coagulation of solid particles in the ultrasonic field, as well, which contributes to the greatest efficiency of the coagulation-sedimentation process. Hydrodynamic coagulation occurs in the ultrasonic field, in which the large particles begin to converge under the action of hydrodynamic forces in the sense of Bjerknes and coagulate due to friction. The coagulation process is described by the Bjerknes equations [8, 17-18].

In works [8-9, 14] experiments were conducted using the ultrasound of different frequencies, power characteristics, different directions of ultrasonic radiation, with different crankshaft rotation speeds. Based on the obtained research results, one of the conclusions is that the greatest cleaning efficiency is achieved by transmitting the ultrasonic waves in the horizontal direction against the direction of movement of exhaust gases [8-9]. The scheme of the ultrasonic muffler is shown in Figure 1.

An assumption was made about the existence of the cleaning efficiency of an ultrasonic device dependence on a number of factors, including the rotation speed of the ICE crankshaft and the intensity of ultrasonic radiation [8-9, 14].

Thus, the experiments carried out on ultrasonic mufflers [8-9, 14] indicate the need for further research in the field of determining the cleaning efficiency dependence on the parameters of ultrasonic equipment, which is required for the design of ultrasonic devices for cleaning exhaust gases of ICEs.

2 Materials and research methods

Several dependences of the coagulation process have been analyzed, such as the Smoluchowski coagulation kinetics, the Einstein diffusion coefficient [19], and the Kidoo dependence [19], of which the last has attracted the greatest interest. The dependence proposed in 1951 by scientist Kidoo Gordon based on the calculations of Vivian and Stokes [17, 20] between the degree of coagulation E, the number of particles G in 1 cm^3 and the time of irradiation t with ultrasound of intensity j allows for identifying the relationship between the degree of coagulation, the time of ultrasonic exposure, which depends on the rotation frequency of the internal combustion engine crankshaft, and the intensity of ultrasonic radiation:

$$\lg(100 - E) = \frac{k}{G \cdot t \cdot \sqrt{J}}, \tag{1}$$

where:

E is the coagulation degree, %;

k is a constant value for the studied design of the ultrasonic muffler depending on the frequency of ultrasound, the nature of the particles and the equipment used;

G is the number of particles in 1 cm^3, $particles/cm^3$. It is determined based on the initial smoke index of the exhaust gas D_0;

t is the time of ultrasound action, s;

j is the ultrasound intensity, W/cm^2. It is determined according to the formula:

$$j = \frac{W}{S},\ W/cm^2, \tag{2}$$

where:

W is the ultrasound power, W;

S is the cross section of the ultrasound muffler, cm^2.

From Equation (1), the constant value k is determined as follows:

$$k = \lg(100 - E) \cdot G \cdot t \cdot \sqrt{j}. \tag{3}$$

The degree of coagulation E is the ratio of changing the smoke content of the exhaust gas to the initial smoke index and is determined as follows:

$$E = \frac{D_0 - D_i}{D_0} \cdot 100,\ \%, \tag{4}$$

where:

D_0 is the initial smoke index of the exhaust gas without the ultrasound action, m^{-1};

D_i is the smoke index of the exhaust gas after the ultrasonic cleaning, m^{-1}.

The most important task not solved in works [8-9, 14], is determining the number of soot particles in 1 cm^3. To determine the number of particles G in 1 cm^3, the smoke index of the exhaust gas is used that corresponds to a certain mass concentration of soot M, g/m^3, determined according to the table “Ratios of units of measurement of smoke and mass concentration of soot” of the Operating Manual for the exhaust gas smoke meter [21]. If the data in the table do not cover the measured range of values D, then the value of M is determined by the empirical dependence on the absorption coefficient D, m^{-1}, determined based on the data in the table:

$$\begin{aligned} M &= 0.00334D^3 - 0.01208D^2 + \\ &+ 0.18064D - 0.01032, \mathrm{g/m^3}. \end{aligned} \tag{5}$$

Knowing the mass concentration of soot and the mass of one soot particle, the number of particles in 1 cm^3 is determined using the formula:

$$G = \frac{M}{m_{s.p.}} \cdot 10^{-6} \text{ particles/cm}^3, \tag{6}$$

where:

M is the mass soot concentration, g/m^3;

$m_{s.p}$ is the soot particle mass, g.

The mass of one soot particle is determined based on the average size of the radius of soot particles r = 15.25 nm, density ρ = 1.9 g/cm^3 [22]:

$$m_{s.p.} = V_{s.p.} \cdot \rho, g, \tag{7}$$

where:

$V_{s.p.}$ is the average volume of the soot particle, cm^3;

ρ is the soot particle density, g/cm^3.

Assuming that the soot particle has the shape of a sphere [15-16], the volume of the soot particle is determined by the formula:

$$\begin{aligned} V_{s.p.} &= \frac{4}{3}\pi r^3, \mathrm{cm}^3; \\ V_{s.p.} &= 1.48483 \cdot 10^{-17}\mathrm{cm}^3; \\ m_{s.p.} &= 2.82118 \cdot 10^{-17}\mathrm{g}. \end{aligned} \tag{8}$$

The time of ultrasonic action t, depending on the speed of the exhaust gas movement depends on the rotation frequency of the crankshaft and the volume of the engine cylinders according to the formula [23]:

$$t = \frac{L \cdot \pi \cdot R^2}{2\omega \cdot Q}, s, \tag{9}$$

where:

ω is the crankshaft rotation frequency, rps;

Q is the engine cylinder volume, cm^3.

Thus, the constant value k is determined as:

$$k = \lg\left(100 - \frac{D_0 - D_i}{D_0}100\right) \cdot G\frac{L \cdot \pi \cdot R^2}{\omega \cdot Q}\sqrt{j}. \tag{10}$$

From Equation (1), the coagulation degree E is determined as:

$$E = 100 - 10^{\frac{k}{Gt\sqrt{j}}}, \%. \tag{11}$$

This formula is applicable to determining the degree of soot particle coagulation in a flow-through muffler equipped with an ultrasonic emitter. The constant k calculated using Equation (10) adapts Equation (11) to a specific muffler design with given geometric dimensions and a set ultrasonic frequency under various engine operating conditions and ultrasonic equipment power levels.

Substituting Equations (6), (9) and (10) into the formula for determining the degree of coagulation E, in Equation (11) and changing the values of ω and j, the dependences of the degree of coagulation that characterize the cleaning efficiency on the rotation frequency of the ICE crankshaft and the intensity of ultrasonic radiation are determined.

The calculation is now performed of a full-size ultrasonic automobile muffler bench (Figure 2) developed in the laboratory of the Transport Equipment and Logistics Systems Department of the Abylkas Saginov Karaganda Technical University (Karaganda, Kazakhstan), where experiments were carried out to determine the efficiency of ultrasonic exposure [9].

The ultrasonic equipment provided the ultrasound radiation with frequency of 25 kHz and power of 50 W, horizontally against the direction of the exhaust gases in the muffler. The inlet pipe of the bench was connected to the muffler of a vehicle equipped with a diesel engine with the volume of 2700 cm^3. The smoke content of the exhaust gas was measured with a smoke meter on the outlet pipe of the ultrasonic vehicle muffler bench.

Figure 2 *Full-size ultrasonic vehicle muffler bench*

The results of the experiments are shown in Table 1.

The average value of the absorption coefficient for five measurements without ultrasound exposure was D_0 = 1.19 m^{-1} with a standard deviation of 0.012, with ultrasound exposure - D_i = 0.86 m^{-1} with a standard deviation of 0.014 [9].

***Table 1** Experimental results*

Measurement number	D_0	D_i
1	1.2	0.86
2	1.17	0.84
3	1.19	0.88
4	1.21	0.85
5	1.18	0.88

***Table 2** The k value calculation*

Indicator	Value
Ultrasound frequency *f*, Hz	25
Ultrasound power *W*, W	50
Absorption coefficient value D_0 without ultrasound exposure, m^{-1}	1.19
Absorption coefficient value D_i with ultrasound exposure, m^{-1}	0.86
Degree of coagulation *E*, %	11.84
Mass concentration of soot *M*, g/m^3	0.122
Number of soot particles in 1 cm^3 *G*, particles/cm^3	4324424448
Engine crankshaft rotation frequency ω, rpm	750
Engine crankshaft rotation frequency ω, rps	12.5
Engine capacity V_{cyl}, m^3	0.0027
Ultrasonic muffler length *L*, m	1
Ultrasonic muffler radius *R*, m	0.055
Ultrasonic muffler cross-sectional area *S*, m^2	0.009499
Ultrasound intensity *j*, W/cm^2	5263.989
Ultrasonic exposure time t, s	0.141
Constant value *k*	82073908106

***Table 3** Calculation of the coagulation degree E in the course of ultrasonic during cleaning with frequency of 25 kHz and power of 50 W and various crankshaft speeds of a diesel engine of a volume of 2700 cm^3*

f, Hz	k	ω, rpm	ω, rpm	V_{cyl}, m^3	L, m	R, m	t, s	J, W/m^2	E, %
25	82073908106	750	12.50	0.0027	1	0.055	0.141	5263.99	27.731
25	82073908106	800	13.33	0.0027	1	0.055	0.132	5263.99	3.865
25	82073908106	850	14.17	0.0027	1	0.055	0.124	5263.99	-27.883
25	82073908106	900	15.00	0.0027	1	0.055	0.117	5263.99	-70.115
25	82073908106	950	15.83	0.0027	1	0.055	0.111	5263.99	-126.293
25	82073908106	1000	16.67	0.0027	1	0.055	0.106	5263.99	-201.025
25	82073908106	1050	17.50	0.0027	1	0.055	0.101	5263.99	-300.435
25	82073908106	1100	18.33	0.0027	1	0.055	0.096	5263.99	-432.675
25	82073908106	1150	19.17	0.0027	1	0.055	0.092	5263.99	-608.586
25	82073908106	1200	20.00	0.0027	1	0.055	0.088	5263.99	-842.589
25	82073908106	1250	20.83	0.0027	1	0.055	0.084	5263.99	-1153.870
25	82073908106	1300	21.67	0.0027	1	0.055	0.081	5263.99	-1567.948
25	82073908106	1350	22.50	0.0027	1	0.055	0.078	5263.99	-2118.772
25	82073908106	1400	23.33	0.0027	1	0.055	0.075	5263.99	-2851.500
25	82073908106	1450	24.17	0.0027	1	0.055	0.073	5263.99	-3826.204

3 Results

Based on the results of the experiment on an ultrasonic muffler with the following parameters: length - 1000 mm, diameter - 110 mm, ultrasonic emitter frequency 25 kHz, power - 50 W, the value of *k* was calculated. The initial data and calculation results are given in Table 2.

The found value *k* = 82073908106 is a constant for the studied design of the ultrasonic muffler and is used to determine the dependences of the coagulation degree on the engine crankshaft speed and ultrasound power. Based on the calculated value *k*, changes in the coagulation degree were determined using Equation (11), when cleaning with frequency of 25 kHz and power of 50 W and various crankshaft speeds of a diesel ICE with the volume of 2700 cm^3. The calculation results are presented in Table 3. The graph of changing the coagulation degree, when cleaning with frequency of 25 kHz and power of 50 W and various crankshaft speeds of a diesel ICE with the volume of 2700 cm^3, is shown in Figure 3.

The maximum smoke index of a diesel engine is usually observed in the range of 1200-1800 rpm [24]. The dependence of the coagulation degree *E* using Equation (11) during the cleaning with ultrasound at frequency of 25 kHz and the maximum rotation frequency of the crankshaft of a diesel internal combustion engine in the

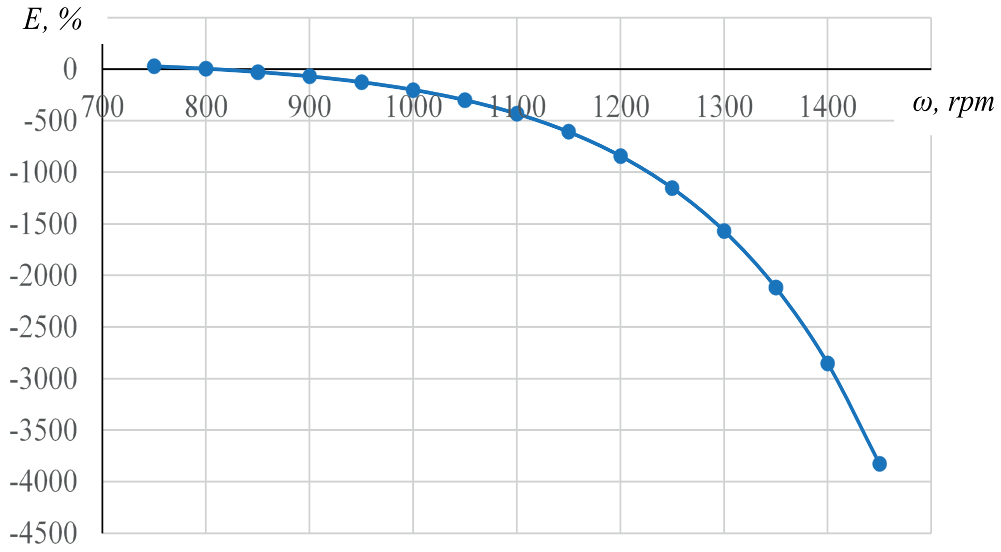

Figure 3 *Graph of changing the degree of coagulation E in the course of ultrasonic cleaning with frequency of 25 kHz and power of 50 W and different crankshaft speeds of a diesel engine of a volume of 2700 cm^3*

Table 4 *Calculation of the coagulation degree E dependence during the cleaning with ultrasound at frequency of 25 kHz and the crankshaft speed of 1800 rpm of a diesel engine of a volume of 2700 cm^3 on the power of ultrasonic radiation W*

f, Hz	k	ω, rpm	ω, rps	V_{cyl}, m^3	L, m	R, m	t, s	W, W	E, %
25	82073908106	1800	30	0.0027	1	0.055	0.059	50	-28839.004
25	82073908106	1800	30	0.0027	1	0.055	0.059	125	-563.269
25	82073908106	1800	30	0.0027	1	0.055	0.059	200	-70.115
25	82073908106	1800	30	0.0027	1	0.055	0.059	275	20.130
25	82073908106	1800	30	0.0027	1	0.055	0.059	350	51.440
25	82073908106	1800	30	0.0027	1	0.055	0.059	425	66.094
25	82073908106	1800	30	0.0027	1	0.055	0.059	500	74.246
25	82073908106	1800	30	0.0027	1	0.055	0.059	575	79.317
25	82073908106	1800	30	0.0027	1	0.055	0.059	650	82.726
25	82073908106	1800	30	0.0027	1	0.055	0.059	725	85.153
25	82073908106	1800	30	0.0027	1	0.055	0.059	800	86.957
25	82073908106	1800	30	0.0027	1	0.055	0.059	875	88.345
25	82073908106	1800	30	0.0027	1	0.055	0.059	950	89.443
25	82073908106	1800	30	0.0027	1	0.055	0.059	1025	90.331
25	82073908106	1800	30	0.0027	1	0.055	0.059	1100	91.063

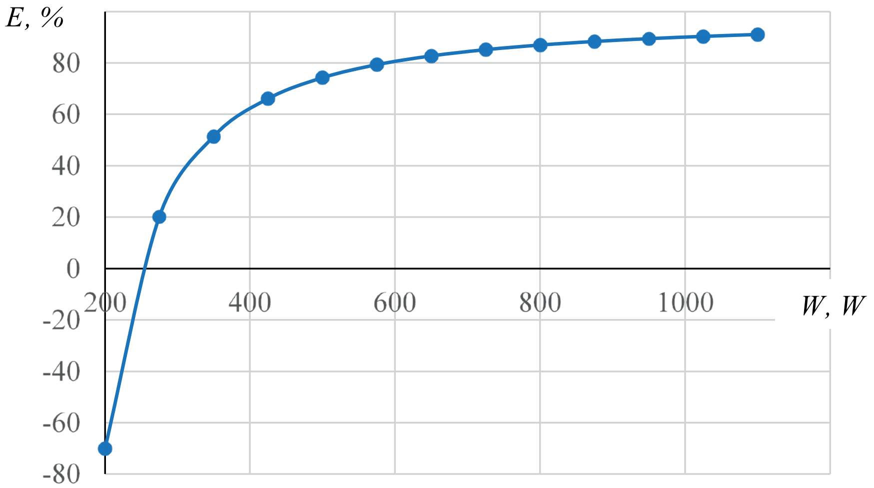

Figure 4 *Graph of the coagulation degree E dependence in the course of cleaning with frequency of 25 kHz and the crankshaft speed of 1800 rpm of a diesel engine of a volume of 2700 cm*^{3} *on the power of ultrasonic radiation W*

Table 5 *Calculation of the coagulation degree E during cleaning with ultrasound with frequency of 25 kHz and power of 600 W and various crankshaft rotation frequencies of a diesel ICE of a volume of 2700 cm*^{3}

f, Hz	k	ω, rpm	ω, rps	V_{cyl}, m^3	L, m	R, m	t, s	J, W	E, %
25	82073908106	750	12.50	0.0027	1	0.055	0.141	63167.869	96.559
25	82073908106	950	15.83	0.0027	1	0.055	0.111	63167.869	95.217
25	82073908106	1150	19.17	0.0027	1	0.055	0.092	63167.869	93.350
25	82073908106	1350	22.50	0.0027	1	0.055	0.078	63167.869	90.754
25	82073908106	1550	25.83	0.0027	1	0.055	0.068	63167.869	87.146
25	82073908106	1750	29.17	0.0027	1	0.055	0.060	63167.869	82.129
25	82073908106	1950	32.50	0.0027	1	0.055	0.054	63167.869	75.155
25	82073908106	2150	35.83	0.0027	1	0.055	0.049	63167.869	65.458
25	82073908106	2350	39.17	0.0027	1	0.055	0.045	63167.869	51.977
25	82073908106	2550	42.50	0.0027	1	0.055	0.041	63167.869	33.234
25	82073908106	2750	45.83	0.0027	1	0.055	0.038	63167.869	7.177
25	82073908106	2950	49.17	0.0027	1	0.055	0.036	63167.869	-29.050
25	82073908106	3150	52.50	0.0027	1	0.055	0.034	63167.869	-79.415
25	82073908106	3350	55.83	0.0027	1	0.055	0.032	63167.869	-149.437
25	82073908106	3550	59.17	0.0027	1	0.055	0.030	63167.869	-246.787

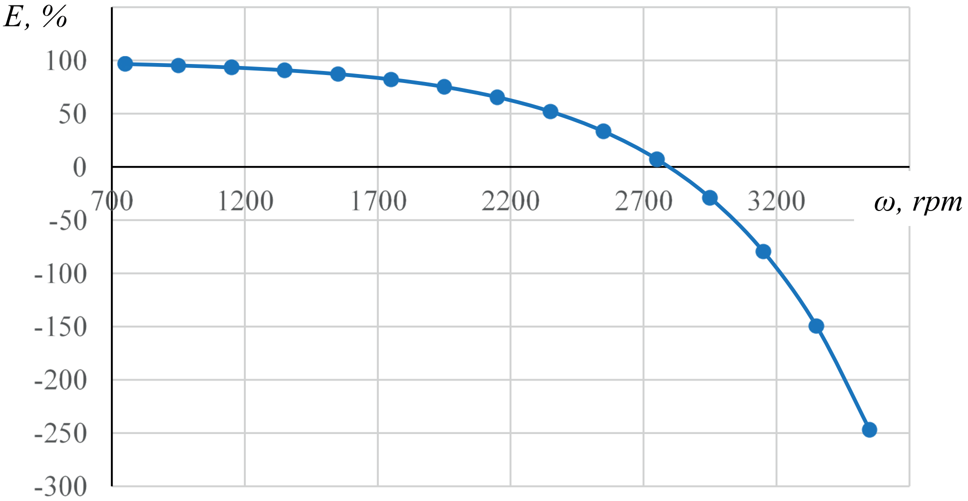

Figure 5 *Graph of changing the degree of coagulation E in the course of ultrasonic cleaning with frequency of 25 kHz and power of 600 W and different crankshaft speeds of a diesel engine of a volume of 2700 cm*^{3}

range at which the maximum smoke is usually observed, i.e., 1800 rpm, on the power of ultrasonic radiation was calculated (Table 4).

Figure 4 shows the graph of the coagulation degree *E* dependence in the course of cleaning with frequency of 25 kHz and the crankshaft speed of 1800 rpm of a diesel engine of a volume of 2700 cm3 on the power of ultrasonic radiation W.

The performance characteristics of the ultrasonic muffler of a calculated parameters of the ultrasonic equipment were determined. The calculation of the coagulation degree *E* during the cleaning with ultrasound with frequency of 25 kHz and power of 600 W and various crankshaft rotation frequencies of a diesel ICE of a volume of 2700 cm^3 using Equation (11), is presented in Table 5.

Figure 5 shows the graph of changing the degree of coagulation *E* in the course of ultrasonic cleaning with frequency of 25 kHz and power of 600 W and different crankshaft speeds of a diesel engine of a volume of 2700 cm^3.

4 Discussion and conclusions

According to the graph of changing the coagulation degree *E* in the course of ultrasonic cleaning with different crankshaft speeds of a diesel ICE of a volume of 2700 cm^3 (Figure 1), it was concluded that the ultrasonic cleaning with frequency of 25 kHz and power of 50 W will still occur at idle crankshaft speeds of the engine of 750 rpm and will amount to 27.73%. With such a cleaning efficiency, the use of an ultrasonic muffler is impractical. To increase the cleaning degree to 80% and higher, it is necessary to increase the power characteristics of ultrasound.

According to the graph of the coagulation degree E dependence in the course of ultrasonic cleaning with frequency of 25 kHz and the crankshaft speed of 1800 rpm of a diesel ICE of a volume of 2700 cm^3 on the ultrasonic radiation power W (Figure 2), the required ultrasonic radiation power was determined. In this case, its value was 600 W.

With ultrasound power of 600 W at idle speed, the purification degree was 96.6% (Figure 3). With increasing the engine crankshaft speed, the coagulation degree decreases. With the crankshaft speed of over 2800 rpm, ultrasonic coagulation does not occur due to insufficient ultrasound power and short time of ultrasonic action on the exhaust gas.

The given calculation method allows for determining the optimal parameters of ultrasonic mufflers for the most effective cleaning of exhaust gases and is suitable for use in designing the exhaust gas purification systems to determine the characteristics of ultrasonic equipment and its operating mode.

Acknowledgements

The authors received no financial support for the research, authorship and/or publication of this article.

Conflicts of interest

The authors declare that they have no known competing financial interests or personal relationships that could have appeared to influence the work reported in this paper.

References

[1] POPE, C. A. III, BURNETT, R. T., THUN, M. J., CALLE, E. E., KREWSKI, D., ITO, K., THURSTON, G. D. Lung cancer, cardiopulmonary mortality, and long-term exposure to fine particulate air pollution. *JAMA* [online]. 2002, **287**(9), p. 1132-1141. ISSN 0098-7484, eISSN 1538-3598. Available from: https://doi.org/10.1001/jama.287.9.1132

[2] YESSENBAYEVA, A., APSALIKOV, B., MASSABAYEVA, M., KAZYMOV, M., SHAKHANOVA, A., MUSSAZHANOVA, Z., KADYROVA, I., SHAIMARDANOV, N. Biomarkers of immunothrombosis and polymorphisms of IL2, IL6, and IL10 genes as predictors of the severity of COVID-19 in a Kazakh population. *PLoS ONE* [online]. 2023, **18**, e0288139. eISSN 1932-6203. Available from: https://doi.org/10.1371/journal.pone.0288139

[3] AKHMALTDINOVA, L., SIROTA, V., BABENKO, D., ZHUMALIYEVA, V., KADYROVA, I., MARATKYZY, M., IBRAYEVA, A., AVDIENKO, O. Proinflammatory cytokines and colorectal cancer - the impact of the stage. *Contemporary Oncology* [online]. 2021, **24**(4), p. 207-210. ISSN 1428-2526, eISSN 1897-4309. Available from: https://doi.org/10.5114/wo.2020.102551

[4] TSESHKOVSKAYA, Y. A., ORALOVA, A. T., GOLUBEVA, E. I., TSOY, N. K., ZAKHAROV, A. M. Dust suppression on the surfaces of storage device of technogenic mineral formations. *News National Academy of Sciences of the Republic of Kazakhstan Series of Geology and Technical Sciences* [online]. 2022, **2**, p. 230-241. ISSN 2224-5278, eISSN 2518-170X. Available from: https://doi.org/10.32014/2022.2518-170X.172

[5] KADYROVA, I. A., MINDUBAEVA, F. A., GRJIBOVSKI, A. M. Prediction of outcomes after stroke: a systematic review. *Human Ecology (Russian Federation)* [online]. 2015, **22**(10), p. 55-64. eISSN 2949-1444. Available from: https://doi.org/10.17816/humeco16983

[6] OSPANOV, O., YELEUOV, G., KADYROVA, I., BEKMURZINOVA, F. The life expectancy of patients with metabolic syndrome after weight loss: study protocol for a randomized clinical trial (LIFEXPE-RT). *Trials* [online]. 2019, **20**(1), 716. eISSN 1745-6215. Available from: http://dx.doi.org/10.1186/s13063-019-3304-9

[7] BANDYOPADHYAY, A. Neurological disorders from ambient (urban) air pollution emphasizing UFPM and PM2.5. *Current Pollution Reports* [online]. 2016, **2**, p. 203-211. eISSN 2198-6592. Available from: https://doi.org/10.1007/s40726-016-0039-z

[8] KADYROV, A., BEMBENEK, M., SARSEMBEKOV, B., KUKESHEVA, A., NURKUSHEVA, S. The influence of the frequency of ultrasound on the exhaust gas purification process in a diesel car muffler. *Applied Sciences* [online]. 2024, **14**(12), 5027. eISSN 2076-3417. Available from: https://doi.org/10.3390/app14125027

[9] KADYROV, A., SARSEMBEKOV, B., KUKESHEVA, A., SINELNIKOV, K. Application of electric pulse and ultrasonic mufflers for increasing the degree of exhaust gas purification in car engines. *International Journal of Innovative Research and Scientific Studies* [online]. 2025, **8**(1), p. 33-40. eISSN 2617-6548. Available from: https://doi.org/10.53894/ijirss.v8i1.3570

[10] IBATOV, M. K., KADYROV, A. S., PAK, I. A., KADYROVA, I. A., ASKAROV, B. S. The results of experimental studies of the capacitive equipment of ultrasonic cleaning of exhaust gases of vehicles. *Ugol/Russian Coal Journal* [online]. 2020, **2**, p. 73-78. ISSN 0041-5790. Available from: https://doi.org/10.18796/0041-5790-2020-2-73-78

[11] GARBARIEN, I., DUDOITIS, V., ULEVICIUS, V., PLAUSKAITE-SUKIEN, K., KILIKEVICIUS, A., MATIJOSIUS, J., RIMKUS, A., BYCENKIENE, S. Application of acoustic agglomeration technology to improve the removal of submicron particles from vehicle exhaust. *Symmetry* [online]. 2021, **13**(7), 1200. eISSN 2073-8994. Available from: https://doi.org/10.3390/sym13071200

[12] KADYROV, A., GANYUKOV, A., PAK, I., SULEYEV, B., BALABEKOVA, K. Theoretical and experimental study of operation of the tank equipment for ultrasonic purification of the internal combustion engine exhaust gases. *Communications-Scientific Letters of the University of Zilina* [online]. 2021, **23**(3), p. B219-B226. ISSN 1335-4205, eISSN 2585-7878. Available from: https://doi.org/10.26552/com.C.2021.3.B219-B226

[13] PAK, I., KADYROV, A., ASKAROV, B., SULEYEV, B., KARSAKOVA, A. Developing and studying the method of ultrasonic purification and utilization of internal combustion engine exhaust gases. *Communications - Scientific Letters of the University of Zilina* [online]. 2023, **25**(3), p. B245-B258. ISSN 1335-4205, eISSN 2585-7878. Available from: https://doi.org/10.26552/com.C.2023.060

[14] KADYROV, A., WARGULA, L., KUKESHEVA, A., DYSSENBAEV, Y., KACZMARZYK, P., KLAPSA, W., WIECZOREK, B. Optimization of vertical ultrasonic attenuator parameters for reducing exhaust gas smoke of compression-ignition engines: efficient selection of emitter power, number, and spacing. *Applied Sciences* [online]. 2025 **15**(14), 7870. eISSN 2076-3417. Available from: https://doi.org/10.3390/app15147870

[15] VON SMOLUCHOWSKI, M. Three lectures on diffusion, Brownian molecular motion, and coagulation of colloidal particles. *Physical Journal/Physikalische Zeitschrift*. 1916, **17**, p. 557-585. ISSN 2366-9373.

[16] VON SMOLUCHOWSKI, M. On Brownian molecular motion under the influence of external forces and its connection with the generalized diffusion equation/Uber Brownsche Molekularbewegung unter Einwirkung außerer Krafte und den Zusammenhang mit der verallgemeinerten Diffusionsgleichung (in German). *Annals of Physics/Annalen der Physik* [online]. 1915, **353**(24), p. 1103-1112. ISSN 0003-3804, eISSN 1521-3889. Available from: https://doi.org/10.1002/andp.19163532408

[17] BERGMAN, L. *Ultrasound and its application in science and technology*. Translation from German. Moscow: Publishing House of Foreign Literature, 1957.

[18] KHMELEV, V. N., SHALUNOV, A. V., GOLYKH, R. N. A method for calculating ultrasonic coagulation of PM2.5 particles in vortex and turbulent acoustic flows. *Journal of Applied and Industrial Mathematics* [online]. 2024, **18**(1), p. 47-59. ISSN 1990-4789, eISSN 1990-4797. Available from: https://doi.org/10.1134/S1990478924010058

[19] SHVYDKIY, V. S., LADYGICHEV, M. G. *Gas purification. Thermal Engineering*. 2002.

[20] KIDDOO, G. Sonic agglomeration: a new solution. *Chemical Engineering*. 1951, **58**(5), p.154-156. ISSN 0009-2460.

[21] Scientific and production company META. Exhaust gas smoke meter. Modifications: META- 01 MP 0.1 LTK, META-01 MP 0.2. Operation manual. Zhigulevsk, OLP NPF META (in Russian) [online]. 2017. Available from: http://www.meta-moscow.ru/upload/iblock/d5a/d5a2f38c7772be2ae586a41766780b86.pdf

[22] LIKHACHEV, V. A., LOPATIN, O. P., KOZLOV, A. N. Modeling of soot formation in a diesel cylinder. *St. Petersburg Polytechnic University Journal of Engineering Science and Technology* [online]. 2019, **25**(1), p. 47-59. ISSN 2782-6724. Available from: https://doi.org/10.18721/JEST.25105.

[23] KADYROV, A., KRYUCHKOV, Y., SINELNIKOV, K., GANYUKOV, A., SAKHAPOV, R., KUKESHEVA, A. Studying the process of the internal combustion engine exhaust gas purification by an electric pulse. *Communications - Scientific Letters of the University of Zilina* [online]. 2022, **24**(4), p. B275-B287. ISSN 1335-4205, eISSN 2585-7878. Available from: https://doi.org/10.26552/com.C.2022.4.B275-B287

[24] SHAROGLAZOV, B. A., FARAFONTOV, M. F., KLEMENTYEV, V. V. *Internal combustion engines: theory, modelling and calculation of processes:* Textbook for the course Theory of working processes and modeling of processes in internal combustion engines. Chelyabinsk: Publishing house of SUSU, 2005. ISBN 5-696-03268-0.

THEORETICAL AND EXPERIMENTAL STUDY OF DIESEL ENGINE EXHAUST GAS PURIFICATION IN A VERTICAL ULTRASONIC MUFFLER STAND

Adil Kadyrov, Aliya Kukesheva, Yermek Dyussenbaev, Zhanara Zhunusbekova*, Pavel Bezkorovainy

Abylkas Saginov Karaganda Technical University NPJSC, Karaganda, Kazakhstan

*E-mail of corresponding author: zhanarazhumashevna@gmail.com

Adil Kadyrov 0000-0001-7071-2300,
Yermek Dyussenbaev 0000-0002-8070-7254,
Pavel Bezkorovainy 0009-0005-0945-1232
Aliya Kukesheva 0000-0002-3063-5870,
Zhanara Zhunusbekova 0000-0003-0473-1954,

Resume

In this article is presented a new method of ultrasonic cleaning of exhaust gases of diesel engines by coagulation of soot particles and their subsequent sedimentation. The analytical modelling of the particle motion in a vertical muffler stand was carried out, taking into account the ultrasonic effect and gravitational forces. Experimental studies of the developed stand confirmed that ultrasound promotes agglomeration and sedimentation of soot, reduces the CO_2 content and increases the O_2 concentration in the exhaust gases. The maximum cleaning efficiency is achieved with the simultaneous use of all the ultrasonic emitters. The results of the work can be used in designing modern exhaust gas cleaning systems.

Article info

Received 8 August 2025
Accepted 23 November 2025
Online 8 January 2026

Keywords:

ultrasonic cleaning
diesel engine exhaust
soot particle coagulation
vertical muffler
transport equipment
agglomeration and sedimentation
environmental impact reduction

Available online: https://doi.org/10.26552/com.C.2026.009

ISSN 1335-4205 (print version)
ISSN 2585-7878 (online version)

1 Introduction

The Diesel engine emissions contain a wide range of harmful substances, including gaseous components and solid particles [1]. One of the most significant factors that affect the environmental safety of diesel engines is the mass concentration of soot in the exhaust gases [2]. Soot that is formed as a result of incomplete combustion of fuel, is a collection of carbon nanoparticles that can penetrate deep into the human respiratory tract and cause serious respiratory and cardiovascular diseases [3]. In addition to the negative impact on health, the soot emissions contribute to formation of smog and increasing the greenhouse effect [4-5].

The soot content in the exhaust gases varies depending on many factors: the engine operating mode, the fuel quality, the fuel system health, and air-fuel mixture characteristics [6-7]. At idle and under a high load, the soot concentration increases significantly, which leads to increasing the smoke index [8]. In particular, lack of oxygen, a low cetane number of fuel and incorrect operation of injectors contribute to the formation of particles whose sizes range from several nanometers to tens of micrometers.

Reducing the mass concentration of soot in the exhaust gases of diesel engines is achieved through various methods and technologies [9]. Among them, there is optimization of fuel combustion, including the use of fuel with a high cetane number, precise control of fuel supply using Common Rail systems, improved mixture formation with turbocharging and increased injection pressure, as well as exhaust gas recirculation (EGR) [10]. However, those technologies are sensitive to the fuel quality and require complex maintenance and precise calibration of systems.

Exhaust gas filtration is also carried out using diesel particulate filters (DPF) and nitrogen oxide filters (LNT) that effectively trap solid soot particles [11]. However, these systems are expensive, they require regular regeneration and are sensitive to fuel contamination. Catalytic technologies, such as selective catalytic reduction (SCR) systems with a urea solution and oxidation catalytic converters (DOC), reduce soot emissions, as well [12]. However, they have a number of disadvantages, such as a high cost, complexity of operation and the need for regular regeneration. In addition, filters are sensitive to the fuel quality, and the accumulation of soot in their structure reduces the engine efficiency [13]. In this regard, an urgent task is to develop alternative methods of reducing the soot concentration in exhaust gases.

Currently, studies are being conducted aimed at cleaning vehicle exhaust gases with the use of ultrasonic technologies. One such study is the work of scientists from Karaganda Technical University, who proposed using the ultrasonic coagulation method to reduce the content of harmful components in exhaust gases directly in the car mufflers [14-15].

Ultrasonic coagulation is based on the effect of high-frequency sound waves on exhaust gas particles. Under the effect of ultrasound, small particles begin to vibrate, to collide and to stick together, forming larger agglomerates [16]. Enlarged particles settle more easily and are better captured, which helps to reduce the content of solid pollutants in the exhaust [17-18].

Special experimental stands of horizontal ultrasonic mufflers were developed for the research. Ultrasonic equipment was installed on these stands, including a generator and emitters-reflectors of ultrasonic waves [19]. Experimental studies conducted on the stands made it possible to study the process of particle coagulation under the effect of ultrasound and to confirm the effectiveness of the proposed method in cleaning exhaust gases. To assess the effectiveness, changes in the oxygen concentration, the gas composition and the smoke level before and after the exposure to ultrasound were analyzed [20].

Despite some positive results obtained, current studies of ultrasonic coagulation for cleaning exhaust gases do not allow solving design issues. In particular, it is necessary to improve the design of the experimental muffler stand to ensure uniform distribution of the ultrasonic field and optimal placement of the emitters. In this regard, the authors proposed the development of a vertical ultrasonic muffler stand.

Unlike the previous horizontal designs [14-20], the proposed vertical configuration provides gravitationally assisted sedimentation, enabling multi-stage acoustic exposure and improved uniformity of ultrasonic field distribution.

The transition to a vertical design of the ultrasonic muffler is caused by the desire to improve the efficiency of settling the coagulated soot particles. In the vertical configuration, soot particles combined under the effect of ultrasound, settle down more easily under the force of gravity, which contributes to their more efficient collection at the bottom of the device. In addition, the vertical arrangement allows for the mounting of several ultrasonic emitters at different heights, providing step-by-step processing of the exhaust gas. This is especially important for removing fine particles that require longer or multiple exposures for effective coagulation.

The hypothesis of this study is that the vertical movement of the exhaust gas and the step-by-step processing of the gas flow with ultrasound contribute to increasing the efficiency of soot particle coagulation, which will lead to their enlargement and subsequent sedimentation. The optimal location and power of the ultrasonic emitters also make it possible to achieve a significant reduction in the mass concentration of soot in the exhaust gases of diesel engines.

The goal of this study was the theoretical and experimental confirmation of the proposed method of ultrasonic cleaning, which allows for reducing the content of harmful emissions in exhaust gases. To achieve this goal, several problems were solved, including the development of a mathematical model of the soot particle motion in a vertical muffler, numerical calculations of particle dynamics under the effect of ultrasound, development of an experimental stand, testing with various combinations of ultrasonic emitters, and comparison of analytical modelling results to experimental data.

The scientific novelty of the study represents the fact that a model of soot particle coagulation in a vertical ultrasonic muffler has been proposed and substantiated for the first time. A differential equation of particle motion has been developed that takes into account the effects of gravity, hydrodynamic resistance, ultrasonic wave pressure and the coagulation process. Comprehensive studies have been conducted, including both analytical modelling and experimental testing on a specially designed stand. The results have shown that ultrasound promotes agglomeration and sedimentation of soot particles, reduces the CO_2 content and increases the O_2 concentration in the exhaust gases. The maximum effect is achieved with the simultaneous use of all the emitters, which confirms the importance of selecting the optimal location and power of ultrasonic action.

The practical significance of the study lies in the fact that the developed method can be used in modern diesel engine emission reduction systems, providing an alternative to expensive and difficult to maintain particulate filters. Ultrasonic cleaning of mufflers can be used in transport and agricultural diesel engines, reducing their environmental impact and increasing the operating efficiency. The results and recommendations obtained can be useful for further modernization of exhaust gas cleaning systems and development of innovative solutions in the field of transport ecology.

2 Materials and methods

Mathematical modelling of the complex process of gas particle coagulation in a muffler under the effect of ultrasound does not allow obtaining strictly deterministic dependences that fully describe the mechanism of soot particle deposition. This is caused by a lot of factors that affect the process, including the gas flow characteristics, acoustic parameters of ultrasonic waves, particle interaction dynamics, and gas movement conditions inside the muffler.

In this regard, the results of the mathematical model study should be presented and supplemented by experimental results. It is necessary to analytically and then experimentally determine the nature of changing the mass of the deposited soot particles, to establish the coagulation coefficient K and the optimal operating modes of the ultrasonic emitters.

A mathematical model is known that describes the movement of a gas particle in an experimental stand of a horizontal muffler:

$$m \cdot a = F_D + F_a - F_G , \tag{1}$$

where:
F_D is the pressure force;
F_a is the ultrasonic pressure force;
F_G is the hydrodynamic resistance force.

The differential equation of motion of a gas particle in a horizontal stand of an ultrasonic muffler is:

$$\begin{gathered} m \cdot \ddot{x} = \frac{\pi \cdot r^2 \cdot d^2 P}{D^2} - \pi \cdot r^2 \cdot \rho \cdot A \cdot c \cdot \\ \cdot \omega \cdot \cos\omega \cdot \left(t - \frac{n}{c}\right) - 6 \cdot \pi \cdot \mu \cdot r \cdot \frac{dx}{dt}. \end{gathered} \tag{2}$$

However, this model cannot be used to describe the mechanism of the soot particle motion, since it considers only the horizontal movement of particles without taking into account the gravitational effect, which leads to insufficient accuracy in describing the coagulation processes in a vertical stand. After all, in the vertical direction, the particle is affected by the gravity force *mg*, which must be included in the equation of motion, since it has a significant effect on the dynamics of particle sedimentation.

Based on the above, the following equation was compiled to describe the motion of a soot particle in a vertical type of experimental muffler:

$$m \cdot a = F_{en} + F_{us} - F_{res} - m \cdot g , \tag{3}$$

where:
m is the mass of a soot particle, kg;
a is the acceleration that a body receives under the action of a force, m/s^2;
F_{en} is the pressure force from the engine, N;
F_{us} is the force of ultrasonic effect from emitters, N;
F_{res} is the hydrodynamic resistance force (Stocks), N;
g is acceleration of gravity, m/s^2.

The pressure force from the engine is:

$$F_{en} = \frac{\pi \cdot r^2 \cdot d^2 \cdot P}{D^2} , \tag{4}$$

where:
F_{en} is the pressure force from the engine, N;
d is the inlet pipe diameter, m;
D is the muffler diameter, m;
r is the particle radius, m;
P is the muffler inlet pressure, Pa.

The ultrasound force is:

$$F_{us}(x) = A \cdot \sin(kx) , \tag{5}$$

where:
F_{us} is the ultrasound force, N;
A is the ultrasound amplitude, m;
$k = \frac{2 \cdot \pi}{\lambda}$ is the wave number.

If there are several emitters *N* and they are installed at the distance *d*, then the resulting ultrasound power has the following dependence:

$$F_{us}(x) = \sum_{i=1}^{N} A_i \cdot \sin(k \cdot (x - x_i) + \varphi_i) , \tag{6}$$

where:
F_{us} is the ultrasound power, N;
x_i is the location of the i-th emitter;
φ_i is the phase shift, m.

The resistance force is:

$$F_{res} = -b \cdot \vartheta_p = -6 \cdot \pi \cdot \mu \cdot r \cdot \vartheta_p , \tag{7}$$

where:
F_{res} is the resistance force, N;
b is the resistance coefficient;
μ is the viscosity, Pa·s;
ϑ_p is the particle velocity, m/s.

Changes in the engine crankshaft speed have a proportional effect on the gas flow velocity $\vartheta_g(n)$. However, the medium resistance depends on the relative velocity of the particle with respect to the gas flow, and not on its absolute velocity. If the particle moves with the gas, the relative velocity is zero and there is no resistance. If the particle moves against the gas flow, it experiences the greatest resistance. Therefore, the equation determining the resistance force is as follows:

$$F_{rf} = -b \cdot (\vartheta_p - \vartheta_g(n)) , \tag{8}$$

where:
F_{rf} is the resistance force, N;
$\vartheta_n(n)$ is the gas flow velocity, m/s;
n is the number of the engine revolutions, rpm;
k_n is the coefficient of the gas velocity dependence on the engine revolutions.

Based on Equation (3) and its components, a differential equation was compiled that describes the motion of a soot particle in a vertical muffler:

$$\begin{gathered} \frac{m \cdot d^2 \cdot x}{dt^2} = \frac{\pi \cdot r^2 \cdot d^2 \cdot P}{D^2 dt^2} + \sum_{i=1}^{N} A_i \cdot \\ \cdot \sin(k(x - x_i) + \varphi_i) - b \cdot (\vartheta_p - \vartheta(n)) - m \cdot g. \end{gathered} \tag{9}$$

When the process of coagulation between particles is being taken into account, the mass of an individual particle m is a function of time $m(t)$, since when interacting, the particles can combine, increasing their size and mass. However, coagulation does not occur at every collision of particles, since its probability depends on a lot of factors, such as the particle velocity, the particle size, the concentration in the gas flow, the temperature of the medium and the intensity of the ultrasonic equipment.

To take this phenomenon into account, the concept of coagulation probability v was introduced. It determines the probability with which the colliding particles will actually combine. Consequently, changing the mass of a particle over time is described by an equation of the following type:

$$\frac{dm}{dt} = v \cdot K \cdot n_c\,, \tag{10}$$

$$m(t) = m_0 + v \cdot K \cdot \int_0^t n_c dt\,, \tag{11}$$

$$\begin{gathered}\left(m_0 + v \cdot K\int_0^t n_c dt\right)\frac{d^2x}{dt^2} = \frac{\pi \cdot r^2 \cdot d^2 \cdot P}{D^2 dt^2} + \\ + \sum_{i=1}^{N} A_1 \cdot \sin(k(x - x_i) + \varphi_i) - \\ - b \cdot (\vartheta_p - \vartheta_g(n)) - m \cdot g.\end{gathered} \tag{12}$$

The resulting equation is a second-order differential equation. The Runge-Kutta method was used to solve it, which allows for transforming a second-order equation into a system of first-order equations. This method has higher accuracy compared to the Euler method, since it uses intermediate calculations at each step to refine the values. In addition, the Runge-Kutta method is well suited for solving nonlinear equations containing integral terms, variable mass, and nonlinear resistance of the medium, which makes it an effective way to solve the problem.

According to the Runge-Kutta method, variables for performing the intermediate calculations were introduced: x - the particle coordinate; $\vartheta = \frac{dx}{dt}$ - the particle velocity; $m(t) = m_0 + vK\int_0^t n_c dt$ - the particle mass taking into account coagulation.

Then, the system of the first-order equations was compiled as:

$$\begin{cases} \dfrac{dx}{dt = \vartheta} \\ \dfrac{d\vartheta}{dt} = \dfrac{1}{m(t)}\left[\begin{array}{l}\dfrac{\pi \cdot r^2 \cdot d^2 \cdot P}{D^2 dt^2} + \sum_{i=1}^{N} A_i \cdot \\ \cdot \sin(k(x - x_i) + \varphi_i) - \\ - b(\vartheta_p - \vartheta_g(n)) - m \cdot g\end{array}\right] \\ \dfrac{dm}{dt} = v \cdot K \cdot n_c. \end{cases} \tag{13}$$

The mathematical model, describing the motion and coagulation of soot particles in the vertical ultrasonic muffler is based on a set of physical assumptions and parameters supported by experimental measurements and literature sources. The model assumes that soot particles are spherical, which allows the use of Stokes' drag law, applicable to micron-sized particles at Reynolds numbers Re < 1. The gas flow inside the muffler is considered as steady and directed along its axis, while the turbulent fluctuations and temperature gradients are neglected due to their negligible influence on particle dynamics compared to acoustic and aerodynamic forces. Ultrasonic waves are assumed to propagate predominantly in the axial direction, without accounting for complex interference patterns, and the acoustic force is modeled as a sinusoidal function of the spatial coordinate, which is typical for standing or quasi-standing waves in narrow cylindrical channels. Coagulation is treated as a probabilistic process, and therefore, a sticking probability v is introduced into the governing equations, based on the exponential collision model. The model parameters were also selected based on experimental measurements and literature data: the ultrasonic frequency of 40 kHz corresponds to the operating range of the transducers used; the vibration amplitude on the order of 10^{-5} m was determined using a laser vibrometer; the particle radius $r = 10^{-6}$ m represents agglomerated soot clusters of micron size; the coagulation coefficient $K_c = 10^{-5}$ and sticking probability $v = 0.6321$ correspond to typical values for micron-sized particles in a low-velocity flow; the dependence of gas velocity on engine speed is defined by the experimentally determined coefficient $k_n = 0.01$; the drag coefficient $b = 6\varpi\mu r$ is calculated using the viscosity of hot exhaust gas $\mu \approx 1.7\times10^{-5}$ Pa·s; the particle concentration $n_c = 10^6$ m^{-3} reflects the typical range observed in diesel exhaust; and the wave number k is calculated from the wavelength of 0.017 m, corresponding to a sound speed of approximately 425 m/s in heated exhaust gas. The combination of these assumptions and parameters ensures an accurate representation of the key processes of particle coagulation and sedimentation.

Then, the initial conditions and the basic data were introduced. They are presented in Table 1.

Then, for each time step h, the intermediate indicators of the coefficients k_1, k_2, k_3, k_4 for the coordinate, velocity and mass of the particle are calculated taking into account coagulation using the following formulas:

Coefficient k_1:

$$\begin{aligned} & k_1^x = h \cdot v_n, \\ & k_1^\vartheta = h \cdot \frac{1}{m_n}\left[\begin{array}{l}\dfrac{\pi r^2 d^2 P}{D^2 dt^2} + \sum_{i=1}^{N} A_i \cdot \\ \cdot \sin(k(x_n - x_i) + \varphi_i) - \\ - b \cdot (\vartheta_p - \vartheta_g(n)) - m \cdot g\end{array}\right], \\ & k_1^m = h \cdot v \cdot K \cdot n_{c.} \end{aligned} \tag{14}$$

Coefficient k_2:

$$k_2^x = h \cdot \left(v_n + \frac{k_1^\vartheta}{2}\right),$$

***Table 1** Initial conditions and basic data*

No.	Initial conditions and basic data	Indicators	Units
1	Initial position	$x_0 = 0$	m
2	Initial velocity	$v_0 = 0$	m/s
3	Initial particle mass	$m_0 = 1 \cdot 10^{-6}$	kg
4	Integration step	$h = 0.00001$	s
5	Maximum simulation time:	$t_{\max} = 0.00004$	s
6	Manifold pressure parameters	$P_{amp} = 500$	Pa
7	Coagulation coefficient	$K_c = 1 \cdot 10^{-5}$ (for particle of the10^{-6} size)	
8	Concentration of soot particles in gas	$n_c = 1 \cdot 10^6$ $1/m^3$(for diesel exhaust from 10^5-10^9 part/m^3)	
9	Coagulation probability	v = 0.6321 (according to the exponential law 1-e^{-Kt})	
10	Amplitude of ultrasonic vibrations	$A = 1 \cdot 10^{-5}$	m
11	Wave number	$k = \frac{2\pi}{0.017}$ (wave length 0.017)	m
12	Gas drag coefficient	$b = 1 \cdot 10^{-6}$	
13	Gas flow velocity coefficient	$k_n = 0.01$	
14	Soot particle radius	$r = 1 \cdot 10^{-6}$	m
15	Inlet pipe diameter	$d = 0.04$	m
16	Muffler diameter	$D = 0.09$	m
17	Gravity acceleration	$g = 9.81$	m/s^2

$$k_2^{\vartheta} = h \cdot \frac{1}{m_n + \frac{k_1^m}{2}} \left[\begin{array}{l} \frac{\pi \cdot r^2 \cdot d^2 \cdot P}{D^2 dt^2} + \sum_{i=1}^{N} A_i \cdot \sin \\ \left(k\left(x_n + \frac{k_1^x}{2} - x_i \right) + \varphi_i \right) - \\ - b \cdot \left(\vartheta_n + \frac{k_1^v}{2} - \vartheta_g(n) \right) - \\ - g \cdot \left(m_n + \frac{k_1^m}{2} \right) \end{array} \right], \quad (15)$$

$$k_2^m = h \cdot v \cdot K \cdot n_{c.}$$

Coefficient k_3:

$$k_3^x = h \cdot \left(v_n + \frac{k_1^{\vartheta}}{2} \right),$$

$$k_3^{\vartheta} = h \cdot \frac{1}{m_n + \frac{k_1^m}{2}} \left[\begin{array}{l} \frac{\pi \cdot r^2 \cdot d^2 \cdot P}{D^2 dt^2} + \sum_{i=1}^{N} A_i \cdot \sin \\ \left(k\left(x_n + \frac{k_1^x}{2} - x_i \right) + \varphi_i \right) - \\ - b \cdot \left(\vartheta_n + \frac{k_2^v}{2} - \vartheta_r(n) \right) - \\ - g \cdot \left(m_n + \frac{k_2^m}{2} \right) \end{array} \right], \quad (16)$$

$$k_3^m = h \cdot v \cdot K \cdot n_{c.}$$

Coefficient k_4:

$$k_4^x = h \cdot (v_n + k_3^{\vartheta}),$$

$$k_4^{\vartheta} = h \cdot \frac{1}{m_n + k_3^m} \left[\begin{array}{l} \frac{\pi \cdot r^2 \cdot d^2 \cdot P}{D^2 dt^2} + \sum_{i=1}^{N} A_i \cdot \sin \\ \left(k\left(x_n + \frac{k_2^x}{2} - x_i \right) + \varphi_i \right) - \\ - b \cdot \left(\vartheta_n + \frac{k_2^v}{2} - \vartheta_r(n) \right) - \\ - g \cdot \left(m_n + \frac{k_2^m}{2} \right) \end{array} \right], \quad (17)$$

$$k_3^m = h \cdot v \cdot K \cdot n_{c.}$$

After calculating the coefficients, the coordinates, velocity, and mass of the particle were determined, taking into account coagulation using the following formulas:

$$\begin{aligned} x_{n+1} &= x_n + \frac{1}{6}(k_1^x + 2 \cdot k_2^x + 2 \cdot k_3^x + k_4^x), \\ \vartheta_{n+1} &= \vartheta_n + \frac{1}{6}(k_1^{\vartheta} + 2 \cdot k_2^{\vartheta} + 2 \cdot k_3^{\vartheta} + k_4^{\vartheta}), \\ m_{n+1} &= m_n + \frac{1}{6}(k_1^m + 2 \cdot k_2^m + 2 \cdot k_3^m + k_4^m). \end{aligned} \quad (18)$$

The coupled ODE system was solved for position, velocity and mass growth due to coagulation in a vertical muffler using the classical 4th-order Runge-Kutta method with fixed step h (Table 1). At each step, engine pressure, acoustic radiation force, hydrodynamic drag and gravity are evaluated; the mass rate follows a probabilistic coagulation term (Figure 1).

The calculation results are presented in Table 2.

According to the calculations, the particle mass increases over time, which indicates a coagulation process in which the particle absorbs the other particles colliding with them in the gas flow. This leads to a gradual increase of its size and mass, which in turn affects its dynamics. As the mass increases, the particle begins to settle faster, since the gravitational forces acting on it become more significant, and the resistance of the environment does not compensate for the increase in mass. This leads to accelerated sedimentation, which is confirmed by decreasing the x coordinate indicating downward movement. At the same time, the particle velocity rapidly increases, which indicates intense downward acceleration. Such a rapid increase in velocity is caused not only by gravitational attraction, but by changing the mass, as well, since the larger particles experience less aerodynamic resistance relative to their mass and therefore, settle faster under the action of external forces.

The obtained analytical dependences require confirmation by experimental studies. In this regard,

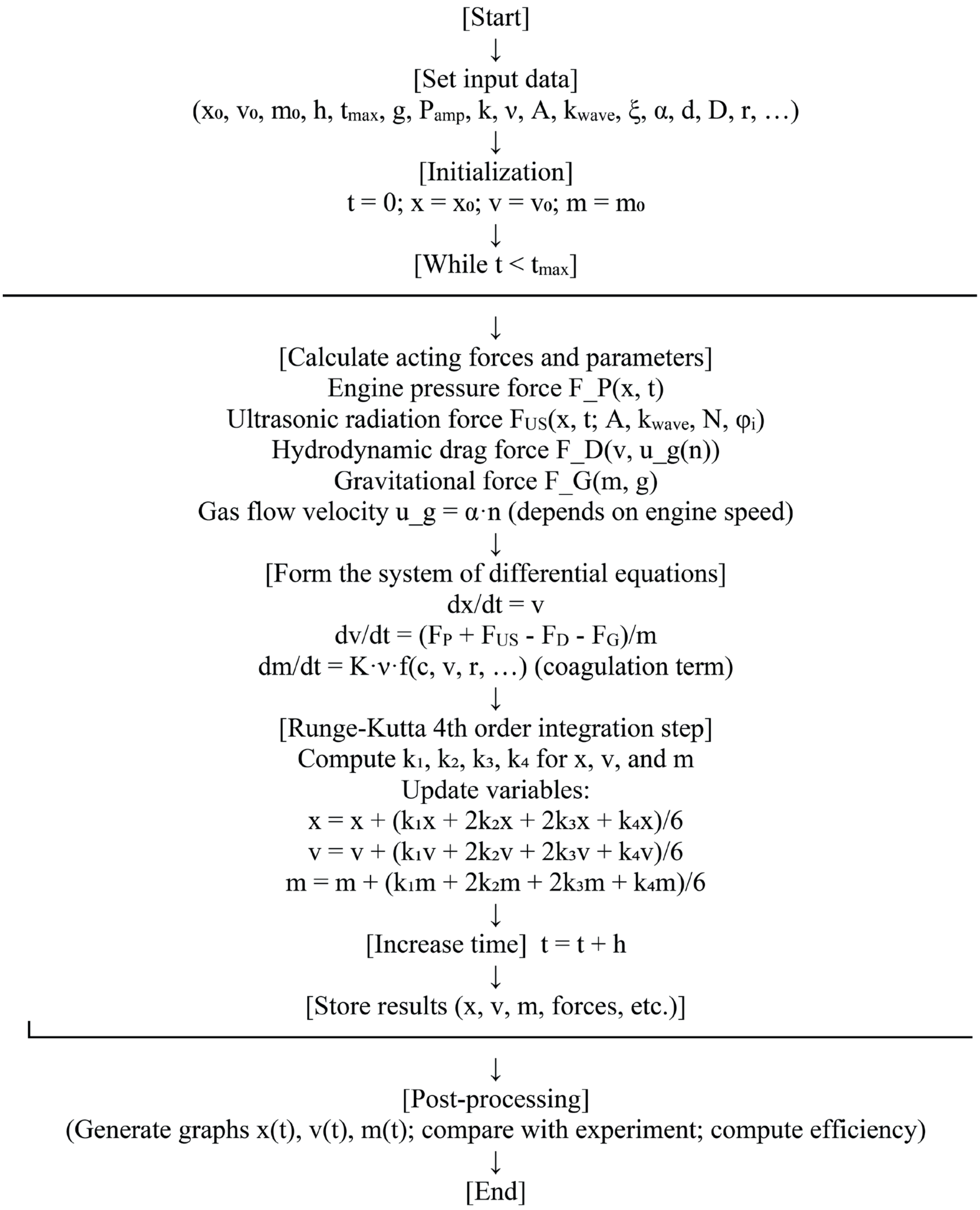

Figure 1 *Flowchart of the modelling algorithm using the 4th-order Runge-Kutta method for particle motion and coagulation in the vertical ultrasonic muffler*

Table 2 *The calculation results*

Time (s)	Coordinate x (m)	Velocity v (m/s)	Mass m (kg)
0	0	0	0
0.00001	-0.000002	-0.608884	0.000064
0.00002	-0.000016	-2.435372	0.0001270
0.00003	-0.000055	-5.479444	0.000191
0.00004	-0.000130	-9.741067	0.000254

Figure 2 *Experimental stand of the ultrasonic muffler of a Diesel engine*

Figure 3 *The process of preparing and weighing paper sheets*

a vertical ultrasonic muffler stand was developed (Figure 2).

The experimental technique consisted of determining the parameters of carbon dioxide, oxygen and the mass of settled soot before and after the exposure to ultrasound depending on changing the combination of ultrasonic emitters, and taking into account the change in the number of revolutions of the engine crankshaft. The experiments were carried out in two stages: Stage 1 - before the gas exposure to ultrasound, Stage 2 - after the gas exposure to ultrasound. The gas was exposed to ultrasound by installing ultrasonic emitters in the muffler housing and with their random connection in various combinations. The frequency and power of the ultrasonic emitters were fixed at the frequency of 25 kHz and the total power of 100 W. The experiments were carried out on an MTZ-80 tractor, the fuel grade was diesel.

The procedure for the conducting experimental studies was as follows:

- experiments to obtain parameters of carbon dioxide, oxygen and the mass of settled soot were carried out without turning on and with turning on the ultrasonic equipment for 5 minutes each;
- the lower part of the device was lined in a semicircle with five numbered sheets of paper measuring 10×10 cm, with the total length of 50 cm, the mass of which was determined before the testing, using high-precision jewelry scales “MH-500” (Figure 3);
- experimental studies were carried out with the engine crankshaft speeds of 1000, 1500, 2000 rpm;
- the exhaust gas was fed into the test stand body through the inlet pipe under pressure depending on the engine speed. In the muffler, with the ultrasonic equipment turned on, the exhaust gas was exposed to ultrasonic waves in the longitudinal direction. In the sections, ultrasonic intensification of coagulation processes and purification of exhaust gases occurred due to sedimentation of coarse particles of exhaust gas at the soot collection point. Purified exhaust gas was discharged through the outlet pipe;
- after each test, numbered paper with settled soot particles was carefully removed and weighed again. The mass of settled soot particles was determined by the difference in mass readings before and after the test.

Then, the process of comparing and processing the obtained results without ultrasound and under the influence of ultrasound took place.

3 Results

The results of experimental studies for obtaining indicators of carbon dioxide (CO_2) and oxygen (O_2) are presented in Table 3, where u/e stands for the ultrasonic emitter.

Table 3 *Results of experimental studies for obtaining indicators of carbon dioxide and oxygen*

Indicators	without u/e	with u/e 1	with u/e 3	with u/e 6	with u/e 1-3	withu/e 1-6	with u/e 3-6	with u/e 1-3-6	all u/e
				1000 rpm					
$CO_{2,}$ %	1.98	1.94	1.84	1.82	1.8	1.77	1.79	1.8	1.73
$O_{2,}$ %	17.9	17.98	17.14	18.19	18.22	18.29	18.33	18.26	18.23
				1500 rpm					
$CO_{2,}$ %	2.22	2.18	2.06	2.03	2	1.98	1.96	2.01	1.9
$O_{2,}$ %	17.92	17.96	18.2	18.3	18.31	18.32	18.4	18.38	18.48
				2000 rpm					
$CO_{2,}$ %	2.36	2.3	2.2	2.18	2.15	2.12	2.1	2.14	2.5
$O_{2,}$ %	17.95	17.98	18.4	18.45	18.46	18.48	18.46	18.349	18.53

Note: u/e - ultrasonic emitter

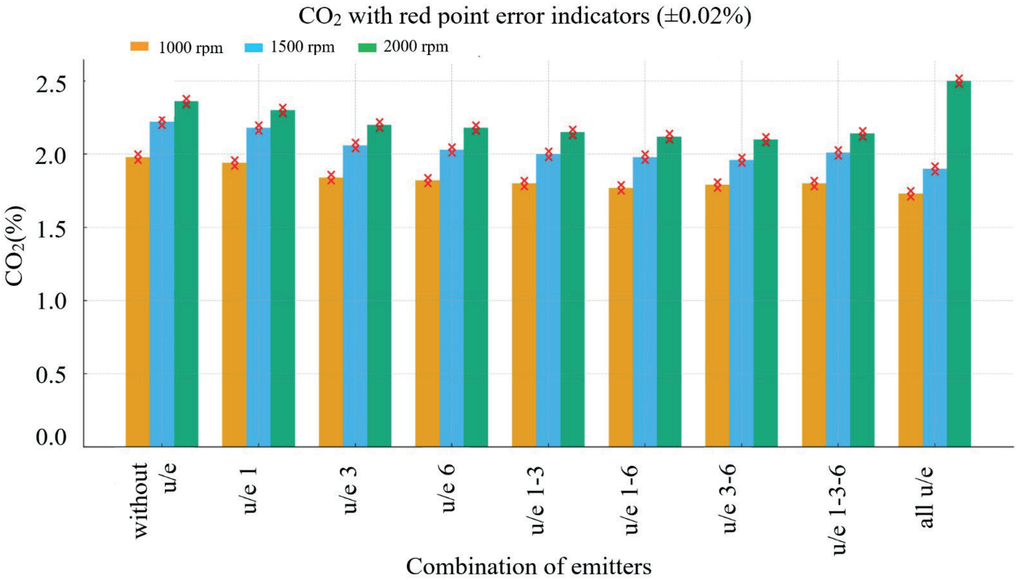

Figure 4 *Changing of the carbon dioxide levels depending on the combination of emitters*

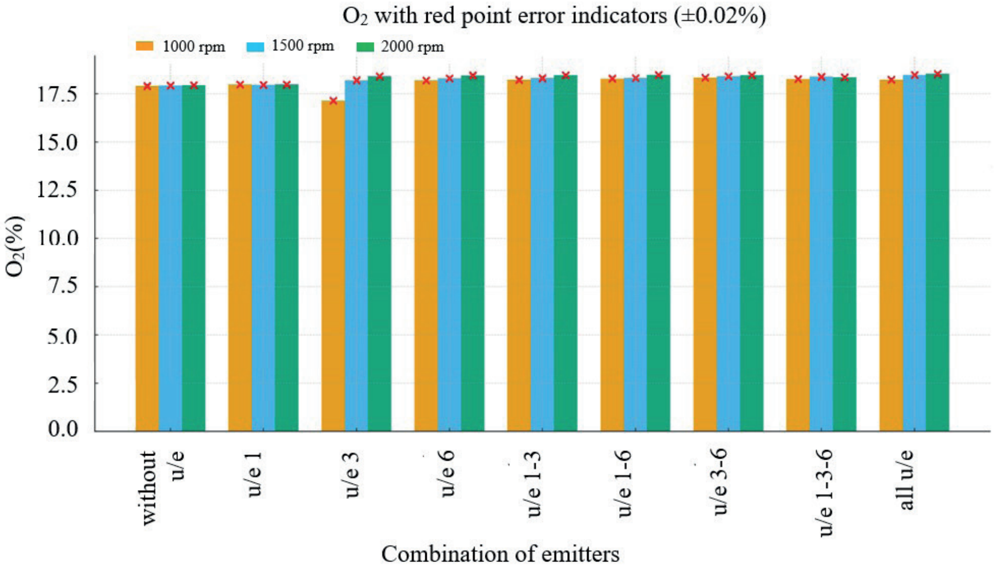

Figure 5 *Changing of the oxygen levels depending on the combination of emitters*

The measurement uncertainty of the gas analyzer was ± 0.02 % for CO_2 and O_2. Based on the obtained results of experimental studies, graphs were drawn of changes in carbon dioxide and oxygen depending on the inclusion and combination of ultrasonic emitters at engine crankshaft speeds of 1000, 1500 and 2000 rpm (Figures 4 and 5).

The observed increase in O_2 concentration indicates more complete oxidation of carbon monoxide and unburned hydrocarbons. Ultrasonic waves intensify gas mixing and promote secondary oxidation reactions due to the formation of localized high-temperature microzones in the acoustic field.

The results of experimental studies have shown that the use of ultrasonic emitters has a significant effect on the composition of exhaust gases. The graph of changes in CO_2 concentration shows a tendency for the level of carbon dioxide to decrease at each value of the engine speed when using different combinations of emitters. Without ultrasonic exposure, the concentration of CO_2 has maximum values, which indicates insufficient intensity of oxidation processes occurring in the exhaust gases. When the individual emitters and their combinations are turned on, such as emitters 1-6 and 1-3-6, the concentration of CO_2 begins decreasing but the maximum effect is achieved only when using all emitters simultaneously, which confirms the intensification of oxidation processes due to complex ultrasonic exposure.

A similar tendency is observed in the graph of changes in O_2 concentration, where the maximum oxygen content is recorded when using all emitters. Without ultrasonic exposure, the oxygen level remains lower than with its effect, which indicates a less intense chemical reaction in the gas environment. When the

***Table 4** The settled soot mass*

Rpm	without u/e	with u/e 1	with u/e 3	with u/e 6	withu/e 1-3	with u/e 1-6	withu/e 3-6	with u/e 1-3-6	all u/e
1000	0.64	0.642	0.645	0.65	0.66	0.662	0.667	0.67	0.68
1500	0.66	0.661	0.663	0.665	0.672	0.675	0.68	0.69	0.71
2000	0.69	0.7	0.672	0.675	0.7	0.713	0.72	0.73	0.75
N, (W)	0	100	100	100	200	200	200	300	600
L, (m)		0.27	0.61	1.12	0.34	0.85	0.51	0.95	1.12

Note: N - Power of the ultrasonic emitter, W;

L - distance from the muffler inlet to the ultrasonic emitter affected by the signal, m.

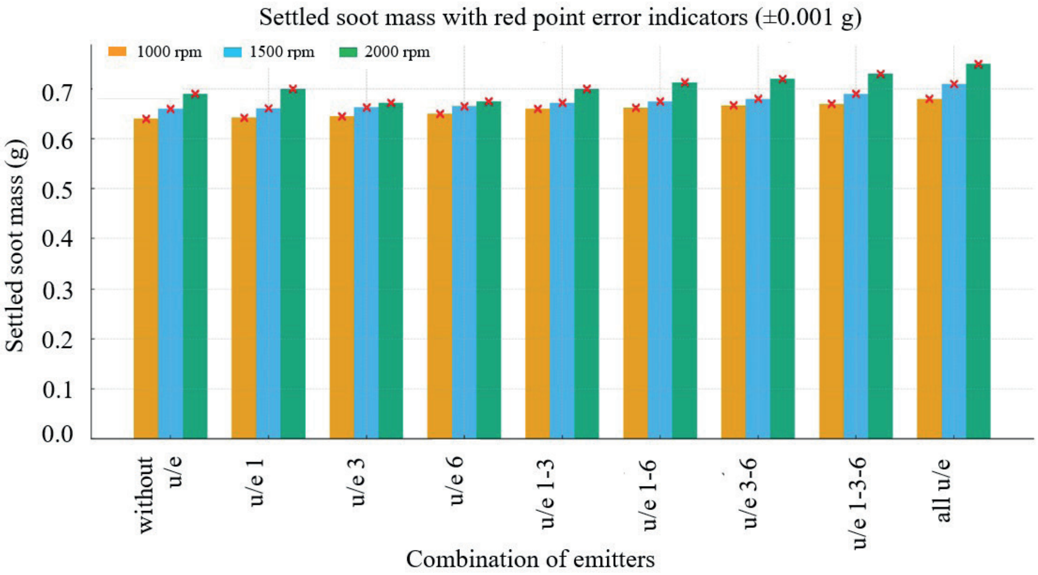

***Figure 6** Change in the mass of settled soot depending on the combination of ultrasonic emitters (at 1000, 1500, and 2000 rpm)*

individual emitters are switched on, the changes are local in nature, but when several emitters are used simultaneously, the O_2 level increases steadily, which confirms the improvement of the oxidation processes of pollutants.

Thus, the conducted studies confirm that ultrasonic cleaning of exhaust gases has a positive effect on their composition. The use of individual emitters also helps to improve the characteristics of the gas environment, but the greatest effect is achieved with the complex inclusion of all the emitters. This confirms the feasibility of using ultrasonic technology in the processes of cleaning exhaust gases, ensuring a decrease in emissions of harmful substances and an increase in the efficiency of their oxidation.

The results of experimental studies of obtaining the mass of settled soot are presented in Table 4.

The weighing error of soot mass determination was ± 0.001 g. Based on the obtained results of the experimental studies, a graph was drawn of the change in the mass of settled soot, depending on the combination of emitters at engine crankshaft speeds of 1000, 1500 and 2000 rpm (Figure 6).

With increasing the engine crankshaft speed from 1000 to 2000 rpm, a general increase in the mass of deposited soot is observed in all the operating modes, which is associated with increasing the volume of exhaust gases passing through the muffler. Turning on the ultrasonic emitters leads to a significant increase in the deposited soot compared to the operating mode without the ultrasonic action, confirming the effectiveness of ultrasonic waves in the gas cleaning process. As the number of active emitters increases, the cleaning efficiency increases, which is especially noticeable when using two or three emitters simultaneously, and the maximum increase in the amount of soot is achieved when all the ultrasonic emitters are turned on simultaneously. The difference in the efficiency of various emitter combinations becomes more pronounced with an increase in the number of revolutions, which confirms the intensification of coagulation processes and the effectiveness of ultrasonic action with a more intense gas flow.

To quantify the efficiency of ultrasonic cleaning, the relative improvement of the exhaust parameters was calculated using the following expressions:

***Table 5** Relative improvement of exhaust gas parameters (%)*

Engine speed, rpm	ΔCO_2, %	ΔO_2, %	Δm, %
1000	-12.6	+1.8	+6.3
1500	-14.4	+3.1	+7.6
2000	-13.1	+3.2	+8.7

$$\Delta CO_2 = (CO_{20} - CO_{21})/CO_{20} \times 100\ \%,$$
$$\Delta O_2 = (O_{21} - O_{20})/O_{20} \times 100\ \%, \tag{19}$$
$$\Delta m = (m_1 - m_0)/m_0 \times 100\ \%,$$

where: the subscript “0” refers to the value before the ultrasound exposure, and “1” - after exposure. The calculation results are presented in Table 5.

Calculations are based on the averaged data from Tables 3 and 4. A negative sign for ΔCO_2 indicates a decrease in concentration, while a positive sign denotes an increase in the parameter.

Thus, the results of analytical modelling and experimental data turned out to be mutually consistent, which confirms the efficiency of the proposed method of cleaning the exhaust gases. Both approaches show that ultrasonic treatment promotes coagulation and accelerated sedimentation of soot particles, reducing their content in the gas environment. The analytical model predicted increasing the mass of particles due to their enlargement and subsequent accelerated sedimentation under the effect of gravity and ultrasound, and the experiments confirmed these conclusions by increasing the mass of settled soot when the ultrasonic emitters were turned on. The comparison between the analytical modelling and experimental data shows a high degree of agreement, with the correlation coefficient R^2 = 0.91. This confirms the adequacy of the developed mathematical model for predicting soot particle coagulation and sedimentation processes.

4 Conclusion

In this research was examined the possibility of using the ultrasound to clean diesel engine exhaust gases. The studies have shown that the efficiency of ultrasonic cleaning of exhaust gases is confirmed both theoretically and experimentally, since ultrasound promotes agglomeration of soot particles and their sedimentation, which reduces the level of air pollution. The mutual complementarity of analytical and experimental methods provides a comprehensive understanding of coagulation processes, where the mathematical modelling makes it possible to predict the dynamics of particles and to determine the optimal parameters of ultrasonic action, and experimental studies make it possible to evaluate the real efficiency of the technology and make adjustments to the model. The maximum effect is achieved when using all the emitters simultaneously, since the more active ultrasonic sources are involved, the higher the level of deposited soot. It is also noted that the concentration of carbon dioxide decreases, and the oxygen content increases, which indicates more complete oxidation of exhaust gases under the effect of ultrasound. In addition, the vertical arrangement of the emitters improves the efficiency of particle deposition, since compared to the horizontal design of the muffler, it promotes more uniform deposition of soot due to the combined action of gravity and ultrasonic waves. As a result, the use of six emitters at 25 kHz reduced CO_2 by ≈ 12 %, increased O_2 by ≈ 3 %, and doubled the mass of deposited soot compared to the baseline mode. The results obtained can be used to further improve the design of ultrasonic mufflers and to adapt them to real operating conditions.

Acknowledgment

The authors received no financial support for the research, authorship and/or publication of this article.

Conflicts of interest

The authors declare that they have no known competing financial interests or personal relationships that could have appeared to influence the work reported in this paper.

References

[1] RESITOGLU, I. A., ALTINISIK, K., KESKIN, A. The pollutant emissions from diesel-engine vehicles and exhaust aftertreatment systems. *Clean Technologies and Environmental Policy* [online]. 2015, **15**(1), p. 15-27. ISSN 1618-954X, eISSN 1618-9558. Available from: https://doi.org/10.1007/s10098-014-0793-9

[2] LUO, J., ZHANG, H., LIU, Z., ZHANG, Z., PAN, Y., LIANG, X., JIANG, CH. A review of regeneration mechanism and methods for reducing soot emissions from diesel particulate filter in diesel engine. *Environmental Science and Pollution Research* [online]. 2023, **30**(37), p. 86556-86597. eISSN 1614-7499. Available from: https://doi.org/10.1007/s11356-023-28405-z

[3] TANG, R., SHANG, J., QIU, X., GONG, J., XUE, T., ZHU, T. Origin, structural characteristics, and health effects of atmospheric soot particles: a review. *Current Pollution Reports* [online]. 2024, **10**(3), p. 532-547. eISSN 2198-6592. Available from: https://doi.org/10.1007/s40726-024-00307-9

[4] NAUREEN, I., SALEEM, A., ASLAM, S., ZAKIR, L., MUKHTAR, A., NAZIR, R., ZULQARNAIN, S. Potential impact of smog on human health. *Haya: The Saudi Journal of Life Sciences* [online]. 2022, **7**(3), p. 78-84. ISSN 2415-623X, eISSN 2415-6221. Available from: https://doi.org/10.36348/sjls.2022.v07i03.002

[5] KADYROVA, I. A., MINDUBAEVA, F. A., GRJIBOVSKI, A. M. Prediction of outcomes after stroke: a systematic review. *Human Ecology (Russian Federation)* [online]. 2015, **4**(10), p. 55-64. ISSN 1728-0869, eISSN 2949-1444. Available from: https://doi.org/10.17816/humeco16983

[6] CHEN, C., YAO, A., YAO, C., WANG, B., LU, H., FENG, J., FENG, L. Study of the characteristics of PM and the correlation of soot and smoke opacity on the diesel methanol dual fuel engine. *Applied Thermal Engineering* [online]. 2019, **148**, p. 391-403 [accessed 2019-02-5]. ISSN 1359-4311, eISSN 1873-5606. Available from: https://doi.org/10.1016/j.applthermaleng.2018.11.062

[7] AKHMALTDINOVA, L., SIROTA, V., BABENKO, D., KADYROVA, I., MARATKYZY, M., IBRAYEVA, A., ZHUMALIYEVA, V., AVDIENKO, O. Proinflammatory cytokines and colorectal cancer - the impact of the stage. *Contemporary Oncology/Wspolczesna Onkologia* [online]. 2021, **24**(4), p. 207-210. ISSN 1428-2526, eISSN 1897-4309. Available from: https://doi.org/10.5114/wo.2020.102551

[8] BURCIU, S. M., COMAN, G. A comparative study of smoke emissions between idling regimes and high load regimes for a standard diesel direct injection car. *IOP Conference Series: Materials Science and Engineering* [online]. 2018, **444**(7), 072018. ISSN 1757-899X. Available from: https://doi.org/10.1088/1757-899X/444/7/072018

[9] BYSHOV, N. V., BACHURIN, A. N., BOGDANCHIKOV, I. Y., OLEYNIK, D. O., YAKUNIN, Y. V., NELIDKIN, A. V. Method and device for reducing the toxicity of diesel engine exhaust gases. *International Journal of Engineering and Technology* [online]. 2018, **7**(4), p. 920-928. ISSN 0975-4024, eISSN 2319-8613. Available from: https://doi.org/10.14419/ijet.v7i4.36.24922

[10] ZAMBONI, G. Influence of fuel injection, turbocharging and EGR systems control on combustion parameters in an automotive diesel engine. *Applied Sciences* [online]. 2019, **9**(3), 484. eISSN 2076-3417. Available from: https://doi.org/10.3390/app9030484

[11] DIMARATOS, A., GIECHASKIEL, B., CLAIROTTE, M., FONTARAS, G. Impact of active diesel particulate filter regeneration on carbon dioxide, nitrogen oxides and particle number emissions from euro 5 and 6 vehicles under laboratory testing and real-world driving. *Energies* [online]. 2022, **15**(14), 5070. eISSN 1996-1073. Available from: https://doi.org/10.3390/en15145070

[12] WEI, Z., GUAN, B., ZHUANG, Z., CHEN, J., ZHU, L., MA, Z., HUANG, Z. Review on solid selective catalytic reduction (SSCR) technology: excellent optimization of selective catalytic reduction technology. *Catalysis Science and Technology* [online]. 2025, **15**(3), p. 647-668. ISSN 2044-4761. Available from: https://doi.org/10.1039/D4CY01045K

[13] LUO, J., ZHANG, H., LIU, Z., ZHANG, Z., PAN, Y., LIANG, X., WU, S., XU, H., XU, S., JIANG, CH. A review of regeneration mechanism and methods for reducing soot emissions from diesel particulate filter in diesel engine. *Environmental Science and Pollution Research* [online]. 2023, **30**(37), p. 86556-86597. eISSN 1614-7499. Available from: https://doi.org/10.1007/s11356-023-28405-z

[14] KADYROV, A., BEMBENEK, M., SARSEMBEKOV, B., KUKESHEVA, A., NURKUSHEVA, S. The influence of the frequency of ultrasound on the exhaust gas purification process in a diesel car muffler. *Applied Sciences* [online]. 2024, **14**(12), 5027. eISSN 2076-3417. Available from: https://doi.org/10.3390/app14125027

[15] KADYROV, A., KRYUCHKOV, Y., SINELNIKOV, K., GANYUKOV, A., SAKHAPOV, R., KUKESHEVA, A. Studying the process of the internal combustion engine exhaust gas purification by an electric pulse. *Communications - Scientific Letters of the University of Zilina* [online]. 2022, **24**(4), p. B275-B287. ISSN 1335-4205, eISSN 2585-7878. Available from: https://doi.org/10.26552/com.C.2022.4.B275-B287

[16] SINELNIKOV, K. A., MOLDABAEV, B. G., ZHUNUSBEKOVA, Z. Z., KUKESHEVA, A. B. Theoretical and experimental analysis of ultrasonic cleaning of internal combustion engine radiators with the development of practical recommendations. *Material and Mechanical Engineering Technology* [online]. 2025, **7**(1), p. 87-95. ISSN 2706-977X. Available from: https://doi.org/10.52209/2706-977X_2025_1_87

[17] MOLDABAEV, B., SINELNIKOV, K., KUKESHEVA, A. Justification of the method of vehicle engine radiator ultrasonic cleaning. *Communications - Scientific Letters of the University of Zilina* [online]. 2025, **27**(1), p. B75-B84. ISSN 1335-4205, eISSN 2585-7878. Available from: https://doi.org/10.26552/com.C.2025.015

[18] KUKESHEVA, A., KADYROV, A., MOLDABAEV, B., SINELNIKOV, K., KARSAKOVA, A., KYZYLBAYEVA, E. Determination of optimal parameters for ultrasonic cleaning of vehicle radiators. *Communications - Scientific Letters of the University of Zilina* [online]. 2025, **27**(3), p. B126-B137. ISSN 1335-4205, eISSN 2585-7878. Available from: https://doi.org/10.26552/com.C.2025.031

[19] SARSEMBEKOV, B. K., KADYROV, 2. S., KUNAYEV, V. 2., ISSABAYEV, M. S., KUKESHEVA, A. B. Experimental comparison of methods for cleaning car exhaust gas by exposure using ultrasound and laser radiation. *Material and Mechanical Engineering Technology* [online]. 2024, **3**, p. 44-54. ISSN 2706-977X. Available from: https://doi.org/10.52209/2706-977X_2024_3_44

[20] KADYROV, A., SARSEMBEKOV, B., KUKESHEVA, A., SINELNIKOV, K. Application of electric pulse and ultrasonic mufflers for increasing the degree of exhaust gas purification in car engines. *International Journal of Innovative Research and Scientific Studies* [online]. 2025, **8**(1), p. 33-40. eISSN 2617-6548. Available from: https://doi.org/10.53894/ijirss.v8i1.3570

RESEARCH OF THE STRESS-STRAIN STATE OF A MOBILE OVERPASS STRUCTURE

Alexandr Ganyukov, Sabit S. Amanbayev*

Transport Engineering and Logistics Systems Department, Abylkas Saginov Karaganda Technical University, Karaganda, Kazakhstan

E-mail of corresponding author: amanbayev.sabit@mail.ru

Alexandr Ganyukov 0000-0002-0651-9781

Resume

The research is aimed at solving the problem of traffic congestion during the underground repair work in cities. The goal is to develop and analyze a modular mobile overpass that ensures continuous traffic without bypassing repair areas. The stress-strain state of the spatial steel frame of the orthogonal overpass module was studied using analytical methods of structural mechanics - the displacement method and the force method. Critical forces are determined, relationships between bending moments and stiffness of elements are revealed, optimal parameters ensuring strength and stability of structure are determined. The results confirm the feasibility of the mobile overpass as an effective engineering solution to reduce the transport delays and environmental load, forming the basis for the design of next-generation mobile bridge systems.

Article info

Received 11 April 2025
Accepted 17 November 2025
Online 23 January 2026

Keywords:

mobile overpass
mobile bridge
traffic jams
repair of utility networks
modular design
bridge on wheels
chassis

Available online: https://doi.org/10.26552/com.C.2026.010

ISSN 1335-4205 (print version)
ISSN 2585-7878 (online version)

1 Introduction

The constantly growing traffic on urban roads leads to the formation of traffic jams and congestions on roads for various reasons: in the case of car accidents, rush hours, holding any city events - sports, holidays, etc. [1-3].

One of these reasons is the repair of utility networks (heating, water supply, etc.) located under the carriageways of urban roads. This is especially true for the cities of Kazakhstan and the CIS (Commonwealth of Independent States) countries. During the repair of urban utilities, vehicles are forced to go around the repair trenches, along other streets that creates traffic jams and worsens the transport picture of the city (Figure 1). The accumulation of vehicles in traffic jams is especially harmful to the ecology of cities, due to the simultaneous constant emission of pollutants into the atmosphere from exhaust gases. In addition, traffic jams cause social and economic damage to residents and enterprises of the city [4-5].

There are many different ways to eliminate the traffic jams and improve the ecology of the city by reducing the emission of harmful substances from exhaust gases [6-8]. One of the possible ideas, that is the use of temporary mobile overpasses, was proposed by authors for the first time [9-11].

The modular overpass is a collapsible temporary bridge structure, which consists of separate parts (modules). This structure is equipped with its own chassis for transportation, as well as special mechanisms for controlling the movement and assembly before operation (Figure 2).

The modular overpass is designed to drive vehicles along it during the repair of underground utilities. Before the start of a repair, the overpass is transported to the place of its operation, then installed above the trench in a perpendicular direction, which allows the transport to cross the trenches along the overpass directly (Figure 2). This eliminates the need to bypass the repair areas and the formation of traffic jams and congestion. After the repair of utility networks is completed, the overpass gets on its wheels and is taken to its place of storage. Transportation can be carried out using the usual tractors.

The idea of using the overpass is to eliminate traffic jams, improve the ecological state of cities by developing and researching the design of a modular overpass. The

Figure 1 *Traffic jam because of repairing the utility networks*

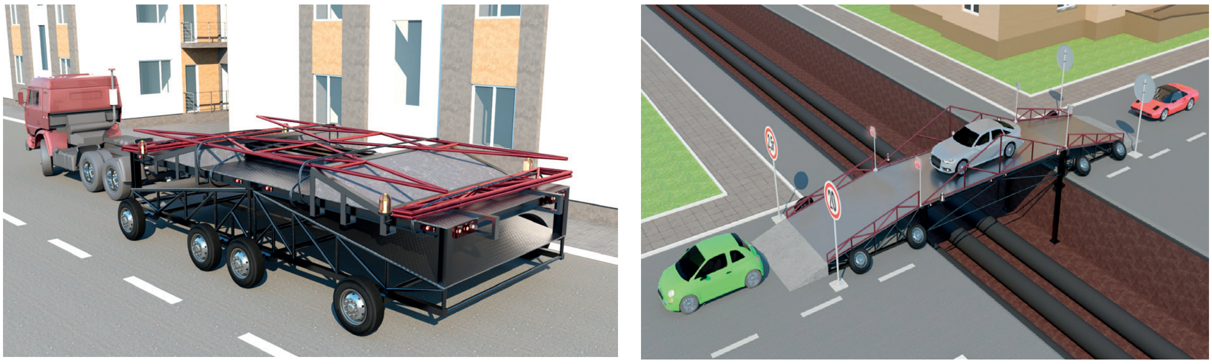

(a) (b)

Figure 2 *Municipal modular mobile overpass: a) transport position with folded modules; b) operational position over a trench*

term ‘overpass’ includes equivalent definitions, such as: modular overpass, mobile overpass, communal overpass. The proposed overpass has no analogues in the world as a new type of transport equipment.

As the world survey showed, such structures are practically absent in urban transport construction. Similar designs are found in the engineering forces: tank bridge layers, tracked cross-over trawls, the Bailey bridges, etc. [12]. In addition to specialized military equipment, there is an extensive direction for the construction of temporary bridges, which are stationary collapsible structures, with limited possibility of their transportation: a temporary scissor-type bridge (Japan) [13]; ASTRA temporary bridge for road repair (Switzerland) [14]; deployable arch bridge launched from a vehicle for rescue or military operations (USA) [15].

The founder of the scientific school for the development of mobile overpasses is prof. A. S. Kadyrov and his Ph.D. students: K. G. Balabekova and A. A. Ganyukov.

A. S. Kadyrov and K. G. Balabekova developed a mobile road overpass designed to eliminate the traffic jams in urban conditions at intersections. The disadvantage of this overpass is the impossibility of its use over repair trenches of utility networks [16-17].

One of the analogues of the proposed overpass is a single-span mobile overpass used in the repair of utility networks, developed and studied in the work by Kadyrov and Ganyukov [18-20]. The disadvantage of such an overpass is the limited width of the repaired trenches up to 6 m, due to the lack of additional modules in the structure. This developed modular overpass eliminates this drawback and can overcome trenches of a width of more than 8 m.

The high costs of tank bridge layers and other similar military equipment, as well as temporary stationary bridges, makes it impossible to use them in urban conditions. For these purposes, a modular mobile overpass is proposed that eliminates the above disadvantages.

However, at the moment, researches have not been fully carried out to develop and calculate the structures of the modular overpass, as well as methods for its installation, transportation and operation. In this regard, conducting research on the calculation and design of overpass structures is an actual task.

The proposed solution is a new direction in engineering practice and ensures the elimination of traffic jams in urban conditions during the underground repair of utility networks without the need to block the traffic and bypass the repaired sections.

The overpass on a rigid coupling with a towing tractor is delivered to the place of its operation in the transport position (transport mode) (Figure 2a, Figure 3). After the delivery, it is transferred to the operational position (bridge mode), above the repair trench by

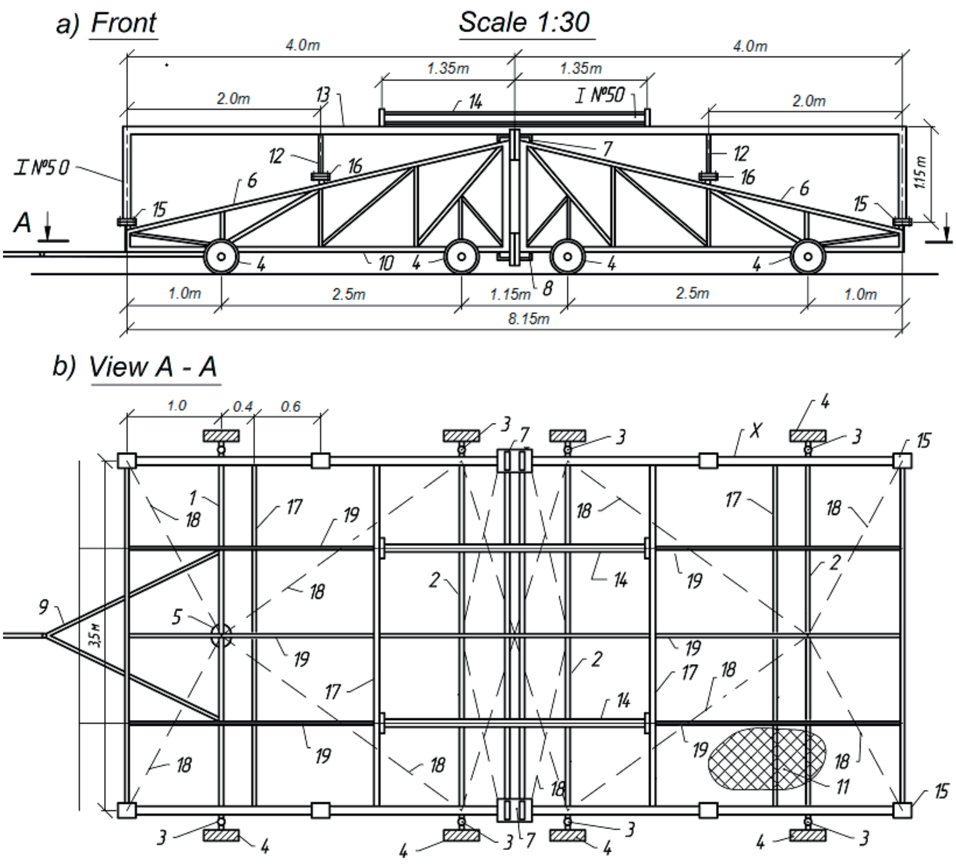

Figure 3 *General view of the modular overpass in the transport position: 1 - front swivel axle; 2 - middle and rear axles; 3 - device for turning wheels; 4 - wheels with low pressure tires; 5 - steering gear; 6 - inclined module with running gear (steel truss); 7 - upper transport locks; 8 - lower transport locks; 9 - towing device; 10 - lower truss chord; 11- metal corrugated flooring; 12 - transportation rack; 13 - an upper portion of an orthogonal Π-shaped module; 14 - lower portion of an orthogonal Π-shaped module; 15 - angular node joint of elements 6 and 13; 16 - intermediate node joint of elements 6 and 13; 17 - transverse beams of chassis frame; 18 - push-pull rods providing rigidity; 19 - longitudinal beams of chassis frame*

specially developed installation methods (Figure 2b, Figure 4) [21]. Thus, the essence of the proposed design is that it is simultaneously a vehicle and a bridge (overpass), which is a new type of transport equipment - a mobile overpass.

The overpass is assembled from unified demountable modules of two types: one orthogonal module (Figure 3, positions 13 and 14; Figure 4, positions 1 and 2) and two inclined modules (Figure 3, position 6; Figure 4, position 3).

The orthogonal module is a spatial steel Π-shaped frame, the base of which is attached to the bottom of the repair trench in special ways (Figure 4, positions 9 and 10). The upper part of the frame is a roadway above the repair trench in the form of an orthotropic slab with stiffeners reinforcing the ribs (Figure 4, positions 4, 7 and 8).

The inclined module (left and right) is a paired steel trusses carrying the roadway, also in the form of an orthotropic slab, and providing entry and exit of vehicles to the roadway of the orthogonal module (Figure 3, position 6; Figure 4 positions 3 and 5). The inclined modules are equipped with undercarriage axles with special mechanisms for raising the wheels and steering (Figure 3, positions 1-5 and 17-20) necessary for transporting the overpass to the place of operation.

The cantilever part of the trusses of the inclined module is founded on reinforced concrete ramps, which ensure the entry of vehicles to the inclined module (Figure 4, position 6) and are made of special concrete that can withstand dynamic loads [22-23]. The hinged part of the trusses is founded on the supporting frame of the orthogonal module using rigid docking units (Figure 4, position 12).

The overall dimensions of the “single-band modules” are as follows: the length of the orthogonal module - 8 m; width - 3.5 m; height (including installation on the trench bottom) - 4.7 m. Inclined module length - 4 m; width - 3.5 m; high height - 0.85 m; lower height - 0.17 m.

After the operation of the overpass is completed, it is dismantled by separate modules and towed to the storage site. For this, the inclined modules are disconnected from the orthogonal one and transferred to the transport position by turning the wheels of the chassis (Figure 4, positions 3 and 4).

The space frame of the orthogonal module is dismantled to the upper space part (Figure 4, position 4; Figure 3, position 13), then the lower racks of the

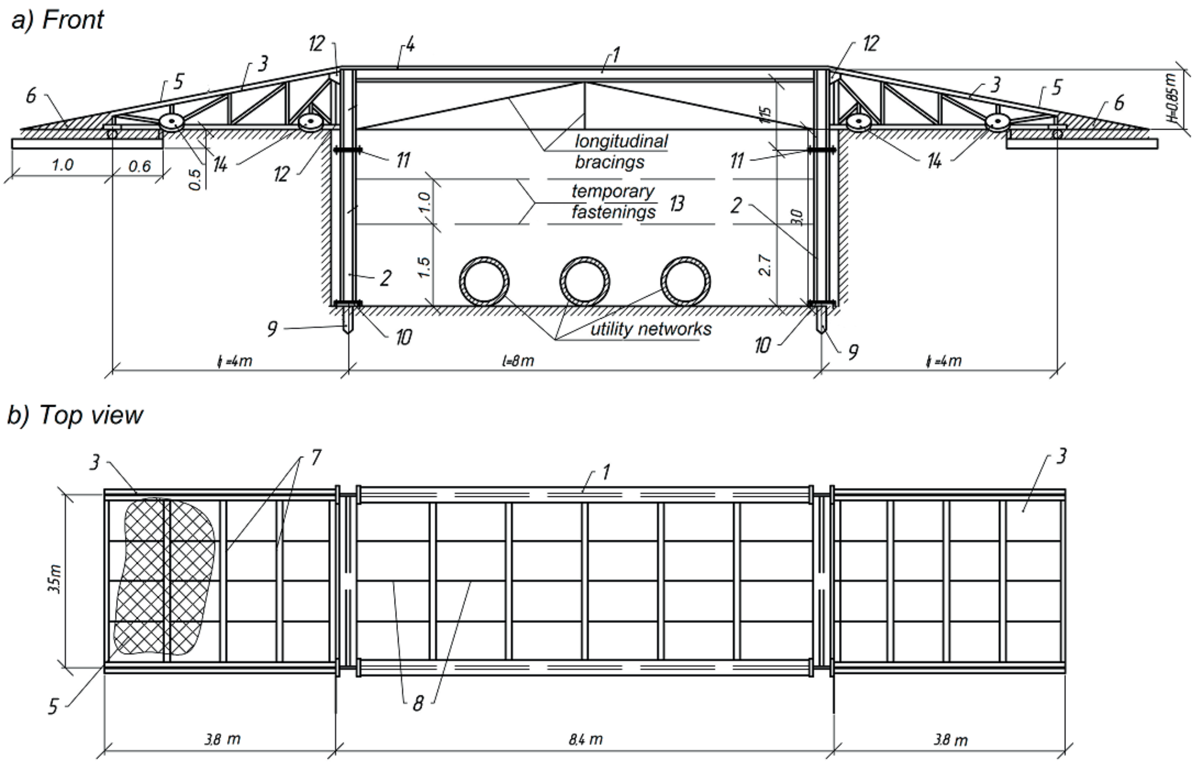

Figure 4 *General view of the modular overpass in operational position: 1 - longitudinal beams of orthogonal module; 2 - vertical racks of the orthogonal module; 3 - inclined modules with a chassis; 4, 5 - metal flooring of orthogonal and inclined modules; 6 - entrance ramps; 7 - transverse bearing beams of the deck; 8 - longitudinal deck beams; 9 - supports of the lower part of the orthogonal module; 10 - support metal mount for racks; 11 - node joint of elements 1 and 2; 12 - node joint of elements 1 and 3; 13 - structures of temporary installation reinforcement of elements; 14 - wheels of undercarriage in turned state*

frame are removed (Figure 4, position 2), disconnecting from the support mounts (Figure 4, position 10). Then the inclined modules are connected with transport locks (Figure 3, positions 7, 8). Further, the upper part of the orthogonal module (Figure 3, position 13) is mounted on the resulting structure from above and fixed using a transport rack (Figure 3, position 12) and a junction joint (Figure 3, position 15). The lower frame posts (4 pcs.) are fixed on the top of the frame (Figure 3, position 14). Entrance ramps, fencing and other additional equipment can also be transported on top of the frame of the orthogonal module [21].

It should be noted that to ensure the safety of transportation, the overpass, being transport equipment, must be equipped with additional equipment: front and rear headlights, side running lights around the perimeter, turn signals, brake lights, flashing yellow beacons and a wheel brake system controlled by the driver of the tractor.

2 Materials and methods

The main bearing structures of the overpass are: a spatial Π-shaped frame of an orthogonal module with a roadway slab, reinforced with stiffeners, as well as inclined modules consisting of paired trusses connected by longitudinal and transverse beams (Figure 4). The carriageway of the orthogonal and inclined modules are covered with a corrugated metal flooring, 20mm thick.

In the proposed article, to analyze the stress-strain state of the supporting metal structures of the overpass in terms of strength, stability and rigidity, the calculation of the spatial frame of the orthogonal module is performed (Figure 4, positions 1 and 2).

The purpose of the study was to develop the design and strength calculation of the orthogonal module of the mobile overpass, which is a spatial frame carrying the carriageway of the overpass.

To achieve this goal, it is necessary to complete the following tasks:

- to perform the study of operation and strength calculation of the longitudinal and transverse frame orthogonally to the overpass module, taking into account the dynamics of mobile vehicles;
- to select cross-sections of structural elements of longitudinal and transverse frame of orthogonal overpass module based on strength and stability conditions;
- to assess and calculate the rigidity of the spatial frame of the orthogonal overpass module in accordance with regulatory documents.

The scientific novelty of this research lies in the development, theoretical justification and study of a

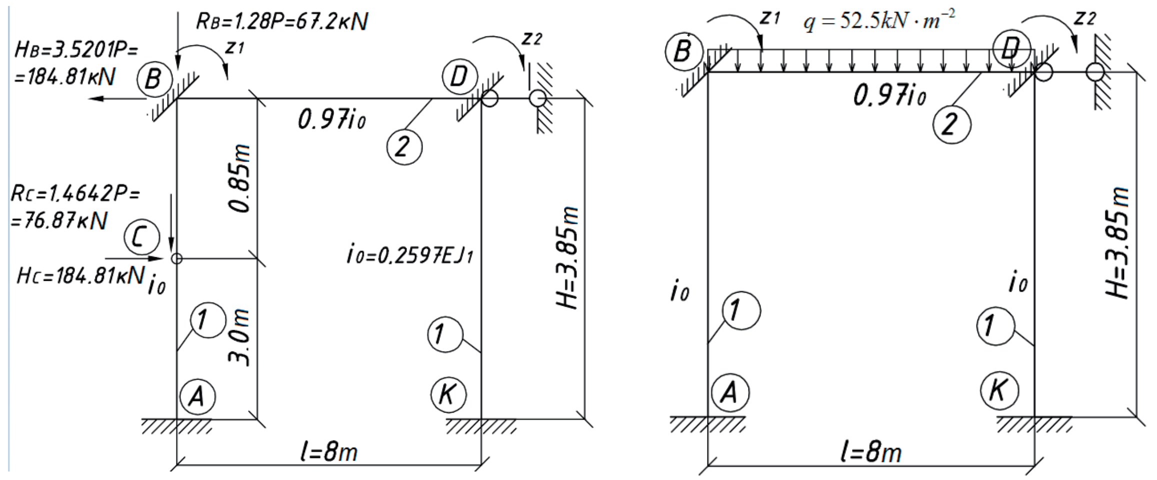

(a) (b)

Figure 5 *Calculation scheme of the longitudinal frame by the displacement method with dangerous loading: a) Variant 1: load on inclined module; b) Vvariant 2: load on orthogonal module*

new type of transport equipment - a modular mobile overpass, which is a combined structure of a bridge structure and a vehicle with its own undercarriage and issues in the following:

- for the first time, as a result of the development and study of a mathematical model, the dependencies for calculating a new type of transport equipment - a mobile overpass were obtained;
- the dependences linking the strength and deformed state of the spatial frame of the orthogonal overpass module from the loads of a mobile vehicle in a static position, taking into account the dynamic coefficient have been established;
- the dependence of bending moment at critical points of the structure of the spatial frame of the orthogonal module on the ratio of bending rigidity of the crossbar and the racks is obtained;
- a methodology for calculating the elements of a modular overpass has been developed, taking into account the complex impact of mobile loads, dynamic factors, strength and stability characteristics, which ensures increased accuracy of calculation and reliability of the structure in operating conditions;
- the design was optimized according to the criteria of strength, stiffness and metal intensity, which made it possible to determine the rational parameters of the spatial frame of the orthogonal module and thereby increase the economic efficiency of the designed structure.

In the methodological approach of the study, novelty manifests itself in the use of a combination of precise analytical displacement and force methods to calculate the spatial frame as flat structures (longitudinal 8 m and transverse 3.5 m) with the correction factors for the spatial work of the elements, taking into account the dynamics of moving loads according to Eurocodes in two critical cases (on inclined and orthogonal modules), parametric stiffness ratio analysis, and stiffness check, enabling design optimization without complex numerical modeling.

The practical significance of the research is determined by the development of a methodology for calculating the structural elements of the overpass based on the results obtained.

With a sufficient degree of accuracy, the spatial frame of the orthogonal module (Figure 4, positions 1, 2) can be calculated as flat structures: a longitudinal frame with a span (longitudinal crossbar) of 8m and a transverse frame with a span (transverse crossbar) of 3.5m. The longitudinal crossbar of the frame covers the length of the trench; the transverse crossbar is the width of the carriageway of the overpass. In this case, the correction factors are introduced to take into account the spatial work of individual elements of the frame structures [24].

To calculate the framework frame of the orthogonal module, the exact analytical method of displacement and the method of forces are adopted [25-26]. Based on the displacement method, the strength calculation of the longitudinal frame, with a span of 8 m and a height of 3.85 m, was considered (Figure 4, positions 1 and 2). The calculation scheme is presented in Figure 5.

Taking into account the fact that the load on the overpass is mobile (from the movement of vehicles), two variants for the most dangerous loading of the calculated frame were considered: variant 1 - the carriageway is located only on the inclined module (Figure 4, position 3, Figure 5a); variant 2 - only on the orthogonal module (Figure 4, position 1, Figure 5b).

The load on 1 m^2 of the overpass carriageway, taking into account overloads and the dynamic effect of mobile vehicles, is accepted as $g = 3000\,\mathrm{kg \cdot m^{-2}} = 30\,\mathrm{kN \cdot m^{-2}}$, according to Eurocodes [27-28]. This can provide safe movement, both for light vehicles and lightly loaded vehicles up to 3.5 tons. Then, the linear load on the upper crossbar of the frame would be $q = g \cdot 1.7585250\,\mathrm{kg \cdot m^{-2}}$ or

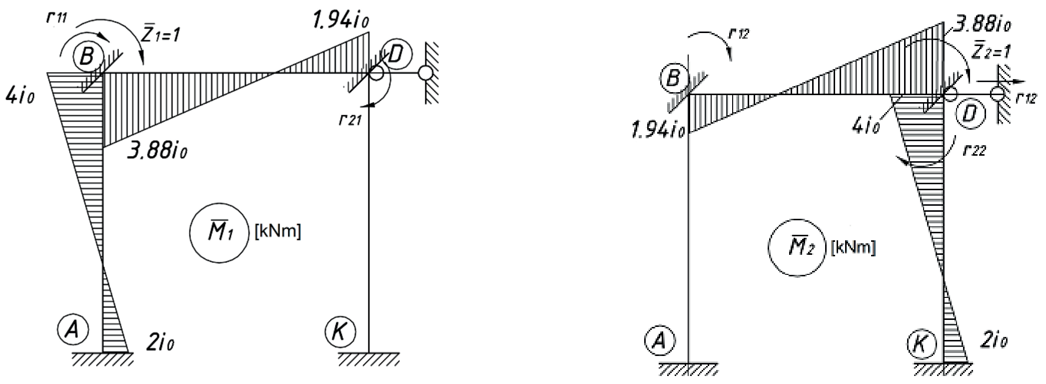

***Figure 6** Diagrams of unit moments* M_1 *and* M_2

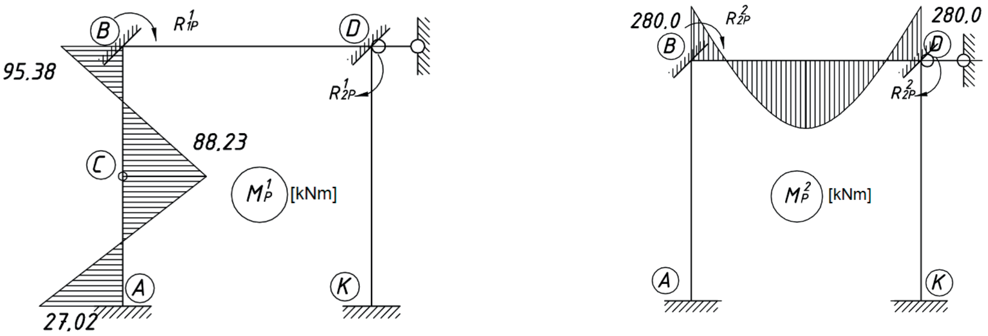

***Figure 7** Loading diagrams of moments* M_P^1 *and* M_P^2 *from loading variants 1 and 2.*

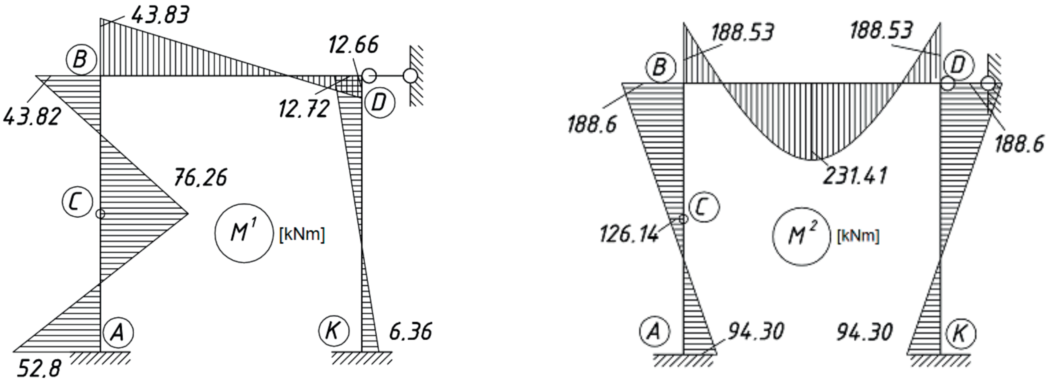

***Figure 8** Moment diagrams from loading variants 1 and 2*

$q = 52.5\,\mathrm{kN \cdot m^{-2}}$ (Figure 5a, 5b). In Figure 5, and at points B and C (points of attachment of the inclined module), the reactions from the inclined module H_B, R_B, H_C, R_C, are applied, which arise from 1 loading variant.

Next are defined the geometric and stiffness relationships of the frames. Indices "1" - indicate vertical racks, indices "2" and "3" - crossbars of longitudinal and transverse frame 3.5 m (Figure 5). The following is obtained: $\alpha_1 = l_1 = H = 3.85\,\mathrm{m}$; $\alpha_2 = l_2/l_1 = L/H = /3.85 = 2.0779; \alpha_3 = l_3/l_1 = 3.5/3.85 = 0.9091$. Stiffness ratio of racks and crossbars: $g_1 = EJ_1 = 16.35 \cdot 10^6 \mathrm{N \cdot m^2}; g_2 = EJ_2/EJ_1 = 2.0;$ $g_3 = 1.5$. Linear stiffness $i_1 = EJ_1/H = 0.2597EJ_1;$ $i_2 = i_1\, g_2/\alpha_2 = 0.25EJ_1; i_0 = i_1 = 0.2597EJ_1; i_2 = 0.97i_0$.

Taking into account the conditions for coupling the frame rods of the orthogonal module, the number of the main unknowns will be equal to two: the angles of rotation of the upper nodes of the frame B and D - z_1 and z_2. The canonical equations of the displacement method in this case are [25-26]:

$$R \cdot z + R_{kp} = 0\,, \tag{1}$$

where, $R = \{r_{ij}\}, (i = 1,2; j = 1,2)$ - matrix of unit coefficients (N·m) obtained based on diagrams of unit moments $\overline{M}_k (k = 1,2)$ arising from angular displacements z_1 and z_2 (Figure 6); $R_{kp}\{r_{1p}, r_{2p}\}$ - vector of load coefficients (N·m), which are calculated from the load diagrams of moments in accordance with loading variants shown in Figure 5 (Figure 7); $z\{z_1, z_2\}$ - unknown vector of angular displacements of the frame in nodes B and D (Figure 5a).

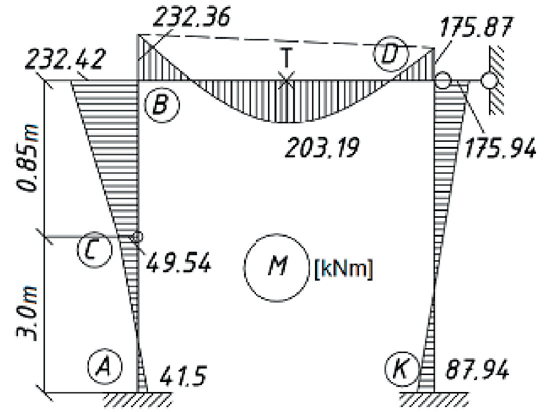

Figure 9 Summary diagram of moments M

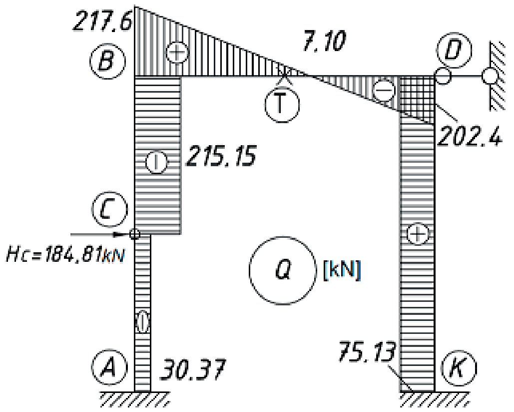

Figure 10 Diagram of shear forces Q

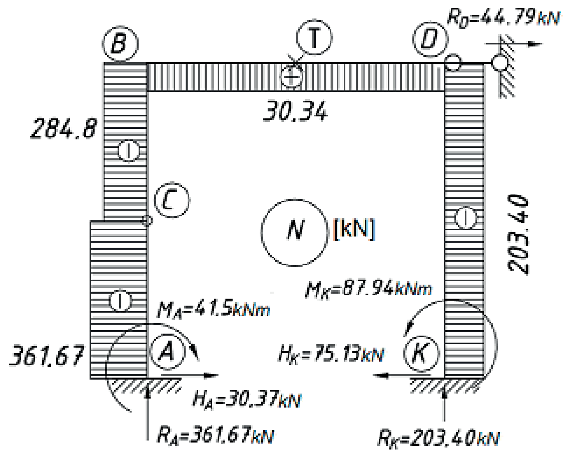

Figure 11 Diagram of longitudinal forces N

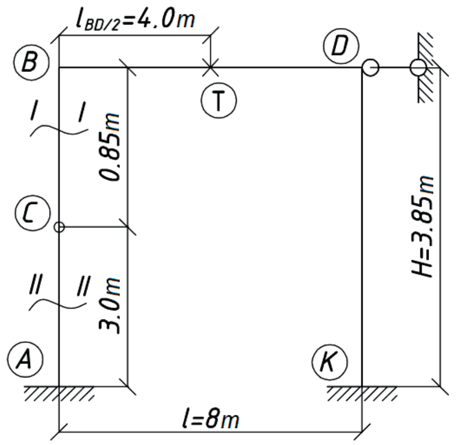

Figure 12 Calculation cross-sections and nodes

After finding R_{kp} and R, the system of linear equations in Equation (1) is solved, and z_1 and z_2 are determined. Further, the diagram of moments from each loading variant is found by the equation [25-26]:

$$M^1 = \overline{M}_1^l z_1 + \overline{M}_2^l z_2 + \overline{M}_p^l , \qquad (2)$$

where z_1, z_2 are the main unknowns of displacement method found from Equation (1); l - index of frame loading variant (l = 1,2). Diagrams of these moments are given in Figure 8.

The total calculating diagram of moments from both loading variants of the frame specified in Figure 5 is found by addition (Figure 9) [25-26]:

$$M = \overline{M}^1 + \overline{M}^2 . \qquad (3)$$

3 Results and discussion

The total calculating diagram of moments M from the two loading variants, according to Equation (3), is given in Figure 9. Figure 10 shows the diagram of transverse forces Q (Figure 10), obtained based on the diagram M. Based on the diagram of shear forces Q, the diagram of longitudinal forces N, presented in Figure 11, was obtained.

Based on the values of calculating diagrams M^1 and M^2, shown in Figure 8, a table of unfavorable loads was compiled for the frame of the orthogonal module, from the load of mobile vehicles moving along the carriageway of the overpass (Table 1). Figure 12 shows the positions of the calculating sections when calculating the stability of the frame pillars.

Table 1 contains data on six calculating points (A, C, B, T, D, K) for the two loading variants of the longitudinal frame of the orthogonal module, as well as total and extreme values of forces (Figures 9, 10 and 11). The critical points of the structure are points B, T and A. At point B, the greatest negative bending moment (-232.42 kNm) and high shear forces (-215.15 and + 214.60 kN) are observed, which makes this point the most loaded. This node requires reinforcement and additional investigation to prevent the shear and additional deformations. At point T, the maximum positive moment (+231.41 kNm) indicates significant stretching of the lower fibers, which requires testing for material strength in this zone. At point A, the maximum

***Table 1** Calculation forces in orthogonal module frame cross-sections*

Calculation points	Values of bending moments M^1 and M^2 (kNm)		Summary moments (kNm)	Calculation moments (kNm)		Values of shear and longitudinal forces (kN)	
	Load variant 1	Load variant 2	$M^1 + M^2$	M_{max}	M_{min}	Q	N
A	-52.8	+94.30	+41.5	+41.5	-52.8	-30.37	-361.67
C	+76.26	-126.14	-49.88	+76.26	-49.54	-30.37 -215.15	-361.67 -284.80
B	-43.82	-188.60	-232.42	-43.82	-232.42	-215.15 +214.60	-284.80 -30.34
T	-28.28	+231.41	+203.19	+231.41	+203.19	+7.10	-30.34
D	+12.72	-188.53	-175.81	+12.72	-175.87	-203.40 +75.13	-30.34 -203.40
K	-6.36	+94.30	+87.94	+94.30	-6.36	+75.13	-203.40

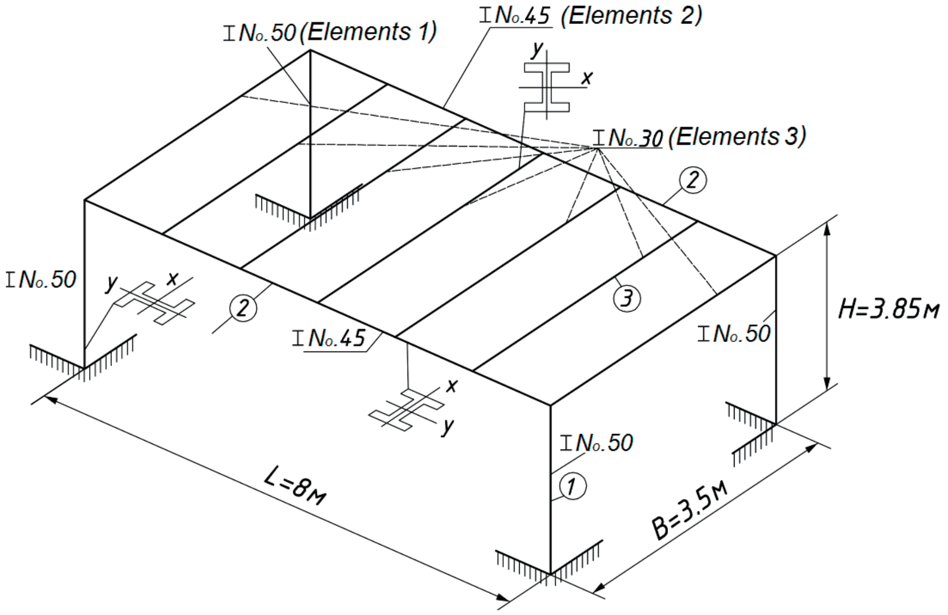

***Figure 13** Obtained set of cross-sections of frame spatial elements of orthogonal module: Elements 1 (vertical racks of the orthogonal module) - I-beam No. 50; Elements 2 (longitudinal beams (girders) 8m long) - I-beam No. 45; Elements 3 (crossbars (girders) with a length of 3.5m) - I-beam No. 30*

compressive force (-361.67 kN) indicates a high axial load, which is important for assessing the stability of the vertical racks of the structure. Similar calculations were made for the transverse frame 3.5 m wide (Figure 13, elements 1 and 3).

Based on the results of the study of the strength state of the longitudinal and transverse frames of the frame, based on the strength and stability of its elements (crossbars and racks), their cross sections were selected as for structures operating under conditions of complex resistance (tension-compression, bending, torsion), taking into account the dynamic effect of mobile vehicles. Vertical racks and crossbars of longitudinal and transverse frames were taken in the form of a rolled I-beam.

The equation of strength condition at eccentric compression-tension reads, [24-26]:

$$\left[\sigma = \pm\frac{N}{A}\left(1 + \frac{x_k x_f}{i_y^2} + \frac{y_k y_f}{i_x^2}\right)\right] \leq \frac{\sigma_{adm} \cdot \gamma}{K_d}, \tag{4}$$

where $\sigma_{adm} = 284\,\text{MPa}$ - allowable stress for steel grade S355JR, according to the European standard EN 10025-2 [27-28]; (x_k, y_k) - coordinates of the design point of the cross section; i_x^2, i_y^2 - squares of the main radii of inertia of the section relative to the corresponding axes; A - cross-sectional area; (x_f, y_f) - coordinates of the point of application of axial longitudinal force N; ($\gamma = 0.9$) - accounting coefficient of spatial work of the structure. The dynamic effect of the movement of the rolling stock along the carriageway of the bridge crossing is taken into account by introducing an empirical dynamic coefficient $K_d = 1.3$. The dynamic coefficient takes into account additional loads from vibrations and shocks

***Table 2** Moments in dangerous node B of the frame depending on parameter "n"*

Values of parameter «n»	Coefficient values					Force values (kN)		Forces in the main system (kNm)			
	a_{11}	a_{12}	a_{22}	b_1	b_2	X_1	X_2	$\overline{M}_1 \cdot X_1$	$\overline{M}_2 \cdot X_2$	$M_{P,B}$	M_B
0.5	4.97	0.485	4.97	-184.6	280	43.05	-49.93	41.76	-24.84	-184.6	-167.68
1.0	5.94	0.97	5.94	-184.6	280	39.83	-53.64	77.28	-53.37	-184.6	-160.69
1.5	6.91	1.455	6.91	-184.6	280	27.78	-48.25	80.84	-72.07	-184.6	-175.83
2.0	7.88	1.94	7.88	-184.6	280	34.25	-43.97	132.89	-85.30	-184.6	-137.01

when moving vehicles along the overpass, increasing the calculated static loads by 30% to ensure the safety of the structure.

The central compression stability is given by the equation [24, 26]:

$$\left(\sigma = \frac{N}{\varphi A}\right) \leq \frac{\sigma_{adm} \cdot \gamma}{K_d}, \tag{5}$$

where φ - coefficient of reduction of the main allowable stress.

For elements of the structure working for bending, the required bending strength moment W of the cross section is determined by the equation [24, 26]:

$$W = \frac{M_{\max}}{\sigma_{adm} \cdot \gamma} K_d, \tag{6}$$

where M_{max} - maximum bending moment on the structure element.

According to the results of calculations according to Equations (4)-(6) based on Table 1 (for longitudinal and transverse frames), the cross sections of the spatial frame of the orthogonal module are taken according to the range. The selected set of cross sections is shown in Figure 13.

The analysis of the obtained solutions (Table 1) showed that during the operation of the overpass in the operational position (transport movement), the crossbar of the longitudinal frame of the orthogonal module (Element 2, Figure 13) experiences the greatest static and dynamic loads. This results in the highest loads and hazardous cross sections at the corner joints of the vertical posts (Figure 13, element 1) and the girder (Figure 13, element 2) (Figures 9, 10 and 11, nodes B, T and A).

In this regard, a study was conducted of the effect of stiffness characteristics on the selection of the cross section of the crossbar (Figure 13, Element 2) of the longitudinal frame orthogonally to the module, taking into account the forces in the dangerous unit B, in which the greatest forces occur (Figures 9 and 10). For these purposes, the force method was used, which is an analogue of the displacement method and has a similar canonical equations in Equation (1), in which unit nodal displacements are replaced by the corresponding unit nodal forces X_1 and X_2 [24-26].

Then, the following value of linear stiffnesses are taken: vertical elements of the longitudinal frame (rack) (Figures 5 and 13, element 1) $i_1 = i_0 = 1$; horizontal frame elements (girders) (Figures 5 and 13, element 2) $i_2 = 0.5$; 1.0; 1.5; 2.0. Denote the ratio of linear stiffnesses of the longitudinal frame struts by $n = i_2/i_1$ (Figure 5).

Then, the coefficients of the canonical equations in Equation (1) $R = \{r_{ij}\}$ and the vector of load coefficients $R_{kp}\{r_{1p}, r_{2p}\}(i = 1,2; j = 1,2; k = 1,2)$ in the general form, will take the following form:

$$\begin{aligned} & a_{11} = r_{11} = 4i_0 + 1.94 \cdot n \cdot i_0 = (4 + 1.94 \cdot n) \cdot i_0; \\ & a_{12} = r_{12} = r_{21} = 0.97 \cdot n \cdot i_0; a_{22} = r_{22} = (4 + 1.94n)i_0; \\ & b_1 = -184.62 = R_{1P}; b_2 = R_{2P} = 280.00. \end{aligned} \tag{7}$$

Solving, in general, the system in Equation (1) taking into account the expressions in Equation (7), one obtains:

$$\begin{aligned} & X_1 = \frac{-b_1 - a_{12}^2 \cdot \left[\dfrac{-b_1 + b_2\left(\frac{a_{11}}{a_{12}}\right)}{(a_{12}^2 - a_{11} \cdot a_{22})}\right]}{a_{11}}; \\ & X_2 = \frac{\left[-b_1 + b_2\left(\frac{a_{11}}{a_{12}}\right)\right] \cdot a_{12}}{(a_{12}^2 - a_{11} \cdot a_{22})}. \end{aligned} \tag{8}$$

Using Equation (8), one finds the values of the main unknown methods of forces X_1 and X_2, having previously determined the coefficients of equations in Equation (7) when varying the parameter n = 0.5; 1.0; 1.5; 2.0. By analogy with Equation (2), the resulting moment M_B at the dangerous node B is defined as:

$$M_B = \overline{M}_{1,B} \cdot X_1 + \overline{M}_{2,B} \cdot X_2 + M_{P,B}. \tag{9}$$

The results of these calculations are shown in Table 2. According to Table 2, the dependence is obtained of the bending moment in the dangerous node B of the longitudinal frame (Figure 5) on the ratio $n = i_2/i_1$ (Figure 14).

The analysis of the dependence in Figure 14 shows that the ratio of the linear stiffnesses of the frame girder and its racks (parameter n) has a significant effect on the value of the bending moment M_B in node B (Figure 5), where the crossbar and the left rack are connected. Maximum absolute value of bending moment M_B occurs at values n within n = 1.5. Optimum value of ratio of cross-bar (i_2) and rack (i_1), at which the minimum values of moment M_B occur is determined within n = 2.0. This allows taking into account the design parameters of the

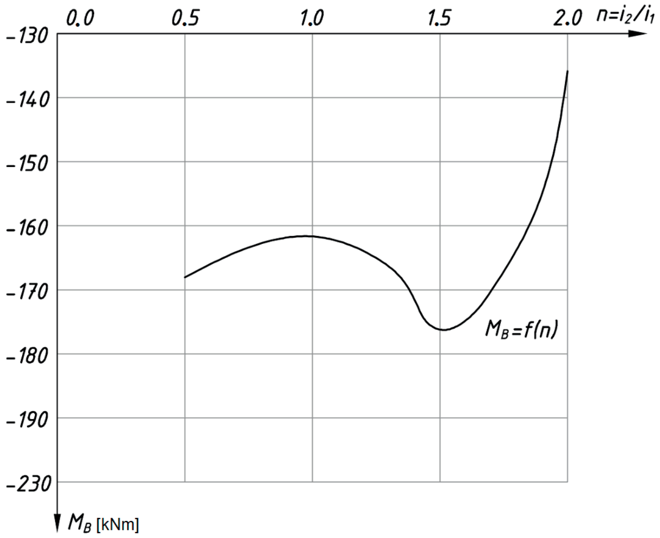

Figure 14 *Dependence of the bending moment M_B on ratio of bending stiffness of crossbar (i_2) and rack (i_1) of longitudinal frame*

longitudinal frame when designing and calculating the orthogonal module of the overpass and reduce the metal consumption of structural elements.

Studies of the operation of the spatial frame of the overpass under the loads of mobile vehicles (taking into account the dynamic coefficient) made it possible to select structure parameters taking into account strength, stability and dynamic impact (Equations (4)-(6)). Additional calculation of orthogonal module frame stiffness is required for the safe operation. Stiffness is a key parameter that determines the resistance to deformations and ensures the reliability of the structure in accordance with the standards of bridge construction [26-28].

During the operation of the overpass in the orthogonal overpass module, the crossbar of the longitudinal frame (Elements 2, Figure 13) and the crossbar of the transverse frame (Elements 3, Figure 13) are subjected to the greatest loads. In this regard, it is necessary to check the stiffness of elements 2 and 3 (Figure 13).

The transverse frames of a width of 3.5 m (Elements 3 and 1) are statically defined frames. Elements 3 (crossbars, Figure 13), length l = 3.5 m, are subjected to a load, the value of which is determined as follows: $q_n = g \cdot c \cdot K_d = 30 \cdot 1.33 \cdot 1.3 = 52\,\mathrm{kN} \cdot \mathrm{m}^{-1}$. Where $g = 30\,\mathrm{kN} \cdot \mathrm{m}^{-1}$ is the load per 1 m^2 due to the mobile transport; c = 1.33m - beam pace; K_d = 1.3 - dynamic coefficient. The cross section of element 3 is I-beam No. 30. Moment of inertia of the _=beam's cross-section is J_x =7080 cm^4. Modulus of elasticity of material is E = 2·105 MPa (for steel).

The maximum deflection in the middle of the beam (Element 3, Figure 13) is calculated by the formula [29]:

$$\upsilon_{\max} = \frac{5 \cdot q_n \cdot l^4}{384 \cdot EJ_x} = 0.715 \cdot 10^{-2}\mathrm{m} = \\ = 0.715\,\mathrm{cm} = 7.15\,\mathrm{mm}. \tag{10}$$

The stiffness check is performed by the equation [30]:

$$\frac{\upsilon_{\max}}{l} \le \left[\frac{1}{f}\right], \tag{11}$$

where $\left[\frac{1}{f}\right] = \frac{1}{400}$ - normative allowable deflection of beams according to the conditions of safe operation of elements of steel structures. By Equation (11) one obtains:

$$\frac{0.715 \cdot 10^{-2}}{3.5} = \frac{1}{4895} \le \left[\frac{1}{400}\right].$$

Thus, the stiffness of the beam (Element 3, Figure 13) is provided with a large margin.

Elements 2 (girders of longitudinal frames, Figure 13), length l = 8.0m, are subjected to the load, which is determined as follows: $q_n = g \cdot c \cdot K_d = 30 \cdot 1.75 \cdot 1.3 = 68.25\,\mathrm{kN} \cdot \mathrm{m}^{-1}$, where c = 1.75 m is the distance equal to half the width of the transverse frame 3.5m to collect loads on the girders of the longitudinal frames (Elements 2).

Crossbars of longitudinal frames (Elements 2, Figure 13) are statically indeterminate beams. To determine the maximum deflection of such beams, the Vereshchagin method was used, based on the multiplication of the coordinates of the centers of gravity of the curves of the resulting moment M (Figure 9) and moments M_1 from the unit force of the longitudinal frame (Figure 15) and determined by the equation [25, 30-31]:

$$\upsilon_{\max} = \upsilon_T = \frac{K_d}{EJ_{1x}}(M) \times (\overline{M}_1), \tag{12}$$

where J_{1x} = 39290 cm^4 - moment of inertia of I-beam No. 50 for the longitudinal frame rack (Element 1, Figure 13).

The diagram of moments $\overline{M}_1$ from a unit force $\overline{P} = 1$, applied in the middle of the longitudinal frame

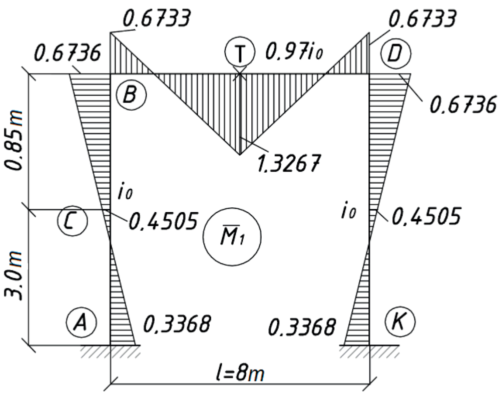

Figure 15 *Diagram of moments* $\overline{M}_1$ *of longitudinal frame from unit force* $\overline{P} = 1$

girder in section BD is shown in Figure 15. Performing calculations by Equation (12) one gets:

$$\upsilon_{\max} = \upsilon_T = \frac{2941.45}{EJ_{1x}}. \tag{13}$$

To take into account the effect on the resulting stiffness of element 2 (Figure 13), its supporting transverse and longitudinal elements 3 (Figure 13) and 4 (Figure 4), a correction coefficient 0.5 is introduced [27-28]. Taking into account the correction coefficient, next is checked the fulfillment of the condition of rigidity of elements 2, which are longitudinal beams with a span l = 8 m with an I-beam section No. 45. According to Equation (13), the maximum deflection is determined as:

$$\upsilon_{\max} = \upsilon_T = 0.5 \cdot \frac{2941.45 \cdot 10^{-3}}{2 \cdot 10^{8} \cdot 39.290 \cdot 10^{-8}} = \\ = 0.0187\ \mathrm{m} = 1.87\ \mathrm{cm} = 18.7\ \mathrm{mm}. \tag{14}$$

Stiffness of element “2” can be checked by Equation (11) considering 14:

$$\left(\frac{1.87}{800} = \frac{1}{428}\right) < \left(\left[\frac{1}{f}\right] = \frac{1}{400}\right) \text{or } \frac{1}{428} \leq \frac{1}{400}. \tag{15}$$

According to Equation (15), the condition of rigidity of element 2 (Figure 12) - longitudinal beams with span l = 8 m consisting of I-beams No. 45 is provided.

4 Conclusion

The presented research demonstrated the first analytical model of a modular mobile overpass - a new class of transport equipment that integrates the functions of a temporary bridge and undercarriage. The conducted studies describe the relationship between the force and deformation characteristics of the overpass structure under moving loads and make it possible to optimize the main parameters according to the criteria of strength and stability.

The design of the orthogonal module, as a key bearing element of the overpass, has been developed, which is a spatial П-shaped steel frame with an orthotropic slab of the carriageway and stiffening ribs. Its analytical force calculation was performed using the displacement method, taking into account the two most unfavorable dynamic loading schemes from mobile vehicles (q = 52.5 kN/m; g = 30 kN/m^2, with a dynamic coefficient of 1.3, according to Eurocodes [27-28]).

The critical internal forces are determined: the maximum bending moment in the junction of the girder and the strut (point B) - M_B = -232.42 kN·m (option 1) and M_B = 280.0 kN·m (option 2); transverse force Q_B = 214.6 kN; axial compressive force in the support N_A = -361.67 kN.

Optimal cross-sections of frame elements made of steel EN 10025-2 ($\sigma_{adm} = 284\ \mathrm{MPa}$) are selected:

- vertical struts - I-beam No. 50 (h = 500 mm, b = 200 mm, t = 15.5 mm);
- longitudinal girders with a span of 8 m - I-beam No. 45 (h = 450 mm);
- transverse girders with a span of 3.5 m - I-beam No. 30 (h = 300 mm).

The checks confirmed the fulfillment of the conditions for stiffness: the maximum deflection of the crossbar = 18.7 mm < [f] = L/400 = 20 mm, which guarantees the rigidity of the structure.

For the first time, the analytical dependence of peak bending moments at critical nodes on the ratio of rigidity of the crossbar and struts $n = i_2/i_1$ was established (Figure 14). The optimal value of n = 2.0 provides a decrease in maximum moments and total metal consumption by 9% compared to the equal-rigidity scheme (n = 1), which increases the efficiency and manufacturability of the design. These two results determine the basic scientific novelty of this research.

Further work can be directed to finite element modelling of the complete system (with inclined modules), field tests and the development of automated installation/dismantling mechanisms. The results obtained form the scientific and methodological basis for the design of a family of modular mobile overpasses adapted to various urban conditions. The implementation of the proposed solutions is important for improving the transport and construction technologies and increasing the efficiency of the use of urban space.

Acknowledgements

The authors are grateful to the Department of Transport Engineering and Logistics Systems for their support in the conduct of this study. We express special gratitude to Professor A. S. Kadyrov for scientific advice and valuable recommendations that contributed to the development of the topic of mobile overpasses.

Conflicts of interest

The authors declare that they have no known competing financial interests or personal relationships that could have appeared to influence the work reported in this paper.

References

[1] ZHANG, L., ZENG, G., LI, D., HUANG, H. J., STANLEY, H. E., HAVLIN, S. Scale-free resilience of real traffic jams. *Proceedings of the National Academy of Sciences* [online]. 2019, **116**(18), p. 8673-8678. ISSN 0027-8424, eISSN 1091-6490. Available from: https://doi.org/10.1073/pnas.1814982116

[2] RUI, C., YUMING, L., HUAN, Y., JIAZHEN, L., YU, L., YONG, L. Scaling law of real traffic jams under varying travel demand. *EPJ Data Science* [online]. 2024, **13**(1), p. 1-17. ISSN 2193-1127, eISSN 2193-1127. Available from: https://doi.org/10.1140/epjds/s13688-024-00471-4

[3] NAGATANI, T. Large traffic jam formation induced by multiple crossings in city network. *Physica A: Statistical Mechanics and its Applications* [online]. 2025, **661,** 130414. ISSN 0378-4371, eISSN 1873-2119. Available from: https://doi.org/10.1016/j.physa.2025.130414

[4] WANG, P., ZHANG, R., SUN, S., GAO, M., ZHENG, B., ZHANG, D., ZHANG, H. Aggravated air pollution and health burden due to traffic congestion in urban China. *Atmospheric Chemistry and Physics* [online]. 2023, **23**(5), p. 2983-2996. ISSN 1680-7316, eISSN 1680-7324. Available from: https://doi.org/10.5194/acp-23-2983-2023

[5] HAIDAR, N., HALEH, H., SHAYESTEH, S., MOHAMMAD, S. M., PARISA, HAJIBADALI. Exploring the dimensions of urban quality of life associated with urban traffic jam: the development and validation of an instrument. *Journal of Transport and Health* [online]. 2022, **26**, 101463. ISSN 2214-1405, eISSN 2214-1405. Available from: https://doi.org/10.1016/j.jth.2022.101463

[6] LEIXIAO, L., JIE, L. A congestion prediction method based on trajectory mining algorithm. *Computational Urban Science* [online]. 2025, **5**(1), p. 1-11. ISSN 2730-6852, eISSN 2730-6852. Available from: https://doi.org/10.1007/s43762-02500163-3

[7] RODRIGUEZ, E., FERREIRA, N., POCO, J. JamVis: exploration and visualization of traffic jams. *The European Physical Journal Special Topics* [online]. 2022, **231**(9), p. 1673-1687. ISSN 1951-6355, eISSN 1951-6401. Available from: https://doi.org/10.1140/epjs/s11734-021-00424-2

[8] KADYROV, A., GANYUKOV, A., PAK, I., SULEYEV, B., BALABEKOVA, K. Theoretical and experimental study of operation of the tank equipment for ultrasonic purification of the internal combustion engine exhaust gases. *Communications - Scientific Letters of the University of Zilina* [online]. 2021, **23**(3), p. B219-B226. ISSN 1335-4205, eISSN 2585-7878. Available from: https://doi.org/10.26552/com.C.2021.3.B219-B226

[9] GANYUKOV, A. A. Calculation of bending of roadway slabs of a modular overpass during the repair of urban utility networks. *Proceedings of the University* [online]. 2017, **1**(66), p. 54-59. ISSN 1609-6282. Available from: http://tu.kstu.kz/issue/issue/download/19

[10] KADYROV, A. S., GANYUKOV, A. A., AMANBAYEV, S. SH., BOGDANOVA, A. A. Development of mobile communal overpasses applied during repairing of urban communal networks. *Material and Mechanical Engineering Technology* [online]. 2023, **3**, p. 11-14. ISSN 3030-3230, eISSN 3030-3230. Available from: https://doi.org/10.52209/2706-977X_2023_3_1

[11] GANYUKOV, A. A., SINELNIKOV, K. A., KABIKENOV, S. Z., KARSAKOVA, A. Z. Research and calculation of the deformed state of the roadway mobile overpass. *Material and Mechanical Engineering Technology* [online]. 2024, **3**, p. 88-95. ISSN 3030-3230, eISSN 3030-3230. Available from: https://doi.org/10.56525/mmet.2024.3.88-95

[12] RUSSELL, B. R., THRALL, A. P. Portable and rapidly deployable bridges: historical perspective and recent technology developments. *Journal of Bridge Engineering* [online]. 2013, **18**(10), p. 1074-1085. ISSN 1084-0702, eISSN 1943-5592. Available from: https://doi.org/10.1061/(ASCE)BE.1943-5592.0000454

[13] ARIO, I., HAMA, Y., CHANTHAMANIVONG, K., CHIKAHIRO, Y., FUJIWARA, A., MA, H. Influence line-based design of scissors-type bridge. *Applied Sciences* [online]. 2022, **12**(23), p. 12170. ISSN 2076-3417, eISSN 2076-3417. Available from: https://doi.org/10.3390/app122312170

[14] ZUMSTEIN, M., CHEN, Q., ADEY, B. T., HALL, D. M. A preliminary investigation of the potential benefits of using the ASTRA Bridge for short-span bridge deck refurbishment projects in Switzerland. *Structure and*

Infrastructure Engineering [online], 2024, **20**(11), p. 1629-1647. ISSN 1573-2479, eISSN 1744-8980. Available from: https://doi.org/10.1080/15732479.2022.2152842

[15] LEDERMAN, G., YOU, Z., GLISIC, B. A novel deployable tied arch bridge. *Engineering Structures* [online]. 2014, **70**, p. 1-10. ISSN 0141-0296, eISSN 18737323. Available from: https://doi.org/ 10.1016/j.engstruct.2014.03.015

[16] KADYROV, A., BALABEKOVA, K., GANYUKOV, A., AKHMEDIYEV, S. The constructive solution and calculation of elements of the unified module of the mobile bridge overcrossing. *Transport Problems* [online]. 2017, **12**(3), p. 59-69. ISSN 1896-0596, eISSN 2300-861X. Available from: https://doi.org/10.20858/tp.2017.12.3.6

[17] KADYROV, A., GANYUKOV, A., BALABEKOVA, K. Development of constructions of mobile road overpasses. *MATEC Web of Conferences* [online]. 2017, **108**, 16002. ISSN 2261-236X, eISSN 2261-236X. Available from: https://doi.org/10.1051/matecconf/201710816002

[18] GANYUKOV, A. A., GEORGIADI, I. V. Calculation and design of structural elements of the mobile overpass. *Proceedings of the University* [online]. 2018, **4**(73), p. 104-111. ISSN 1609-6282. Available from: http://tu.kstu.kz/issue/issue/download/10

[19] KADYROV, A. A., GANYUKOV, A. A., BALABEKOVA, K. G., ZHUNUSBEKOVA, Z. Z., SULEEV, B. D. Scientific and engineering bases for development of mobile overpasses. *Material and Mechanical Engineering Technology* [online]. 2020, **2**, p. 7-13. ISSN 3030-3230, eISSN 3030-3230. Available from: https://mmet.kstu.kz/download/articles/29062023033626_digest.pdf

[20] GANYUKOV, A. Research of operation of mobile overpass constructions. *Proceedings of the University* [online]. 2022, **1**(86), p. 195-200. ISSN 16096282. Available from: https://doi.org/10.52209/1609-1825_2022_1_195

[21] GANYUKOV, A. A., KADYROV, A. S., AMANBAYEV, S. S. Development of methods for assembling a modular overpass. *Proceedings of the University* [online]. 2022, **2**(87), p. 217-223. ISSN 1609-6282. Available from: https://doi.org/10.52209/1609-1825_2022_2_217

[22] VYSHAR, O., STOLBOUSHKIN, A., RAKHIMOVA, G., STANEVICH, V., RAKHIMOV, M. Study of the properties of overburdened rocks from coal mining: overburden - as a raw material in the production of ceramic bricks. *International Journal of GEOMATE* [online]. 2023, **25**(107), p. 86-94. ISSN 2186-2982, eISSN 2186-2990. Available from: https://doi.org/10.21660/2023.107.g12288

[23] MARDONOV, B. T., SHEROV, K. T., TOIROV, M. S., MAKHMUDOV, L. N., YAKHSHIEV, S. N., KONGKYBAYEVA, A. N., SHEZHAU, K. Features of engineering methods of research results on butt welding on metal pipelines. *Material and Mechanical Engineering Technology* [online]. 2024, **1**, p. 3-8. ISSN 3030-3230, eISSN 3030-3230. Available from: https://doi.org/10.52209/2706977X_2024_1_3

[24] BOGDANOV, G. I. *Design of bridges and pipes*. KUZMIN, Y. G. (Ed.). Moscow: Marshrut, 2015. ISBN 978-5-89035-842-4.

[25] DARKOV, A. V., SHAPOSHNIKOV, N. N. *Structural mechanics*. Moscow: High School, 2014. ISBN 978-5-06-006589-3.

[26] SNiP RK 5.04-23-2002. Steel Structures. Design Standards. Astana: Committee for Construction and Housing and Communal Services of the Republic of Kazakhstan, 2003.

[27] EN 1990: Eurocode - Basis of structural design. Brussels: European Committee for Standardization (CEN), 2002.

[28] EN 1991-2: Eurocode 1: Actions on structures - Part 2: Traffic loads on bridges. Brussels: European Committee for Standardization (CEN), 2003.

[29] HIBBELER, R. C. *Mechanics of materials*. 10. ed. Upper Saddle River, NJ: Pearson, 2016. ISBN 978-0-13-431965-0.

[30] American Institute of Steel Construction (AISC). *Steel construction manual*. 16. ed. Chicago, IL: AISC, 2023. ISBN 978-1-56424-116-0.

[31] GERE, J. M., GOODNO, B. J. *Mechanics of materials*. 9. ed. Boston, MA: Cengage Learning, 2018. ISBN 978-1-337-09334-7.

ENHANCING THE TRANSPORT SAFETY THROUGH DISDROMETER-BASED ENVIRONMENTAL SENSING

Matúš Nečas[1,*], Tomáš Ranuša[1], Dušan Maga[2], Gabriel Gašpar[1,3]

[1]University of Zilina, Faculty of Electrical Engineering and Information Technologies, Department of Control and Information Systems, Zilina, Slovakia
[2]Czech Technical University in Prague, Faculty of Electrical Engineering, Prague, Czech Republic
[3]University of Zilina, Research Centre, Zilina, Slovakia

*E-mail of corresponding author: matus.necas@feit.uniza.sk

Matúš Nečas 0009-0002-5145-2835,
Tomáš Ranuša 0009-0008-7624-1587,
Dušan Maga 0000-0001-8176-2151,
Gabriel Gašpar 0000-0002-2550-1675

Resume

In this study is presented a system for real-time precipitation measurement integrating the laser disdrometer with adaptive control. The system manages large sensor data streams dynamically, enhancing robustness and accuracy under intense weather conditions. Meteorological inputs, combined with communication, enable scalable infrastructure supporting automated safety interventions. Experimental deployment showed improved data fidelity, anomaly detection, and detailed analysis of drop size and velocity distributions. The approach advances intelligent transportation safety and operational reliability through comprehensive environmental sensing and real-time adaptive data processing.

Article info
Received 14 November 2025
Accepted 4 December 2025
Online 16 January 2026

Keywords:
disdrometer
environmental monitoring
ETL pipeline
intelligent transportation systems
real-time data collection

Available online: https://doi.org/10.26552/com.C.2026.012

ISSN 1335-4205 (print version)
ISSN 2585-7878 (online version)

1 Introduction

In the current geographical and climatic context, the accurate measurement of precipitation is considered essential for the safety and efficiency of transportation systems. The flow of traffic and the risk of accidents have been significantly affected by extreme weather events, including heavy rainfall and snowfall. Consequently, advanced meteorological measurement devices have been developed to provide precise and reliable real-time data to support decision-making processes in traffic management [1].

Modern optical instruments, such as the *Thies Clima Laser Precipitation Monitor*, are capable of detailed monitoring of raindrop size, velocity, and distribution. Compared to the conventional rain gauges, disdrometers provide enriched information on the characteristics of precipitation, which is critically important for transportation engineering when analyzing the impact of rainfall on pavement conditions, tire adhesion, and accident rates [2-3].

From a process control perspective, it is recognized that not only data acquisition from sensors, but also effective integration, processing, and adaptive control of these systems in real-time, are critical. Large volumes of data are generated by modern meteorological sensors, such as laser disdrometers, which require processing by advanced algorithms and cybernetic approaches for noise filtering, anomaly detection, and reliable estimation of precipitation parameters. The accuracy and robustness of measurements are enhanced by implementing adaptive regulatory mechanisms within sensor networks, which is fundamental for the real-time management of traffic systems.

The integration of meteorological sensors into intelligent transportation systems (ITS) has become increasingly important with the advancement of digitalization and IoT technologies. Contemporary road meteorological stations combine multiple types of sensors (temperature, humidity, wind speed, precipitation) and employ advanced communication protocols (4G/5G, Ethernet, RS-485, or RFID) to enable the prompt data transmission to centralized control systems. Such data processing facilitates weather forecasting and allows the automated activation of safety measures, such as dynamic speed limit adjustments or warnings about hazardous ice conditions [4-5].

Numerous studies have been conducted to evaluate the accuracy and reliability of laser disdrometers. Different optical disdrometer models have been compared, highlighting their capability to precisely capture raindrop size and velocity while acknowledging their limitations under extreme conditions such as very intense precipitation. Furthermore, significant research has focused on integrating meteorological data with traffic management systems to improve road safety and coordinating with broader environmental monitoring networks [6-9].

Challenges encountered within the sensor technology and cybernetics include the necessity for calibration, compensation for environmental influences, such as temperature and wind, and the mitigation of interference and signal loss under varying climatic conditions. These aspects are regarded as crucial for designing cybernetic systems with high reliability and autonomy in data acquisition units [10].

The objective of the presented research was to develop an optimized system for the automated collection and analysis of meteorological data using the *Thies Clima Laser Precipitation Monitor* for applications within intelligent transportation systems. The focus was on minimizing the measurement errors during high precipitation intensities, integrating the data into existing traffic control platforms, and evaluating the effects of environmental factors on data quality [11-12]. The expected outcomes are anticipated to contribute to enhanced safety and efficiency of transportation infrastructures under adverse meteorological conditions.

A distinctive feature of this study is the incorporation of adaptive cybernetic control mechanisms within the sensor networks for the real-time data processing and anomaly detection. This integration notably enhances the robustness and accuracy of the collected data. While prior research was predominantly concentrated on static sensor calibration, or isolated data processing techniques, this work focus was on the dynamic and autonomous management of information streams derived from sensors, thereby enabling more responsive and precise interventions in traffic management [13-15]. The research presents a holistic approach that combines advanced laser disdrometer measurements with multi-sensor meteorological inputs and IoT communication protocols. Such a comprehensive integration supports the development of a resilient and scalable infrastructure capable of executing automated safety responses, including dynamic speed regulation and hazard warnings, all driven by high-resolution environmental data. The novelty of this research is embodied in the synthesis of cutting-edge laser disdrometer technology, adaptive cybernetic control strategies, and intelligent transportation system applications. This synergy establishes a new standard in environmental sensing, aiming to enhance transport safety and operational efficiency.

2 Materials, methods, algorithms

The proposed system ensures automated collection, processing, and archiving of environmental data generated by a laser disdrometer. System components, including the system architecture, the mathematical model of the device, and the data component of the solution, are discussed in the following sections.

2.1 System architecture

The solution architecture integrates the sensor, communication, and software layers into a single functional unit that enables continuous monitoring of precipitation activity and subsequent data analysis. The block diagram of the system components is shown in Figure 1 and consists of four main blocks: *Disdrometer, RS-485 to Ethernet Converter, Server,* and a *Client*.

The measurement part of the system consists of a *Thies Clima Laser Precipitation Monitor*, a device designed to detect and classify atmospheric particles based on the principle of optoelectronic measurement. This principle uses a laser diode with a wavelength of 785 nm, situated in the infrared spectrum, to detect individual particles. An infrared transmitter (*IR Transmitter*) generates a collimated beam that passes through the measurement volume. On the other side, an infrared receiver (*IR Receiver)* records changes in radiation intensity. When a particle, such as a raindrop or snowflake, passes through, it partially shades the beam, which the *Control Unit* evaluates as a measurement event. The *Control Unit* subsequently digitizes the resulting signal, computes the relevant physical quantities (such as diameter, velocity, volume, and precipitation intensity), and stores them in a *FIFO Buffer*, serving as a memory cache. Data transfer to the higher communication level is ensured by the *RS-485 Interface*, which provides robust differential communication resistant to electromagnetic interference.

The RS-485-Ethernet converter *GNOME 485* from the company *Papouch* is used to connect the serial interface of the disdrometer to the network infrastructure. This module converts the data stream from the differential serial RS-485 format to the TCP/IP network protocol, enabling the integration of the device into a standard computer network without requiring hardware modifications. The converter supports configuration of communication parameters (speed, parity, IP address, port) and operates with the TCP, UDP, Telnet, HTTP, and DHCP protocols. In the proposed solution, it functions in TCP server mode, with the disdrometer periodically sending data to a defined port. The server layer represents the core of the system,

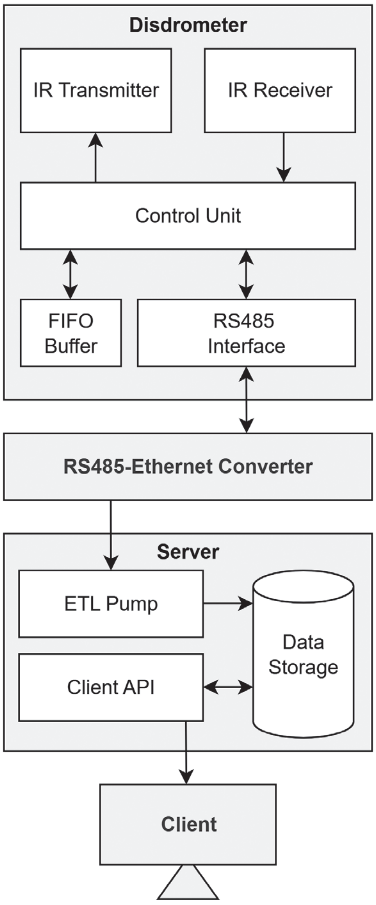

Figure 1 *Architecture of the proposed data acquisition system*

responsible for receiving, processing, and storing the data. The main software component is the *ETL Pump* (*Extract, Transform, Load*) implemented in Python:

Extraction (*Extract*) - Data are received via a network socket that maintains a persistent TCP connection with the converter. The received messages are processed as text strings and split into individual fields according to the protocol structure.

1. Transformation (*Transform*) - The data are decoded, validated, and converted into numerical values. During the transformation process, completeness checks, unit conversions, and timestamp validations are performed.
2. Loading (*Load*) - The processed data are stored in a non-relational database, which offers a flexible structure and allows easy extension with new types of variables without altering the database schema.
3. The server also provides data access through a client API, which enables visualization, export, and querying of historical data.

2.2 Mathematical model of disdrometer data processing

Based on the measured variables, specifically the diameter d and the fall velocity of individual particles, the disdrometer calculates several derived meteorological parameters [16]. Those parameters provide a comprehensive description of the precipitation event, enabling the classification of precipitation type, estimation of its intensity, and modelling of microphysical processes in the atmosphere.

The calculations are performed in the control unit according to a set of defined equations that form the mathematical data processing model. Among the most important derived variables are precipitation intensity, radar reflectivity, meteorological optical range (MOR), and other characteristics of the precipitation field.

The precipitation intensity I is calculated from the volume of all particles per unit time:

$$I = \frac{1}{A \cdot \Delta t} \sum_{i=1}^{N} V_i , \tag{1}$$

where A is the cross-sectional area, Δt is the measurement interval, N is the number of detected particles, and V_i is the volume of the i-th particle, expressed as follows:

$$V_i = \frac{\pi}{6} d_i , \tag{2}$$

where d_i is the diameter of the i-th particle.

Radar reflectivity represents the sum of the sixth powers of the diameters of all particles in the measured volume:

$$Z = \sum_{i=1}^{N} d_i^6 \,. \tag{3}$$

For comparability to meteorological radar measurements, reflectivity is often expressed on a logarithmic scale (dBZ):

$$dBZ = 10\log(Z)\,. \tag{4}$$

Meteorological Optical Range (MOR) characterizes visibility, that is, the distance at which an object with a certain contrast edge can still be recognized. It is defined as:

$$MOR = \frac{3.912}{\beta}\,, \tag{5}$$

where β is the absorption coefficient (m^{-1}), calculated from the cross-sectional area of individual particles and their concentration in the measured volume.

2.3 Data structure and measurement processing

The data output of the disdrometer is implemented in the form of telegrams - structured data frames with a fixed format, containing a sequence of values representing physical quantities derived from the optoelectronic measurement principle. In this application, the following telegram types are utilized:

- *Telegram #3* provides microphysical data about individual particles, such as diameter, velocity, beam attenuation duration, and internal environment temperature.
- *Telegram #8* transmits aggregated meteorological indicators - precipitation intensity and total amount, radar reflectivity, visibility (MOR), and automatic weather type classification.

Since the disdrometer transmits data in discrete telegrams, the proposed system was designed to operate as a cyclic communication model that transitions between three defined operational states (Figure 2):

- *Short-term Measuring State* (*Telegram #3)* - continuous sensing of microphysical parameters of individual particles,
- *Long-term Aggregation State* (*Telegram #8*) - periodic collection and transmission of aggregated meteorological variables, and
- *Data Processing State* - validation, transformation, and storage of received data.

The *Short-term Measuring State* and *Long-term Aggregation State* operate in a blocking mode because they are limited by a single physical bus. Parallel to this is the *Data Processing State*, which is designed to avoid blocking the execution of further measurements.

Data processing is implemented as an ETL (Extract, Transform, Load) process [17]. In the *Extract phase*, data telegrams are received via a TCP/IP connection and decoded into a tabular structure, which serves as the basis for subsequent analysis. In the *Transform phase*, validation of values, format checking, calculation of supplementary parameters, and filtering of erroneous frames are performed. Since the disdrometer does not perform internal validation of data correctness, erroneous or physically improbable measurements may be transmitted. The basic measurement parameters - particle diameter d, its velocity v, and measurement time t, serve as reference variables from which all other microphysical and meteorological indicators are derived.

The filtering function f_{filt} formally defined as:

$$f_{filt}(d,v,t) = \begin{cases} 1, & v \in V_d \quad t < t_{now}, \\ 0, & \text{otherwise} \end{cases} \tag{6}$$

where $V_d = \langle 0.2, 40 \rangle$ m/s represents the set of all allowable velocities that the disdrometer is capable of recording, $D_d = \langle 0.16, 5 \rangle$ mm determines the range of physically possible diameters of atmospheric particles and t_{now} is the current time during the data processing. Values outside these intervals are automatically discarded as invalid.

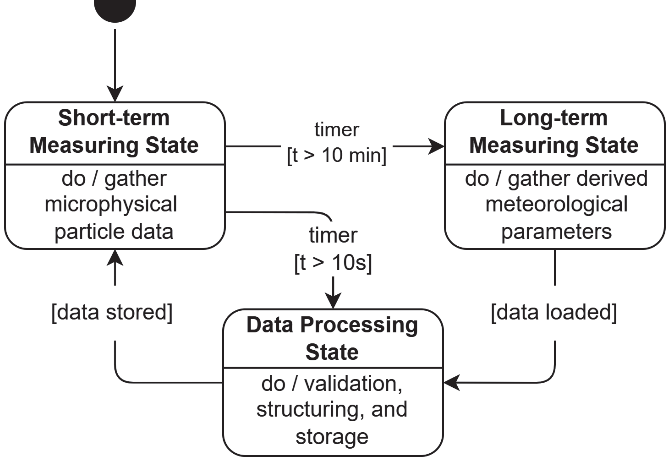

Figure 2 *State model of Measurement Processing*

Timestamps are then verified for consistency to avoid time jumps, duplicates, or data loss, ensuring the chronological integrity of the dataset. In the *Load phase*, processed data are stored in a time-oriented non-relational database (*InfluxDB*), which allows compact access to historical measurements and subsequent analytical processing. To reduce the database load, a local buffer with a capacity of 360 measurements (equivalent to one hour of data) is utilized, allowing for the batch insertion of records.

Cyclic switching between the measurement states ensures a balance between high temporal resolution and long-term data continuity. During the normal operation, continuous recording of *Telegram #3* occurs at 10-second intervals. Every 10 minutes, the system briefly switches to *Telegram #8* mode, receives aggregated data, and returns to the basic measurement state. Data integrity mechanisms have been implemented, including frame checks, automatic reconnection on errors, and timed delays during mode switches. Damaged or incomplete telegrams are automatically discarded to maintain dataset consistency.

3 Results

Within the framework of a pilot study, a system was deployed to collect environmental data, focusing on monitoring precipitation parameters, including daily totals, droplet size and velocity distributions, as well as their relationship to air temperature.

The test system was placed in a laboratory environment and used a *Raspberry Pi 5* as the main control and data collection node. Communication with the *Thies Clima Laser Precipitation Monitor*, connected to the university network, was conducted via a secure VPN connection.

Measurements were conducted continuously over a three-month period, during which millions of individual records were logged. For detailed analysis, the 41st calendar week of 2025 was selected, representing a typical pattern of autumn precipitation. During this period, 1,460,532 individual droplets were detected, which subsequently underwent filtering (see Equation (6)), validation, and visualization.

The average diameter of the recorded droplets was 0.35 mm ± 0.153 mm. The smallest detected droplets had a size of 0.16 mm, while the maximum value of 4.74 mm was at the boundary of the so-called “breakup limit” - the physical stability limit of raindrops. At this size, the droplet deforms due to air resistance and subsequently breaks apart into smaller particles. Droplets larger than 4.5-5 mm occur rarely in the atmosphere and typically correspond to short-term intense precipitation events.

The average terminal velocity of the particles was 1.716 ± 0.593 m/s, with a minimum value of 0.21 m/s and a maximum of 10.09 m/s. The size and velocity distributions of the droplets are shown in Figure 3.

The data were subsequently aggregated into hourly averages and used for analysis of the temporal course of precipitation intensity and air temperature (Figure 4). During the observed period, the temperature ranged from 9 to 16 °C, with an average value of 11.46 °C.

The velocity of raindrops in the range of 0.7-5 mm was analyzed through cluster analysis according to ambient air temperature to quantify its influence on droplet dynamics. The largest number of observations was concentrated in the cluster at the reference temperature of 10-11 °C, where a power-law dependence of velocity v on droplet diameter d was identified:

$$v = 3.663d^{0.676}\,. \tag{7}$$

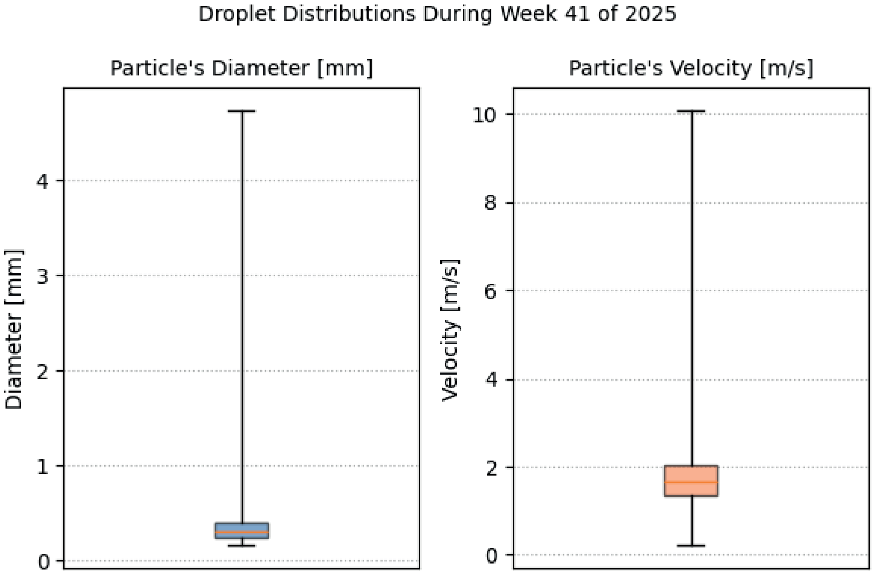

***Figure 3** Distribution of particle diameter and velocity displayed using a boxplot*

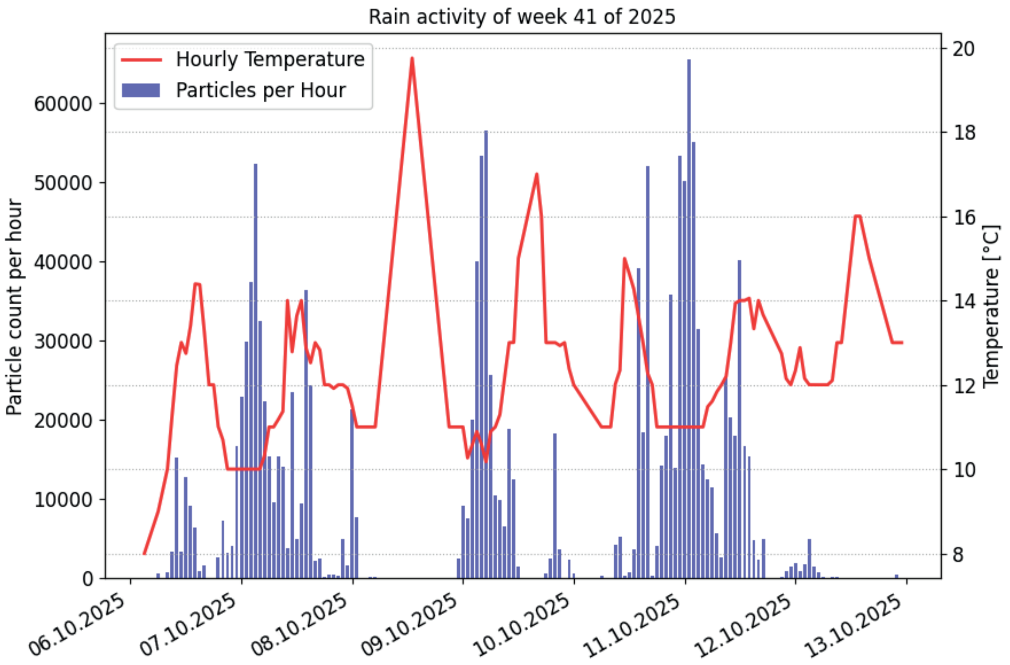

***Figure 4** Relationship between the temperature and a number of particles detected*

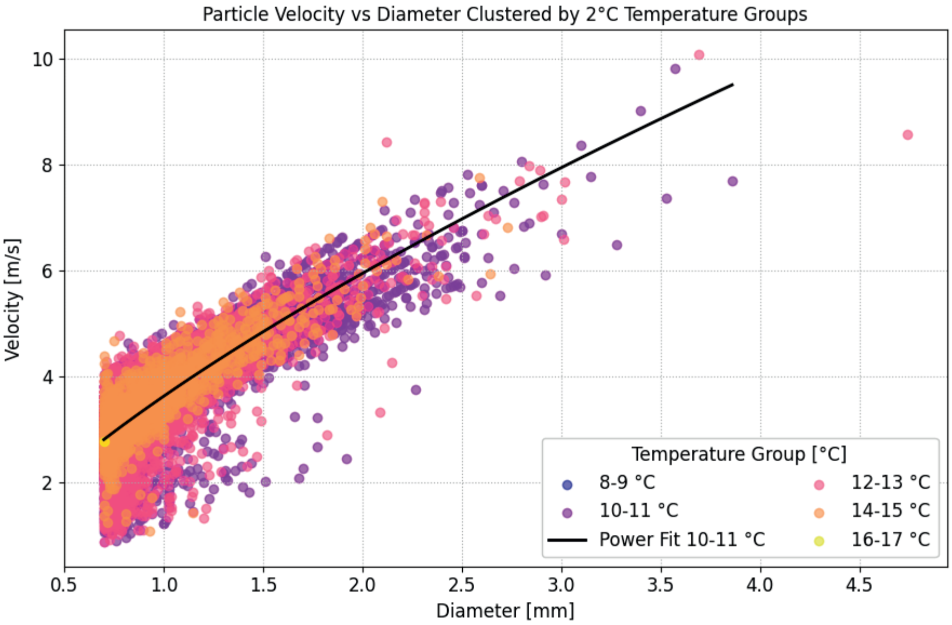

***Figure 5** Relationship between the particle velocity and its diameter*

Temperature did not significantly influence the relationship between the droplet velocity and diameter; the shape and parameters of the power-law function remained consistent across the individual temperature clusters. The results are shown in Figure 5.

4 Discussion

During the experimental period, the capability of the *Thies Laser Precipitation Monitor* to provide extensive and detailed information on precipitation characteristics, including particle size, velocity, and temperature, was confirmed. However, several technical and methodological limitations must be considered that may affect the accuracy and interpretation of the obtained data.

One of the main limitations is the device throughput during very intense precipitation events. According to the manufacturer's documentation, incomplete capture of falling particles may occur because *Telegram #3*, used for continuous measurement of individual particle parameters, has limited throughput under extreme rainfall density [16]. Data loss, however, is not directly detectable since the data stream remains high even with incomplete recording. Therefore, in short time intervals, the output may be slightly underestimated. Still, given the large number of recorded particles, this effect does not significantly impact the statistical values of overall precipitation parameters.

Another limitation arises from the constructional characteristics of the device. According to the technical department of *Thies Clima*, the disdrometer is not designed for dynamic switching of measurement modes during operation. The device is optimized for the long-term data transmission in a single telegram rather than periodic switching between different modes. The designed automated ETL system allowed switching between *Telegram #3* (raw particle data) and *Telegram #8* (processed aggregated data), thus obtaining a more comprehensive information set. However, this approach brings risks, particularly the potential damage or loss of data at the moment of switching, which was observed during measurements and corresponds to the expected system behavior.

In evaluating the measured data, focus was placed on particles with diameters ranging from 0.7 to 5 mm, although the technical range of the disdrometer begins at 0.16 mm. Particles smaller than 0.7 mm exhibited significant scatter, likely due to fog, dust, or other atmospheric particles dispersed by wind. The identified power-law dependence of velocity on droplet diameter corresponds to the expected theory of Stokes' equation, but further study is required for verification and quantification of this relationship. Additionally, the assumption that the disdrometer captures all the particles may lead to result bias; therefore, it would be appropriate to develop a more precise classification of atmospheric particles in the future.

Wind conditions may partially influence the measured velocity of precipitation particles at the measurement site. During the experiment, no wind shield or protective element was used to mitigate airflow effects. As a result, the measured droplet velocities may deviate from their actual terminal velocities, particularly in strong winds or near the sensor under turbulence. To address this limitation, it would be appropriate to complement the measurement system with an additional instrument, such as an anemometer, to quantify wind speed and apply corrections to the measured droplet velocities. In this study, data quality was improved only through a simple outlier filtering, particularly for droplets exhibiting abnormally high velocities, which were likely due to environmental conditions or measurement errors.

The results of this study indicate the potential for integrating adaptive control and advanced data processing in sensor networks for the real-time rainfall monitoring. Dynamic management of sensor data flows has improved measurement accuracy and robustness, especially under challenging weather conditions. The combination of laser disdrometer technology with advanced processing logic demonstrated clear benefits, while challenges remain related to environmental interference and ensuring sensor reliability during extreme climatic events.

Future research should focus on enhancing the multi-sensor data fusion, utilizing machine learning for anomaly detection, and developing decentralized processing architectures to minimize latency and improve system autonomy. Incorporating additional environmental parameters, such as fog density or road surface conditions, could further enrich the sensor framework. Moreover, extensive field deployments and long-term performance evaluations are crucial for validating the efficiency and sustainability of the system across diverse operational scenarios. This will contribute to development of smarter and more resilient transportation infrastructures, capable of proactively adapting to changing environmental conditions.

5 Conclusion

In this article, a system for collecting and processing environmental data (ETL), based on the *Thies Laser Precipitation Monitor* and *Raspberry Pi 5*, was proposed and implemented. This pilot study serves to verify the functionality and reliability of the designed system. The system demonstrated the ability to continuously collect and process detailed precipitation information, including the distribution of droplet sizes and velocities, while ensuring the reliable aggregation and visualization of this data.

The main contribution of the proposed solution lies in its ability to integrate the data collection, filtering, and processing into a single flexible framework, enabling robust precipitation monitoring even under challenging environmental conditions. Despite the presence of measurement errors, caused by extreme conditions - such as strong wind, fog, condensation on optical components, or snow, the system provides a consistent and high-quality dataset suitable for long-term trend monitoring and droplet distribution analysis.

Precipitation represents a key meteorological factor influencing the transport safety, particularly during extreme events, such as intense rainfall or snowfall. Such conditions can substantially reduce visibility, impair road surface adhesion, and increase the risk of aquaplaning or loss of vehicle control. Laser disdrometers not only measure rainfall intensity but also determine the droplet size distribution and velocity, providing more detailed information than conventional rain gauge systems. These data can support the detection of hazardous situations that pose direct risks to road traffic. Potential implementation scenarios include integrating precipitation measurements into the traffic management centers, where warning mechanisms could inform drivers via variable traffic signs or navigation applications. In a broader context, meteorological data from disdrometers could also support advanced driver-assistance systems or autonomous vehicle control.

The results presented in this article confirm that the designed ETL system represents an effective and modular tool for environmental monitoring, serving as a foundation for further development of intelligent sensor networks and real-time monitoring applications. For future implementations, a more stable software realization and cross-validation with alternative sensors are recommended to more precisely quantify the impact of environmental factors and minimize data loss.

Acknowledgements

This work was supported by VEGA through the Research on motion data analysis methods for applications in diagnosis and therapy of gnostically relevant symptoms under Grant 1/0147/25.

Conflicts of interest

The authors declare that they have no known competing financial interests or personal relationships that could have appeared to influence the work reported in this paper.

References

[1] JOHANNSEN, L. L., ZAMBON, N., STRAUSS, P., DOSTAL, T., NEUMANN, M., ZUMR, D., COCHRANE, T. A., BLOSCHL, G., KLIK, A. Comparison of three types of laser optical disdrometers under natural rainfall conditions. *Hydrological Sciences Journal* [online]. 2020, **65**(4), p. 524-535. ISSN 0262-6667, eISSN 2150-3435. Available from: https://doi.org/10.1080/02626667.2019.1709641

[2] TAFAZZOL, S., SHARIF, H., GHOLIKHANI, M., AHSAN, M., GHEBREYESUS, D., BILLAH, K., FURL, C. Relative crash risk and road safety during rainfall in Texas from 2006 to 2021. *Scientific Reports* [online]. 2025, **15**(1), 36749. ISSN 2045-2322. Available from: https://doi.org/10.1038/s41598-025-20760-w

[3] MINDA, H., MAKINO, T., TSUDA, N., KANEKO, Y. Performance of a laser disdrometer with hydrometeor imaging capabilities and fall velocity estimates for snowfall. *IEEJ Transactions on Electrical and Electronic Engineering* [online]. 2016, **11**(5), p. 624-632. eISSN 1931-4981. Available from: https://doi.org/10.1002/tee.22280

[4] TOKAY, A., WOLFF, D. B., PETERSEN, W. A. Evaluation of the new version of the laser-optical disdrometer, OTT Parsivel^2. *Journal of Atmospheric and Oceanic Technology* [online]. 2014, **31**, p. 1276-1288. ISSN 0739-0572, eISSN 1520-0426. Available from: https://doi.org/10.1175/JTECH-D-13-00174.1

[5] VAGAS, M., GALAJDOVA, A., SIMSIK, D., CVITIC, I. Proposal of an algorithm for data collection and processing via RFID technology. *Research Papers Faculty of Materials Science and Technology in Trnava Slovak University of Technology in Bratislava / Vedecke Prace Materialovotechnologickej Fakulty Slovenskej Technickej Univerzity v Bratislave so Sidlom v Trnave* [online]. 2019, **27**(45), p. 19-25. ISSN 1336-1589, eISSN 1338-0532. Available from: https://doi.org/10.2478/rput-2019-0021

[6] SHEN, E., LIU, G., ABD ELBASIT, M. A. M., ZHAN, X., FENG, Q., DAN, CH., SHI, H., CHEN, X., ZHANG, Q., GUO, Z. Comparison of a laser precipitation monitor, piezoelectric transducer and particle imaging transient visual measurement technology under simulated rainfall in laboratory conditions. *Journal of Hydrology* [online]. 2022, **610**, 127978. ISSN 0022-1694, eISSN 1879-2707. Available from: https://doi.org/10.1016/j.jhydrol.2022.127978

[7] KRAJEWSKI, W. F., KRUGER, A., CARACCIOLO, C., GOLE, P., BARTHES, L., CREUTIN, J.-D., DELAHAYE, J.-Y., NIKOLOPOULOS, E. I., OGDEN, F., VINSON, J.-P. DEVEX-disdrometer evaluation experiment: basic results and implications for hydrologic studies. *Advances in Water Resources* [online]. 2006, **29**(2), p. 311-325. ISSN 0309-1708, eISSN 1872-9657. Available from: https://doi.org/10.1016/j.advwatres.2005.03.018

[8] FEHLMANN, M., ROHRER, M., VON LERBER, A., STOFFEL, M. Automated precipitation monitoring with the Thies disdrometer: biases and ways for improvement. *Atmospheric Measurement Techniques* [online]. 2020, **13**, p. 4683-4698. ISSN 1867-8610, eISSN 1867-8548. Available from: https://doi.org/10.5194/amt-13-4683-2020

[9] PAO, W. Y., LI, L., VILLENEUVE, E., WHALLS, E., AGELIN-CHAAB, M., GULTEPE, I., KOMAR, J. Perceived precipitation intensity prediction model based on simultaneous dynamic and static observations for evaluating weather impacts on vehicle applications. *Journal of Traffic and Transportation Engineering (English Edition)* [online]. 2025, **12**(3), p. 639-651. ISSN 2095-7564, eISSN 2589-0379. Available from: https://doi.org/10.1016/j.jtte.2024.05.003

[10] CELAR, N., STANKOVIC, S., KAJALIC, J. The role of intelligent transportation systems in mitigating adverse weather effects on traffic safety and efficiency. In: 8th International Conference on Road and Rail Infrastructure: proceedings [online]. 2024. ISSN 1848-9842, eISSN 1848-9850. Available from: https://doi.org/10.5592/CO/CETRA.2024.1618

[11] PROKHORCHUK, A., MITROVIC, N., MUHAMMAD, U., STEVANOVIC, A., ASIF, M. T., DAUWELS, J., JAILLET, P. Estimating the impact of high-fidelity rainfall data on traffic conditions and traffic prediction. *Transportation Research Record: Journal of the Transportation Research Board* [online]. 2021, **2675**(11), 1285. ISSN 0361-1981, eISSN 2169-4052. Available from: https://doi.org/10.1177/03611981211026309

[12] WANG, J., WU, Z., LIANG, Y., TANG, J., CHEN, H. Perception methods for adverse weather based on vehicle infrastructure cooperation system: a review. *Sensors* [online]. 2024, **24**(2), 374. eISSN 1424-8220. Available from: https://doi.org/10.3390/s24020374

[13] HSIEH, CH-W., CHI, P.-W., CHEN, CH.-Y., WENG, CH.-J., WANG, L. Automatic precipitation measurement based on raindrop imaging and artificial intelligence. *IEEE Transactions on Geoscience and Remote Sensing* [online]. 2019, **57**(12), 10276. ISSN 0196-2892, eISSN 1558-0644. Available from: https://doi.org/10.1109/tgrs.2019.2933054

[14] KETTELGERDES, M., ELGER, G. In-field measurement and methodology for modeling and validation of precipitation effects on solid-state LiDAR sensors. *IEEE Journal of Radio Frequency Identification* [online]. 2023, **7**, 192. eISSN 2469-7281. Available from: https://doi.org/10.1109/jrfid.2023.3234999

[15] SANDHIP, R., et al. Intelligent traffic monitoring and autonomous navigation system with real-time weather and incident alerts. In: 2025 International Conference on Data Science and Business Systems ICDSBS: proceedings [online]. IEEE. 2025. ISBN 9798331585617, p. 1-17. Available from: https://doi.org/10.1109/icdsbs63635.2025.11031650

[16] Adolf Thies GmbH and Co. KG. Laser precipitation monitor: instruction for use 5.4110.xx.x00, V2.7x STD [online]. Document No. 021341/08/22. Gottingen, 2022. Available from: https://www.thiesclima.com/db/dnl/5.4110.xx.x00_Laser_Precipitation_Monitor_eng.pdf

[17] SEENIVASAN, D. ETL for IoT data: integrating sensor data into data warehouses. *SSRN Electronic Journal* [online]. 2025, preprint. ISSN 1556-5068. Available from: https://doi.org/10.2139/ssrn.5143321

CLOUD-BASED MODULAR SYSTEM FOR ACQUISITION AND VISUALIZATION OF OCO-2 REMOTELY SENSED CO_2 DATA

Maroš Valášek[1,*], Roman Budjač[2], Martin Hanzely[3], Neven Vrček[4]

[1]Department of Control and Information Systems, Faculty of Electrical Engineering and Information Technology, University of Zilina, Zilina, Slovakia
[2]Research Centre, University of Zilina, Zilina, Slovakia
[3]Travelco s.r.o., Oscadnica, Slovakia
[4]Department of Information Systems Development, University Zagreb, Varazdin, Croatia

*E-mail of corresponding author: maros.valasek@feit.uniza.sk

Maros Valasek 0009-0006-4781-4628,
Martin Hanzely 0009-0002-5383-7288,
Roman Budjac 0000-0001-6840-1706,
Neven Vrcek 0000-0002-4037-1522

Resume

In this paper is presented a cloud-based framework for automated acquisition and visualization of Orbiting Carbon Observatory-2 (OCO-2) satellite CO_2 data. The system employs an ETL pipeline with OPeNDAP protocol for selective data retrieval, reducing network overhead while processing L2 Standard and L2 Lite FP products. Built on Amazon Web Services (AWS) infrastructure, using Python (Pandas, Dash, Plotly) and Docker orchestration, the modular architecture implements dependency injection for runtime flexibility. The deployed system achieves daily automated ingestion with 2.25 km × 1.29 km spatial resolution, enabling the real-time monitoring through interactive web visualization. The system is designed as a foundation for future analytical research, providing ready integration points for machine learning models to perform advanced CO_2 pattern recognition and predictive analysis.

Article info

Received 14 November 2025
Accepted 5 December 2025
Online 16 January 2026

Keywords:

CO_2
data acquisition
remote sensing
machine learning

ISSN 1335-4205 (print version)
ISSN 2585-7878 (online version)

Available online: https://doi.org/10.26552/com.C.2026.013

1 Introduction

The current level of CO_2 in the atmosphere has increased in the last decades significantly, necessitating advanced monitoring techniques such as those offered by satellite-based remote sensing [1]. These platforms offer a unique vantage point for comprehensive atmospheric observations, enabling the precise quantification of greenhouse gas concentrations and their spatial and temporal variations [2]. This approach is critical for identifying emission hotspots, such as large urban centers, power plants, and industrial facilities, which are major contributors to anthropogenic CO_2 emissions [3-4]. However measurements are not consistent and not all localities have the same measurement fidelity, with current methods facing challenges in distinguishing anthropogenic CO_2 signals from background concentrations and limitations in spatio-temporal resolution [5]. Furthermore, the distribution of CO_2 satellite measurements exhibits significant latitudinal bias [6]. This necessitates the integration of data from diverse observational platforms, including ground-based in-situ sensors and atmospheric models, to enhance the accuracy and robustness of CO_2 emission estimates [7]. Most high-quality observations are concentrated in the Northern Hemisphere, especially between 30°N and 70°N, where the industrial activity is most intensive. In the future, a more uniform global coverage is essential for a comprehensive understanding of carbon cycle dynamics and for supporting climate mitigation strategies [8]. This uneven coverage creates substantial data gaps, especially in polar regions and over the oceans, which play a crucial role in carbon sequestration. This fact limits our understanding of global carbon cycle dynamics. To address these limitations, a scalable cloud-based data storage and visualization tool is imperative for managing the multi-type geospatial data generated from satellite-derived CO_2 flux measurements [9].

Transportation represents one of the most significant sources of anthropogenic CO_2 emissions, contributing nearly a quarter of global energy-related greenhouse gases. Freight road activity alone accounts for a substantial portion of these emissions, approximately 29.4% of all the transport-related carbon output [10]. Accurate monitoring of CO_2 in transport corridors, urban traffic zones, and major logistic hubs is therefore essential for assessing the environmental impact of mobility systems and evaluating the effectiveness of decarbonization policies. Leveraging modern cloud-based solutions can overcome the complex demands of air quality management and policy monitoring by providing advanced tools for environmental monitoring and policy formulation [11]. Satellite-based CO_2 measurements provide valuable large-scale insights into emission patterns from road, air, and maritime transport, complementing ground-based inventories that often lack spatial coverage or temporal consistency. Specifically, satellites like the Orbiting Carbon Observatory-2 offer high-resolution spatiotemporal data of CO_2 concentrations [12].

Global energy consumption is strongly coupled with CO_2 emissions: as the number of IoT devices, deployed for CO_2 monitoring, continues to increase, the associated energy demand likewise increases and is still largely met by fossil-based generation within the current energy mix. These trends motivate the use of hybrid energy-harvesting techniques to enable large-scale sensor networks to operate more sustainably, without further amplifying the carbon footprint of the monitoring infrastructure [13].

In this paper, the development of a cloud-based system, specifically designed for the acquisition and transmission of carbon dioxide data from satellite sources to a custom visualization platform, is detailed. This system leverages Amazon Web Services for its scalable and flexible infrastructure, enabling the robust data processing and monitoring capabilities [14]. The architecture integrates satellite-derived CO_2 measurements, facilitating their secure streaming and storage within the AWS ecosystem [15].

2 Related works

The cloud-based Earth Observation (EO) data processing platforms have evolved significantly to address the challenges of managing and analyzing large-scale satellite datasets. The openEO initiative represents a key advancement in this field, establishing an open API standard that abstracts away infrastructure complexities. Developed within the H2020 project (2017-2020) [16], openEO provides a unified framework for accessing diverse satellite data sources through high-level abstractions that treat image collections as data cubes, enabling scientists to focus on analysis rather than data handling. The Application Programming Interface (API) supports multiple client libraries (Python, R, JavaScript, QGIS) and integrates with existing image analysis services.

Recent studies highlight the growing need for structured data processing architectures to manage the massive volumes of geospatial and satellite information generated by modern EO missions. Romero et al. [17] introduced an ETL-based framework for integrating remote sensing data from multiple satellites, demonstrating a modular architecture that enables extraction, transformation, and loading of heterogeneous data formats (e.g., NetCDF, HDF, GeoTIFF) into unified analytical repositories. Implemented in Python, and compatible with workflow systems, such as Apache Airflow and Dagster, their design facilitates flexible and scalable data fusion across instruments like GOES-16 and CloudSat, though its focus remains primarily on cloud profiling and radiometric data.

Similarly, Boudriki Semlali and El Amrani [18] proposed a hybrid ETL and stream-processing architecture combining the SAT-ETL-Integrator for satellite data preprocessing with the SAT-CEP-Monitor for real-time analysis based on Complex Event Processing (CEP). Their system integrates multisource datasets from NASA, NOAA, and ESA satellites with ground-based observations, performing multi-stage ETL operations and CEP aggregation to compute air-quality indices in near-real time. The approach demonstrated high processing efficiency and strong agreement with ground-based data ($r = 0.75$), underscoring the potential of ETL + CEP frameworks for environmental satellite data analytics.

While these works advance data integration and real-time processing, existing architectures remain limited in handling satellite-based CO_2 column measurements. For example, Boussaada et al. [19] describe a multilayer system architecture comprising *Data Acquisition*, *Data Processing and Communication*, *Data Storage*, and *Application Layer*, that primarily targets ground-based IoT sensors and citizen monitoring.

In contrast, this new approach extends the architectural model with dedicated modules for satellite CO_2 data, including an ETL pipeline, georeferencing, spatio-temporal interpolation, and integration with emission and meteorological models. This design establishes a systematic preprocessing layer for satellite-derived CO_2 datasets, addressing a critical gap in current EO data processing frameworks.

3 Materials and methods

In this section, an innovative and methodological framework for the systematic acquisition, processing, and interactive spreading of the large-scale atmospheric carbon dioxide (CO_2) data was introduced. Conventional approaches often face challenges related to voluminous data transfer, inflexible processing pipelines, and the presentation of findings in static, non-interactive formats. The system presented in this work addresses these limitations by combining a selective data-access mechanism with a modular, high-performance processing pipeline and a dynamic, web-based visualization interface. The research led up to the instantiation of this framework as a web application for visualizing global CO_2 concentrations derived from satellite measurements, thereby demonstrating its efficacy and utility.

The main functions of the data module are the acquisition, processing, analysis, and storage of data from satellite measuring stations. One of the first tasks, therefore, was to find a suitable data source and secure programmatic access to the storage. We designated the Orbiting Carbon Observatory-2 (OCO-2) satellite measuring station as the primary data source. The measured data is stored in a publicly accessible repository managed by the Goddard Earth Sciences Data and Information Services Center (GES DISC) at NASA Goddard Space Flight Center. The data available in the storage facility are at various levels of processing, typically 0 to 4. The proposed application works with level 2 data, which are mapped to the relevant latitude and altitude and contain error indicators that specify whether the data are suitable for use. Two types of data products are the most suitable for processing: L2 Standard and L2 Lite FP. The L2 Standard data product is usually available one to two days after the measurement itself, but only for the current calendar year. The L2 Lite FP represents condensed data files that have undergone more thorough correction. Those files have been available approximately one month after the measurement itself since 2014. In this case, one data file represents one day, which allows for easier processing compared to L2 Standard files. In the proposed application, L2 Standard data was selected for daily downloads of new data and L2 Lite FP for downloading historical data.

There are several ways to access data. For the purposes of the proposed application, the OPeNDAP (Open-source Project for a Network Data Access Protocol) protocol was chosen. This is an open protocol for accessing data files based on http technology [20]. This protocol allows only selected variables of data files to be downloaded in NetCDF format, which makes it possible to work with a much smaller volume of data, resulting in less network load and faster processing. On the data provider side, the OPeNDAP protocol uses Hyrax server software with support for THREDDS catalogs [21]. The THREDDS catalogs are XML files that organize and describe data files and folders in the repository, making it possible to navigate the repository folders and find the desired files by date [22]. The storage has a root folder with a fixed address. The root folder, like all others, contains a catalog with a list of files, their address for access via the OPeNDAP protocol, and a list of nested folders. Access to data files depends on the selected type of data product, L2 Standard or L2 Lite FP. The folder structure and file naming are different in both cases. The program must be designed to work with both cases. The application must also include a function that works with these catalogs. The following flowchart shows the process of obtaining the addresses of the required data files from the THREDDS catalog.

The Requests library is employed to access the data repository, as it provides essential authentication support and significantly simplifies interface for working with HTTP protocol compared to Python's standard library. The retrieved data files must subsequently be converted to DataFrame objects implemented by the Pandas library. A DataFrame is a highly efficient data structure specifically designed for tabular data, rigorously supports critical operations such as filtering, such as filtering, aggregations and statistical operations. Pandas itself is a high-level data manipulation library, primarily engineered for advanced data analysis tasks. Its core components are implemented in the C programming language, which ensures high performance, while maintaining the simplicity and flexibility of Python.

After the processing and analysis, the obtained and transformed data need to be stored in a persistent storage system. Several storage options were designed for the needs of the application, such as CSV file stored on a local disk or Parquet file stored on a network-accessible data repository.

The first option, a CSV file on the local disk, is primarily intended for local testing, as CSV files are text based and human readable without requiring specialized software. In contrast, the Parquet files are binary and not directly readable without required tools, however, they provide higher efficiency for reading and writing operations and require less disk space. They are, therefore, more suitable for cloud storage environments.

For the data processing, the Extract, Transform, Load (ETL) process was adopted. This process consists of three main phases: extraction, transformation, and loading of the data.

The extraction phase involves acquiring data from one or more internal or external sources that may contain structured or unstructured data. It includes the initial validation of received data, ensuring that they are in the correct format and structure. During the transformation phase, various functions and rule sets are applied to the data, including filtering, filling in missing values, aggregation, and merging. The loading phase refers to storing the processed data in internal storage, which may include a file system, database, or data warehouse. All acquired data are stored to enable subsequent analysis.

Within this process, a function for analyzing the newly acquired and cleaned data is also executed. During this analysis phase, various aggregations and computations of supplementary information are performed, operations that would be inefficient to execute during each visualization. The analyzed data are likewise stored in the internal storage for further use. In addition, the processed data are continuously supplied to external machine learning model using the provider interface for further analysis and predictions.

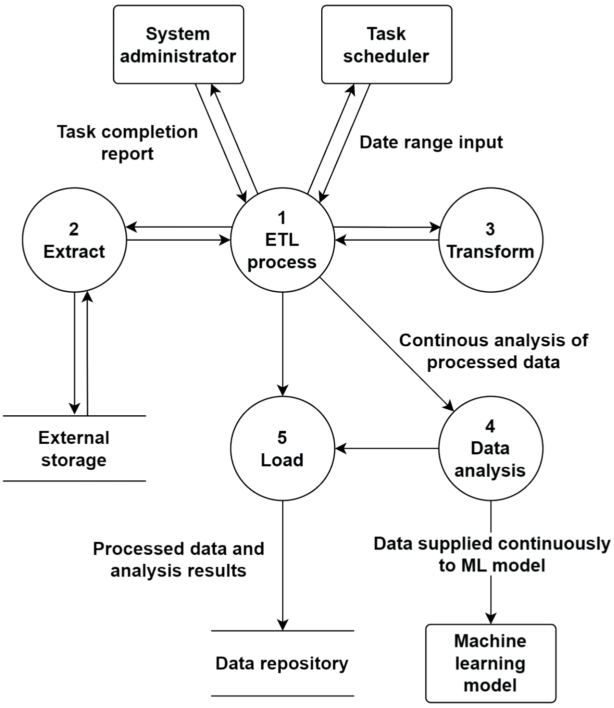

Figure 1 *Data Flow Architecture of the ETL Pipeline with integrated Data Analysis Module*

Figure 1 illustrates the main components and interactions within the ETL workflow. The central ETL process receives user-defined inputs through the task scheduler and system administrator, which trigger extraction, transformation, and loading operations. The Extract module retrieves raw data from external storage, while the Transform module performs preprocessing and normalization of the extracted datasets. The processed data is then passed to the Data analysis component, which is connected to the machine learning model and subsequently stored in the database through the *Load module*. Feedback on the task completion is returned to the system administrator, ensuring the controlled execution and monitoring of the ETL pipeline.

Figure 2 illustrates the class diagram of the application's data module. The entire ETL process is managed by the ETL Pipeline class through the dependencies *extract_strategy* and *load_strategy*, which are provided to the ETL Pipeline object via its constructor, depending on the configuration of the runtime environment. The data module was designed in accordance with the principles of object-oriented programming: abstraction, encapsulation, polymorphism, and inheritance.

The abstract class *BaseExtracto*r provides a basic interface for the data acquisition. The method *extract_date_range* accepts a date range as its parameter specifying the period for which data should be downloaded, and returns a pair consisting of the date and a DataFrame object. The actual implementation of data retrieval is encapsulated within concrete subclasses.

The TestExtractor class represents the straightforward implementation of the abstract BaseExtractor class, operating without access to real online data. It returns a *DataFrame* object supplied through the constructor and is used exclusively for automated testing purposes. This allows testing of the ETL Pipeline logic with controlled input data and without the need for an internet connection.

The abstract class *BaseOpendapExtractor* overrides the constructor of *BaseExtractor* by introducing a mandatory parameter, *opendap_client*, of type *OpendapClient*. The *OpendapClient* class defines and implements a simple interface for communication with a server via the OPeNDAP protocol and for interaction with the THREDDS catalog.

The classes *OpendapExtractor_L2Standard* and *OpendapExtractor_L2LiteFP* implement access to the actual data repository, managing authentication against the storage system and searching for files based on the specified date range.

The abstract class *BaseLoader* provides the fundamental interface for the data storage. The method save_dataframe accepts a parameter of type *DataFrame* and a desired filename, which it saves to persistent storage. Conversely, the method retrieve_dataframe accepts the name of the file to be opened and returns a *DataFrame* object. The retrieve_dataframe method is also utilized in the design of the application's visualization module. The implementation of the data storage operations is encapsulated within individual concrete subclasses.

The *TestLoader* class represents the implementation of the abstract *BaseLoader* class, operating without the use of a database system or file storage. It works exclusively with a *DataFrame* object in system memory,

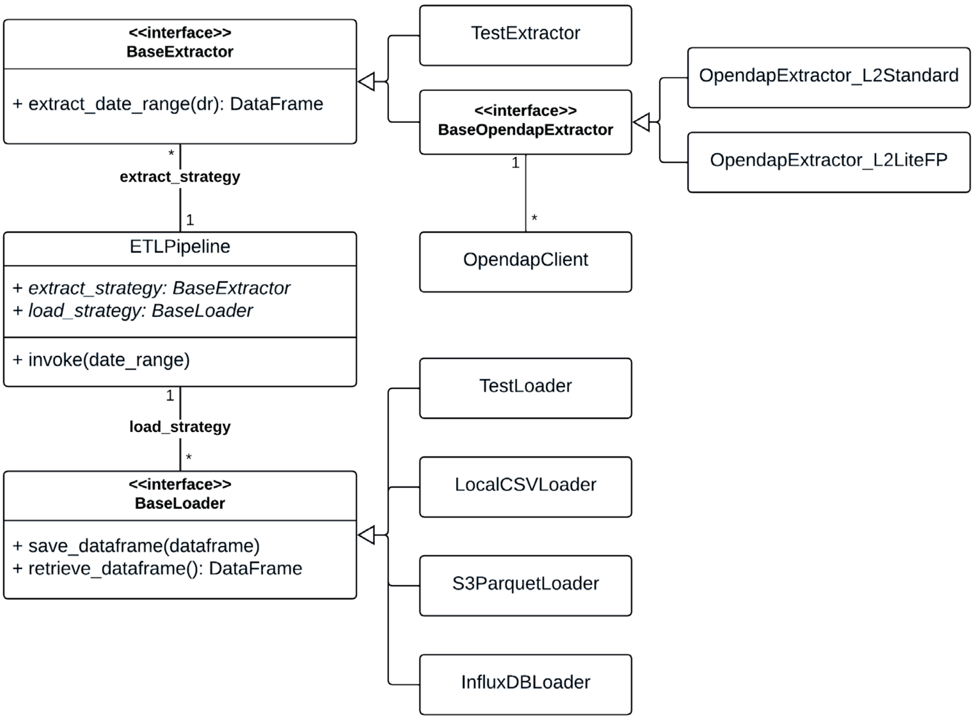

Figure 2 *Class diagram of the data module for application*

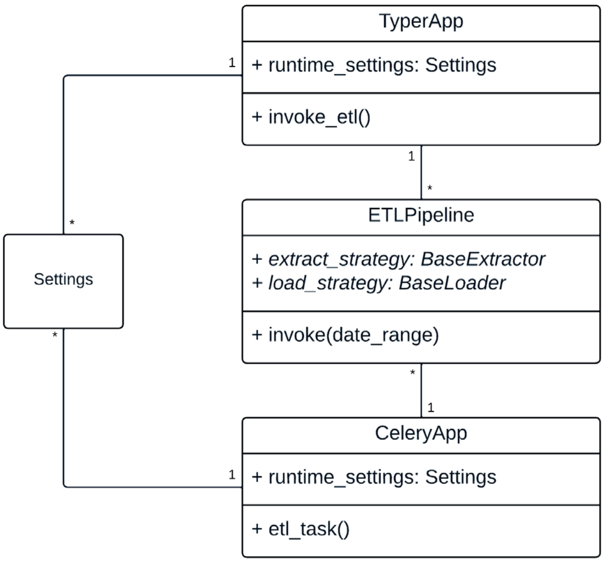

Figure 3 *Class diagram of data module for application with ETL Pipeline*

allowing testing of the ETLPipeline logic without the overhead of time-consuming data storage operations.

The *LocalCSVLoader* class stores the provides *DataFrame* object as a CSV file on disk and retrieves data only from that file. It is primarily intended for local testing of the application.

The *S3ParquetLoader* class stores the provides *DataFrame* object as a Parquet file in a data repository. The design assumes the use of Amazon Web Services (AWS) S3 storage, as the application is intended to be deployed in the AWS environment. This storage system supports file versioning. When a file is overwritten, its previous version is preserved and can be restored in cases such as data corruption. Therefore, the implementation of *S3ParquetLoader* also requires an interface for accessing the S3 storage.

The ETL Pipeline class itself provides a minimal interface, exposing only the invoke function, which initiates the process and manages the provided concrete dependencies. The design follows the Dependency Injection pattern, in which an object receives its dependencies externally rather than creating them

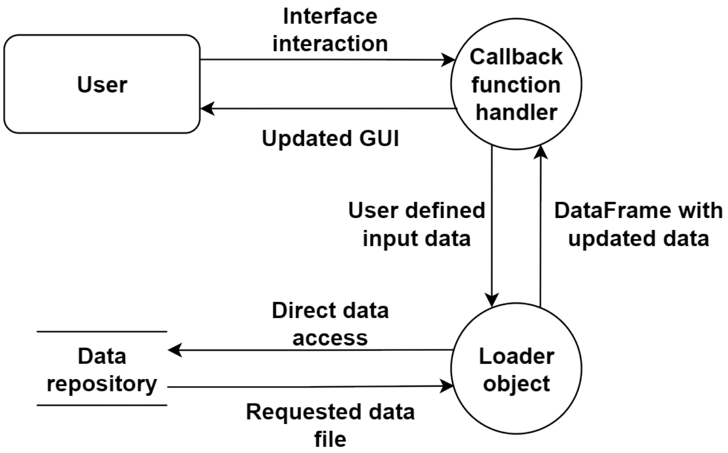

Figure 4 *Class diagram of data module for application with ETL Pipeline*

internally. Injecting dependencies that implement a common interface into the controller class allows the replacement of components at runtime without modifying the controller's source code. The ETL process in the application can be initiated from two sources: the Command-Line Interface (CLI) or a task scheduler. The CLI interface is managed by the Typer library, which simplifies the definition and parsing of command parameters. This allows for selection of a specific subclass of type BaseExtractor at the moment the command is executed. The function called by the command invoke-etl is defined in Figure 3. The pipeline_factory function supplements the required dependencies and returns an ETLPipeline object ready for execution. The example code below illustrates the *invoke_etl* function, which is triggered by the invoke-etl command within the CLI environment. Besides specifying the input dates, the user can also select the class used for data extraction.

Another method of triggering the ETL process is through a task scheduler. For this purpose, the Celery library is deployed, which enables the execution of scheduled and background tasks within the application. The configuration file defines the schedule read by Celery at startup. The schedule includes a single task, *daily_etl_task_L2_Standard*, which runs daily at 06:00, along with the definition of the task itself. The provided code snippet represents the Celery configuration, including the setup of periodic task scheduling.

3.1 Visualization module design

The main function of the visualization module is to display the results of data analysis to the user in the form of a web interface. Consequently, it is necessary to select appropriate software libraries for implementing an HTTP server and for generating and rendering various types of plots. For this purpose, the Dash and Plotly libraries were chosen. Both are open-source software libraries developed by Plotly Technologies Inc. and are freely available. They provide a simple interface for working with graphical visualizations and offer seamless mutual integration.

An application built using the Dash library functions as a lightweight web interface that listens on a predefined port, processes the HTTP requests, and returns responses. The user interface (UI) is defined using Python code. The library includes an html module, whose classes are translated at runtime into the corresponding HTML elements. Objects of these html classes are inserted into the application's layout attribute along with their properties. Based on this declarative structure, the corresponding HTML user interface is generated automatically.

The library provides a variety of interactive components, such as buttons and forms, which can be utilized in the application's design. Interaction with these elements is linked to specific application functions through unique element identifiers. Such a function is referred to as a callback and governs the modification of one or more HTML elements in response to user interaction - for example, re-rendering graphs with updated data when the user changes the selected date range. The design of these callback functions should follow the functional programming paradigm, meaning that they should not modify the internal state of the application but instead return output based only on input parameters.

The visualization components of the user interface are rendered using the Plotly library, which supports a wide range of chart types, including bar charts, line charts, maps, and correlation diagrams. Plotly functions accept *DataFrame* objects as their primary data source, allowing direct integration with the *BaseLoader* objects introduced in the previous section for data access.

Figure 4 presents a conceptual data flow diagram, illustrating the user interaction with the graphic user interface and sequential data processing components. The callback function handler accepts the input and calls the loader object for updated data. Loader object plays an intermediary role between the callback handler and a data repository. Such architecture allows for

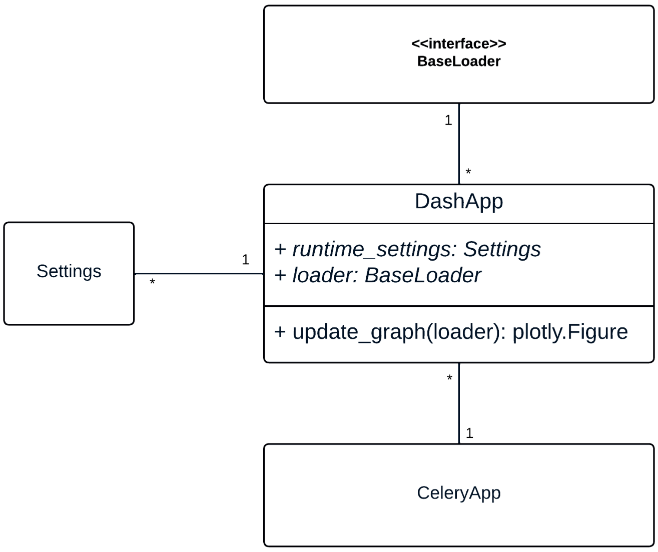

Figure 5 *Class diagram for the visualization module of application*

various persistent storage implementations. Loader then fulfills the query and passes the data to the callback handler, which then updates the graphic user interface accordingly.

A function that responds to user interaction must repeatedly establish connections to the database or the local file system and query large volumes of data. Consequently, situations may arise in which the response time exceeds the default timeout settings of the web server or the user's browser. Furthermore, a large number of long running calls could potentially overload all threads of the web application process. To mitigate these issues, background execution is employed.

Upon user interaction, the interactive input elements are temporarily disabled, and the execution request is placed into a dedicated task queue. Once the task is completed, the relevant element of the user interface is updated accordingly. The task queue management and sequential execution of commands are handled by the Celery library, which also serves as a task scheduler in the application's data module.

Figure 5 presents the class diagram of the application's visualization module. The abstract class *BaseLoader*, similar to its counterpart in the data module, provides an interface for loading data from a database or local disk. A specific implementation object is injected as a dependency into the *update_graph* function. This dependency injection design allows for the *update_graph* function logic to be tested without requiring an active database connection. As in the data module, a Settings class is also used and injected as a dependency during the application's startup.

Figure 6 displays a system architecture diagram with the technologies used to support the system. The application integrates external data sources from NASA GES DISC, including the OCO-2 L2 LITE FP and OCO-2 L2 STANDARD datasets. Those datasets are accessed through THREDDS Catalogue and OPENDAP NetCDF4 services.

The core of the architecture is Celery, a distributed task queue that operates as a worker to handle scheduled tasks for the data processing module. Data is stored in AWS S3 cloud storage and structured using Apache Parquet for optimal performance and accessibility. The Plotly App serves as the user interface, facilitating initial data preload and user interactions. Celery‘s callback functions are specifically used to respond to user interface requests, enabling seamless communication between the data processing module and the user interface. Redis is employed for caching and message brokering, enhancing system performance and responsiveness. Additionally, a machine learning service provider is integrated to supply the advanced analytics and enhance data analysis capabilities. This architecture emphasizes the seamless flow of data from external sources through processing and storage to user interaction, leveraging the robust open-source technologies to support environmental data processing and distribution.

4 Results

After the deployment, the application operated as expected. It downloaded the new data daily from the L2 Standard data product, provided that the data were available. If no data were accessible, the application reported an error, which was automatically communicated to the system administrator via the Sentry monitoring service. For historical data dating back to the beginning of 2023, the L2 Lite FP data product was utilized. Although those data were uploaded to storage with a monthly delay, they were of higher quality and underwent more rigorous validation procedures.

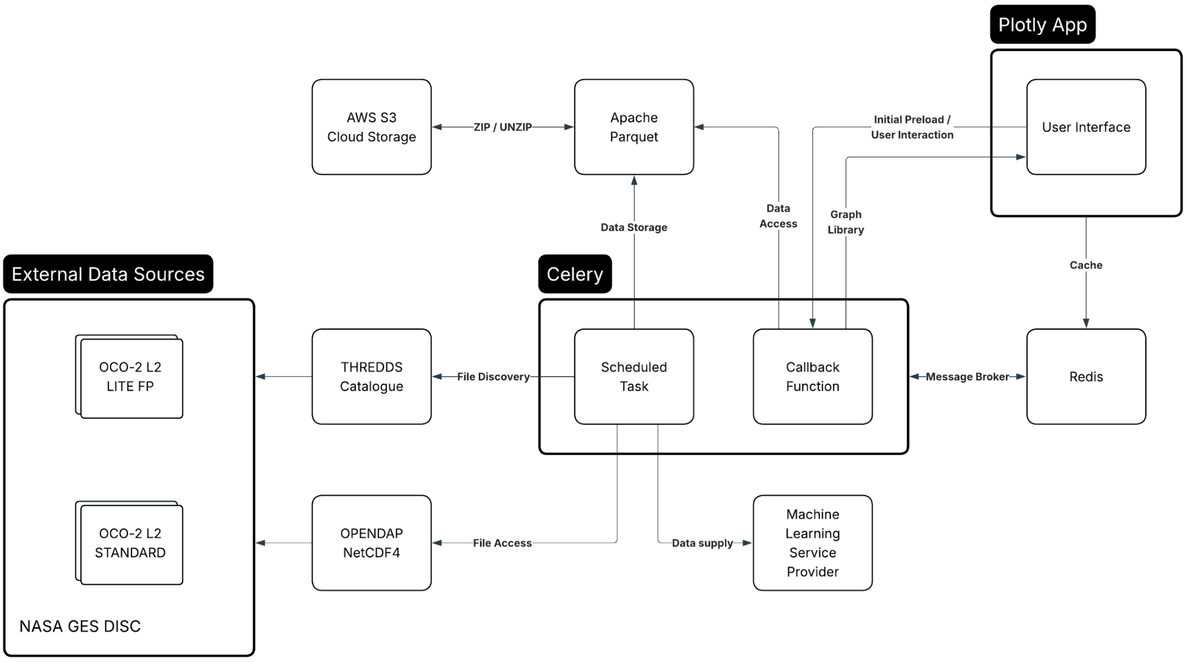

Figure 6 *The class diagram for GUI module of application*

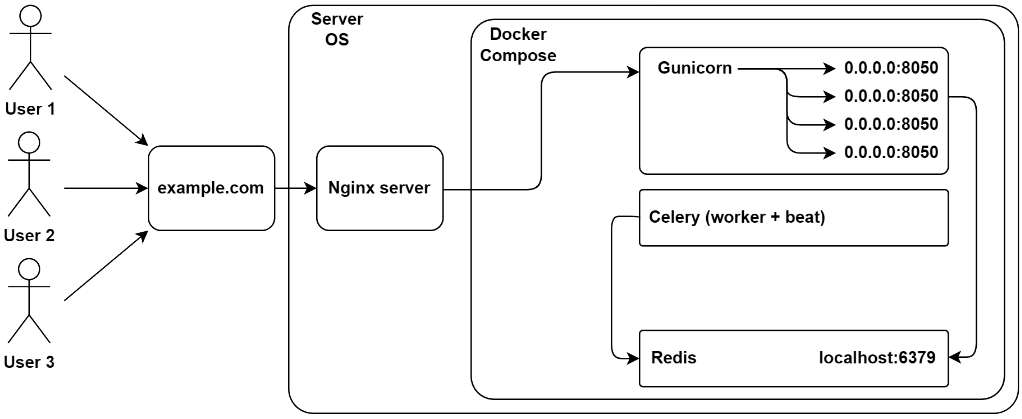

Figure 7 *System architecture of the container-based deployment environment*

The spatial resolution of the satellite sensors is 2.25 km × 1.29 km. Consequently, the acquired data can also be used for analyses of smaller geographic regions, provided that sufficient satellite coverage is available. A preliminary analysis of the dataset indicates that the satellite-based measurements closely follow the trends observed in ground-based monitoring stations, including seasonal variations and hemispheric extremes. Furthermore, the dataset enables the observation of global trends and anomalies, as well as the identification of sources, sink regions, and regional variations in atmospheric carbon dioxide concentration throughout the year.

The use of satellite data has also made it possible to isolate the CO_2 concentration values over the territory of Slovakia, a region where no open access ground-based measurement stations are available. These data can be employed for the more complex analyses of regional and global trends or for predictive modeling; however, such analyses are typically conducted in conjunction with meteorological and other complementary models.

Figure 7 illustrates the cloud-based deployment of the ETL and data processing services using Docker Compose. Incoming HTTP requests are routed through an Nginx reverse proxy running on the host operating system. The proxy forwards the requests to a Gunicorn application server that handles multiple worker instances on port 8050. The background data processing tasks are managed by a Celery service (worker and scheduler), which interacts with two supporting components: All the components run as Docker containers orchestrated within a single server environment, ensuring scalability, modularity, and fault isolation across services.

The examples in Figures 8 and 9 show the user interface of application for the two different user-

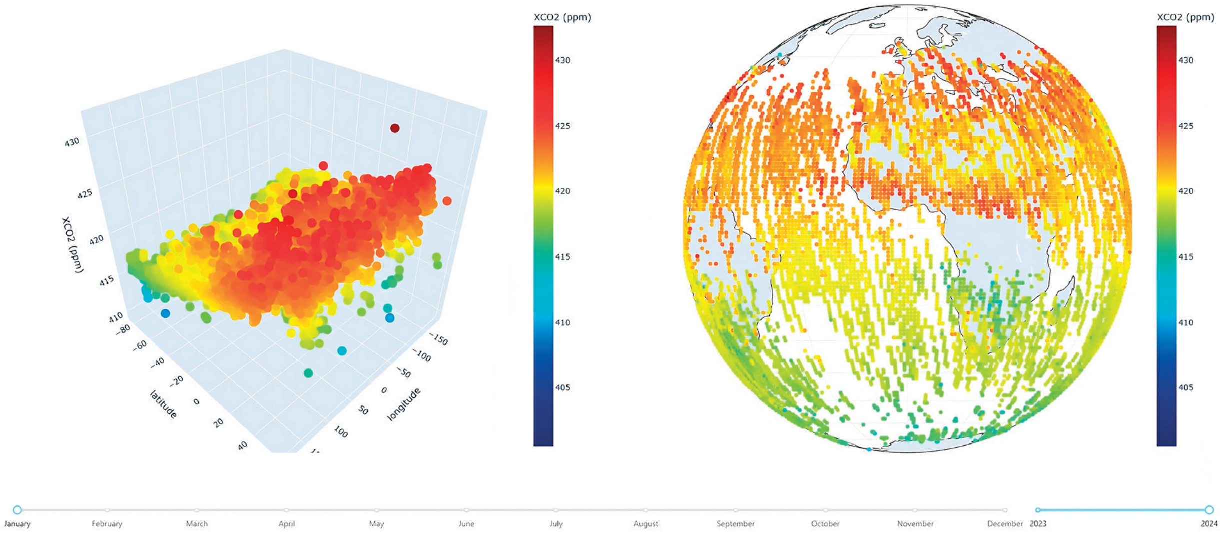

Figure 8 *Graph and visualization for average monthly values - January 2024*

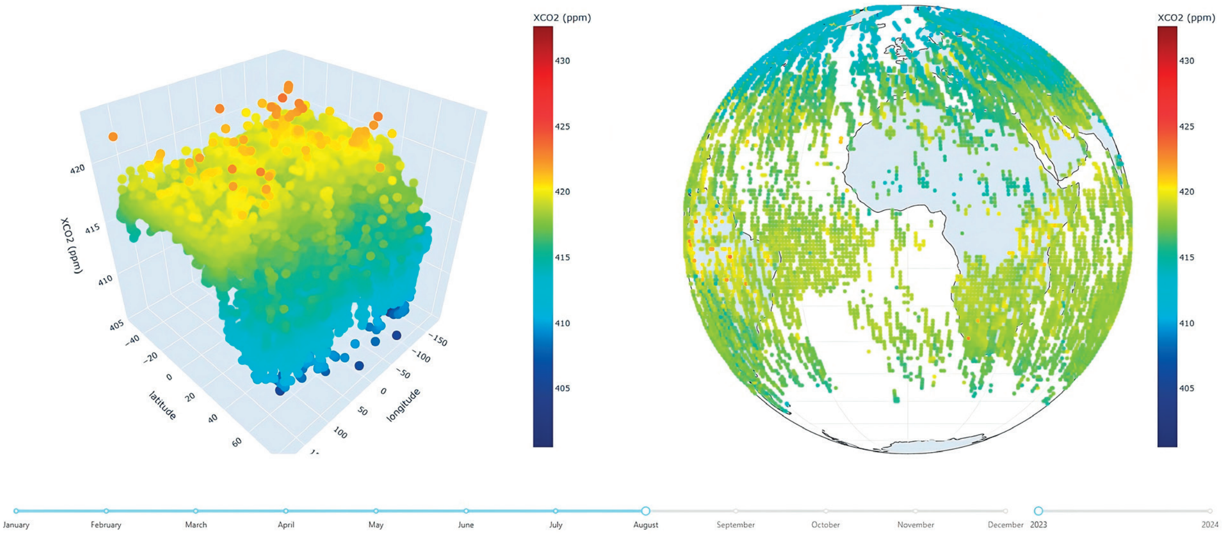

Figure 9 *Graph and visualization for average monthly values - October 2023*

selected datasets. For each selection, the visual outputs are updated dynamically to the chosen time period, enabling direct comparison of spatial and temporal variations in atmospheric CO_2 using both the 3D scatter plots and global map projections.

The left-hand panels of Figures 8 and 9 present the 3D scatter plots of mean XCO_2, the column-averaged dry-air mole fraction of atmospheric CO_2, as a function of latitude (x-axis) and longitude (y-axis) for January 2024 and October 2023 respectively. Each marker corresponds to the average of XCO_2 value per degree of latitude and one degree of longitude. Marker color follows the adjacent color bar (ppm) and encodes the same XCO_2values shown on the vertical axis - warmer colors indicate higher concentrations. Since the plot projects many closely spaced retrievals, regional gradients are best read by following the color and height trends across latitude/longitude ranges rather than individual markers. This representation effectively captures the spatial structure of the XCO_2 field and highlights broad geographic variations.

The right-hand panel shows the corresponding global map projection for the same month and uses the identical color scale and marker values, emphasizing the spatial variability and regional patterns for the same period. Regions without colored symbols correspond to areas where no OCO-2 satellite measurements were available for the selected month. A common color scale (ppm) is applied to both panels to ensure consistent comparison of concentration levels. When considered together, the 3D scatter plots and global map projections provide complementary perspectives on the distribution and magnitude of observed XCO_2. Both panels incorporate interactive functionality that enables detailed exploration of localized spatial patterns. This integrated visualization framework provides a compact, interactive environment for data exploration, anomaly detection, and trend analysis, without the need for extensive preprocessing or specialized external visualization tools.

5 Discussions

The results indicate that the automated ingestion of OCO-2 Level 2 Standard and Level 2 Lite FP products, facilitated by the OPeNDAP protocol, ensures dependable access to high-resolution atmospheric CO_2data while concurrently minimizing data transfer overhead. This selective data retrieval mechanism, synergistically integrated with the ETL pipeline, decreases the latency between the data availability and its subsequent visualization. In contrast to alternative solutions, such as openEO or SAT-CEP-Monitor, which primarily emphasize interoperability or event processing, the proposed framework distinguishes itself by prioritizing modularity and maintainability within a cohesive cloud environment. Consequently, this design renders the framework suitable for sustained deployment, integration with prospective satellite missions, and the potential for synergistic fusion with ground-based observational data.

The implemented visualization module, built with Dash and Plotly, provides an intuitive interface for the real-time analysis, offering users the ability to examine both global and regional CO_2 patterns. The ability to isolate the CO_2 concentrations over specific territories, demonstrates the adaptability of the system even in regions without open-access in-situ monitoring stations. This highlights the framework's potential to fill the observational gaps and to support environmental research in countries with limited measurement infrastructure.

Despite its advantages, several limitations must be acknowledged. The system's performance depends on the availability and quality of satellite data, which may vary due to orbital coverage, atmospheric conditions, or latency in dataset publication. Furthermore, while the AWS-based deployment ensures scalability, the long-term sustainability could benefit from cost optimization strategies or the adoption of hybrid cloud-edge architectures. The current model also primarily focuses on CO_2 data. Extending it to include other greenhouse gases, such as CH_4 or NO_2, would improve its utility for comprehensive climate monitoring.

6 Conclusion

In this paper are presented the design and implementation of a modular, cloud-based information system for automatic acquisition, processing, and visualization of satellite-derived CO_2 data. The system combines the OCO-2 Level 2 Standard and Level 2 Lite FP products into an ETL pipeline using the OPeNDAP protocol, is deployed on AWS, and offers an interactive web interface for exploring global and regional XCO_2 distributions, including areas without in-situ monitoring.

The main contribution of this study is a unified framework that combines a scalable ETL architecture, modular software design, cloud-native deployment, and advanced visualization. The ETL pipeline extracts only the essential variables from the large NetCDF files, reducing the data transfer and processing time, while maintaining native spatial resolution. A modular, object-oriented design with clearly defined extractor and loader interfaces simplifies testing, maintenance, and adaptation to new data sources or storage back ends. Additionally, a containerized deployment with an interactive Dash/Plotly interface enables the 3D scatter plots and global map projections for detailed analysis of spatial and temporal XCO_2 patterns, even in regions lacking ground observations.

Several limitations must be recognized. The quality and completeness of outputs depend on the availability and latency of OCO-2 products, which are affected by orbital coverage, cloud interference, and publication delays. Relying solely on AWS introduces potential long-term costs and vendor lock-in risks for sustained, high-volume operations. Methodologically, the system currently emphasizes descriptive visualization of CO_2 only, and has not yet integrated the data fusion with other greenhouse gases, meteorological data, or ground-based observations, nor implemented advanced uncertainty quantification.

Future work will expand the framework to include additional satellite missions and trace gases such as CH_4 and NO_2, incorporate external atmospheric and emission models, and systematically validate satellite-based indicators against the in-situ networks. it is also planned to leverage the existing integration points for machine-learning services to enable automated pattern recognition, anomaly detection, and predictive analytics for applications such as transport corridors and industrial regions. Finally, the user experience and computational performance under realistic workloads would be assessed, to further optimize the system for decision support in environmental monitoring, transportation, and industrial informatics.

Acknowledgements

Funded by the EU NextGenerationEU through the Recovery and Resilience Plan for Slovakia under the project No. 09I03-03-V04-00562.

Conflicts of interest

The authors declare that they have no known competing financial interests or personal relationships that could have appeared to influence the work reported in this paper.

References

[1] SELTENRICH, N. A Satellite view of pollution on the ground: long-term changes in global nitrogen dioxide. *Environmental Health Perspectives* [online]. 2016, **124**(3), A56 [accessed 2025-11-20]. ISSN 0091-6765, eISSN 1552-9924. Available from: https://doi.org/10.1289/ehp.124-A56

[2] HAKKARAINEN, J., IALONGO, I., KOENE, E., SZELĄG, M. E., TAMMINEN, J., KUHLMANN, G., BRUNNER, D. Analyzing local carbon dioxide and nitrogen oxide emissions from space using the divergence method: an application to the synthetic SMARTCARB dataset. *Frontiers in Remote Sensing* [online]. 2022, **3**, 878731 [accessed 2025-11-20]. eISSN 2673-6187. Available from: https://doi.org/10.3389/frsen.2022.878731

[3] KUHLMANN, G., HENNE, S., MEIJER, Y., BRUNNER, D. Quantifying CO_2 emissions of power plants with CO_2 and NO_2 imaging satellites. *Frontiers in Remote Sensing* [online]. 2021, **2**, 689838 [accessed 2025-10-19]. eISSN 2673-6187. Available from: https://doi.org/10.3389/frsen.2021.689838

[4] CAJOVA KANTOVA, N., BELANY, P., HOLUBCIK, M., CAJA, A. Energy consumption depending on the durability of pellets formed from sawdust with an admixture of FFP2 masks. *Energies* [online]. 2022, **15**(13), 4813 [accessed 2025-10-28]. eISSN 1996-1073. Available from: https://doi.org/10.3390/en15134813

[5] LIN, X., VAN DER A, R., DE LAAT, J., ESKES, H., CHEVALLIER, F., CIAIS, P., DENG, Z., GENG, Y., SONG, X., NI, X., HUO, D., DOU, X., LIU, Z. Monitoring and quantifying CO2 emissions of isolated power plants from space. *Atmospheric Chemistry and Physics* [online]. 2023, **23**(11), p. 6599-6611 [accessed 2025-10-15]. ISSN 1680-7375, eISSN 1680-7324. Available from: https://doi.org/10.5194/acp-23-6599-2023

[6] DIMDORE-MILES, O. B., PALMER, P. I., BRUHWILER, L. P. Detecting changes in Arctic methane emissions: limitations of the inter-polar difference of atmospheric mole fractions. *Atmospheric Chemistry and Physics* [online]. 2018, **18**(24), p. 17895-17907 [accessed 2025-10-29]. ISSN 1680-7375, eISSN 1680-7324. Available from: https://doi.org/10.5194/acp-18-17895-2018

[7] BLACKHURST, M., MATTHEWS, H. S. Comparing sources of uncertainty in community greenhouse gas estimation techniques. *Environmental Research Letters* [online]. 2022, **17**(5), 053002 [accessed 2025-10-15]. ISSN 1748-9326. Available from: https://doi.org/10.1088/1748-9326/ac6084

[8] LIU, F., DUNCAN, B. N., KROTKOV, N. A., LAMSAL, L. N., BEIRLE, S., GRIFFIN, D., MCLINDEN, C. A., GOLDBERG, D. L., LU, Z. A methodology to constrain carbon dioxide emissions from coal-fired power plants using satellite observations of co-emitted nitrogen dioxide. *Atmospheric Chemistry and Physics* [online]. 2020, **20**(1), p. 99-116 [accessed 2025-10-15]. ISSN 1680-7375, eISSN 1680-7324. Available from: https://doi.org/10.5194/acp-20-99-2020

[9] WU, S., YAN, Y., DU, Z., ZHANG, F., LIU, R. Spatiotemporal visualization of time-series satellite-derived CO2 flux data using volume rendering and GPU-based interpolation on a cloud-driven digital earth. *ISPRS Annals of the Photogrammetry, Remote Sensing and Spatial Information Sciences* [online]. 2017, **IV-4/W2**, p. 77-85 [accessed 2025-10-11]. ISSN 2194-9042, eISSN 2194-9050. Available from: https://doi.org/10.5194/isprs-annals-IV-4-W2-77-2017

[10] YAVARI, A., MIRZA, I. B., BAGHA, H., KORALA, H., DIA, H., SCIFLEET, P., SARGENT, J., TJUNG, C., SHAFIEI, M. ArtEMon: artificial intelligence and internet of things powered greenhouse gas sensing for real-time emissions monitoring. *Sensors* [online]. 2023, **23**(18), 7971 [accessed 2025-11-05]. eISSN 1424-8220. Available from: https://doi.org/10.3390/s23187971

[11] RUSHTON, C. E., TATE, J. E., SJODIN, A. A modern, flexible cloud-based database and computing service for real-time analysis of vehicle emissions data. *Urban Informatics* [online]. 2025, **4**(1), 1 [accessed 2025-10-17]. eISSN 2731-6963. Available from: https://doi.org/10.1007/s44212-024-00066-4

[12] CAI, K., GUAN, L., LI, S., ZHANG, S., LIU, Y. Full-coverage estimation of CO2 concentrations in China via multisource satellite data and Deep Forest model. *Scientific Data* [online]. 2024, **11**(1), 1231 [accessed 2025-10-29]. eISSN 2052-4463. Available from: https://doi.org/10.1038/s41597-024-04063-9

[13] OTHMAN, A., HRAD, J., HAJEK, J., MAGA, D. Control strategies of hybrid energy harvesting - a survey. *Sustainability* [online]. 2022, **14**(24), 16670 [accessed 2025-10-28]. eISSN 2071-1050. Available from: https://doi.org/10.3390/su142416670

[14] TANIMOTO, H., MATSUNAGA, T., SOMEYA, Y., FUJINAWA, T., OHYAMA, H., MORINO, I., YASHIRO, H., SUGITA, T., INOMATA, S., MÜLLER, A., SAEKI, T., YOSHIDA, Y., NIWA, Y., SAITO, M., NODA, H., YAMASHITA, Y., IKEDA, K., SAIGUSA, N., MACHIDA, T., FREY, M. M., LIM, H., SRIVASTAVA, P., JIN, Y., SHIMIZU, A., NISHIZAWA, T., KANAYA, Y., SEKIYA, T., PATRA, P., TAKIGAWA, M., BISHT, J., KASAI, Y., SATO, T. O. The greenhouse gas observation mission with Global Observing SATellite for Greenhouse gases and Water cycle (GOSAT-GW): objectives, conceptual framework and scientific contributions. *Progress in Earth and Planetary Science* [online]. 2025, **12**(1), 8 [accessed 2025-10-28]. eISSN 2197-4284. Available from: https://doi.org/10.1186/s40645-025-00684-9

[15] JANAIRO, A. G., CONCEPCION, R., GUILLERMO, M., FERNANDO, A. A Cloud computing framework for space farming data analysis. *AgriEngineering* [online]. 2025, **7**(5), 149 [accessed 2025-10-28]. eISSN 2624-7402. Available from: https://doi.org/10.3390/agriengineering7050149

[16] SCHUMACHER, B., GRIFFITHS, P., PEBESMA, E., DRIES, J., JACOB, A., THIEX, D., MOHR, M., BRIESE, C. openEO Platform - showcasing a federated, accessible platform for reproducible large-scale Earth Observation analysis. In: EGU General Assembly 2023: abstracts [online]. 2023. EGU23-8526 [accessed 2025-10-25]. Available from: https://doi.org/10.5194/egusphere-egu23-8526

[17] ROMERO JURE, P. V., CABRAL, J. B., MASUELLI, S. ETL for the integration of remote sensing data. In: Argentine Symposium on Images and Vision / Simposio Argentino de Imagenes y Vision (SAIV 2023) - JAIIO 52: proceedings [online]. 2023 [accessed 2025-10-22]. Available from: http://sedici.unlp.edu.ar/handle/10915/165724

[18] SEMLALI, B.-E. B., AMRANI, C. E., ORTIZ, G., BOUBETA-PUIG, J., GARCIA-DE-PRADO, A. SAT-CEP-monitor: An air quality monitoring software architecture combining complex event processing with satellite remote sensing. *Computers and Electrical Engineering* [online]. 2021, **93**, 107257 [accessed 2025-10-26]. ISSN 0045-7906, eISSN 1879-0755. Available from: https://doi.org/10.1016/j.compeleceng.2021.107257

[19] SEMLALI, B.-E. B., AMRANI, C. E. A Stream processing software for air quality satellite datasets. In: Advanced Intelligent Systems for Sustainable Development (AI2SD'2020). KACPRZYK, J., BALAS, V. E., EZZIYYANI, M. (Eds.). Cham: Springer International Publishing, 2022. ISBN 978-3-030-90633-7, p. 839-853. Available from: https://doi.org/10.1007/978-3-030-90633-7_71

[20] OPeNDAP at American Geophysical Union (AGU) 2024 - OPeNDAP [online] [accessed 2025-11-20]. Available from: https://www.opendap.org/opendap-at-american-geophysical-union-agu-2024/

[21] OPeNDAP at American Geophysical Union (AGU) 2023 - OPeNDAP [online] [accessed 2025-11-20]. Available from: https://www.opendap.org/opendap-at-american-geophysical-union-agu-2023/

[22] University Corporation for Atmospheric Research [online] [accessed 2025-10-27]. Available from: https://www.ucar.edu/

PROPOSAL FOR THE ELECTRIC VEHICLE DRIVE SIMULATOR CONFIGURATION - CASE STUDY AND SIMULATION MODELLING

Ján Markovič, Pavol Špánik, Michal Frivaldský*

Department of Mechatronics and Electronics, Faculty of Electrical Engineering and Information Technologies, University of Zilina, Zilina, Slovakia

*E-mail of corresponding author: michal.frivaldsky@uniza.sk

Michal Frivaldský 0000-0001-6138-3103

Resume

Road traffic remains a major contributor to carbon dioxide emissions, making innovative energy solutions essential. Electric vehicles (EVs) offer a promising alternative, however, current lithium-ion batteries face limitations in power output, energy density, and cost. To address these challenges, hybrid energy storage systems (HESS) combine batteries for energy storage with supercapacitors for rapid power delivery. In this study was explored an optimization tool for EV operation using HESS configurations and evaluates performance through MATLAB Simulink simulations across various driving cycles. The results highlight trade-offs between the performance, weight, and cost, which vary by vehicle class. While HESS improves energy efficiency and extends battery life, its complexity and expense limit feasibility for medium and high-class vehicles. Lower-class vehicles benefit most from this approach. Ultimately, tailored HESS designs adapted to specific driving conditions can enable more sustainable and efficient electric vehicles.

Article info

Received 1 September 2025
Accepted 4 December 2025
Online 16 January 2026

Keywords:

electric drive
simulator
hybrid energy storage system
modeling

Available online: https://doi.org/10.26552/com.C.2026.014

ISSN 1335-4205 (print version)
ISSN 2585-7878 (online version)

1 Introduction

Research in the actual extensive electrification of transport infrastructure calls for improvement suggestions and verification of gathered data, further improving the potential of the implementation of electrical vehicles (EVs) and confirm the proposed solutions. It is a vital part of the continuous EVs development since their implementation in transportation structure. Limitations of the EV body construction narrows down usable space for the powerline system, consisting mainly of large volume battery pack and driveline, electrical machines (EMs). Adequate sizing of the energy storage system (ESS) and EMs is critical, as it directly contributes to the final performance levels of the EV. Capacity of the ESS, directly tied to the potential drive range, is limited by its size [1-3].

To obtain the required parameters, calculations and simulations with real time driving scenarios, drive cycles, are done. The drive cycle evaluates the performance of the EV through the defined map, which states acceleration, braking, standing and cruising segments in time. It is defined by change of the vehicle speed through time [1, 4]. Implementation of described benchmark done by drive cycle poses as an experimental method, which is able to optimize parameters of the powertrain system, formulating improved performance and energy consumption [5-7].

Recent researches in HESS designs implemented in EVs indicate improved characteristics in simulated operation of the vehicle during the drive cycle experiments. Researchers implemented two types of HESS systems, single and dual HESS. Experiments have been done in computer simulations, achieving numerous data results, which have been analyzed and compared. Dual HESS systems have been utilized for minimalizing battery discharge peaks by splitting vehicle's traction power demand between the two independent traction systems, while each one was powered by HESS system. Optimized dual HESS configuration in EV reached increased driving range, battery storage life compared to the single HESS configuration, presenting a better configuration in long term operation of a vehicle. Comparison of the configuration of dual HESS and battery-only configuration proposes possible increased battery-pack life, improving the long-term effect of vehicle's operation [7].

Alternatively, verification of the implemented powertrain systems can be done by a physical experimental setup, consisting of two motors, connected together by an axle and inverter for powering the motors. Two motors are required, as one motor is a drive motor and the second is a load motor. Proposed method requires additional calculations, for controlling the torque load on the load motor, simulating inertia from EV's parameters and selected drive cycle [8].

Verification of the parameters of the implemented powertrain system and its further optimization is crucial for prototyping efficient and improved EV, which brings a considerable requirement for a simulator of the EV powertrain. Applying the simulator to the prototyping sequence of the EV enables to design its parameters, suited for the expected operational conditions, based on the expected driving course and calculations. Further details in designing the simulator are described in the next section, as research in actual state-of-art simulators, used in research and development (R&D) centers, universities and training programs.

2 Research in state-of-the-art simulators of electrical drives for EVs

Development centers in universities present numerous experimental setups for developing the electrical drives for electrical vehicles. Conventional and preferred implementations of control methods for electrical drives are being replaced by innovative techniques developed by researchers in focus of improving operating conditions of electrical drives as poor torque ripple, flux ripple and flux instability at low RPMs (Figure 1). Innovative techniques are done by implementation of artificial neural network (ANN) enhanced control methods as direct torque control (DTC) [9].

Faults occurring in EV powertrain appearing e. g. under inverter switch faults, reduce operational reliability of the EV. The fault tolerant control methods of electrical drives are developed, by implementation of ANN control methods to improve stability and improved EV operation [10].

Described approaches are being tested on experimental prototypes of electrical drives for EV powertrain, which are mostly composed of inverters, isolation and auto transformers, voltage source inverters (VSIs), dSPACE controllers and electric motors linked together with torque sensor or shaft. Instead of transformers, a dual-isolated battery emulator is commonly used to power the VSIs, [6]. Electrical motor selected in experimental setups usually use lower power rating, e. g., 5 kW and low operating speed around 1500 RPMs [11].

Alternatively, there are available electrical vehicle simulators on market, used primarily for theoretical training and demonstration purposes for automotive students. Described educational stands are composed of main systems of EVs as electrical motor, inverter, high-voltage (HV) battery and charging port. Components are sourced from commercial EVs, e. g., Renault ZOE. Stand is suitable for training diagnosticians and EV repair specialists.

Educational stands can have alternative form, in electrical vehicle trainer, which is based on a commercial

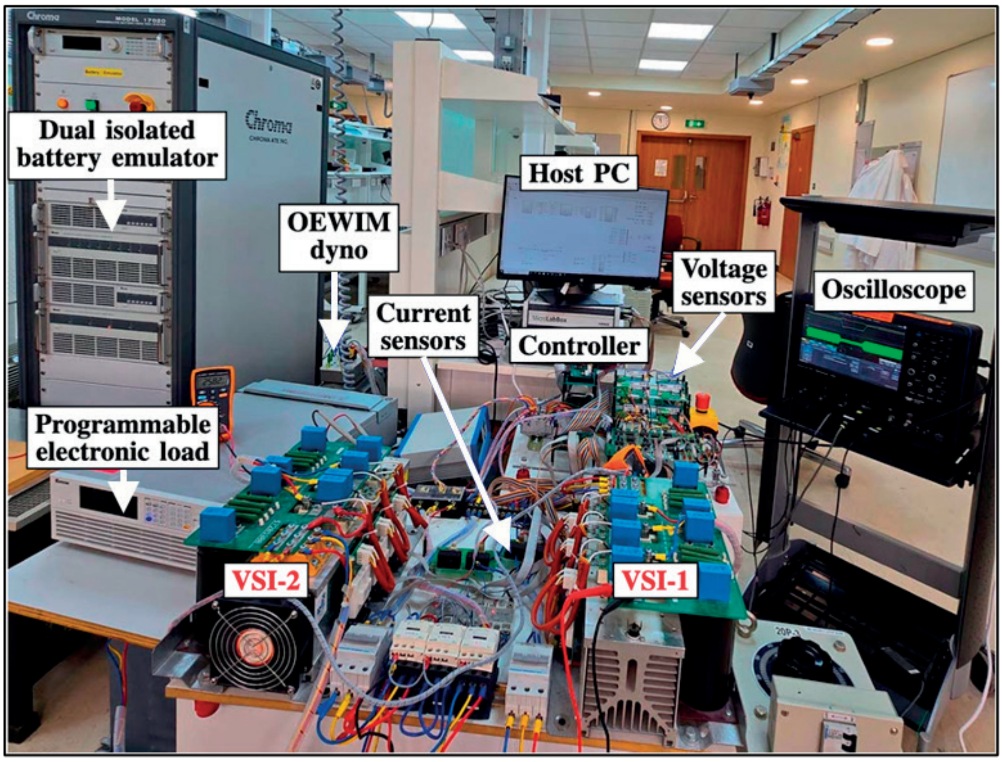

Figure 1 *Experimental prototype of electrical drive, [6].*

EV, e. g., Tesla Model 3. The vehicle is complete, but various panels are removed, with exposed components of the vehicle's system. Measurement devices are connected to the key components to illustrate the dynamic changes in electrical system while it is operating.

Described research and obtained details revealed possible solutions, which are already available on the market, or being used in R&D sector. Experimental setups are the most advanced and useful approach suited for drive cycle experiments, as the training stands, built from EV components, are not suited well for described experiments. Even when they are simpler to operate and easier to manage, they do not allow to build custom operation method, based on the selected drive cycle, which would be usable in experimental field.

3 Specification of the parameters based on the research

Advanced experimental setup of the simulator, described in the previous section, suits required needs for proposed simulator prototype, by utilizing custom drive cycle control method. To be useful and usable in the research and educational sector of university, the prototype must be built on a smaller scale.

The proposed prototype consists of three main operation blocks, energy storage and conversion, primary motor control and drive and secondary motor control and drive. Energy storage and conversion part consists of hybrid battery pack, composed of battery pack and super-capacitor (SC)bank and a DC-DC converter. The battery pack is the main energy storage, posing as a standard EV battery pack and supplying required energy for the motor drive and control. The SC bank is fundamental for improvising the dynamic operational parameters of the EV, mainly acceleration, possibly recuperative braking. The DC-DC converter is a fundamental part, required for converting voltage levels of the battery pack and SC to a HV DC bus level. For this application, buck-boost topology was selected, as it meets the criteria for voltage and current conversion. The primary motor control and drive is the powertrain part of the simulator, used as a simulation of propulsion. The primary, propulsion EM is an asynchronous motor (ASM). The ASM was selected as it is simple to operate and was/is used in EV production. For powering the primary motor, three-phase inverter was used, together with field-oriented control (FOC) and motor speed controller, enabling precise control of the primary motor by utilizing torque or speed control method. In addition, a braking chopper is added as a safeguard from HV spikes by back EMF from primary motor. The secondary motor control and drive block is the load part of the simulator, creating a torque load on the primary motor. Torque load poses as a simulation of the physical laws, hidden behind operation of the EV. This ensures that the simulator does not absolutely omit physical properties of the EV operation. Control and powering method is the same as for the primary motor, by FOC and speed controller.

The proposed diagram offers flexible solution since both the primary and secondary motors can be

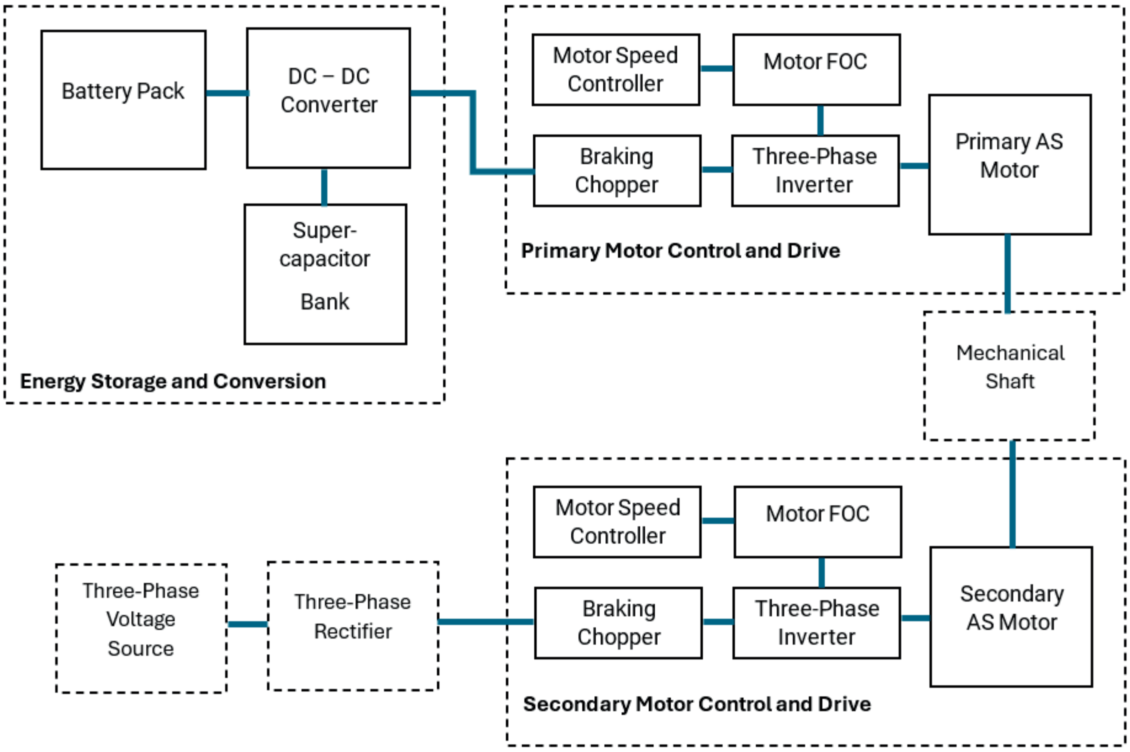

Figure 2 *Block diagram of the prototyped electrical vehicle drive simulator*

operated as synchronous motor, e. g., permanent magnet synchronous motor (PMSM), but only with adjusting the control method and controller accordingly. The FOC control is not mandatory, as there are more advanced and effective control methods available, while the direct torque control (DTC) and maximum torque per ampere (MTPA) can deliver better results, possibly even with artificial neural network (ANN).

Motor speed/torque controllers require external input parameters based on calculations from:

- Physical parameters of the subjected vehicle's body, rolling, resistance and drag coefficients, gravitational constant, with the grade of incline or decline, as the calculations are for the kinematic scenario;
- Selected drive cycle or another predefined plot as the source of the desired speed of the vehicle;
- Electrical parameters of the controlled motor;
- PI controller proportional, integral gain.

As proposed simulator gains complexity in terms of selected strategy of simulating the propulsion and torque load on the driveline components, there is an alternative for reducing the complex nature of it. With the desired drive cycle, parameters set for the vehicle body and other physical parameters, calculations can be done to obtain desired power of the driveline to cover the route of the drive cycle. Calculated power can be used in current load, which can replace powerline components, both motors, inverters and motor controllers. Described change would bring the simulation to more of an ideal nature than of the real-world scenario. Additional calculations, forming an efficiency coefficient (substituting the operational efficiency of omitted powerline components) forms aid in composing simulations of the simulator, taking it closer to the real-life scenario. With the assistance of calculations from [4, 12] in section 3, simulation is light-weight on the computational power and covers only the most important calculations required to successfully cover the stated requirements.

Figure 2 represents the block diagram of the proposed simulator, forming an example, prepared for building simulations of the simulator. Simulations are required for validating functionality of the proposed concept, as it must meet criteria. Necessary calculations and parameters are described in the next section.

4 Composition and description of simulation models of the simulator

Simulations of the simulator are done in Simulink, branch of the Matlab software. Strategy with the two models was selected, as each model represents different stage. Based on the initialrequirements, concept with current load, omitting the powerline components, was selected. First stage (Figures 3 and 4) aims to gather the data of vehicle operation by selected drive cycle. Drive cycle sends reference speed to kinematic calculation subsystem, forming an output of required force to accomplish the selected route. The total force from subsystem, multiplied by reference speed, determines the total power, consumed and created by vehicle operation. Additionally, ideal required and recuperated power from the battery pack and SC bank are calculated, as are required for the next stage. Described total power creates baseline for powertrain calculations, which are done in the second stage of simulations. Requested power from SC bank is set by "SC limit" block, which sets points of charging and discharging current intervals.

The second stage consists of calculations, energy storage system and a DC-DC converter with a controller

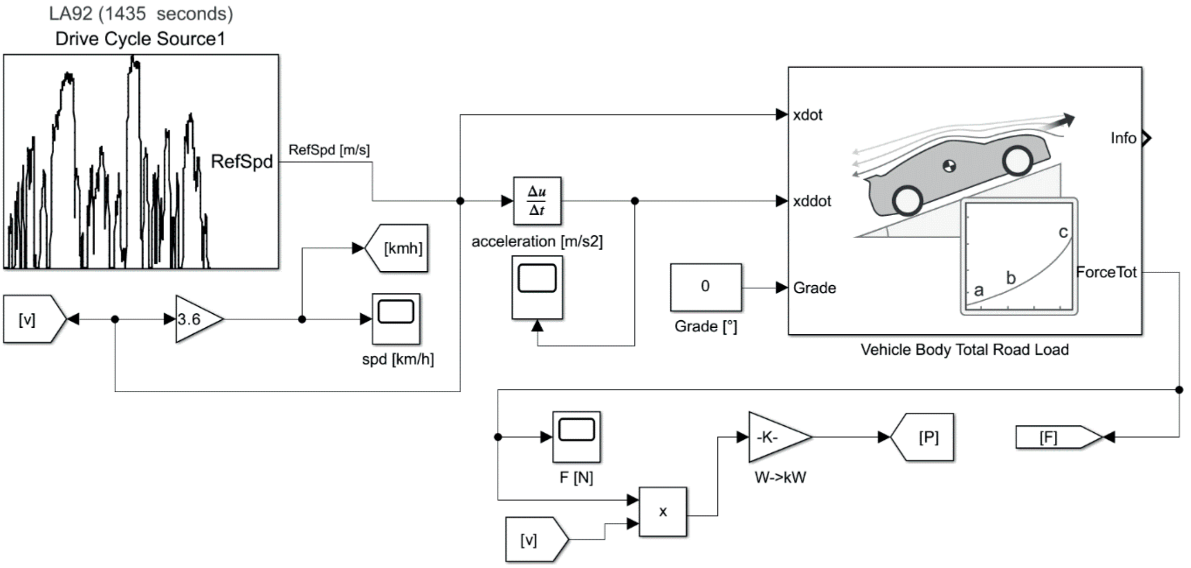

Figure 3 *The first stage of simulation- total force and power calculation*

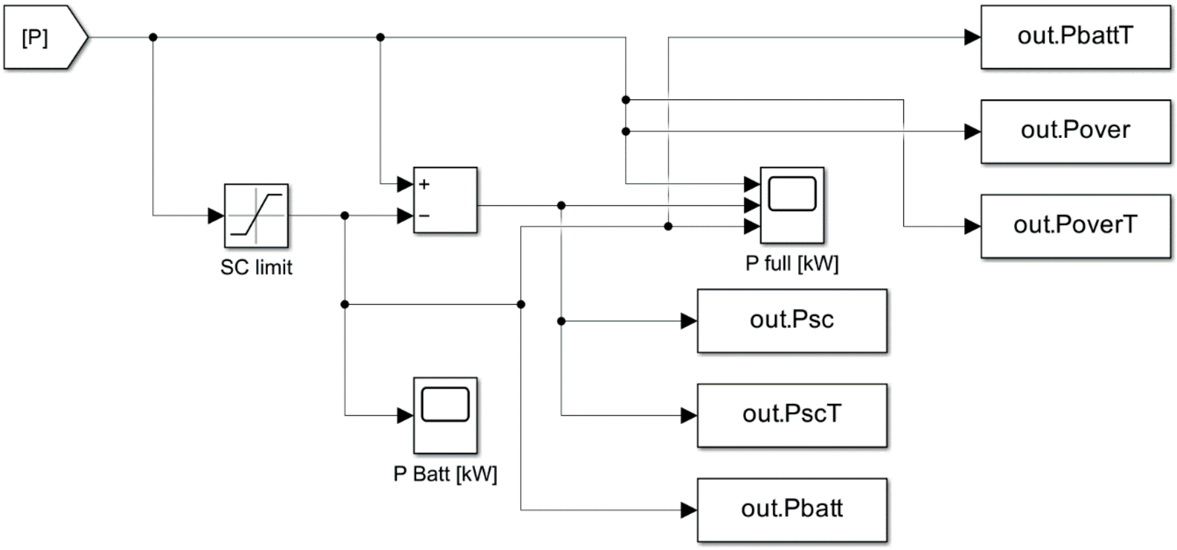

Figure 4 *The first stage of simulation - power of battery and SC calculation*

Table 1 *Component parameters for DC-DC converter*

Parameter	Value	Unit
C1	1.50E-03	[F]
C2	4.00E-03	[F]
L1	2.00E-03	[L]
L2	2.00E-03	[L]
fsw1	5.00E-03	[Hz]
fsw2	5.00E-03	[Hz]
Ts	1.00E-03	[Hz]

Table 2 *Baseline parameters for simulation*

Model	Type	Set parameter	Unit
Vehicle body	Drive cycle	LA92	[-]
	Vehicle mass	1550	[kg]
	Aerodynamic drag coef.	0.3422	[N*s/m]
	Rolling and driveline drag coef.	3.21	[N*s^2/m^2]
Battery pack	Nominal voltage	400	[V]
	Rated capacity	30	[Ah]
	Initial SoC	75	[%]
Super-cap bank	Rated capacitance	5.5	[F]
	Equivalent DC series resistance	155	[mOhm]
	Rated voltage	260	[V]
	Initial voltage	250	[V]

(Figures 5 and 6). Calculations gather data from the first stage, converting power into an electrical current. Calculated current is used as a variable for current load, which is consuming the required current from ESS or producing back to it, substituting a current load or production (recuperation) of EMs. Energy storage system contains battery pack with SC bank, while the battery pack is connected directly to the DC bus in a HV operation. The values of the main circuit components are listed within Table 1, while the baseline parameters for simulation are given in Table 2.

SC bank uses two-level converter to transform current levels, based on a requirement from calculations of the current flow from/to SC bank. The converter operates with current loop, controlling the amount of current flow.

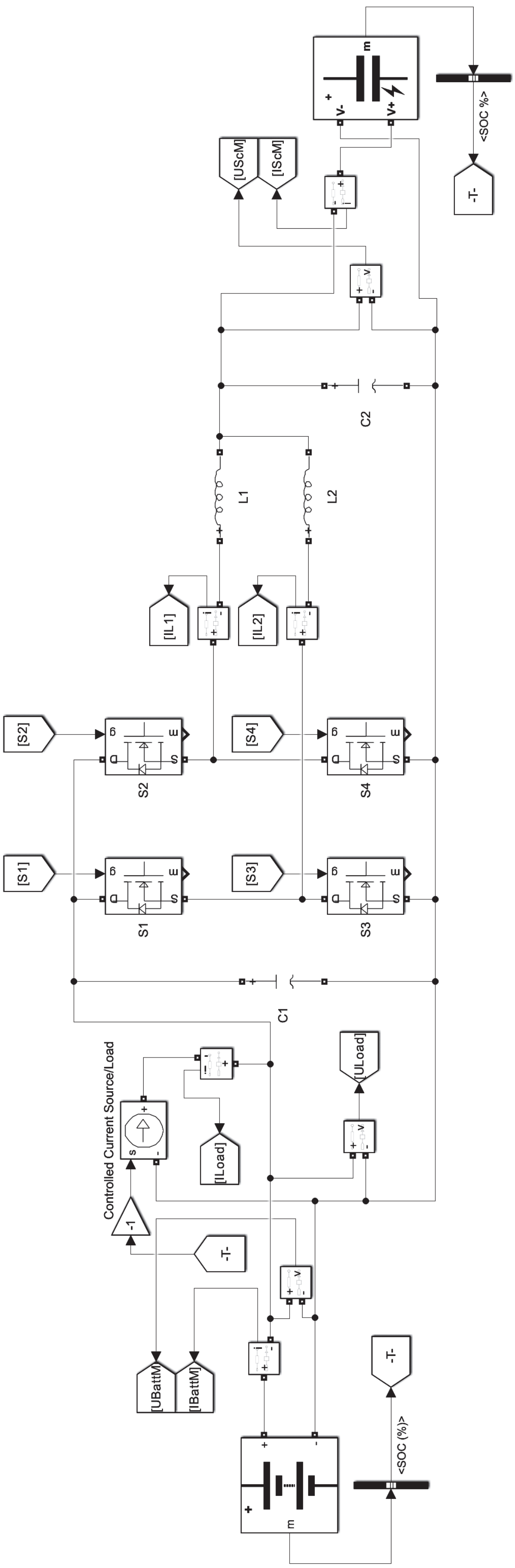

***Figure 5** The second stage of simulation -DC-DC converter with SC and battery*

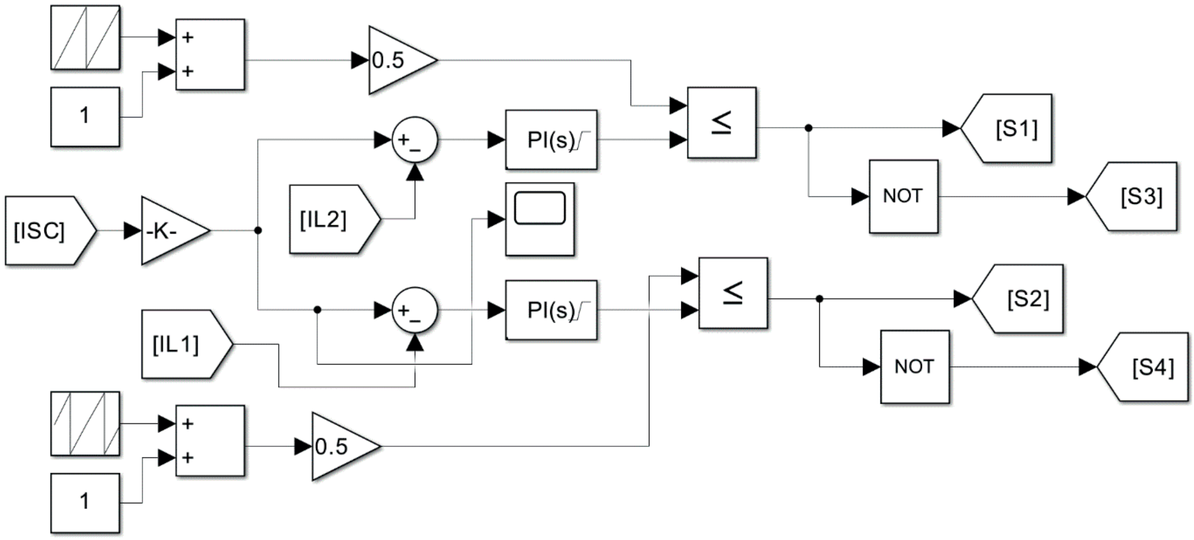

Figure 6 *The second stage of simulation - DC-DC converter controller*

5 Drive cycle experiments

The first parameter setup for simulation has set the baseline, to observe the system functionality without any optimization of parameters. The main points of interest (POI) are power, current flows and state of charge (SoC). Power and current flows describe the requested (calculated) and measured values, allowing throughout comparison. The SoC values show the current state of charge for ESS to observe sufficiency of the battery pack and SC bank capacities. Monitoring the parameters confirms functionality and correctness of the simulation, allowing further optimization of parameters if needed.

Due to the nature of the randomly attributed input parameters for rated capacitance of SC bank, discharging limit at 25 A, charging limit at 25 A, the discharged SC bank is expected even before the major energy consumption by load during the test.

Measured current flows in Figure 7 describe the functionality of the ESS, as SC bank delivers required current in the set intervals, discharged above 25 A and recharged above 25 A. However, the expected depletion of charge of the SC has occurred at simulation time 25 s, pointing out to inadequately set parameters for SC bank. As the charge of SC has depleted, all the required power from the SC bank had to be covered by battery pack.

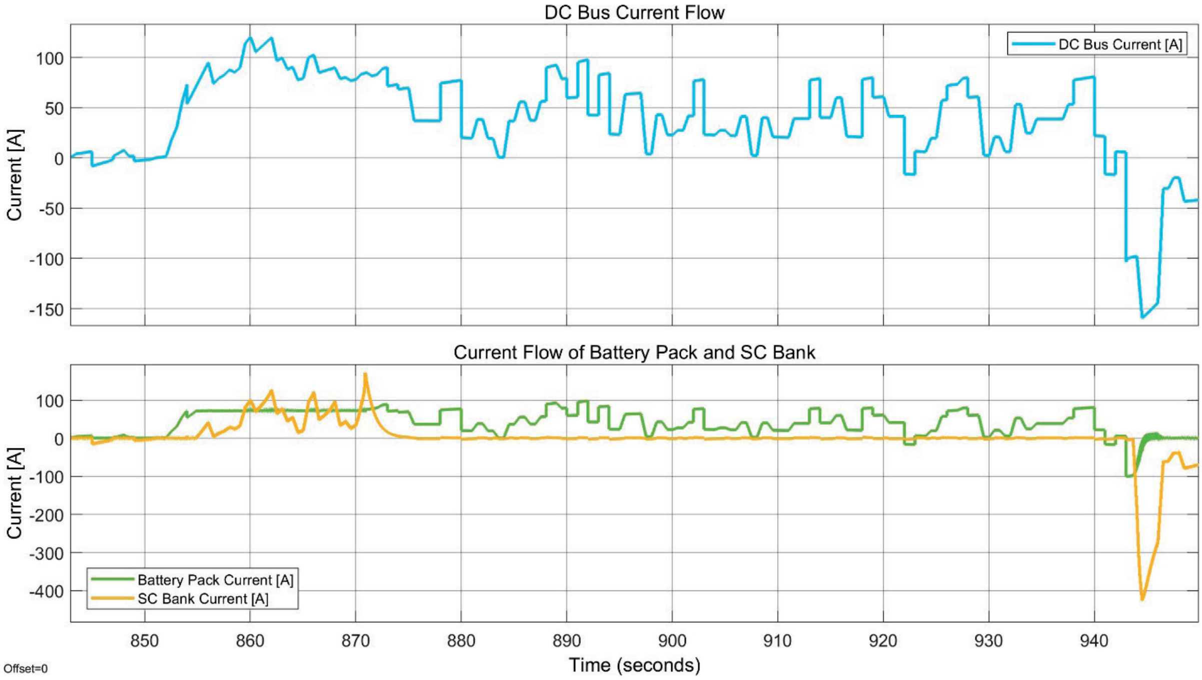

Figure 7 *Measured current flows of DC Bus and ESS from baseline simulation*

This point of switch can be seen in Figure 8, where the measured current flow of battery pack is different that calculated/requested current flow of the system. Around the same time of simulation, 25 s, measured battery current flow increased and distanced from the calculated values. Same phenomena can be seen in Figure 9, where the discharged SC bank could not provide any more energy to the system. The complete discharge of the SC bank is confirmed in Figure 10, where the SoC of the SC bank fell to minimum operational limit under 10 %.

For further examination in the experiment, the drive cycle stays same - LA92. Changes have been done in parameters for the SC bank, as rated capacitance is set to 6.6 F, discharge limit at 30 A and charging limit

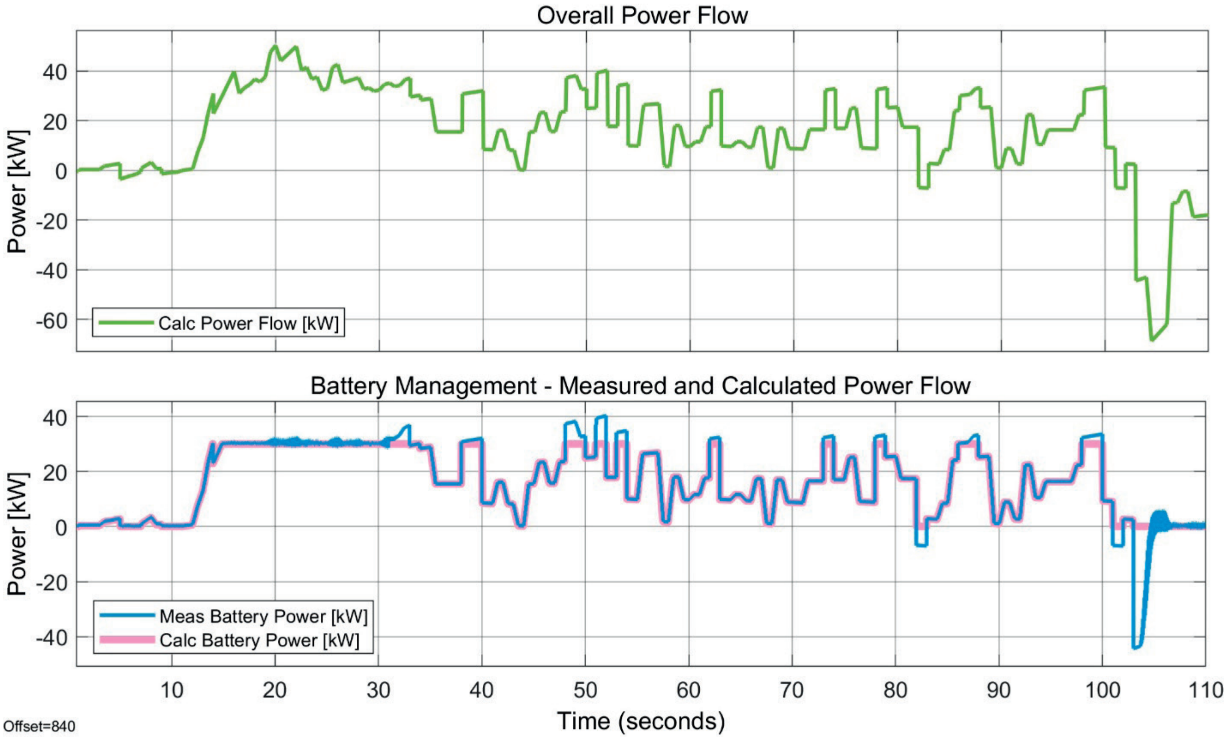

Figure 8 *Calculated and measured battery pack power flow from baseline simulation*

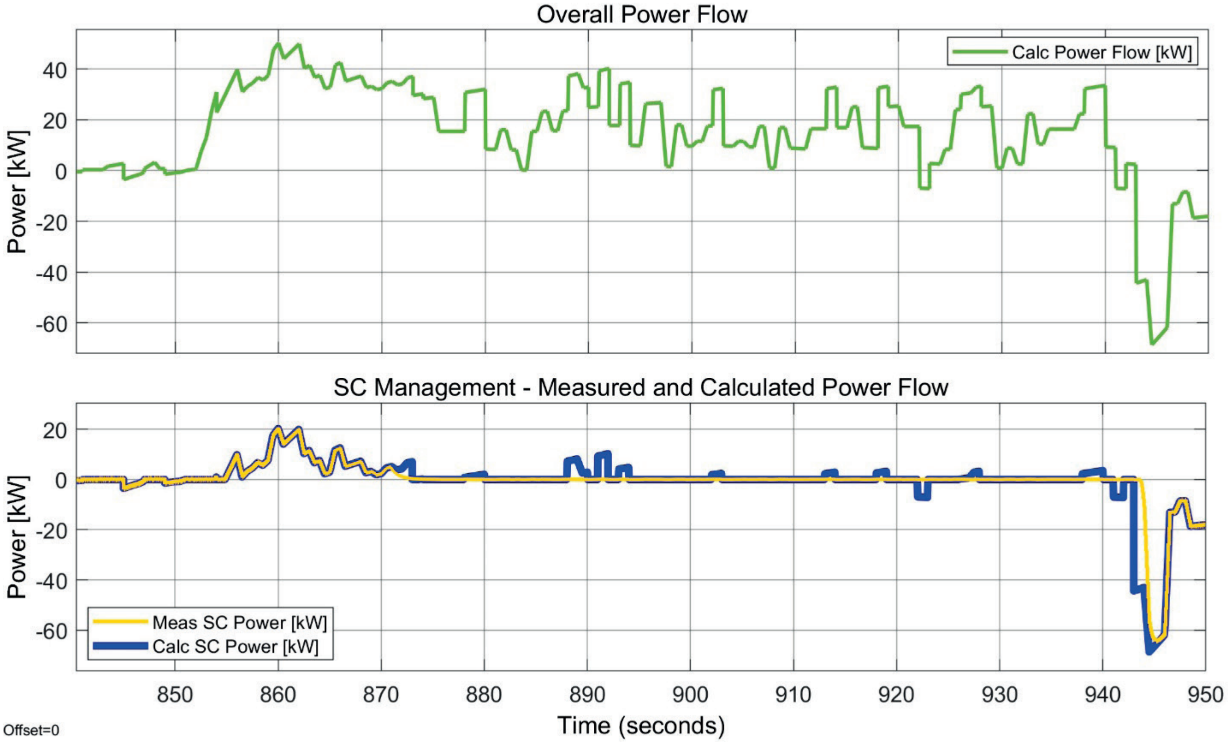

Figure 9 *Calculated and measured SC bank power flow from baseline simulation*

at 25 A. Altered parameters should bring more stored energy in SC bank, allowing it for extended operation and not discharging completely.

Experimental simulation was successfully completed with an expected outcome as altered parameters of the SC bank has increased its available stored energy. Figure 11 displays the successful operation of the ESS system, as SC bank has discharged and charged adequately to set limits. Figure13provides insight into operation of the SC bank, as it was able to cover the required energy by system, without discharging completely as in baseline simulation. This is confirmed in Figure14, where SoC of the SC bank stayed above minimum operational limit of 10 %. Figure12further evaluates the operation of ESS, as measured power flow of battery pack closely followed requested/calculated power flow by the system. Accuracy of measured parameters following closely required/calculated parameters determines ability of the ESS to cover load of the EV drive. Any error or margin between the described parameters indicate requirement of further adjustment or optimization of the SC bank or battery pack parameters.

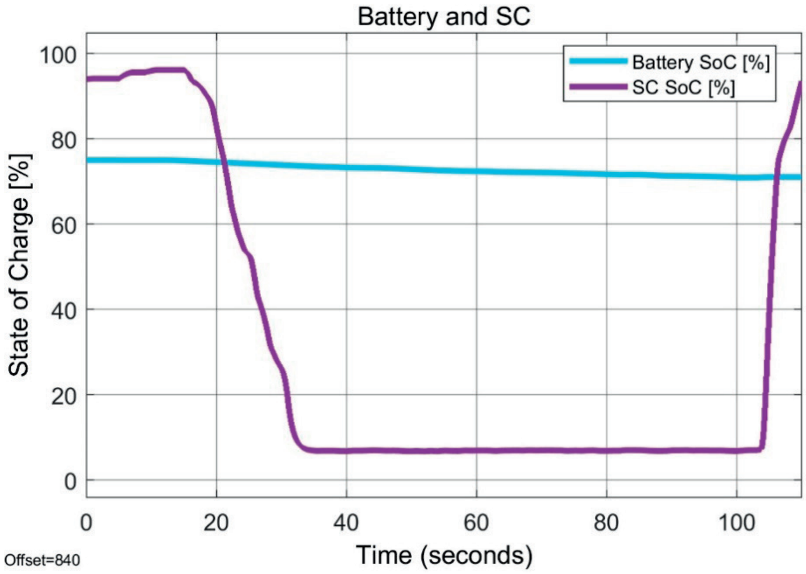

***Figure 10** Measured battery pack and SC bank SoC of baseline simulation*

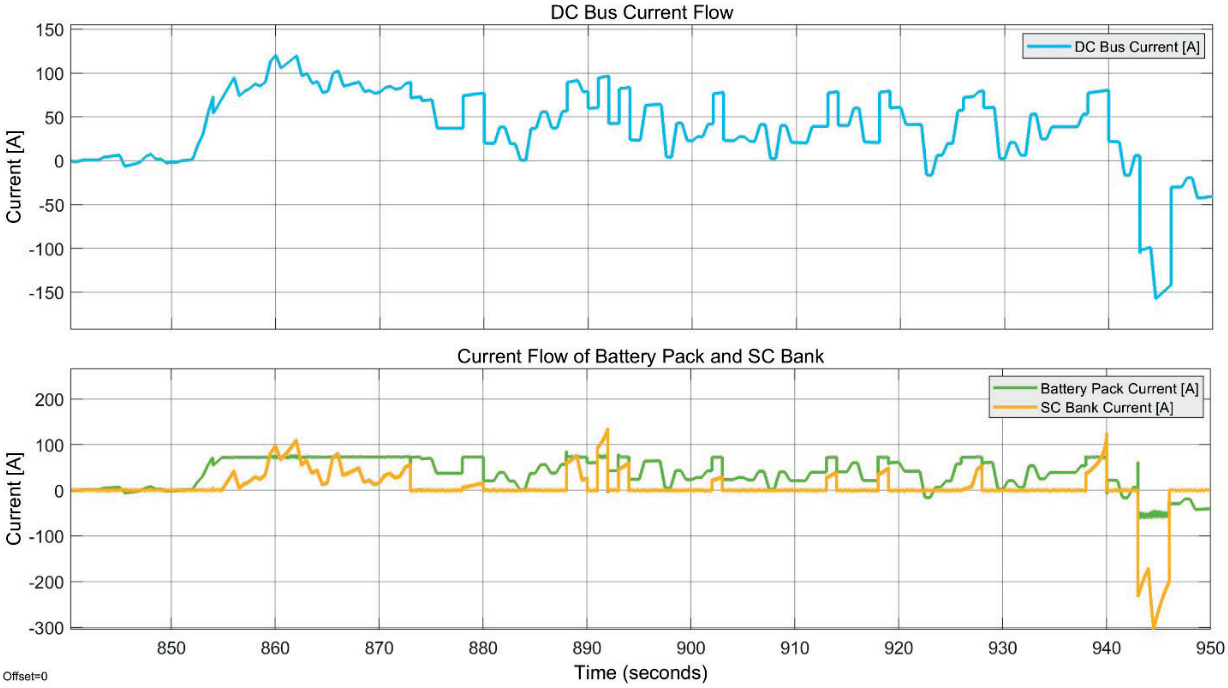

***Figure 11** Measured current flows of DC Bus and ESS from experimental simulation*

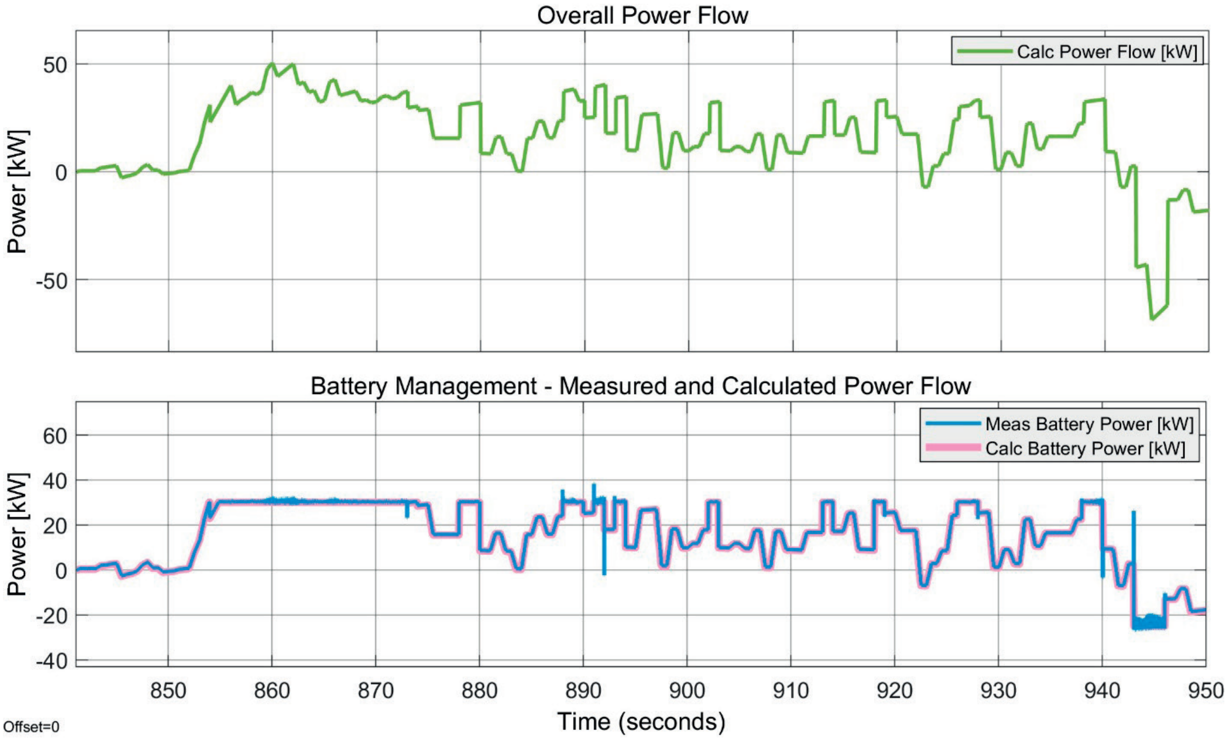

__Figure 12__ Calculated and measured battery pack power flow from experimental simulation

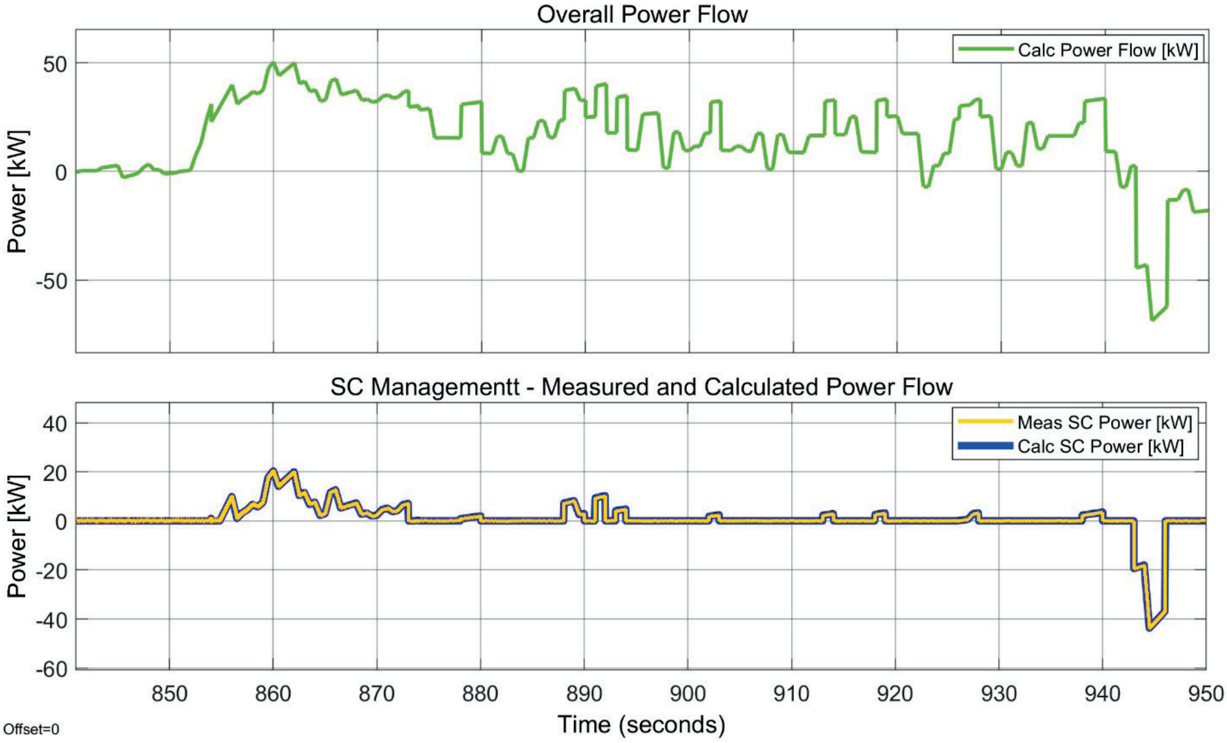

__Figure 13__ Calculated and measured SC bank power flow from experimental simulation

6 Results

Baseline simulations confirmed correctly functioning simulated model of the EV drive simulator. By utilizing input data from Table 2, the first stage of simulations provided operational data required for the second stage of simulations, where required and calculated parameters stated operation of the system. The second stage of simulator has provided baseline data, in form of figures describing current, power flows

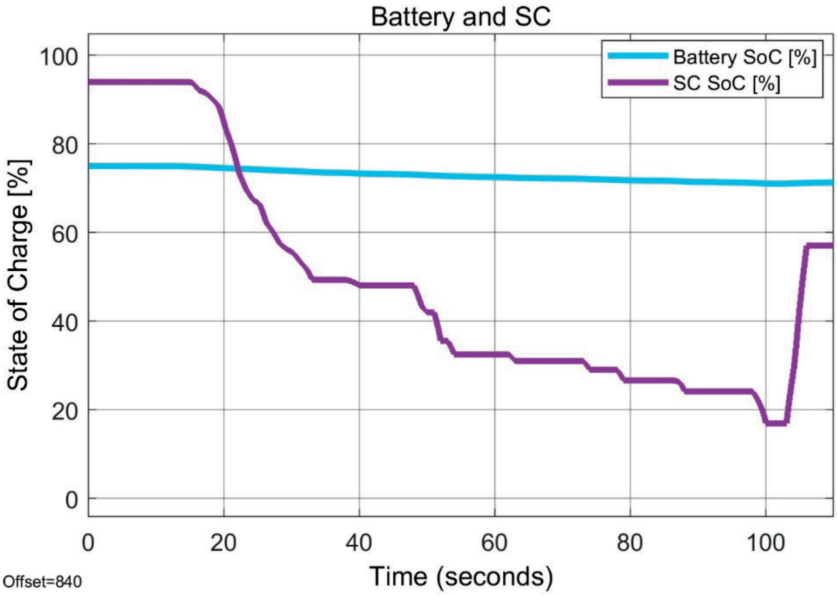

Figure 14 *Measured battery pack and SC bank SoC from the experimental simulation*

in the system and SoC values from ESS. Baseline input parameters resulted in SC bank not holding enough energy for covering extensive power load by system for long time period. Discharging limit of the SC bank has allowed it to discharge sooner than was needed, resulting in quick discharging. Low capacitance of SC bank also could not contain enough energy for extended period of it's operation.

Continuing with experimental simulations, where altered parameters of the SC bank have been used, resulted in operation of simulator meeting the requirements, where the SC bank was able to cover required energy. The SC bank provided enough power for the entire investigated spectrum, while having fraction of energy as a reserve. Experimental simulations confirmed correctness of the system's operation and expected results.

However, glitches have occurred during simulations, creating margins, where improvements are required. In Figure 12 occurred several spikes of current flow from and to battery pack, pointing to a potential error in the DC-DC converter controller, lowering operational efficiency of the system. The same can be seen in Figure 8, where one spike in current flow can be seen before the end of simulation.

7 Conclusion

Research in the field of the state-of-the-art electric vehicle (EV)powerline simulators displayed promising solutions, already utilized at the research and development (R&D) centers and universities. Advanced powerline simulator models, with setup consisting of multiple electrical motors and dSPACE controller, are used for the R&D of the most modern and advanced motor control methods. While described simulator model helps with extensive research of motor control methods, its setup can be adjusted and used in alternative experiments. As this research suggested, simulator of the electrical vehicle drive based on drive cycle would bring an experimental setup, suited to test and verify the prototyped EV drive by subjecting the drive to various drive cycle scenarios. Experimental setup was described by specifications, sourced from the initial research and delivered suitable prototype model. To verify the functionality of the simulator before building the physical model, simulations were preferred as a verification method.

Simulation setup was built from the two stages, delivered baseline data, confirming successful implementation of the simulator into simulations, while being controlled by reference speed of the selected drive cycle. The first stage created timeline data of the requested electrical power from driveline. Requested power needs to be covered by battery pack and supercapacitor (SC) bank. The second stage used generated data to simulate the load/generation of the calculated current and operation of the energy storage system (ESS). For simulations, baseline simulation was done with inadequate capacity of the SC bank and low discharging limit.

The baseline simulation resulted in an SC bank not holding enough charge to cover extensive load caused by the EV drive. Situation projected state, where the SC bank could not deliver any more power to the system and battery pack had to cover the remaining required charge from the SC bank. Increasing and optimizing rated capacitance of the SC bank would recover the system from being subjected to described state, which has been utilized in experimental simulation. Experimental simulation resulted in successful operation of EV drive, where the SC bank was able to cover extensive power requirements, without discharging to operational limit.

Proposed simulations can simulate the EV driveline with a modest and simplified approach. Vehicle body parameters, drive cycle and component parameters can be adjusted according to the requirements, to verify the prototyped vehicle setup, while being operated by reference speed of the selected drive cycle. Simulations generate data of calculated and measured voltage, current and power flows occurring in the EV system during the experiment. User can adjust parameters according to the generated data, as the data confirms the determined requirements stated by user.

Described experimental setup contains unexplained problems of oscillating and spiking current flow during various segments. With omitted powertrain components such as inverters, electrical machines and drive controllers, the simulation is close to an ideal scenario, since the losses from the components are not calculated and included. Before building the physical model of a simulator, simulation must be supplemented by missing components and the necessary calculations for control method of motors must be designed. Due to more of an ideal scenario nature of described simulations, they are valid only to a certain point, as they cannot be compared to the real-life scenarios.

For future research with proposed simulations and experiments, there is an important question left to answer, since it was not in merit of this research. How does the proposed HESS configuration affect the performance efficiency of the EV drive, compared to conventional battery-only system?

Acknowledgement

The authors would like to thanks to the Slovak national grant agency VEGA for project funding 1/0274/24.

Conflicts of interest

The authors declare that they have no known competing financial interests or personal relationships that could have appeared to influence the work reported in this paper.

References

[1] WANG, Y., ZHU, W., SCHAEFER, U. Study on the real time driving cycles and its influence on design of the electrical motor of EV. In: 2014 IEEE Conference and Expo Transportation Electrification Asia-Pacific ITEC Asia-Pacific: proceedings [online]. IEEE. 2014. eISBN978-1-4799-4239-8. Available from: https://doi.org/10.1109/ITEC-AP.2014.6940810

[2] LI, CH., HUANG, T., CHEN, L., LIN, Q., ZHU, Q. A power parameter optimization method for pure electric buses based on urban driving cycle. In: 2024 7th International Conference on Advanced Algorithms and Control Engineering ICAACE: proceedings [online]. IEEE. 2024. eISBN979-8-3503-6144-5. Available from: https://doi.org/10.1109/ICAACE61206.2024.10548912

[3] ITAGAKI, M., YOSHIMOTO, K. A consideration of a mini model suitable for a small motor evaluated on a driving cycle. In: 2024 IEEE 10th International Power Electronics and Motion Control Conference IPEMC2024-ECCE Asia: proceedings [online]. IEEE. 2024. eISBN979-8-3503-5133-0. Available from: https://doi.org/10.1109/IPEMC-ECCEAsia60879.2024.10567775

[4] SOUFFRAN G., MIEGEVILLE L., GUERIN P. Simulation of real-world vehicle missions using a stochastic Markov model for optimal powertrain sizing. In: 2011 IEEE Vehicle Power and Propulsion Conference: proceedings [online]. IEEE. 2012. ISBN 978-1-61284-248-6, eISBN978-1-61284-246-2. Available from: https://doi.org/10.1109/VPPC.2011.6043130

[5] LODI, K. A., BEIG, A. R., AL JAAFARI, K. A. ANN assisted improved Duty-DTC algorithm for open-end winding induction motor drive. *IEEE Transactions on Industrial Electronics* [online]. 2025, **72**(5), p. 4588-4600. ISSN 0278-0046, eISSN1557-9948. Available from: https://doi.org/10.1109/TIE.2024.3477011

[6] LODI, K. A., BEIG, A. R., AL JAAFARI, K. A. Enhancing open-end winding induction motor performance for fault-tolerant all-wheel drive EVs with ANN-based DTC. *IEEE Transactions on Transportation Electrification* [online]. 2025, **11**(5), p. 10739-10754. eISSN2332-7782. Available from: https://doi.org/10.1109/TTE.2025.3566711

[7] LODI, K. A., BEIG, A. R., AL JAAFARI, K. A. ANN based high performance induction motor drive for EV. In: 2024 IEEE Transportation Electrification Conference and Expo ITEC: proceedings [online]. IEEE. 2024. eISBN979-8-3503-1766-4. Available from: https://doi.org/10.1109/ITEC60657.2024.10599016

[8] FRIVALDSKY, M., PRIC, M., KINDL, V., SKALA, B., ZAVREL, M. Analysis of the hybrid energy storage system design for electric vehicle. In: 2024 ELEKTRO: proceedings [online]. IEEE. 2024. eISSN 2691-0616. Available from: https://doi.org/10.1109/ELEKTRO60337.2024.10556837

[9] LIU, P., YANG, K., LI, X. Construction of vehicle driving cycle based on Markov model. In: 2023 3rd Asia-Pacific Conference on Communications Technology and Computer Science ACCTCS: proceedings [online]. IEEE. 2023. eISBN979-8-3503-1080-1. Available from: https://doi.org/10.1109/ACCTCS58815.2023.00049

[10] GROMBA, J., SOBIERAJ, S., SYKULSKI, R. Designing of road loads simulator for EV. In: 2018 International Symposium on Electrical Machines SME: proceedings [online]. IEEE. 2018. eISBN978-1-5386-5210-7. Available from: https://doi.org/10.1109/ISEM.2018.8442898

[11] GRUNDITZ, E. A, THIRINGER, T. Modelling and scaling procedure of a vehicle electric drive system. Technical report. Goteborg: Chalmers University of Technology, 2017.

[12] DA SILVA, S. F., JAVORSKI ECKERT, J., CORREA, F. C., SILVA, F. L., SILVA, L. C. A., DEDINI, F. G. Dual HESS electric vehicle powertrain design and fuzzy control based on multi-objective optimization to increase driving range and battery life cycle. *Applied Energy* [online]. 2022, **324**, 119723. ISSN 0306-2619, eISSN1872-9118. Available from: https://doi.org/10.1016/j.apenergy.2022.119723c

EVALUATION OF BUS LANE IMPLEMENTATION EXPEDIENCY ON STREETS WITH DIFFERENT LANE NUMBERS: CASE STUDY

Fuad Dashdamirov*, Turan Verdiyev

Logistics and Transport Institute, Azerbaijan Technical University, Baku, Azerbaijan

*E-mail of corresponding author: fuad.dashdamirov@aztu.edu.az

Fuad Dashdamirov 0000-0003-3781-3542, Turan Verdiyev 0000-0002-9520-5038

Resume

The introduction of bus lanes on streets may not be feasible from the standpoint of reducing the overall time loss for road users. The goal of this study was to develop a method for checking the effectiveness of bus lane implementation. Using simulation experiments, conducted in PTV VISSIM, for a different number of traffic lanes, the speeds of buses and vehicles were determined both when buses are moving in the general flow and after the introduction of a bus lane, at different values of flow intensity and bus frequency. Regression equations, describing the dependence of speed on the traffic flow intensity and frequency of buses for different numbers of traffic lanes, are formulated. A mathematical model has been developed to calculate and compare the time losses of road users before and after the introduction of a bus lane, based on determining the average speed of traffic flow and buses.

Available online: https://doi.org/10.26552/com.C.2026.003

Article info

Received 22 August 2025
Accepted 28 November 2025
Online 12 December 2025

Keywords:

bus lane
traffic flow
speed
intensity
bus arrival frequency
time loss
simulation

ISSN 1335-4205 (print version)
ISSN 2585-7878 (online version)

1 Introductıon

In cities, comprehensive provision of mobility is envisaged, which is the most appropriate. The measures taken in this direction influence each other and are interdependent. Bicycle trips and walking are effective for certain short distances. Therefore, one of the main measures, aimed at increasing mobility for longer trips in cities, is to stimulate the use of public transport with an increase in the quality of services provided. The main indicators of the quality of service in public transport are considered to be travel time, travel comfort and traffic safety. To improve the quality of travel on public transport, it is first necessary to consider organizational solutions, such as events for reducing the travel time. One of the main ways to achieve this goal on congested streets is to create lanes for buses. Lanes organized for buses can be used in different ways depending on the conditions and needs. For example, there is experience in using bus lanes that allow only buses to travel, serve only buses at certain hours of the day, allow the general use of buses, taxis, bicycles and allow the movement of other vehicles. The following main methods for creating the bus lanes are distinguished [1]:

- Exclusive (dedicated permanently) - only for buses, all day.
- Part-time (temporary) - valid only during rush hours.
- High-occupancy vehicle lanes (HOV) - for buses and cars with ≥ 2-3 passengers.
- Queue jump lanes - short sections with priority at intersections.

Fast passenger travel by buses should not lead to a significant increase in the time lost by private vehicle owners. Like other mobility solutions, the creation of bus lanes should be carried out on the condition that they do not create additional problems in accordance with the traffic patterns on city streets. For example, bus lanes lead to a narrowing of the area of use for other vehicles. The introduction of bus lanes can be more effective in combination with various other solutions. For this reason, it is especially important to evaluate the way they are used and their effectiveness before creating bus lanes. It is advisable to use the time lost by road users for comparison. Thus, the main criterion for choosing a specific type of bus lane is the minimum number of traffic participants.

The proportion of private car users in different cities may differ. This may be due to local conditions, mental characteristics and other factors. With the expansion of the bus network, a certain number of private car owners may prefer public transport.

The aim of this article was to develop a method for checking the effectiveness of the implementation of dedicated lanes for public transport on streets with different numbers of lanes based on the total time lost by road users under given conditions. The criterion for selecting a lane type in mixed-use corridors, or those with spatial restrictions, is the simulated time loss. Both passenger and vehicle throughput are taken into account. Due to statistical indicators and road conditions, solving this problem on a real street network is an extremely labor-intensive and lengthy process. Therefore, it is proposed to implement an operational solution to the problem by processing the results of a simulation experiment. Modern simulation tools make it possible to accurately account for dynamic changes in the behavior of road users, including after the introduction of bus lanes. The PTV VISSIM, used for scenario modelling, allows for the modelling of vehicle behavior on different traffic lanes and the generation of lost time data for each mode of transport. The results of the simulation experiments are based on data on traffic flow speed and bus speed, allowing for dynamic changes in traffic flow due to changes in flow intensity and bus frequency. Based on flow intensity and bus arrival frequency for given conditions on a given road section, the speed and lost time are estimated.

2 Literature review

In the research of Cesme et al. (2018) is noted that the introduction of bus lanes should have sufficient public support and the traffic rules on the lanes should be strictly enforced. The work, based on the experience of implementing the bus lanes, proposes a reliable traffic management plan for bus lanes and presents a strategic plan [2].

Since the cars and buses are the main means of transportation in most major cities, more and more attention has been paid to the distribution of road space between them. Giving priority to buses, i.e., creating the bus lanes, is considered a generally accepted method for relieving traffic congestion. However, when implementing the bus lanes, previously studied strategies in this direction should be carefully examined. Dadashzadeh and Ergun (2018) summarized the studies conducted for this purpose, determined the minimum requirements for a bus priority system, and divided the studies devoted to the advantages and disadvantages of a bus priority system in terms of time and space [3].

Russo et al. (2022) also noted that bus transport is the main mode of transport in most cities, but it is a subject to delays due to the impact of general traffic. A study conducted in Rome, Italy, found that the introduction of bus lanes reduced the overall travel time of buses by approximately 18%. The authors noted that the number of bus lanes in the city is small [4]. In another study, conducted in Thessaloniki, Greece, was examined the feasibility of introducing a bus lane on an one-way road connecting the city centre to the outskirts with a low bus frequency on a real city route [5]. The measurements showed that the introduced bus lane was fully justified, reducing the time buses spent on the road and ensuring a smooth bus flow. The researchers noted the importance of enforcing parking and other traffic regulations when introducing bus lanes.

Bayrak and Guler (2021) noted that, although the use of bus lanes is generally considered the best strategy to improve bus performance, it can lead to significant bottlenecks and queues for other vehicles [6]. They proposed a two-level optimization algorithm aimed at reducing the overall time loss of all users when introducing bus lanes. The results show that the introduction of bus lanes can lead to a reduction in the overall time loss only in certain strategic locations.

When buses move in the general traffic flow, their reliability becomes dependent on the general flow. However, sometimes it is impossible to create bus lanes due to lack of space on the roads or restrictions on the traffic flow or its excessive impact on the flow. As an alternative solution, the authors proposed the introduction of dynamic bus lanes, which are reserved for buses only when necessary [7]. For this purpose, a simulation model of traffic management was built and calibrated using an urban highway with several bus lanes based on real indicators. In this paper, the variants with introducing dynamic lanes, the variants with buses moving in the general flow, and the variant with introducing exclusive bus lanes were compared. The results show that despite the positive effect of introducing dynamic lanes, the time passengers spend on the road increases slightly. At the low bus traffic intensity, the lanes remain unused for a long time. The dynamic use of bus lanes is a new strategic approach and allows the use of lanes in the absence of buses. Othman et al. (2023) noted that the implementation of dynamic bus lanes is promising, but its effectiveness needs to be tested under different traffic conditions [8]. To do this, they compared the impact of implementing dynamic bus lanes with the impact of implementing conventional exclusive bus lanes under different demand levels. To do this, they modelled the Eglinton East corridor in Toronto using Aimsun Next and considered different behavior patterns. It was found that the dedicated bus lane is more effective at high bus density and high traffic flow rates. Li et al. (2025) also proposed to improve the efficiency of bus lane usage by implementing a dynamic lane usage strategy [9]. The dynamic time and space priority strategy uses infrastructure and vehicle status information to determine the available time and space resources in the bus lane. Based on these resources, a usage optimization model is developed for the vehicles that would use the bus lane.

Xue et al. (2025) analyzed various factors of bus lane sharing. After analyzing the impact of bus lane sharing strategy on commuters' sharing decisions and traffic flow pattern, the authors constructed a bus lane performance evaluation model using the TOPSIS method [10]. Zhang et al. also investigated the performance of multi-functional bus lanes and found that the proposed strategy improves the intensity balance, reduces delays by 80.56% and stops by 89.35% when CAV demand increases [11].

The use of bus lanes by cars under certain conditions may be appropriate to ensure the efficient use of bus lanes when the car demand is high and bus demand is low. To ensure the balance, Yin et al. (2024) propose a bus lane usage rule for private cars by modeling based on the speed of the adjacent lane [12]. The measured results show that the travel time is significantly reduced as a result of cars using bus lanes.

Kong et al. (2024) proposed a management strategy for intermittent bus lanes to optimize the use of road resources in small and medium-sized cities [13]. In this paper, a methodology was developed to determine the feasibility of implementing intermittent bus lane signs based on factors such as road congestion, vehicle traffic volume, and bus traffic volume.

Qiao et al. (2024) proposed a comprehensive evaluation method using a bus lane implementation priority index based on vehicle traffic volume data collected from multiple sources. A classification table of the importance of implementing bus lanes was constructed, and a corresponding range was determined for each level. In this way, bus lanes corresponding to a specific index were divided into excellent, good, average, neutral, and poor classes [14].

In the work of Tsitsokas et al. (2021), the optimal allocation of bus lanes was studied [15]. A model structure was proposed according to the dynamic characteristics of the density distribution. The problem was considered as a non-combinatorial optimization problem with binomial variables. In another work devoted to the design of bus lane infrastructure, an optimization model was developed taking into account the number of road users and the size of streets and tested in Beijing [16].

Meliti and Kadar (2011) investigated the impact of dedicated bus lanes on ridership and travel time loss [17]. The difference between the average travel time of cars and buses during the off-peak and peak hours on weekdays and weekends was determined. For this, the Student's t-test was used. It was found that the ridership of buses is generally low, and the impact of introducing dedicated lanes on ridership is very weak. Research conducted in Kuala Lumpur has shown that the time lost by buses travelling in a dedicated lane is greater than the time lost by vehicles travelling in the general flow of traffic in the adjacent lane.

Fadyushin and Zakharov (2020) studied the time losses of buses and other vehicles in the bus stop zone using field studies, microsimulation experiments and mathematical models, found that improving the parameters of bus lanes does not lead to a significant increase in the speed of buses, but has a negative impact on the travel parameters of other vehicles [18].

The introduction of bus lanes can also cause certain problems at intersections. Zhang (2023), analyzing the evaluation indicators of a discontinuous bus lane, showed that when the traffic intensity is a certain percentage of the throughput, the speed of vehicles increases, but the time losses of buses increase, as well [19].

De Oliveira et al. (2024) analyzed the change in the speed of other vehicles as a result of the creation of bus lanes in the city of Sao Paulo in 2020-2025 and concluded that this change varies depending on the area of the city and the mode of operation of the bus lane (fully separated and temporarily separated) [20]. There is also a study examining the impact of the creation of lanes reserved for public transport on the speed of buses [21].

Arasan et al. (2009) proposed to determine the ratio of vehicle traffic intensity to road capacity to assess the restriction of the traffic conditions of other vehicles as a result of creation of the bus lanes. It is noted that the introduction of bus lanes on some streets, while improving the quality of service for passengers, does not have a negative impact on the movement of other vehicles. In the research defined the initial conditions for the introduction of bus lanes [22].

There are many studies devoted to simulation experiments of the organization of bus lanes. Szarata (2021) tested the implementation of bus lanes on 4 road sections in the city of Rzeszow, Poland, using PTV VISSIM. The simulation experiment was conducted for 3 cases (no bus lane, dedicated lane, dynamic lane). The final evaluation was made on the average time loss for all vehicles. The author found out from the tests that the time spent by vehicles on the road does not increase significantly as a result of the implementation of dynamic bus lanes [23]. Tran et al. (2013) conducted a comparative analysis of 3 popular bus lanes using simulation experiments using a model created in the PARAMICS program based on the assumed input parameters. The experimental values were used in the tests for exclusive bus lanes, regular lanes and lanes with bus priority. The time-saving value that can be achieved by implementing the bus lanes on a 500-meter-long street section was determined [24]. Hawas (2013) proposed a method for estimating bus route travel times using microsimulation [25]. The parameters used are the route length, network traffic volume, specified speed limit, bus frequency, and number of passenger boardings and alightings. The regression model proposed for forecasting was calibrated taking into account the time lost on the route and in transit. The reliability of the calibrated regression model was demonstrated.

In the work of Liu et al. (2020), the joint use of bus lanes by automated vehicles was simulated using intelligent control systems. It was found that, as a result of proper organization of control taking into account the operating modes of buses on the route, it is possible to significantly increase the speed of buses and automated vehicles [26].

As can be seen from the results of the research, the effectiveness of the introduction of bus lanes significantly depends on the conditions of their use and the importance of justifying that use by taking into account the change in the main parameters under the given conditions is great. The effectiveness of bus lane implementation can be assessed using time loss, which is a universal performance indicator that takes into account delays in lanes, stops, transfers, etc.

Systematic aproach to using bus lanes usually prevents overall time losses. However, if negative impacts are observed with bus lane use, it's possible to test the effectiveness of dynamic lanes, consider reconfiguring the network, determine time losses across all streets, and model the network using macromodeling tools.

3 Methodology

In the article is developed a methodology for assessing the effectiveness of introducing bus lanes based on the total time losses of road users under given conditions (speed limit, lane width, length of a street section) in various values of vehicle traffic intensity, bus arrival frequency, and the number of bus passengers transported along a given section for different numbers of street lanes. To assess the speed of buses and vehicles when buses move in the general flow and along a bus lane, numerous simulation experiments were conducted on a street with 2, 3, 4, and 5 traffic lanes using a micromodel created in the PTV VISSIM program. The constructed in PTV VISSIM model was used the Weidemann 99 psychophysiological model of following the leader (car-following model), built in by default, which simulates, in a microscopic format, the behavior of a driver when driving behind another car. It takes into account the personal characteristics of the driver (aggressiveness, attentiveness), the distance between cars, the reaction to the deceleration/acceleration of the leader, the relative speed.

During the simulation experiments, the speeds of buses and other vehicles were determined before and after the introduction of a bus lane. First, regression equations were obtained for the dependence of the speed on the intensity of vehicle traffic and the frequency of bus traffic when buses move in the general flow on a street with 2, 3, 4 and 5 traffic lanes. Then, the regression dependencies of the flow speed on the intensity of the traffic flow, as well as the dependence of the speed of buses on the frequency of bus arrivals after the introduction of the bus lane were determined.

Based on the speed value, determined using the regression dependencies, a method for determining the total time losses of road users on roads with different numbers of traffic lanes (2, 3, 4 and 5) is proposed. The condition for the effectiveness of introducing a bus lane for considered period (hour) based on the values of time losses is adopted. The proposed method was tested on a two-lane road based on the values of traffic flow intensity, the number of bus passengers and the frequency of bus arrivals taken from real road conditions.

The proposed model does not impose restrictions on use for city streets with more than five lanes. The consideration of the effectiveness of using bus lanes on streets with a maximum of 5 lanes is related to local road conditions (specifically for the city of Baku).

4 Requirements for the implementation of bus lanes on city streets

According to various methodologies, bus lanes are introduced primarily when the hourly frequency of buses is more than 30 bus/h and the traffic intensity is more than 1000-1200 veh/h. In addition, it is considered appropriate to use the bus lanes when the speed is less than 15 km/h. Lane allocation should prioritize buses, even if private vehicles predominate, as long as

Table 1 *Recommended solutions for organizing the bus lanes taking into account the frequency of bus arrivals and the number of passengers*

Treatment	Minimum one-way peak-hour volume		Related land use and transportation factors
	bus	passanger	
Bus streets or malls	80-100	3200-4000	Commercially oriented frontage
CBD curb bus lanes, main streets	50-80	2000-3200	Commercially oriented frontage
Curb bus lanes, normal flow	30-40	1200-1600	At least 2 lanes available for other traffic in same direction
Merdian bus lanes	60-90	2400-3600	At least 2 lanes available for other traffic in same direction; ability to separate vehicular turn conflicts from buses
Contraflow bus lanes, short segments	20-30	800-1200	Allow buses to proceed on normal route, turn around or bypass comgestion on bridge aproach
Contraflow bus lanes, extended	40-60	1600-2400	At least 2 lanes available for other traffic in opposite direction/ Signal spacing greater than 150 m intervals

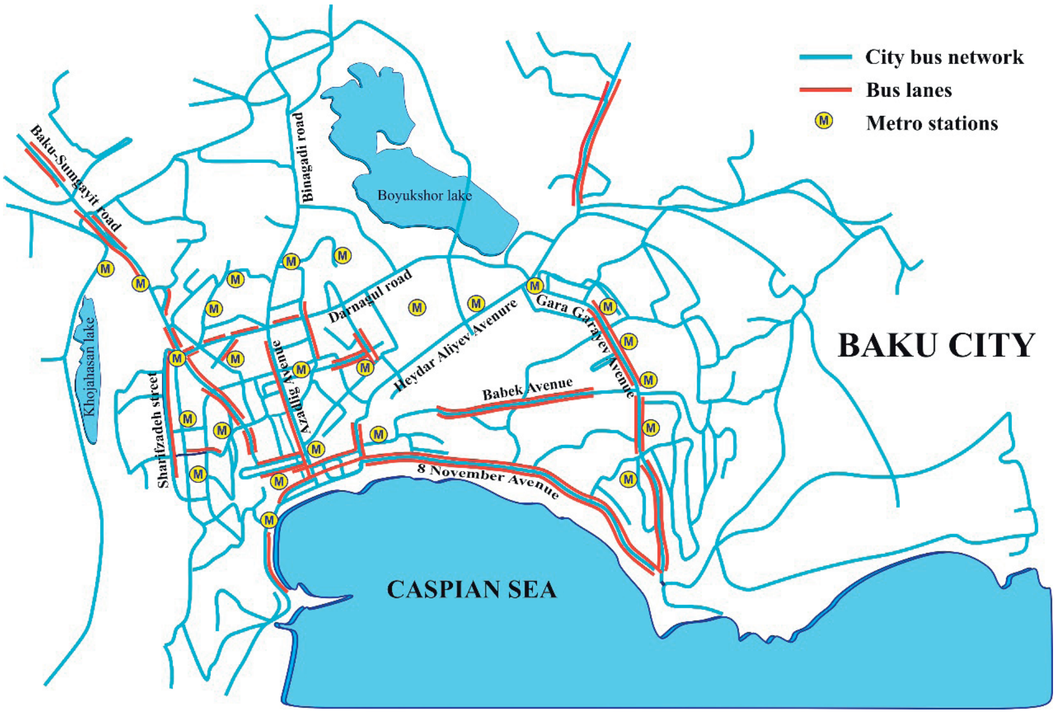

Figure 1 *Streets with dedicated bus lanes in the Baku city bus route network*

Table 2 *Number of bus lanes and number of routes passing through some streets in Baku*

Streets where bus lanes are used	Forward direction			Reverse direction		
	Total number of lanes	Number of bus lanes	Number of bus routes	Total number of lanes	Number of bus lanes	Number of bus routes
Gara Garayev ave.	3	1	27	3	1	26
Y.Safarov street	5	1	11	6	1	11
28 May street	4	1	10	0	0	0
A.M. Sharifzade street	4	1	8	4	0	5
Khoyski street	3	1	12	3	1	11
Tbilisi ave.	3	1	7	4	1	7
Moskow ave.	2	1	17	2	1	19
Sh.Badalbayli street	5	1	9	0	0	0
Rovshan Jafarov street	2	1	12	2	1	2

efficiency criteria are met. Priority to buses is justified if the bus ridership is higher than that of private cars (even if there are fewer cars). Furthermore, the city's goal is to optimize the transportation of people, not cars. The recommended solutions for the use of bus lanes depending on the frequency of buses and the number of passengers, presented in the TRB TCQSM report [1], are shown in Table 1.

As can be seen from Table 1, the creation of bus lanes is recommended in heavy traffic conditions, when the frequency of bus arrivals is 11-20 buses per hour and the flow intensity is 800-1500 vehicles per hour. Observations conducted on the Baku bus route network show that on many streets the frequency of bus arrivals often exceeds 80 vehicles per hour and the flow intensity is over 800 vehicles per hour, not only during the peak hours but also at normal times. Figure 1 shows the streets where the bus lanes have been created in Baku. The total number of traffic lanes on streets with bus lanes in Baku by direction is given in Table 2.

The flow indicators can vary over short periods, such as 10-15 minutes. However, obtaining data over a longer period, such as an hour, can improve reliability. For these experiments, the data from hourly measurements of traffic flow and bus speeds under real-world conditions were used, reflecting dynamic changes in traffic flow as bus intensity and frequency change. Taking measurements during the peak and off-peak hours and incorporating these indicators also improves reliability and ensures that dynamic variability is accounted for.

Table 2 shows the values of the number of lanes and the number of bus routes passing along some streets in the forward and reverse directions.

The road capacity for general traffic on the streets shown in Table 2 varies from 1,800 vehicles per hour to 6,400 vehicles per hour, depending on the number of lanes and traffic organization. Bus lanes are located on the right and are demarcated from the general traffic flow by a solid line. Parking near the sidewalk is prohibited.

Over the past 10-15 years, the traffic density in cities has increased as a result of a sharp increase in the number of private car owners, and serious traffic jams have begun to be observed in all the cities with a population of over 1 million people. Observations show that on all the streets where the bus lanes are created, traffic jams occur during the peak hours, and the speed of the traffic flow decreases. To prevent conflicts with other traffic participants, when allocating lanes for buses on narrow city streets, a solution can be time-based lanes, shared or alternating lanes, the use of reverse traffic, priority of buses at traffic lights, point allocation of lanes, creating space for the lane. It is advisable to check the effectiveness of creation of bus lanes based on the total time losses of all the road users. A test based on the total time lost by all the road users, when creating bus lanes, initially requires determining the speeds of buses and vehicles on streets with different number of lanes for given conditions.

5 Assessment of the impact of vehicle traffic intensity and bus arrival frequency on flow speed

The following relationship exists between the main parameters of the transport flow [27]:

$$N = kv, \tag{1}$$

where:
N is the traffic flow intensity, veh/hour;
k is the traffic flow density, veh/km,
v is the average flow speed, km/h.

As can be seen from the formula, there is a mathematical relationship between the speed of movement and the intensity of vehicles. Traffic density can change under the influence of various factors. At the same time, the speed of the flow can be affected by the composition of flow, the width of the lanes, permitted maneuvers, methods of traffic control and other factors. In addition, when introducing, the bus lanes, the number of lanes used by the general traffic flow decreases, the density of vehicles increases, and the speed of the traffic flow decreases. Therefore, when creating the bus lanes on each section of the street and on the street as a whole, the effect of the frequency of bus arrivals and the intensity of the traffic flow on the speed of movement should be studied, based on the actual values of the indicators.

As already mentioned, based on the classical approach, the conditions for the use of bus lanes are determined by certain maximum values of traffic speed, bus arrival frequency and traffic flow intensity. Even if all these conditions were met, in real conditions, problems, such as an increase in the overall time loss of road users, may arise when using the bus lanes. A dedicated lane reduces overall delay time if the lane is used by many buses and passengers. A dedicated lane shifts delays if buses arrive infrequently, the capacity of the remaining lanes is not taken into account, and there are no alternative routes for passenger vehicles. Therefore, it is important to test the situation that will arise when using the bus lanes under the given conditions using simulation modelling. The TRB TCQSM report also notes that before making a decision on allocating lanes for the bus traffic, it is advisable to conduct simulation experiments based on parameters corresponding to current road conditions [1]. Such programs as SUMO, Aimsun, PARAMICS [28-30] are used to simulate traffic on streets and roads. In the models created to test the effectiveness of bus lanes on a street section using PTV VISSIM, it is possible to take into account the values of the quantities (number and size of lanes, speed limit, bus arrival frequency, traffic intensity of vehicles, etc.).

In the simulation model, created in PTV VISSIM to analyze the speed of buses and other vehicles in the flow, before and after the introduction of a special lane for buses, the lane width was taken to be 3.5 meters, and the permitted speed was taken to be 50 km/h in accordance with real traffic conditions based on observations made on the streets of Baku. The situation that may arise when introducing the bus lanes was simulated by entering the obtained traffic parameters and behavior models of vehicles and buses. The length of the measured street section was taken to be 800 meters. Measurements were carried out when the bus arrival frequency changed from 80 to 240 buses per hour, and the traffic intensity of the flow from 800 to 2400 vehicles per hour. Figure 2 shows the exemplary images of the resulting situation as a result of simulation tests, when buses move in the general flow and through a bus lane on a 3-lane road.

Based on the results of simulation tests of a bus traffic in the general flow and on the bus lane, the obtained values of the indicators were processed. As a result of numerous measurements carried out using the created micromodel, it was found that the frequency of bus traffic and the hourly traffic intensity of other vehicles, when moving in the general flow on a street with a different number of traffic lanes, are completely independent of each other. Thus, there is no correlation between the frequency of bus traffic and the traffic intensity of the flow. Therefore, it is possible to consider the regression dependence of the influence of these parameters on the speed of movement. The correlation coefficients of the dependence of the traffic flow speed on the intensity of vehicles and the frequency of bus arrivals when buses move in the general flow are given in Table 3, for different numbers of traffic lanes.

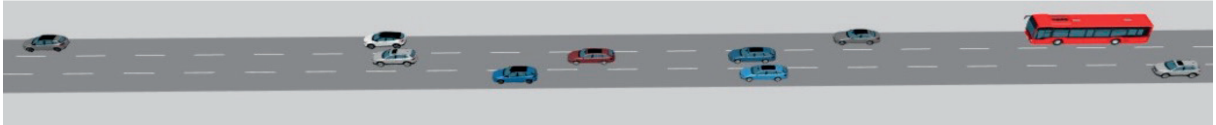

Buses move in general flow through 3 lanes

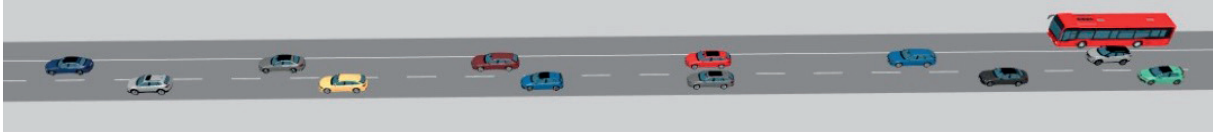

Buses move through bus lane in a street with 3 lanes

Figure 2 *3D visualization example of the model before and after the introduction of bus lanes in PTV VISSIM for a 3-lane road*

Table 3 *Correlation coefficients of the dependence of the speed of movement in the general flow on the intensity of movement and the frequency of arrival of buses*

Number of lanes	Correlation coefficients of the dependence of the speed of movement in the general flow on:	
	Bus arrival frequency	Intencity of vehicles
2	-0.32049738	-0.805978864
3	-0.1824384	-0.793671492
4	-0.14571551	-0.741598638
5	-0.27796198	-0.647205939

Table 4 *Parameters of the dependence of the speed of movement on the frequency of bus arrivals and the intensity of car traffic on 2, 3, 4 and 5 lane roads when buses move in the general flow*

Lanes	R^2		Coefficients	Standard deviation	t-statistics	P-value	Significance F
2	0.752	Y intersection	64.391605	1.274799	50.51118	$2.39 \cdot 10^{-61}$	$2.3 \cdot 10^{-24}$
		Veh. intensity	-0.003124	0.000549	-5.68757	$2.15 \cdot 10^{-7}$	
		Bus arrival freq.	-0.078561	0.005493	-14.3030	$1.66 \cdot 10^{-23}$	
3	0.663	Y intersection	62.93425	1.296197	48.55301	$4.75 \cdot 10^{-60}$	$3.69 \cdot 10^{-19}$
		Veh. intensity	-0.00155	0.000559	-2.77636	0.006897	
		Bus arrival freq.	-0.06746	0.005585	-12.0785	$1.53 \cdot 10^{-19}$	
4	0.613	Y intersection	61.0832	1.295880	47.13647	$4.44 \cdot 10^{-59}$	$4.55 \cdot 10^{-15}$
		Veh. intensity	-0.00110	0.000558	-1.96529	0.005294	
		Bus arrival freq.	-0.055846	0.005584	-10.0021	$1.25 \cdot 10^{-15}$	
5	0.576	Y intersection	59.23299	0.994523	59.55918	$8.64 \cdot 10^{-67}$	$2.46 \cdot 10^{-12}$
		Veh. intensity	-0.001482	0.000428	-3.45842	0.00088	
		Bus arrival freq.	-0.034506	0.004285	-8.05256	$7.44 \cdot 10^{-61}$	

Table 4 shows the parameters of the regression dependence of the speed on the frequency of bus arrivals and the intensity of vehicle traffic when buses move in the general flow on 2, 3, 4 and 5 lane roads.

As can be seen from Table 4, with an increase in the number of traffic lanes, the influence of the frequency of bus arrivals and the intensity of vehicles on the speed of movement decrease. Analysis of the parameters of movement of vehicles passing through the bus stop zone, carried out using the simulation experiments, also shows that with an increase in the number of lanes, the impact of bus maneuvers at the stop on the loss of flow time decreases sharply [31].

According to Table 4, the regression equation, describing the dependence of the speed of movement of vehicles in the general flow on the intensity of movement of vehicles and the frequency of arrival of buses on a street with a two-lane road, will have the following form:

$$v_{flow} = 64.39 - 0.003N_{veh} - 0.079N_{bus}\,, \tag{2}$$

where:

N_{veh} is intensity of vehicles, veh/h;

N_{bus} is frequency of bus arrivals, bus/h.

Since in this case only the buses use the bus lane, the speed in this case is affected by the frequency of bus arrivals. Furthermore, the obtained R^2 value shows that the speed of buses in the dedicated lane is fairly well described by the proposed model.

Based on the values from Table 4, it is possible to similarly create the regression equations describing the dependence of the speed of movement of vehicles in the general flow on the frequency of arrival of buses and the intensity of movement of other vehicles for a street with 3, 4 and 5 traffic lanes.

As a result of creating a dedicated lane for buses, the number of lanes used by the general flow will decrease. For instance, when creating a dedicated lane on a two-lane road, one lane will remain for vehicle traffic and the speed of movement will depend only on the intensity of vehicle traffic.

During the simulation experiment it was found that when the buses move along a dedicated lane, for an increase in the frequency of movement from 80 to 240 bus/h the speed of buses decreases from 53.8 km/h to 36.7 km/h. The speed of buses along the dedicated lane does not decrease significantly until the frequency of arrival of buses reaches 180 bus/h, but then decreases sharply.

Based on the results of statistical analysis, the dependence of the speed of buses on the dedicated lane on the frequency of buses will be determined by the regression equation:

$$v_{bus} = -0.0013N_{bus}^2 + 0.3058N_{bus} + 37.066, \quad R^2 = 0.9139 \tag{3}$$

When the bus lanes are introduced, the traffic flow speed may decrease due to increased density. The frequency of bus arrivals in this case does not affect the average flow speed.

After the introduction of a bus lane, the impact of traffic volume on the speed of the remaining lanes must also be considered. Table 5 shows the regression equations describing the dependence of traffic speed on vehicle intensity for different numbers of traffic lanes. The regression equations in the Table 5 account for the dependence of traffic speed on the traffic volume after the bus lane is used (after reducing the number of lanes by one unit).

As can be seen from Table 5, it is possible, with sufficient accuracy to describe, the dependence of speed on the traffic intensity of vehicles on 2, 3, 4 and 5-lane roads after the implementation of a bus lane. With an increase in the number of lanes, vehicle time loss decreases comparatively. Furthermore, as can be seen from the values of the constant terms in the regression equations, the impact of traffic volume on speed decreases.

6 Checking the effectiveness of bus lane implementation due to lost time

The key performance indicators for public transport passengers using a bus lane include a reduction in average travel time, average delays on the lane, increased bus speeds, and an increase in the proportion of passengers served on time. For the entire transport system, these include the total time lost by all the users and the lane's throughput capacity for people and vehicles. The total time lost can be quantified by calculating the difference in travel time compared to the baseline scenario (without the lane). This takes into account the number of vehicles and passengers by mode, as well as the change in travel time.

Using the time lost as the sole criterion ignores effects such as reduced emissions, increased public transport reliability, and safety. However, it is clear that the creation of a bus lane improves safety by reducing conflicts between vehicles and increases reliability by increasing delivery speed. Furthermore, by regulating and coordinating the operation of buses operating on different routes, the dedicated lane can significantly reduce passenger time lost [32].

Using the obtained dependencies, the efficiency of introducing a bus lane is evaluated based on a comparison of the time losses of vehicles and bus passengers during the period under consideration. A bus lane will be efficient if the total time losses of vehicles and passengers before introducing the bus lane are greater than the total time losses after introducing the bus lane:

$$\sum T_{tl.bbl} > \sum T_{tl.abl}\,. \tag{4}$$

The time losses of all the vehicles and passengers before introducing the bus lane, during the period under consideration, are determined as follows:

Table 5 *Description of the dependence of the speed of movement of vehicles on the traffic intensity corresponding to different numbers of lanes after the introduction of bus lanes*

Number of lanes	Regression equations	R^2
2	$v_{veh} = -3 \cdot 10^{-6}N_{veh}^2 + 0.0069N_{veh} + 48.143$	$R^2 = 0.9648$
3	$v_{veh} = -2 \cdot 10^{-7}N_{veh}^2 + 0.002N_{veh} + 52.362$	$R^2 = 0.9643$
4	$v_{veh} = 9 \cdot 10^{-9}N_{veh}^2 + 0.0002N_{veh} + 52.648$	$R^2 = 0.9152$
5	$v_{veh} = 3 \cdot 10^{-7}N_{veh}^2 + 0.0015N_{veh} + 54.108$	$R^2 = 0.973$

$$\sum T_{tl.bbl} = \frac{l(N_{pass} + N_{veh})}{v_{flow}}, \tag{5}$$

where:

l is length of the section under consideration, km;

N_{pass} is a number of passengers passing through the section under consideration in one hour.

The value N_{pass} can be defined as $N_{pass} = N_{bus} \cdot D_{bus}$, where D_{bus} is the average number of passengers carried on one bus. It is also possible to obtain accurate information on the number of passengers carried per hour from the transport companies or directly from buses by direct observation.

The total time losses of all the road users after the creation of a bus lane are determined as:

$$\sum T_{tl.abl} = \sum T_{plt.abl} + \sum T_{vlt.abl}, \tag{6}$$

where:

$\sum T_{plt.abl}$ is total passangers loss time after implementation of bus lane, hour;

$\sum T_{vlt.abl}$ total vehicless loss time after implementation of bus lane, hour.

$$\sum T_{plt.abl} = \frac{lN_{pass}}{v_{bus.abl}}, \tag{7}$$

$$\sum T_{vlt.abl} = \frac{lN_{veh}}{v_{veh.abl}}. \tag{8}$$

Thus, the implementation of a bus lane on the road is advisable when the time loss values, calculated using Equations (5) and (6), satisfy the condition in Equation (4). If this condition was met throughout the day (for all hours of operation of buses), then the use of an exclusive bus line is required. Otherwise, the effectiveness of implementation other types of bus lanes should be checked.

7 Discussion

Now is checked the expediency of implementation a bus lane for a given section of a two-lane road for considered period (hour). According to Equations (2) and (5), the total time loss of all the road users, on a given section of a two-lane road before the bus lane implementation, is determined as:

$$\sum T_{tl.bbl} = \frac{l(N_{pass} + N_{veh})}{64.39 - 0.003N_{veh} - 0.079N_{bus}}. \tag{9}$$

According to Equations (3) and (7), the time loss of passengers on a given section of a two-lane road, after the bus lane implementation, is determined as:

$$\sum T_{plt.abl} = \frac{lN}{-0.0013N_{bus}^2 + 0.3058N_{bus} + 37.066}. \tag{10}$$

According to data in Table 5 and Equation (8) the time loss of vehicle users on a given section of a two-lane road, after the bus lane implementation, is determined as:

$$\sum T_{vlt.abl} = \frac{lN_{veh}}{-3 \cdot 10^{-6}N_{veh}^2 + 0.0069N_{veh} + 48.143}. \tag{11}$$

Thus, the total time losses of all the road users after the creation of a bus lane will be:

$$\sum T_{tl.abl} = \frac{lN_{pass}}{-0.0013N_{bus}^2 + 0.3058N_{bus} + 37.066} + \\ + \frac{lN_{veh}}{-3 \cdot 10^{-6}N_{veh}^2 + 0.0069N_{veh} + 48.143}. \tag{12}$$

For example, let the number of passengers transported by buses on a given section of a two-lane road be 2000 pass/h, the intensity of vehicle traffic - 1800 veh/h, the frequency of buses - 90 buses per hour, then, based on Equations (9) and (12), one obtains:

$$\sum T_{tl.bbl} = 58.6\ h; \ \sum T_{tl.abl} = 57.909\ h. \tag{13}$$

In this case, the traffic density according to the obtained speed values and according to Equation (1), before using the dedicated lane for one traffic lane will be $k = 26 veh/km$, and after using the dedicated lane for one traffic lane of the general flow $k = 35 veh/km$.

If the condition in Equation (4) was satisfied for the case under consideration, during all the periods of the day, the use of an exclusive bus lane is appropriate. If the condition in Equation (4), was not satisfied, it is then logical to conduct a check for each hour separately and determine the appropriateness of introducing a specific type of bus lane. Since the off-peak hours reduce the traffic density and the flow becomes free, it does not particularly affect delays for buses moving in the flow. More precisely, it is possible, for example, to determine hours, which allow the movement of other vehicles on the bus lane during these hours (temporary bus lane). For comparison to the last example, if the number of passengers transported by buses on a given section of a two-lane road was 1350 pass/h, the intensity of vehicle traffic - 1200 veh/h, and the frequency of buses - 60 buses per hour, based on Equations (9) and (12) one gets:

$$\sum T_{tl.bbl} = 36.4\ h; \ \sum T_{tl.abl} = 39.7\ h. \tag{14}$$

In this case the traffic density before the application of a dedicated lane for one traffic lane would be $k = 12 veh/km$, and after the application of a dedicated lane for one traffic lane of the general flow $k = 22 veh/km$.

Similarly, the effectiveness of introducing a bus lane on a road with a large number of traffic lanes can be checked. Moreover, it is possible to check the expediency of bus lane implementation permitted for the movement of taxis or vehicles with 2-3 passengers, then the values of the traffic intensity of these vehicles should be taken into account in Equation (6) separately.

The formulas take into account the variability of traffic flow. However, in the event of unexpected disruptions, other approaches can be used, such as risk management methods.

8 Conclusion

Reducing the travel time is one of the main goals in organizing traffic in cities. Assessing the traffic efficiency, based on individual vehicle delays does not yield the desired results. Depending on the current state of the traffic flow, individual vehicle delays can fluctuate significantly, so it is important to assess the overall delay. Therefore, when introducing the bus lanes in the section under consideration, it is also advisable to check whether the overall time losses for all the road users are reduced.

Simulation experiments can be used to estimate the speed of vehicles on a given section for the given road conditions. Statistical processing of the results of simulation experiments in the PTV VISSIM program shows that the dependence of the speed of buses and other vehicles on the intensity of the traffic flow and the frequency of bus arrivals is well described by regression equations. Based on the speed of movement obtained by the regression models, it is possible to calculate the time losses of vehicles and buses (and therefore passengers).

The proposed methodology for determining the feasibility of using dedicated bus lanes, based on a comparison of the total time lost by all the road users for bus travel in the general traffic flow and in a dedicated bus lane, can be applied for each hour of the day, taking into account the dynamic changes in traffic flow and the frequency of bus arrivals under given conditions (lane width, speed limit, street section length, stop placement, etc.).

Taking into account the intensity of other vehicles allowed to use the bus lane, the proposed methodology can be used to test the effectiveness of other forms of bus lane implementation.

Acknowledgment

The authors received no financial support for the research, authorship and/or publication of this article.

Conflicts of interest

The authors declare that they have no known competing financial interests or personal relationships that could have appeared to influence the work reported in this paper.

References

[1] National Academies of Sciences, Engineering, and Medicine. Transit capacity and quality of service manual [online]. 3rd ed. Transit Cooperative Highway Research Program (TCRP) Report 165. Washington, DC: The National Academies Press, 2013. ISBN: 978-0-309-28344-1. Available from: https://doi.org/10.17226/24766

[2] CESME, B., ROISMAN, R., BURNS, R., LIST, K., KOUDOUNAS, A., CUELLAR, J., SANDERS, M., LEE, K., MILLER, D. Strategies and barriers in effective bus lane ımplementation and management: best practices for use in the Greater Washington, D. C. Region. *Transportation Research Record: Journal of the Transportation Research Board* [online]. 2018, **2672**(8), p. 29-40. ISSN 1361-1981, eISSN 2169-4052. Available from: https://doi.org/10.1177/0361198118791914

[3] DADASHZADEH, N., ERGUN, M. Spatial bus priority schemes, implementation challenges and needs: an overview and directions for future studies. *Public Transport* [online]. 2018, **10**, p. 545-570. eISSN 1613-7169. Available from: https://doi.org/10.1007/s12469-018-0191-5

[4] RUSSO, A., ADLER, M. W., VAN OMMEREN J. N. Dedicated bus lanes, bus speed and traffic congestion in Rome. *Transportation Research Part A: Policy and Practice* [online]. 2022, **160**, p. 298-310, ISSN 0965-8564, eISSN 1879-2375. Available from: https://doi.org/10.1016/j.tra.2022.04.001

[5] PANAGIOTIS, V., IOANNA, Z., GEORGIA, L., SOKRATES, B. Considerations about an outbound bus lane in an urban area. *Ekistics and the New Habitat* [online]. 2022, **81**(1), p. 14-19. eISSN 2653-1313 Available from: https://doi.org/10.53910/26531313-E2021811509

[6] BAYRAK, M., GULER, I. Optimization of dedicated bus lane location on a transportation network while accounting for traffic dynamics. *Public Transport* [online]. 2021, **13**, p. 325-347. eISSN 1613-7169. Available from: https://doi.org/10.1007/s12469-021-00269-x

[7] OLSTAM, J., HALL, C. H., BHATTACHARYYA, K., GEBREHIWOT, R. Traffic impacts of dynamic bus lanes: a simulation experiment of real-world bus operations. *European Transport Research Review* [online]. 2025, **17**(1), p. 1-17. eISSN 1866-8887. Available from: https://doi.org/10.1186/s12544-025-00712-1

[8] OTHMAN, K., SHALABY, A. S., ABDULHAI, B. Dynamic bus lanes versus exclusive bus lanes: comprehensive comparative analysis of urban corridor performance. *Transportation Research Record: Journal of the Transportation Research Board* [online]. 2023, **2677**(1), p. 341-355. ISSN 1361-1981, eISSN 2169-4052. Available from: https://doi.org/10.1177/03611981221099517

[9] LI, H., YUAN, Z., YUE, R., YANG, G., CHEN, S., ZHU, CH. A lane usage strategy for general traffic access on bus lanes under partially connected vehicle environment. *Transportmetrica A: Transport Science* [online]. 2025, latest articles, p. 1-16. ISSN 2324-9935, eISSN 2324-9943. Available from: https://doi.org/10.1080/23249935.2025.2467750

[10] XUE, Y., ZHANG, B., TAN, C., CHEN, H., BAO, G., LIU, J., BI, Y., LI, J., GUAN, H. Decision analysis and benefit evaluation of ridesharing behavior in bus lanes based on cumulative prospect theory. *Sustainability* [online]. 2025, **17**(5), 1991. eISSN 2071-1050. Available from: https://doi.org/10.3390/su17051991

[11] ZHANG, Z., RONG, L., XIE, Zh., YANG, X. Dynamic multi-function lane management for connected and automated vehicles considering bus priority. *Sustainability* [online]. 2024, **16**(18), 8078. eISSN 2071-1050. Available from: https://doi.org/10.3390/su16188078

[12] YIN, Z., YUAN, K., ZHENG, S. Optimization of traffic flow by allowing private cars to merge into the bus lane at specific locations. *Journal of Advanced Transportation* [online]. 2024, **1**, p. 1-15. eISSN 2042-3195. Available from: https://doi.org/10.1155/2024/9076413

[13] KONG, Y., YANG, Y., LI, A. Design and simulation study of a variable bus lane system. In: 2024 International Conference on Rail Transit and Transportation ICRTT 2024: proceedings [online]. 2024. ISBN 978-94-6463-610-9. Available from: https://doi.org/10.2991/978-94-6463-610-9_6

[14] QIAO, W., YANG, Z., PENG, B., CAI, X., ZHANG, Y. Integrated evaluation method of bus lane traffic benefit based on multi-source data. *Mathematics* [online]. 2024, **12**(17), 2664. eISSN 2227-7390. Available from: https://doi.org/10.3390/math12172664

[15] TSITSOKAS, D., KOUVELAS, A., GEROLIMINI, N. Modeling and optimization of dedicated bus lanes space allocation in large networks with dynamic congestion. *Transportation Research Part C: Emerging Technologies* [online]. 2021, **127**, p. 1-40. ISSN 0968-090X, eISSN 1879-2359. Available from: https://doi.org/10.1016/j.trc.2021.103082

[16] SUN, X., LU, H., FAN, Y. Optimal bus lane ınfrastructure design. *Transportation Research Record: Journal of the Transportation Research Board* [online]. 2014, **2467**(1), p. 1-11. ISSN 1361-1981, eISSN 2169-4052. Available from: https://doi.org/10.3141/2467-01

[17] MELITI, S., KADAR, H. A. A. Evaluating the effects of exclusive bus lanes on passenger ridership and travel time in Kuala Lumpur city roads. *Journal of the Eastern Asia Society for Transportation Studies* [online]. 2011, **9**, p. 986-999. ISSN 1881-1124. Available from: http://irep.iium.edu.my/id/eprint/4048

[18] FADYUSHIN, A., ZAKHAROV, D. Influence of the parameters of the bus lane and the bus stop on the delays of private and public transport. *Sustainability* [online]. 2020, **12**(22), 9593. eISSN 2071-1050. Available from: https://doi.org/10.3390/su12229593

[19] ZHANG, W., ZHU, H., SONG, Z. A study on setting program for ıntermittent bus lanes at urban road ıntersections. *Journal of Transport Information and Safety* [online]. 2023, **41**(5), p. 158-166. ISSN 1674-4861. Available from: https://doi.org/10.3963/j.jssn.1674-4861.2023.05.016

[20] DE OLIVEIRA, R. M., DE PRINCE, D., MACHADO, E. L., DE ARAUJO, V. C. Impact of bus lanes on the speed of other vehicles in Sao Paulo. *Planning and Public Policies / Planejamento E Politicas Publicas* [online]. 2024, **65**, p. 47-74. eISSN 2359-389X. Available from: https://doi.org/10.38116/ppp65art2

[21] BURINSKIENE, M., GUSAROVIENE, M., GABRULEVICIUTE, S. K. the ımpact of public transport lanes on the operating speed of buses. In: 9th International Conference Environmental Engineering: proceedings. 2014. ISBN 978-609-457-640-9. p. 1-6.

[22] ARASAN, V. T., VEDAGIRI, P. Planning for dedicated bus lanes on roads carrying Highly heterogeneous traffic. In: 50th Annual Transportation Research Forum: proceedings [online]. 2009. p. 1-20. Available from: https://doi.org/10.22004/ag.econ.207621

[23] SZARATA, M., OLSZEWSKI, P., BICHAJLO, L. Simulation study of dynamic bus lane concept. *Sustainability* [online]. 2021, **13**, 1302. eISSN 2071-1050. Available from: https://doi.org/10.3390/su13031302

[24] TRAN, V. T., KAZUSHI, S., NGUYEN, C. Y., DOAN, T. T. Comparative analysis of bus lane operations in urban roads using microscopic traffic simulation. *Asian Transport Studies* [online]. 2013, **2**(3), p. 269-283. eISSN 2185-5560 Available from: https://doi.org/10.11175/eastsats.2.269

[25] HAWAS, Y. E. Simulation-based regression models to estimate bus routes and network travel times. *Journal of Public Transportation* [online]. 2013, **16**(4), p. 107-130. ISSN 1077-291X, eISSN 2375-0901. Available from: https://doi.org/10.5038/2375-0901.16.4.6

[26] LIU, Y., HE, S., ZHENG, S., LIN, Y., LONG, S., GE, L. Research on the traffic strategy of ıntermittent bus lane in ıntelligent network environment. In: 2021 6th International Conference on Transportation Information and Safety: proceedings [online]. IEEE. 2021. eISBN 978-1-6654-9713-8, p. 446-454. Available from: https://doi.org/10.1109/ICTIS54573.2021.9798494

[27] KNOOP, V. L. *Traffic flow theory: an introduction with exercises*. Delf: Delft University of Technology, 2018. ISBN 9789463663786.

[28] RIDA, N., HASBI, A. A Collaborative road traffic regulation approach using a wireless sensor network. *International Journal of Service Science, Management, Engineering, and Technology (IJSSMET)* [online]. 2022, **13**(1), p. 1-19. ISSN 1947-959X, eISSN 1947-9603. Available from: https://doi.org/10.4018/IJSSMET.290330

[29] FABIAN, P., CULIK, K., KALASOVA, A., CERNICKY, L. The ımpact of road realignment on the traffic load in the surrounding area. *Vehicles* [online]. 2024, **6**(4), p. 1942-1962. eISSN 2624-8921. Available from: https://doi.org/10.3390/vehicles6040095

[30] YU, CH., CHEN, J., XIA, G. Coordinated control of ıntelligent fuzzy traffic signal based on edge computing distribution. *Sensors* [online]. 2022, **22**, 5953. eISSN 1424-8220. Available from: https://doi.org/10.3390/s22165953

[31] DASHDAMIROV, F., ABDURRAZZOKOV, U., ZIYAEV, K., VERDIYEV, T., JAVADLI, U. Simulation testing of traffic flow delays in bus stop zone. *E3S Web of Conferences* [online]. 2023, **401**, 01070. Available from: https://doi.org/10.1051/e3sconf/202340101070

[32] DASHDAMIROV, F. Improving of ınteraction of routes at high density stops by adjusting bus arrival time. *Transport and Telecommunication* [online]. 2023, **24(3)**, p. 309-319. ISSN 1407-6160, eISSN 1407-6179. Available from: https://doi.org/10.2478/ttj-2023-0025

INFLUENCE OF TRAFFIC FLOW PARAMETERS ON THE DELAY DURATION AT SIGNALIZED INTERSECTIONS

Taras Postranskyy*, Mykola Boikiv, Maksym Afonin, Ihor Mohyla

Department of Transport Technologies, Lviv Polytechnic National University, Lviv, Ukraine

*E-mail of corresponding author: taras.m.postranskyi@lpnu.ua

Taras Postranskyy 0000-0001-6120-9914,
Maksym Afonin 0000-0001-5850-7478,
Mykola Boikiv 0000-0002-4997-3677,
Ihor Mohyla 0000-0001-9710-6191

Resume

In this study is examined the influence of traffic flow parameters on delay duration at signalized intersections of urban multi-lane streets. The findings show that traffic composition strongly affects delays at low volumes, while its influence decreases as total volume grows. These results highlight the need to account for traffic composition, not only volume, when optimizing the signal timing and managing flows. The novelty of the study lies in modelling delay as a joint function of traffic volume and traffic flow composition, where the share of passenger cars is varied independently, rather than through the generalized passenger car unit-based growth, enabling a more accurate assessment of delay formation under heterogeneous traffic conditions.

Article info

Received 1 September 2025
Accepted 21 November 2025
Online 16 December 2025

Keywords:

traffic volume
microsimulation
traffic delay
signalized intersection

Available online: https://doi.org/10.26552/com.C.2026.004

ISSN 1335-4205 (print version)
ISSN 2585-7878 (online version)

1 Introduction

Every year, a constant increase in the number of vehicles can be seen on the streets and roads of settlements. In return, that leads to several negative phenomena, such as traffic delays [1], increased environmental pollution [2], noise pollution [3], etc. Among all the above-mentioned consequences of motorization, the most significant impact is a sharp increase in traffic volume, which leads to traffic congestion. That can be explained by the fact that although the number of vehicles on streets and roads is increasing, the capacity of transportation routes usually remains unchanged. One of the reasons for this challenge is that reconstructing an existing roadway, or creating a new one, incurs significant financial costs. However, intersections are often the bottlenecks in the road network.

In compliance with the aforementioned, the existing indicators of traffic flows were measured and the traffic characteristics at signalized intersections on city streets were analyzed. These data were the input information for creating simulation models of traffic flows in the PTV VISSIM microsimulation environment (PTV - Planung Transport Verkehr). This approach enables the analysis of the dynamics of changes in traffic flows and traffic delays. In addition, the relevance of this approach lies in reducing the probability of erroneous engineering solutions in traffic management and predicting the behavior of traffic flows at signalized road network facilities.

The aim of this research was to identify the patterns of composition and intensity's influence on the duration of traffic delay at regulated intersections, providing an input for the management and setup of adaptive traffic signal control systems. In this case, the proven methods of traffic simulation at controlled city street intersections were used. Such modern approaches enable the identification of patterns in traffic delays within the dynamics of traffic flows, allowing for the intelligent control of traffic lights at intersections. Finding optimal solutions by analyzing existing intersection parameters and traffic flow characteristics is essential. The following main tasks needed to be accomplished to achieve this goal:

- to analyze the performance of a standard four-leg signalized intersections of city streets and determine the existing indicators of traffic flow on them;
- to create models of street intersections and calibrate them to the existing traffic conditions;
- to simulate traffic and determine the duration of traffic delays based on the results;
- to analyze the data and identify patterns of change

in the duration of traffic delays based on the characteristics of transport flows.

The next section of this article includes literature review with recent publications, which are related to traffic optimization. The research methodology is described in "Materials and methods" section. In the section "Main results", presented are most important graphs and dependencies obtained during the survey. The sections with discussion and conclusions are given at the end of the paper.

2 Literature review

Delays at signalized intersections can occur due to several reasons. One of them is stopping of vehicles, which is directly caused by the operation of traffic lights.

These also include delays caused by the control process (Figure 1), particularly during the vehicle's acceleration and deceleration in the traffic light object area and its direct idle time [4-5].

The diagram in Figure 1 is rather generalized. This is because, depending on the dynamic characteristics of vehicles, the processes of braking and acceleration can be carried out to varying extents.

Webster's delay model can also be used to mathematically describe the duration of vehicle delays at signalized intersections. It involves considering the following quantities [6-7]: cycle length, effective green time, arrival flow rate, saturation flow, and exit capacity. However, as the composition of the traffic flow changes, the impact of a particular indicator may change. For example, the effective duration of a green signal for a traffic flow consisting of passenger cars will differ from that of slow-moving vehicles. It is primarily due to their starting delays after the permissive signal is turned on. In particular, the authors of [8] found a difference in the processes of car queue accumulation before the stop line and its dissipation, depending on the composition of the traffic flow. For example, as the share of trucks and buses in the queue grows, it leads to longer intervals in the movement of vehicles at the beginning of the permissive signal. At the same time, the authors noted that the dissipation process also depends on the directions in which the traffic is allowed to move simultaneously.

The Highway Capacity Manual is an important document that reflects transport processes in automotive transport and recommendations for traffic management. The manual also displays acceleration-deceleration delay patterns [9]. At the same time, the average values of the speed, acceleration, and deceleration are considered. It should be noted that the values of these indicators will be strongly related to the types of vehicles and their technical parameters. Thus, it is not enough to determine the duration of the delay based on average values. It is also essential to consider the composition of the traffic flow. Its distribution will change to varying degrees, both the initial delays of cars and the dispersion of the vehicles` queue during the traffic signal cycle.

Adaptive control systems can also be used to reduce the impact of traffic lights on traffic delays [6, 10]. They can consider the characteristics of traffic flows and various changes in movement conditions, including seasonal and short-term [11]. At the same time, adaptive traffic signal control systems can operate based on pre-created sustainable behavioral algorithms [12], as well as using approaches that involve the use of machine learning [13], fuzzy logic [14], deep reinforcement learning [15], multi-agent broad reinforcement learning [16], meta-heuristic search algorithms [17], etc. All of the above-mentioned traffic signal control options are designed to improve the traffic flow, reduce delays, and

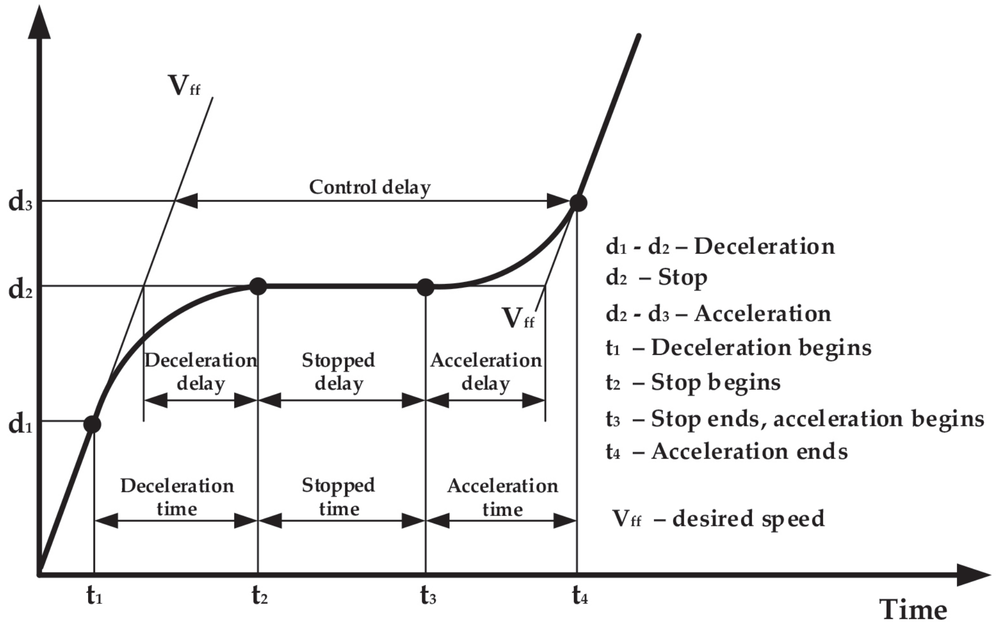

Figure 1 *The formation of traffic delays at signalized intersections [4]*

minimize congestion on the road network. However, each of the above cases requires input information and the training or adjustment of the system and traffic signal control algorithms. Therefore, an important task is conducting the field studies directly on the road network and obtaining initial traffic delay patterns and their causes.

It is equally important to note that today, numerous tools are available for analyzing traffic management design solutions. First, it is possible to use specialized software for simulation modelling. Simulation models enable the reproduction of complex transport processes under conditions as close as possible to the real-world ones. In its turn, it helps to determine the effectiveness of design solutions at the stage of their development. These tools contribute to an objective assessment of the road network's capacity and its elements [18], analysis of road safety and identification of accident sites [19], identification of areas for further development, and prioritization of public transport [20], among other applications. Additionally, the use of simulation tools enables the comparison of alternative traffic management options with the overall reconstruction costs of the study object and its associated facilities [21]. It should also be noted that the issue of using the simulation modelling tools is particularly relevant in the context of a dynamic increase in traffic volume and the need to make informed management decisions.

Thus, summarizing the above information, today, various scientific dependencies and models can reflect the formation of transport delays and allow for their measurement. However, they often consider generalized traffic flow indicators, including the calibrated passenger car equivalent. In contrast, the proposed model suggests considering the composition of the traffic flow, in particular, due to the passenger cars' share in the flow. In addition, a wide range of hardware and software solutions are available to adapt the operation of traffic signal control systems to traffic conditions and flow characteristics. However, the effective implementation of such solutions requires a deep understanding of the patterns of change in the traffic flow parameters, depending on the volume, composition of traffic, and traffic conditions at the intersection. Therefore, in any case, the primary task will continue to be field research and identification of patterns to make initial adjustments to the regulatory tools. Additionally, simulation modelling tools can currently be utilized to obtain initial data for machine learning and the adaptation of traffic signal activation programs by controllers, thereby achieving the aforementioned goals.

To summarize the state-of-the art from the presented research it should be noted that research devoted to assessing traffic queues, among methods of optimization and traffic light settings, should also focus on the causes of these delays. Therefore, studying the composition of traffic flow as one of the causes of increased congestion at the signalised intersections is a relevant task at this time.

3 Materials and methods

Delays in traffic flow at intersections lead to a decrease in the efficiency of the transportation network and a decline in road safety. Modelling the traffic flows at intersections of varying complexity helps to optimize traffic on streets and roads, reduce congestion, and increase the capacity of transport infrastructure [22]. Improving urban infrastructure (by building new roads or junctions) and analyzing the growth of motorization levels using simulation modelling helps to predict how the traffic flows would behave under different traffic conditions and intersection operations [23]. For the successful design of new transport systems or the modernization of existing ones, evaluating their performance in advance, under different traffic flow parameters, is crucial.

To clarify up the research methodology, there is step-by step survey chart, presented on Figure 2, dividing this work for two stages: research and analytics.

First, field data on traffic volume, composition and signal timings are collected at two standard four-leg signalised intersections, followed by a detailed characterisation of their lane geometry and phase structure. based on

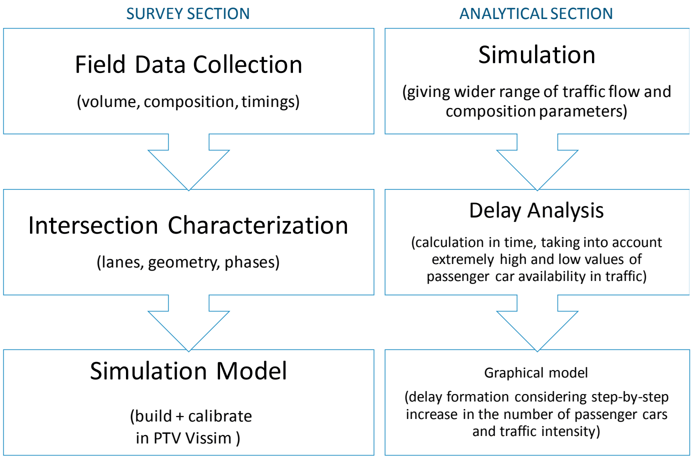

Figure 2 *Step-by-step methodology chart*

that, the calibrated microsimulation models are built in PTV VISSIM to reproduce the existing conditions. In the analytical section, those models are used to run a series of simulation experiments in which traffic flow parameters are systematically varied and the resulting delays are evaluated and summarised in graphical form.

The key novelty of the method lies in the analytical stage: instead of increasing only the total traffic volume, expressed in generalized passenger car units, the simulations independently vary both the traffic volume and the share of passenger cars in the flow, while keeping the presence of heavy vehicles and buses explicit. This allows the model to capture how changes in traffic composition, not just total intensity, influence the delay formation at signalised intersections and to identify the critical regimes associated with heterogeneous flows.

The challenge of improving the traffic flow at such standard four-leg signalized intersections lies in considering traffic from all directions. This requires a careful approach to the distribution of time duration between phases within

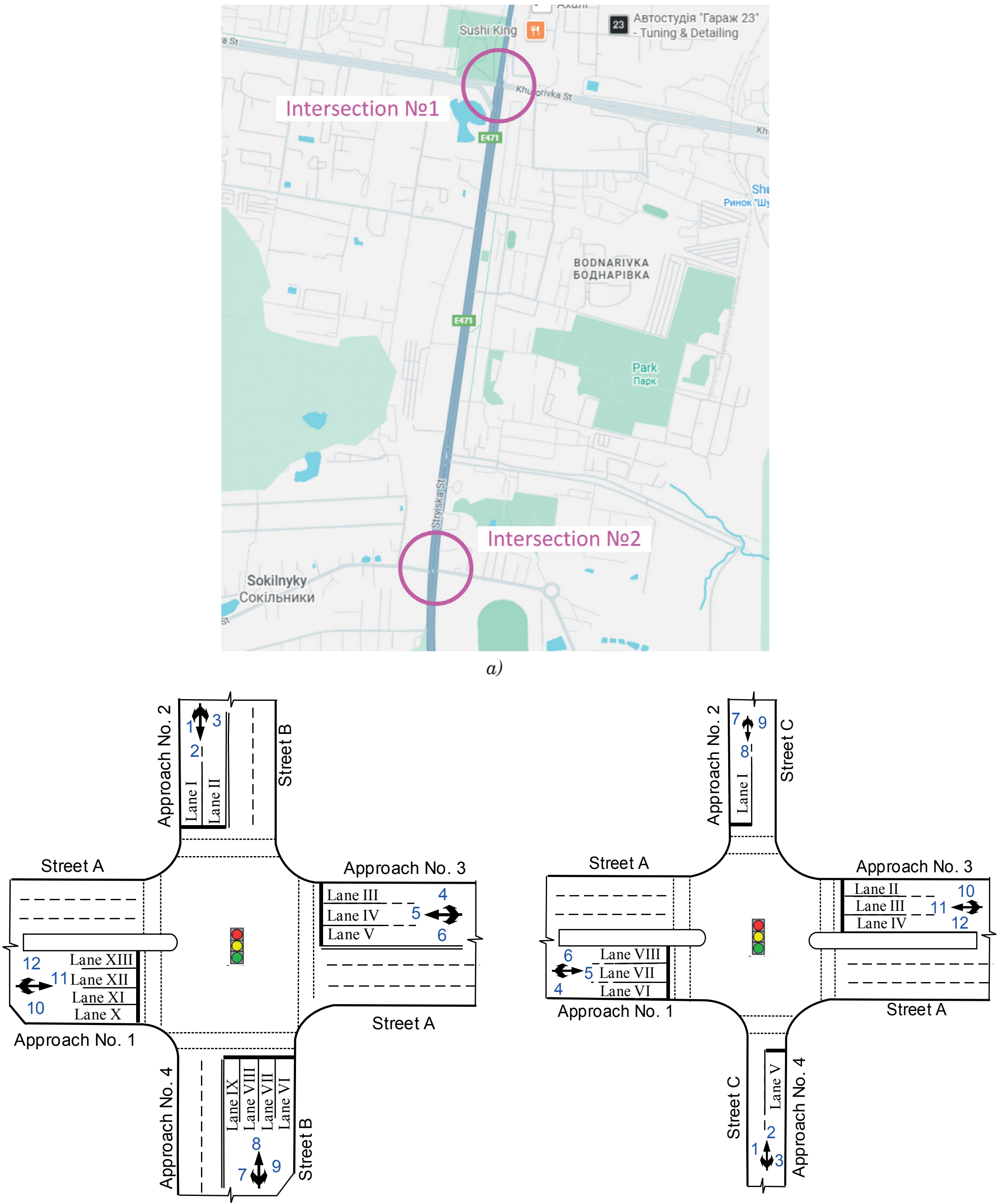

a)

b)

c)

Figure 3 *Scheme of the two studied signalized intersections of urban arterial multi-lane streets: (a) Locations of intersections (b) Intersection of streets No. 1 (Streets A and B); (c) Intersection of streets No. 2 (Streets A and C)* the control cycle. In conditions of high urban traffic, it is crucial to ensure a balance between safety, capacity, and minimization of traffic delays. Traffic control in three or more phases at an intersection requires a more flexible formation of the control cycle, including the conflictology of flows, the configuration of the intersection, and the main parameters of traffic flows. This complicates the development of measures to improve traffic management at standard four-leg signalized intersections, but allows for an increase in the efficiency of intersections in urban traffic conditions. Therefore, there is a close relationship between the traffic flow indicators and the effective operation of signalized intersections. For a comprehensive study of the peculiarities of signalized intersection functioning, a series of studies on existing traffic flow indicators at the standard four-leg signalized intersections on city streets is proposed. In particular, the first stage of the research involved analyzing the permitted traffic directions and planning parameters of two standard four-leg signalized intersections (Figure 3) located on the same urban arterial street section (Street A).

The planning characteristics of the studied signalized intersections are analyzed (Figure 3a), with particular emphasis on the geometric parameters of the traffic lanes at each approach. They both share the common characteristics that the main road at the two signalized intersections is Street A, the arterial Street, and, in general, the fact that both intersections form city streets that intersect at 90 degrees. In addition, it was found that at intersection No. 1 (Figure 3b) each approach features a multi-lane roadway with a lane width of 3.75 m, allowing for all possible maneuvers. Additionally, approach 1 (Street A) features a 3.5-meter-wide separation lane. It is also important to note that Street B, which also forms this intersection, is a major arterial street of general city significance. At intersection No. 2 (Figure 3c), there are three lanes in each direction in the main direction, with a width of 3.75 m, and a 3 m wide separation lane. The roadway surface on all approaches to the intersections is characterized by flatness and satisfactory technical condition. Street A here has the same arterial significance, as on previous intersection. Minor streets (streets B and C) have a lane width of 3.75 m. These streets belong to local significance, which corresponds to both their geometric parameters and traffic volume. In addition, the sufficient width of the lanes on these streets allows for the combination of turning and straight traffic flows from one lane during the control phases. There are no transverse and longitudinal roadway slopes on minor streets.

The next stage of the study involved investigating the parameters of traffic flows at two adjacent signalized intersections. The study of traffic flow parameters was carried out using the field method, manually counting the intensity and composition of the traffic flow. The short-term (15 min) measurements were made during the peak traffic periods on every hour from Tuesday to Thursday. Peak periods in the city under study (Lviv, Ukraine) are considered to be the morning hours from 8:00 to 9:30. It should also be noted, that intensity measurements were taken in dry and warm weather (in May 2025). A comparative analysis of the traffic flow`s composition and intensity was conducted based on the obtained data. In addition, it was established whether there were any random discrepancies in the measurements, including calculating the weighted average percentage of different types of vehicles. The results of the study on traffic volumes for each approach and by traffic direction are shown in Figure 4. In this scheme, the estimated traffic volume for each approach is the maximum intensity observed during the busiest hour of all days of the study.

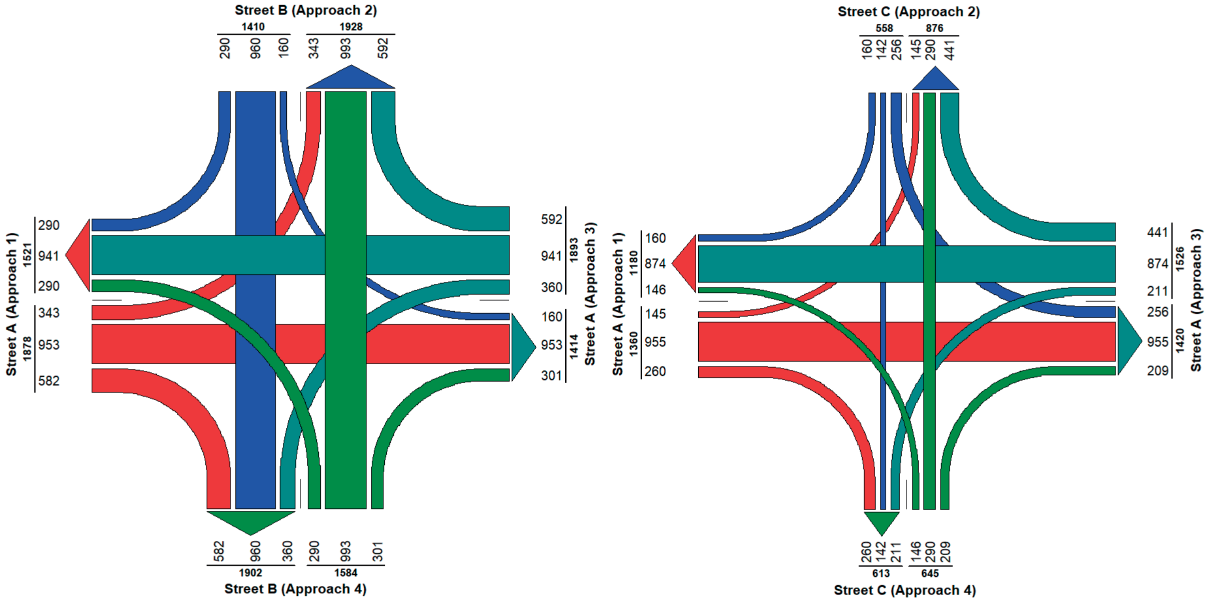

a) *b)*

Figure 4 *Cartogram of traffic volume by directions at intersection No. 1 (a) and intersection No. 2 (b)*

***Table 1** Percentage distribution of traffic flows by direction on the approaches to the studied signalized intersections*

Type of vehicle maneuver from the approach	Approach No. 1	Approach No. 2	Approach No. 3	Approach No. 4
	Intersection No. 1			
Right-turn	31%	21%	31%	18%
Straight	51%	68%	50%	63%
Left-turn	18%	11%	19%	19%
	Intersection No. 2			
Right-turn	19%	29%	29%	23%
Straight	70%	25%	57%	45%
Left-turn	11%	46%	14%	32%

According to the above data, it was found that the highest values were recorded in the direction of the main road (Street A). Additionally, the direct driving vehicles (whose share ranges from 25% to 70%, depending on the approach) dominate the traffic flow. In turn, the share of right-turn flows varies from 11% to 46%, depending on the approach and direction of travel. Detailed information about the distribution of vehicles by traffic direction at the studied intersections is provided in Table 1.

It should be noted that on the main direction of the intersections (Street A), the largest share of vehicles moves straight ahead, and the smallest share of traffic flow is attributed to the left-turning maneuvers. In addition, it should be noted that the distribution of traffic flows by type of maneuver differs between different approaches to the same intersection and between intersections themselves. It indicates the various configurations and purposes of city streets, as well as the points of attraction near each intersection. According to the current law, the speed limit for settlements in all directions and at intersections is 50 km/h. Within the intersection, during the field studies, traffic speeds were observed that did not exceed the established standards, and sometimes were lower and ranged from 25-40 km/h. Different traffic flows and the automatic speeding cameras at these study intersections explain this speed.

At the studied intersections, there is also significant heterogeneity in traffic flows, which varies depending on the growth of total traffic volume on the approaches and different periods of the day. According to the results of field studies, it was found that passenger cars predominate in traffic flows, and public transport has the smallest share.

According to the results of field studies, it was found that the passenger cars predominate at all approaches to signalized intersections. The largest share is observed on Main Street A, where the highest traffic volume was recorded. It should also be noted that the studied intersections are located in urban areas, so the freight transport here is primarily represented by vehicles of small and medium capacity (2-5 tons) used to supply goods and deliver products within the settlement. Additionally, it is worth noting that at intersection No.

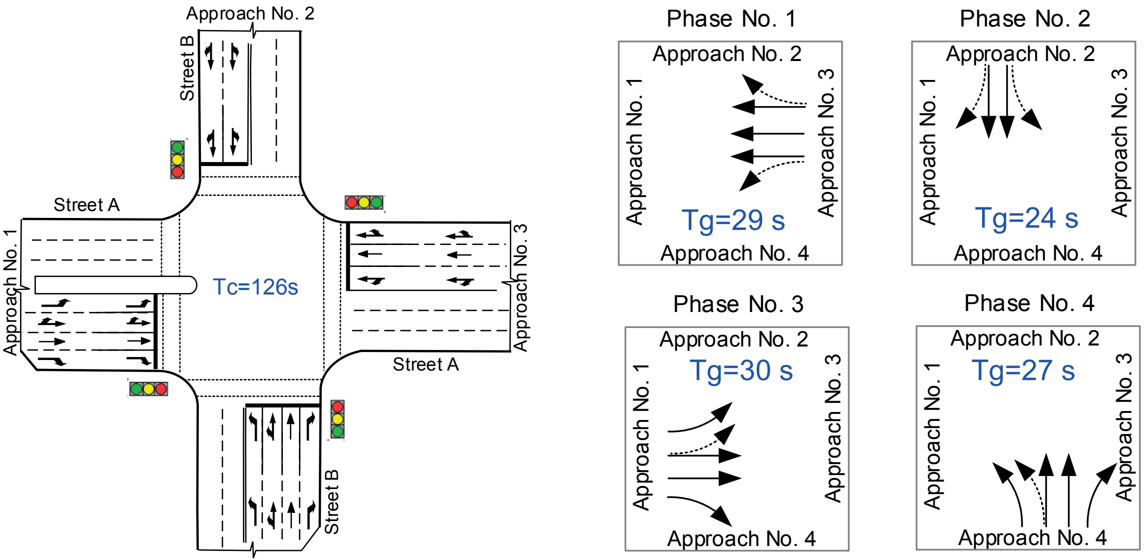

a) *b)*

***Figure 5** Permitted directions of traffic flow by lanes at intersection No. 1 (a) and the phase sequence of vehicles (b)*

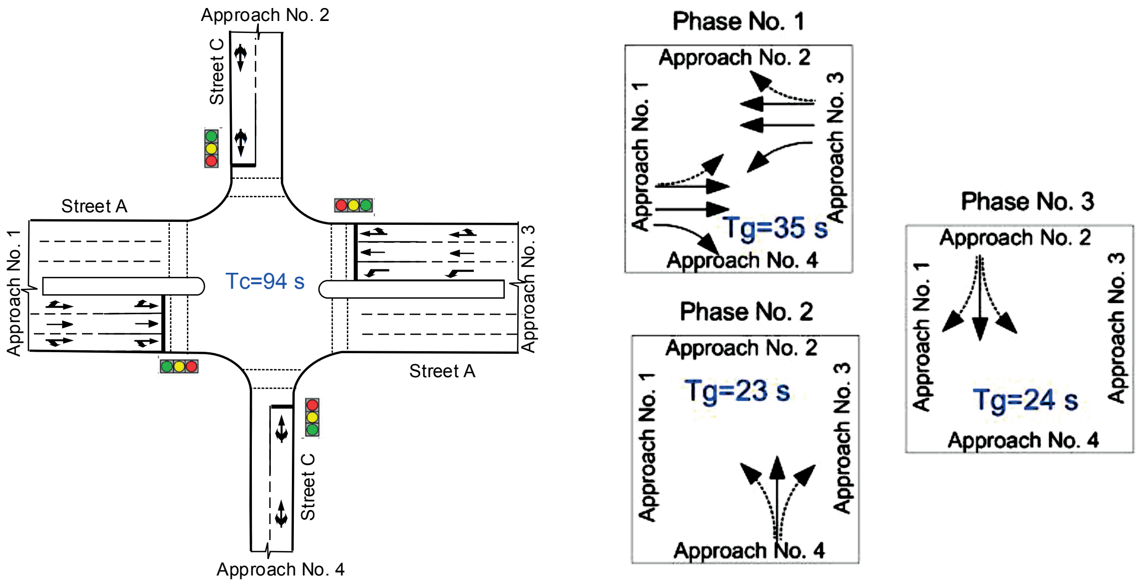

a) *b)*

Figure 6 *Permitted directions of traffic flow by lanes at intersection No. 2 (a) and the phase sequence of vehicles (b)*

1, the public transportation is represented by medium-sized buses and trolleybuses, whereas at intersection No. 2, it is only represented by buses. Therefore, due to the absence of trolleybus traffic within the intersection No. 2, the share of public transport there is only 8%.

Based on the results of field studies, the parameters of the traffic signal operation modes were also determined. The phase sequence at intersection 1 consists of four phases, as shown graphically in Figure 5. The total duration of the traffic light cycle at this intersection is 126 seconds.

At the intersection of Streets No. 1 and No. 2, there is a low volume of pedestrian traffic that does not conflict with the traffic flow. At the same time, their movement occurs in each phase, but they were not taken into consideration. It is also worth noting that the intersection has good traffic conditions, with a minimal longitudinal slope of the roadway.

At intersection No. 2, the traffic light cycle time is 94 seconds. The phase sequence of traffic flows at the intersection consists of three control phases, which are graphically shown in Figure 6.

At each of the studied intersections, the duration of the yellow signal is 4 seconds. Both study objects are the standard four-leg signalized intersections with a significant control cycle of over 80 seconds. Their common characteristics is that the main direction of traffic passes along a city arterial street. It has three or more lanes on each approach, which allows for the distribution of traffic flows in separate directions. At the intersections, the traffic organization is realized using the multi-phase traffic signalization (three or more phases of regulation), considering the most congested directions of the intersection. As for the main difference between these intersections, unlike intersection No. 1, intersection No. 2 has combined turning and straight traffic on approaches No. 2 and No. 4 (on secondary streets) in one lane.

The field studies have shown that the heterogeneity of traffic flow at signalized intersections of city streets affects the duration of traffic delays. This phenomenon is prevalent during the peak periods, when traffic volume increases significantly. In addition, this phenomenon depends on the composition of the traffic flow, as different types of cars have distinct dynamic characteristics and, therefore, require varying times to maneuver and pass through the intersection. In turn, that affects the capacity and overall functioning of signalized intersections.

Based on the obtained numerical parameters and characteristics of traffic flows, the simulation models of street intersection functioning were created in the PTV VISSIM software environment. It should be noted that the design and operation of the traffic model of a signalized intersection in PTV VISSIM were based on its characteristics and structural components:

- planning characteristics of streets on the approaches to the intersection (number of lanes, their width, permitted directions);
- peculiarities of the operation of the system's controlled intersections and traffic signal control in general (number of control phases and their duration, total duration of the traffic light cycle);
- parameters of traffic flows (traffic volume, composition of the traffic flow, and its distribution by directions).

Considering the above, models of the studied intersections' functioning were created in the PTV VISSIM environment (Figure 7). This approach enables the collection of necessary data through the simulation and identification of dependencies between changes in traffic delay.

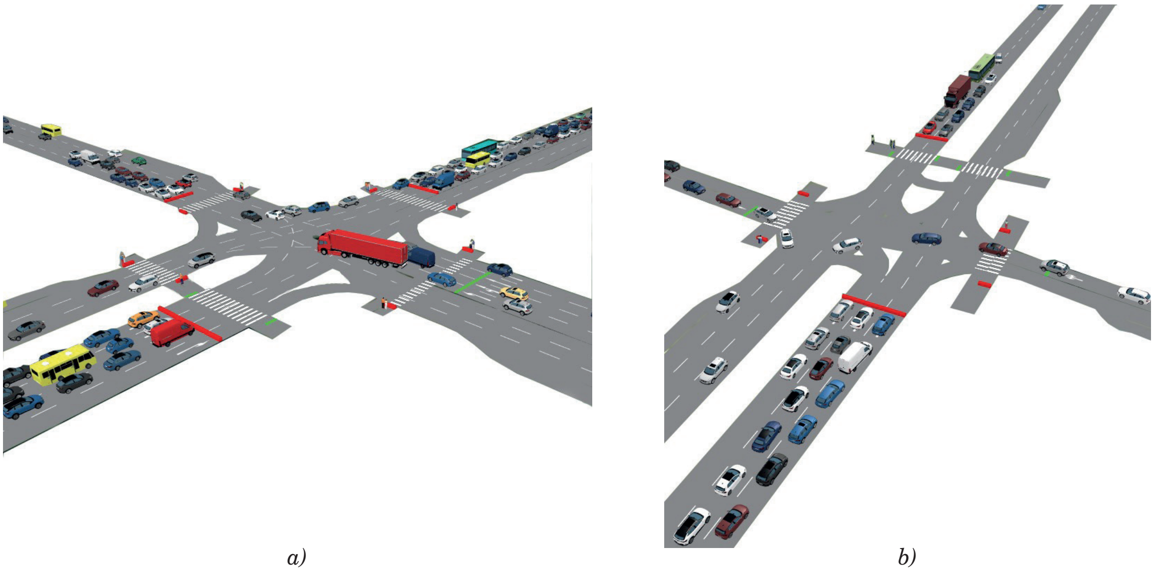

Figure 7 *Created simulation models of the functioning of intersection No. 1 (a) and No. 2 (b) in the PTV VISSIM software environment*

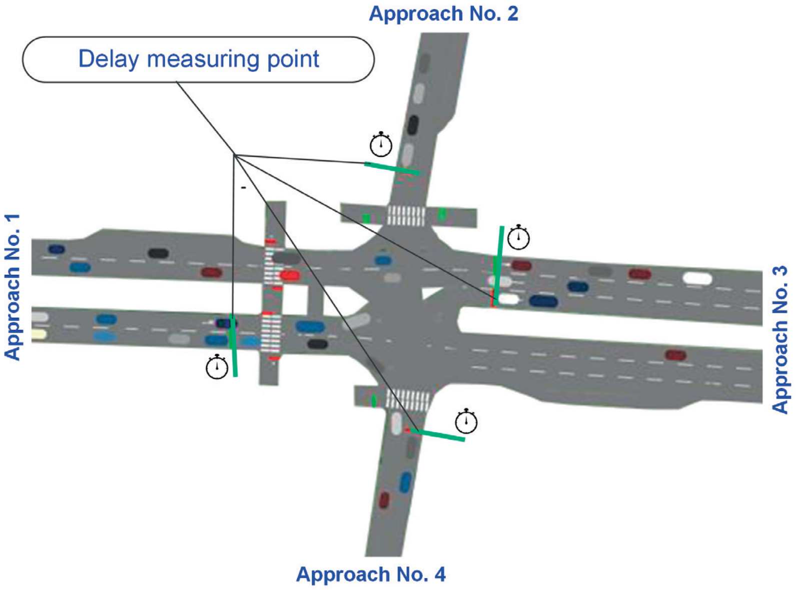

Figure 8 *An example of the placement of traffic delay counters at a signalized intersection*

Considering the accuracy of the forecast, the basic models of the standard four-leg signalized intersections under study are calibrated to reflect the existing traffic conditions. During calibration, the process of setting up the planning characteristics of the intersection and the initial parameters of the traffic flow in the specialized PTV VISSIM software environment is performed. The model of the intersection, with its initial parameters, is tested and verified for compliance with real data.

Given these inputs, it is planned to install counters at signalized intersections to record the duration of vehicle delays on all approaches to intersections (Figure 8). It is also necessary to model the traffic at the intersection under different scenarios of changes in traffic volumes, taking into account the different shares of passenger vehicles in the flow.

During the study of the operation of controlled intersections under different modelling scenarios, the traffic intensity at the intersection varied from 100 to 2800 vehicles per hour. This is due to the need to evaluate the efficiency of the regulated intersection. This range allows to model the intersection operation when traffic is moving. At a traffic volume of more than 2800 vehicles per hour on one of the approaches, a traffic jam occurs in the intersection area, and there is practically no movement. This leads to significant queues, and the traffic flow loses its dynamism. Under such conditions, further modelling becomes impossible, the intersection overloads, and cannot be reproduced adequately.

As noted earlier, the selected objects are typical intersections of arterial streets with controlled traffic and streets of district significance, where traffic control

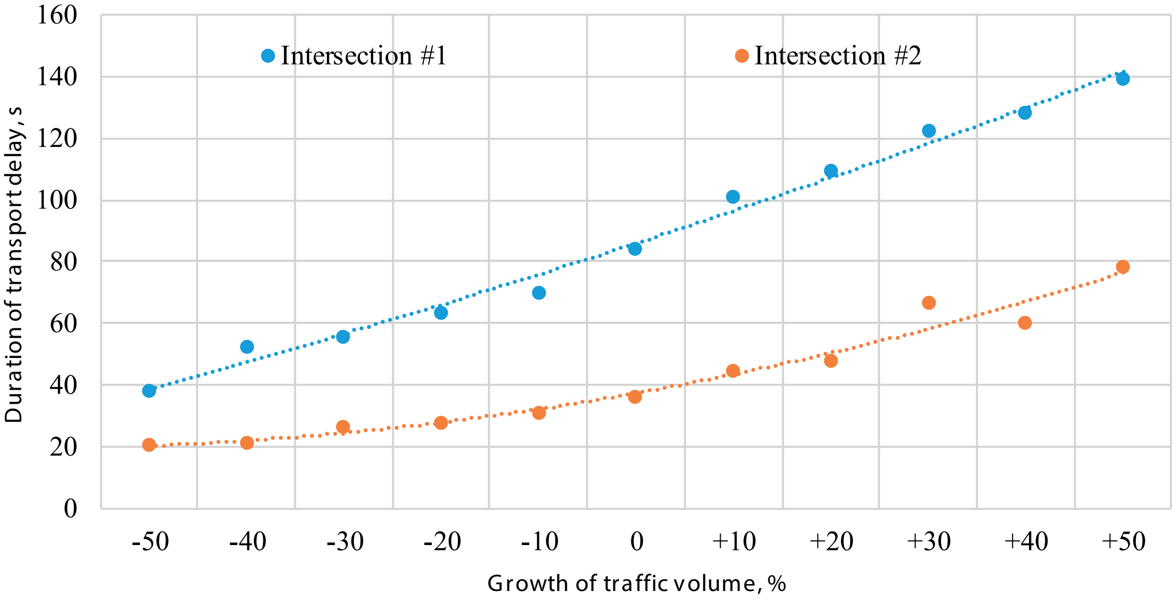

Figure 9 *Changes in the duration of traffic delays based on the traffic volume growth at controlled intersections*

Table 2 *Statistical indicators of transport delay depending on the increase in traffic intensity*

Indicator	Intersection #1	Intersection #2
Arithmetic Mean, s	85.5	42.3
Median, s	85.0	42.0
Mode, s	85.0	42.0
Variance	1093.2	345.8
Standard Deviation	33.07	18.59
Range, s	101.0	57.0
Skewness Coefficient	0.12	0.08

is implemented in three to four phases. Therefore, an important task is to identify the limit value of traffic volume at the intersection and the share of cars in the flow, at which the total traffic delay will be the smallest. It should also be noted that in this case, determining the total traffic delay duration for the entire signalized intersection would be the sum of the delays at each of its approaches.

4 The main results

In the basic intersection model, traffic flows consist of cars, trucks, and public transport. The intersection operation model incorporates the parameters of the roadway and traffic flow characteristics obtained during the field studies. In addition, the settings of the traffic light control system corresponded to the existing characteristics (the duration of the traffic light cycle was 126 seconds for intersection No. 1 and 94 seconds for intersection No. 2). The modelling involved changing the composition of the traffic flow by increasing or decreasing the share of cars. Additionally, there was a change in traffic volume (Figure 9). Creating such conditions gives an insight into the close relationship between the traffic flow indicators and the overall duration of traffic delays at signalized intersections.

The statistical analysis of the traffic flow parameters at intersections took into account the dynamic character of traffic composition changes and their impact on traffic delay. Therefore, normalization of the sample, data filtering, and calculation of the main statistical characteristics (Table 2) were performed during the processing of these parameters. After that, the correlation and regression analysis were used to determine the dependencies between the transport delay and the composition and volume of traffic flow.

For intersections, the arithmetic mean, median, and mode have almost the same value, indicating a symmetrical distribution of values around the center. The variation characteristics show a significant variance and standard deviation, indicating a wide range of delay fluctuations with a low skewness ratio.

The graph shows that as the traffic volume decreases from +50% to -50% (moving left to right along the X-axis), the average delay at Intersection #1 rises from approximately 40-45 s to nearly 150 s, indicating a strong sensitivity to reduced capacity and increased load

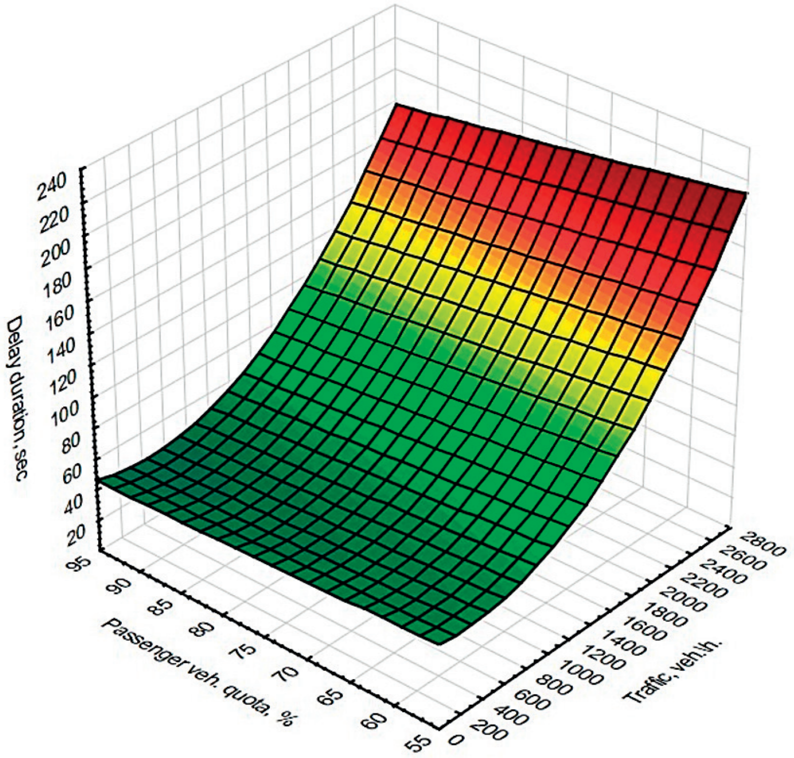

Figure 10 *Graphical dependence of the change in the total duration of traffic delay at a signalized standard four-leg signalized intersection, considering the traffic volume and the share of passenger cars in the traffic flow*

on the approaches. For Intersection #2, the delay grows more moderately - from about 20-22 s at +50% volume to roughly 75-80 s at -50% - demonstrating a more stable response to volume fluctuations. Overall, Intersection #1 experiences an increase of more than 100 s across the examined range, while Intersection #2 increase is about 55-60 s, confirming that the first intersection is significantly more affected by adverse changes in volume conditions.

Statistical analysis of the data obtained during the simulation indicates that, under existing traffic conditions at signalized intersections, the average delay duration at the entire intersection increases even with a slight increase in traffic volume. This, in turn, directly affects the intersection's capacity and, as a result, the overall delay for all the road users. The results differ somewhat for the two intersections because the planning characteristics of the secondary roads (Street B and Street C) are distinct. However, it was found that, in general, the dynamics of the growth of the share of passenger cars in the flow on all approaches to the intersection help to reduce the total delay at the intersection.

Additionally, it is worth noting that the composition of the traffic flow significantly impacts the duration of traffic delays on the approaches to the intersection. For example, as the number of slow-moving vehicles approaching the intersection from all directions increases, the probability of queuing increases.

There is a rather long traffic light cycle at the two signalized intersections. It allows determining the delay duration in more detail, considering the share of different types of vehicles and their interaction at urban signalized intersections. In addition, the operation of intersections with increased traffic volume was simulated to obtain an accurate and realistic estimate of the delay duration. This approach enables the prediction of moments when the intersection will operate in congestion mode, resulting in a significant increase in traffic delays.

Under the existing control cycle, minor congestion was observed on the secondary directions of the intersection. In turn, the most considerable delays were formed on the approaches No. 1 and No. 3 from Street A (both intersections). Therefore, the total delay at the intersection was taken into account. The simulation involved creating different loads under multiple options for changing the share of passenger cars in the traffic flow and their overall volume. The change in traffic delay, when the permissive signal was turned on, was evaluated over 10 simulation cycles. Based on the obtained values and the application of mathematical analysis tools, a graphical relationship between the traffic delay, traffic volume, and the proportion of cars in the traffic flow was established (Figure 10).

Figure 10 illustrates a three-dimensional geometric surface that displays the area of critical traffic volumes and various scenarios of fluctuations in the share of passenger cars in the flow, allowing for the visualization of changes in traffic delay at signalized intersections.

5 Discussion

The lowest average traffic delays are observed at traffic volumes of no more than 1500 vehicles per hour and a share of passenger cars in the traffic flow of more than 85%. Under such conditions, the signalized intersection is potentially efficient, as it has the lowest total traffic delay. In turn, a significant accumulation of traffic delays is observed on the main road, with a traffic volume exceeding 2000 vehicles per hour and a share of passenger cars of less than 80%. In the traffic volume range of 1600-2000 vehicles per hour on the approach to the intersection, even with a share of passenger cars of less than 90%, a significant increase in the duration of traffic delays was observed. These results are explained by the simulation conditions, under which forward and turning flows move from one lane of the road in one phase of traffic light control. Thus, the increase in the traffic delay duration at high traffic volumes on the same approaches to the intersection (in terms of the number of lanes and permitted maneuvers) is significantly affected by the share of cars in the flow. Such a delay is typical for complex signalized intersections of city streets, where the traffic light cycle has a significant duration and the phase sequence consists of three or more phases. Therefore, the data visualization demonstrates a clear functional relationship between the traffic delay and traffic volume, considering its share of passenger vehicles.

Taking into account the increase in traffic volume and the share of passenger cars in the flow, a general mathematical dependence of the delay duration was developed based on the traffic modelling under various scenarios of changes in traffic flow parameters (T_d):

$$T_d = 0.00003 \cdot N^2 - 0.4\mu + 50\,, \tag{1}$$

where N - traffic volume at the intersection; μ - share of passenger cars in traffic flow, %.

Reducing the traffic delays at an intersection can be achieved by changing the homogeneity of traffic flow in the lanes. Generally, the most significant delays occur on approaches where there is a substantial difference in the composition of the traffic flow and the dynamic characteristics of the vehicles. At the same time, the traffic safety and capacity of a signalized intersection depend on the parameters of the traffic management scheme. Additionally, the study results demonstrate a clear relationship between the duration of traffic delay and both traffic volume and the proportion of passenger cars in the traffic flow. It is of great importance for planning and optimizing traffic signaling, as well as improving traffic management.

Based on the model of changes in traffic delay as a function of traffic flow parameters (volume and composition), algorithms can be developed for the operation of traffic signal control systems. This would enable the consideration of predicted traffic delay values during traffic management. The proposed model, in contrast to the existing ones, focuses on the composition of the traffic flow and its intensity at a standard four-leg signalized intersection when determining the traffic delay. This scientific method allows to enable the adaptive traffic control, which helps to reduce the accumulation of vehicle queues on the approaches to the intersection and lowers the probability of traffic jams.

Traffic modelling, considering the growth in traffic volumes, enables the prediction of moments when the intersection will start operating in saturation or overload mode. Such conditions can lead to a significant increase in traffic delays. Additionally, the approach to modelling various traffic flow parameters at the intersection enables the estimation of traffic delays before the intersection without altering the duration of the traffic light phases. It is especially relevant for intersections where all the traffic from one approach moves in one phase. In addition, this approach not only allows for determining the current values of traffic delays but also for predicting their change, as the volume capacity ratio on city streets and roads increases.

Simulation of options for adjusting the share of passenger cars in the traffic flow at a signalized intersection revealed that the best results in terms of minimizing the total traffic delay are achieved with a homogeneous traffic flow. According to the results, the duration of the delay at the intersection increases significantly when the traffic volume on the approach exceeds 800 vehicles per hour and the share of passenger vehicles is less than 70%. This increase was especially noticeable if traffic was moving simultaneously from one lane. It highlights the need to regulate the entry of freight transport, clearly zoning lanes by direction of traffic, and allocating lanes for public transportation. It will reduce conflicts between vehicle types and ensure uniform and smooth traffic flow.

The correlations obtained between delay, traffic intensity, and traffic flow composition can be directly used as input parameters or training data for adaptive traffic light control systems based on machine learning. Since the simulation covers a wide range of traffic intensity and passenger car share, these results provide a structured dataset that helps algorithms learn how heterogeneous flows affect delay formation. Integrating delay predictions that account for flow composition into the real-time optimization will allow controllers to proactively adjust green light times, especially in conditions where small changes in vehicle composition cause disproportionate increases in delays. Thus, the proposed model supports the development of more accurate, predictable, and reliable adaptive traffic signal control strategies.

Future research may extend this approach by incorporating pedestrian flows, examining the effects of public transport prioritization, and analyzing coordination strategies between adjacent signalized intersections, all of which may further influence delay formation and overall network performance.

6 Conclusions

1. The study of planning features, phase sequence, and traffic flow parameters by direction was conducted at the signalized intersections. It was found that the highest traffic volumes were recorded on approaches No. 1 and No. 3 of the main direction of Street A. The straightforward traffic flows predominate at intersections, and there is a significant share of trucks, which averages 20%. At signalized intersections, each phase is designed to accommodate the flows of a particular approach or direction of the main road.
2. As a part of the study, a simulation of signalized intersections was developed to determine the traffic delays at them. The application of the basic model enabled the analysis of changes in traffic delays resulting from variations in traffic flow indicators. The analysis of the modelling results shows that the most significant increase in traffic delay, over 10 consecutive simulation cycles, is observed on the main road approaches. In particular, the traffic delay on such approaches within the modelling period ranges from 50 to 240 seconds. Additionally, it was found that at the current traffic volume level, the traffic flow structure also significantly affects traffic delay.
3. In the PTV VISSIM software environment, a study was conducted to investigate the impact of traffic flow parameters on traffic delay indicators at a signalized intersection. As a result of the modelling, the average values of traffic delays were determined, which varied with the growth of traffic volume and fluctuations in the composition of the traffic flow. The analysis of scenarios in which the share of passenger cars changed with a constant duration of traffic signal phases revealed a clear link between the traffic flow parameters and delays. In particular, the average traffic delay did not change significantly when the traffic volume was up to 1,600 vehicles per hour and the share of passenger cars was up to 70%. However, at traffic volumes exceeding 1,800 vehicles per approach, even a slight decrease in the share of passenger cars (below 60% of the total flow) resulted in a significant increase in both the average and maximum values of traffic delay for the entire intersection. The results demonstrate a high sensitivity of the duration of delays to the structure of the traffic flow, particularly the share of passenger cars, which should be considered when optimizing the traffic control modes and traffic management at complex intersections where flows separate into more than three phases of control.
4. Based on the developed simulation model, clear graphical and mathematical dependencies were obtained linking delay duration with both traffic volume and the share of passenger cars in the flow. The 3D delay surface shows that for mid-range volumes of 1,200-1,500 veh/h, increasing the passenger-car share from 55% to 90% reduces the total intersection delay by approximately 20-35 seconds, demonstrating the strong influence of flow homogeneity even before reaching saturation. At higher intensities above 2,200 veh/h, the model indicates that each additional 5% decrease in passenger-car share can add 10-15 seconds to overall delay, even when the total volume is kept constant. These numerical patterns confirm that delay growth is not only a function of intensity but strongly depends on structural changes in the traffic stream as well, reinforcing the need to incorporate flow composition into optimisation of traffic control strategies and into the development of adaptive or machine-learning-based signal control systems.

Acknowledgment

The authors received no financial support for the research, authorship and/or publication of this article.

Conflicts of interest

The authors declare that they have no known competing financial interests or personal relationships that could have appeared to influence the work reported in this paper.

References

[1] KEYVAN-EKBATANI, M., CARLSON, R. C., KNOOP, V. L., PAPAGEORGIOU, M. Optimizing distribution of metered traffic flow in perimeter control: queue and delay balancing approaches. *Control Engineering Practice* [online]. 2021, **110**, 104762. ISSN 0967-0661. Available from: https://doi.org/10.1016/j.conengprac.2021.104762

[2] ROSSI, R., CECCATO, R., GASTALDI, M. Effect of road traffic on air pollution. Experimental evidence from COVID-19 lockdown. *Sustainability* [online]. 2020, **12**(21), 8984. eISSN 2071-1050. Available from: https://doi.org/10.3390/su12218984

[3] JANDACKA, D., DECKY, M., HODASOVA, K., PISCA, P., BRILIAK, D. Influence of the urban intersection reconstruction on the reduction of road traffic noise pollution. *Applied Sciences* [online]. 2022, **12**(17), 8878. eISSN 2076-3417. Available from: https://doi.org/10.3390/app12178878

[4] ALKAISSI, Z. A., HUSSAIN, R. Y. Delay time analysis and modelling of signalised intersections using global positioning system (GPS) receivers. *IOP Conference Series: Materials Science and Engineering* [online]. 2020, **671**, 012110. eISSN 1757-899X. Available from: https://www.doi.org/10.1088/1757-899X/671/1/012110

[5] FORNALCHYK, Y., KERNYTSKYY, I., HRYTSUN, O., ROYKO, Y. Choice of the rational regimes of traffic light control for traffic and pedestrian flows. *Scientific Review Engineering and Environmental Sciences* [online]. 2021, **30**(1), p. 38-50. ISSN 1732-9353. Available from: https://doi.org/10.22630/PNIKS.2021.30.1.4

[6] YALCINLI, F., AKDEMIR, B., DURDU, A. Adaptive traffic management model for signalised intersections. *Elektronika Ir Elektrotechnika* [online]. 2024, **30**(3), p. 72-82. eISSN 2029-5731. Available from: https://doi.org/10.5755/j02.eie.36536

[7] ZHANG, L., YANG, K., ZHANG, K., WEI, W., LI, J., TAN, H. Estimating traffic flow at urban intersections using low occupancy floating vehicle data. *Alexandria Engineering Journal* [online]. 2025, **112**, p. 374-383. ISSN 1110-0168. Available from: https://doi.org/10.1016/j.aej.2024.11.005

[8] MUROVANYI, I., MAZYLIUK, P. Analysis of saturation flow on isolated lanes of controlled intersections with significant traffic intensity. *Transport Technologies* [online]. 2020, **2**(1), p 1-12. eISSN 2709-5223. Available from: https://doi.org/10.23939/tt2020.02.001

[9] Highway Capacity Manual [online]. Washington, DC: TRB, 2010. ISBN 978-0-309-16077-3. Available from: https://www.jpautoceste.ba/wp-content/uploads/2022/05/Highway-Capacity-Manual-2010-PDFDrive-.pdf

[10] MCKENNEY, D., WHITE, T. Distributed and adaptive traffic signal control within a realistic traffic simulation. *Engineering Applications of Artificial Intelligence* [online]. 2013, **26**(1), p. 574-583. ISSN 0952-1976. Available from: https://doi.org/10.1016/j.engappai.2012.04.008

[11] WANG, Y., YANG, X., LIANG, H., LIU, Y. A review of the self$_2$adaptive traffic signal control system based on future traffic environment. *Journal of Advanced Transportation* [online]. 2018, **2018**(1), 1096123. eISSN 2042-3195. Available from: https://doi.org/10.1155/2018/1096123

[12] NOAEEN, M., NAIK, A., GOODMAN, L., CREBO, J., ABRAR, T., ABAD, Z. S. H., FAR, B. Reinforcement learning in urban network traffic signal control: a systematic literature review. *Expert Systems with Applications* [online]. 2022, **199**, 116830. ISSN 0957-4174. Available from: https://doi.org/10.1016/j.eswa.2022.116830

[13] NAVARRO-ESPINOZA, A., LOPEZ-BONILLA, O. R., GARCIA-GUERRERO, E. E., TLELO-CUAUTLE, E., LOPEZ-MANCILLA, D., HERNANDEZ-MEJIA, C., INZUNZA-GONZALEZ, E. Traffic flow prediction for smart traffic lights using machine learning algorithms. *Technologies* [online]. 2022, **10**(1), 5. ISSN 2227-7080. Available from: https://doi.org/10.3390/technologies10010005

[14] LIN, H., HAN, Y., CAI, W. JIN, B. Traffic signal optimization based on fuzzy control and differential evolution algorithm. *IEEE Transactions on Intelligent Transportation Systems* [online]. 2022, **24**(8), p. 8555-8566. ISSN 1524-9050. Available from: https://doi.org/10.1109/TITS.2022.3195221

[15] MA, D., ZHOU, B., SONG, X., DAI, H. A deep reinforcement learning approach to traffic signal control with temporal traffic pattern mining. *IEEE Transactions on Intelligent Transportation Systems* [online]. 2021, **23**(8), p. 11789-11800. ISSN 1524-9050. Available from: https://doi.org/10.1109/TITS.2021.3107258

[16] ZHU, R., LI, L., WU, S., LV, P., LI, Y., XU, M. Multi-agent broad reinforcement learning for intelligent traffic light control. *Information Sciences* [online]. 2023, **619**, p. 509-525. ISSN 0020-0255. Available from: https://doi.org/10.1016/j.ins.2022.11.062

[17] JAMAL, A., RAHMAN, M. T., AL-AHMADI, H. M., ULLAH, I., ZAHID, M. Intelligent intersection control for delay optimization: using meta-heuristic search algorithms. *Sustainability* [online]. 2020, **12**(5), 1896. ISSN 2071-1050. Available from: https://doi.org/10.3390/su12051896

[18] GAO, Y., QU, Z., SONG, X., YUN, Z. Modelling of urban road network traffic carrying capacity based on equivalent traffic flow. *Simulation Modelling Practice and Theory* [online]. 2022, **115**, 102462. ISSN 1569-190X. Available from: https://doi.org/10.1016/j.simpat.2021.102462

[19] WANG, C., XIE, Y., HUANG, H., LIU, P. A review of surrogate safety measures and their applications in connected and automated vehicles safety modelling. *Accident Analysis and Prevention* [online]. 2021, **157**, 106157. ISSN 0001-4575. Available from: https://doi.org/10.1016/j.aap.2021.106157

[20] ROYKO, Y., FORNALCHYK, Y., KODA, E., KERNYTSKYY, I., HRYTSUN, O., BURA, R., POLYANSKY, P. Public transport prioritization and descriptive criteria-based urban sections classification on arterial streets. *Sustainability* [online]. 2023, **15**(3), 2363. ISSN 2071-1050. Available from: https://doi.org/10.3390/su15032363

[21] KOVALCHUK, V., RYBAK, R., HNATIV, Y., TKACHENKO, V., ONYSHCHENKO, A., KRAVETS, I., VELHAN, I. Assessment of the stressed-strained state of a reinforced transport pipe under the combined effect of ambient temperature and static loads. *Eastern-European Journal of Enterprise Technologies* [online]. 2022, **6**(7), 120. ISSN 1729-3774. Available from: https://doi.org/10.15587/1729-4061.2022.268904

[22] RUAN, T., ZHOU, L., WANG, H. Stability of heterogeneous traffic considering impacts of platoon management with multiple time delays. *Physica A: Statistical Mechanics and its Applications* [online]. 2021, **583**, 126294. ISSN 0378-4371. Available from: https://doi.org/10.1016/j.physa.2021.126294

[23] SAMUEL, L., SHIBIL, M., NASSER, M., SHABIR, N., DAVIS, N. Sustainable planning of urban transportation using PTV VISSIM. In: International Conference on Structural Engineering and Construction Management SECON´21: proceedings [online]. 2021. ISSN 2366-2557, ISBN 978-3-030-80311-7, eISBN 978-3-030-80312-4, p. 889-904. Available from: https://doi.org/10.1007/978-3-030-80312-4_76

ENHANCING VISIBILITY AND SAFETY OF THERMOPLASTIC ROAD MARKINGS WITH PHOSPHORUS ADDITIVES AND ROSIN ESTER BINDER

M. Isya, Cut Mutiawati*, Fadhlullah Apriandy, Hadhrat Alfajri

Department of Civil Engineering, Syiah Kuala University, Banda Aceh, Indonesia

*E-mail of corresponding author: cutmutiawati@usk.ac.id

M. Isya 0000-0001-5648-9456,
Cut Mutiawati 0000-0001-9391-8037,
Fadhlullah Apriandy 0000-0002-0354-1924

Resume

Road markings are essential traffic control devices that guide drivers, particularly at night and under adverse weather conditions common in tropical regions. In this study is investigated the performance of thermoplastic road markings enhanced with phosphorescent phosphorus using rosin ester as a binder. Laboratory experiments with varying phosphorus concentrations were conducted to evaluate luminance, retroreflectivity, and skid resistance under dry and wet conditions. The results show that a 30% phosphorus content provides the best overall performance by improving the nighttime visibility and retroreflective properties without compromising the skid resistance. All measured parameters comply with the Indonesian SKh-1.M-03 road marking standard. The proposed material demonstrates strong potential to enhance the road marking visibility and driving safety in tropical environments.

Article info

Received 8 July 2025
Accepted 2 December 2025
Online 13 January 2026

Keywords:

thermoplastic road marking
phosphorus additive
rosin ester
retroreflectivity
driving visibility
skid resistance

Available online: https://doi.org/10.26552/com.C.2026.007

ISSN 1335-4205 (print version)
ISSN 2585-7878 (online version)

1 Introduction

Road markings are among the most crucial elements in modern transportation systems, serving as indicators for lane boundaries, stop zones, and vehicle movement directions. Their presence is critical in supporting the road safety, especially at night or during adverse weather conditions. According to the World Health Organization (WHO), more than 1.3 million people die annually due to traffic accidents, with a significant portion occurring during nighttime or in poor visibility conditions. In Indonesia, data from the National Police Traffic Corps (Korlantas Polri) show that over 50% of accidents are caused by low visibility, particularly in poorly lit areas.

The visibility of road markings is thus a vital component of transportation infrastructure aimed at improving the road user safety. Under conditions such as heavy rainfall or nighttime darkness, adequate visibility of road markings can be a determining factor in preventing collisions. One common strategy to enhance visibility is the use of thermoplastic road marking paint, which is widely applied and regulated due to its durability, abrasion resistance, and long-lasting performance under various lighting conditions [1].

In recent years, phosphorescent pigments, especially those based on strontium aluminate, have emerged as promising additives for increasing the road marking visibility. These materials can absorb energy from sunlight or vehicle headlights and re-emit it gradually in darkness, providing a glow-in-the-dark effect without requiring external power sources [2-3]. Various activation methods have been explored to optimize glow performance in phosphorus-based luminescent systems, including UV irradiation for persistent phosphors and chemical oxidation routes in which phosphorus-containing materials exhibit chemiluminescence when exposed to oxidizers, such as hydrogen peroxide [4-5], as well as thermal processing inherent to thermoplastic road marking production and application [6].

Additionally, studies have shown that phosphate-based or phosphorus-containing luminescent materials with specific crystal structures can enhance glow intensity and emission stability [7-8]. Furthermore, in a previous study [9] the chemiluminescent activation of phosphorus-based compounds using oxidants such as hydrogen peroxide, was investigated, demonstrating potential applications in sensing, forensic detection, and diagnostics.

Among various phosphorescent materials, strontium aluminate-based pigments are widely recognized for their high brightness and long afterglow duration, outperforming older phosphorescent compounds such as zinc sulfide [4-5]. To effectively incorporate these active materials into the road markings, suitable binders are required to ensure optimal adhesion and durability. Rosin ester, a natural resin derivative, has been identified as an effective binder due to its superior adhesion, chemical resistance, and water resilience, compared to conventional hydrocarbon resins [6]. Previous research [7] demonstrated that modified rosin sources, such as pine and tall oil rosin, can improve softening point, UV resistance, and esterification efficiency, thereby enhancing paint performance.

Several studies have investigated the use of phosphorescent pigments in road markings. Earlier studies [4-5] reported that incorporating phosphorescent additives significantly increases reflectivity and improves durability under extreme weather conditions. Various concentrations of glow-in-the-dark phosphorus powder were evaluated in [10], which reported that a 30% content produced maximum luminance with acceptable skid resistance, while [11] and [12] confirmed improvements in reflective performance under nighttime visibility conditions.

In addition to physical performance, some studies have utilized spectroscopic techniques, such as Fourier Transform Infrared (FTIR) and FT-Raman spectroscopy, to characterize the chemical structure and microscopic stability of thermoplastic materials. The methods described in [13] were successfully applied to irradiated starch, and similar analytical approaches can be adopted in future studies to investigate the molecular interactions between the phosphorus pigments and binder matrices in road marking paints.

However, research specifically evaluating the integration of strontium aluminate-based phosphorescent pigments, with rosin ester binders in thermoplastic road marking formulations, remains limited, particularly under tropical environmental conditions characterized by high rainfall and limited street lighting. Previous studies have predominantly focused on epoxy or polyurethane-based systems [14-15], while the practical application and performance evaluation of phosphorescent thermoplastic paints incorporating natural resin binders for improving road safety in developing regions has not been extensively explored [16-17]. Therefore, in this study is addressed this gap by evaluating the novel combination of strontium aluminate-based phosphorescent pigment with rosin ester binder in thermoplastic road marking paint. The effects on luminance intensity, retroreflectivity, and skid resistance under both dry and wet tropical conditions were quantitatively examined, aiming to develop safer, more durable, and environmentally conscious road marking materials to improve nighttime driving safety in regions with limited lighting.

2 Research methodology

In this section are outlined the procedures for data collection, material formulation, sample preparation, testing, and data analysis conducted to evaluate the safety performance improvements of thermoplastic road markings enhanced with phosphorescent phosphorus additives.

2.1 Research location

The research was conducted in the Highway Engineering Laboratory at the Faculty of Engineering, Syiah Kuala University, Banda Aceh, Indonesia. This laboratory is equipped with facilities to perform experimental studies in transportation materials, including equipment for visibility and skid resistance testing under controlled conditions.

2.2 Research approach

A quantitative experimental approach was employed to assess the effects of phosphorus addition on the visibility and surface safety performance of thermoplastic road markings. The independent variable was phosphorus concentration (0%, 10%, 20%, 30%), while the dependent variables included luminance intensity, retroreflectivity, and skid resistance. This approach is categorized as experimental research, involving the collection of empirical data through direct observation and manipulation of variables within controlled environments [18]. In addition, a quantitative approach was utilized to gather data in numerical or measurable form, which was subsequently analyzed statistically to identify specific patterns, relationships, or trends [19]. Such an analysis provides a deeper understanding of the direct impact of phosphorus additives on driving visibility, ultimately contributing to improved traffic safety. Experiments were carried out under controlled laboratory conditions simulating field environments to ensure systematic, reproducible, and measurable outcomes. This approach enables rigorous evaluation of how phosphorus additives influence the road marking performance and potential contributions to traffic safety improvement [9].

The phosphorus concentration range of 0-30%, adopted in this study, was determined based on previous findings [10], which indicated that a 30% phosphorus content yielded the highest luminance while maintaining adequate skid resistance. Concentrations below 10% showed minimal improvement in glow intensity, whereas higher proportions reduced mixture uniformity and surface smoothness. Therefore, this range was selected to verify and extend earlier results under tropical conditions using rosin ester as a natural binder, representing the main research gap addressed in this study.

2.3 Materials and testing equipment

All materials were sourced from local suppliers in Banda Aceh, Indonesia. The material descriptions were based on established standards and manufacturer specifications, including:

- Glow-in-the-dark phosphorus powder, a phosphorescent additive based on strontium aluminate, containing $SrAl_2O_4:Eu^{2+},Dy^{3+}$,
- Thermoplastic road marking paint, containing a rosin ester binder with a main composition of approximately 20.05% binder, 39.68% glass beads, 10.11% TiO_2 (titanium dioxide), and 30.16% $CaCO_2$ with inert fillers,
- Glass beads, used as a standard reflective additive for road markings.

The equipment utilized for testing comprised:

- Lux meter, for measuring luminance intensity,
- British Pendulum Tester, for evaluating skid resistance,
- Thermometer and oven, for temperature control during sample preparation,
- Digital balance, with a precision of 0.01 g, for accurate material weighing,
- Beakers and impact testing apparatus, for sample preparation and testing.

All testing procedures were conducted in accordance with standard laboratory safety protocols to ensure researcher protection and environmental compliance. Illustrations of the materials and preparation procedures are presented in Figures 1 and 2.

2.4 Physical properties testing

The physical properties of thermoplastic road marking paint were evaluated to assess their compliance with the Indonesian National Standard SNI 06-4826-1998 [20] and the Ministry of Public Works guideline SKh-1.M.03 [21]. The paint formulations tested included a control sample without phosphorus additive and experimental samples with phosphorescent phosphorus powder added at concentrations of 10%, 20%, and 30% by total weight. All samples were formulated using a rosin ester binder as the main adhesive component. The phosphorus powder was thoroughly mixed into the thermoplastic paint before heating to ensure homogeneity. Each formulation was then heated, molded into standardized test specimens, and cooled to room temperature before testing. This preparation ensured consistency and allowed direct comparison between the baseline (control) and phosphorus-enhanced samples to evaluate the effect of the additive on physical and optical performance. The physical tests conducted included:

Figure 1 *Thermoplastic road marking paint and phosphorus powder*

Figure 2 *Phosphorus addition to road marking paint and heating of thermoplastic paint*

***Table 1** Composition and distribution of test specimens*

Thermoplastic paint (g)	Phosphorus powder (g)	Luminance test	Skid resistance	Reflectivity test
400	-	2	2	2
400	40	2	2	2
400	80	2	2	2
400	120	2	2	2

Total specimens: 8 (per test type) → Total: 24 specimens

1. Specific gravity
   Samples (400 g) were heated at 218 ± 2°C for 4 hours, stirred for 10 seconds, then poured into a container for vacuum treatment to remove trapped air. After the cooling, specific gravity was calculated by weighing samples in air and water, following standard immersion methods.
2. Drying time
   Paint was heated to 211 ± 7°C, poured to a thickness of 3.2-4.8 mm at 32 ± 2°C, and drying time was recorded using tack-free tests conducted at 60-second intervals until the paint surface no longer deformed or adhered to the testing tool.
3. Low-Temperature crack resistance
   Samples were heated (400 g, 218 ± 2°C for 4 hours), stirred, and molded to a thickness of 3-5 mm. After reaching the room temperature, they were stored in a freezer at −9.4 ± 2°C for 24 hours and subsequently inspected for cracks under uniform indirect lighting from a distance of 305 mm.
4. Softening point
   Test specimens were mounted with steel balls in a glass vessel containing distilled water at 5 ± 1°C. After the temperature stabilization for 15 minutes, the vessel was heated at 5°C per minute, and the softening point was recorded when the specimen deformed under the ball load, in line with standard ring-and-ball test procedures.
5. Flow resistance
   Heated samples (400 ± 0.1 g at 218 ± 2°C for 4 hours) were stirred and immediately placed on a 45° inclined surface. Residual material was weighed to calculate flow resistance as a percentage of the original sample mass.
6. Flow resistance with overheating
   Similar to the standard flow resistance test, but samples were heated for 8 hours, stirred after 6 hours, and then tested to assess material stability under prolonged heating.

This integrated testing approach allowed for systematic evaluation of specific gravity, drying time, low-temperature crack resistance, softening point, and flow resistance of thermoplastic road marking paint formulations with varying phosphorus concentrations. Results from these tests provided a comprehensive assessment of how the addition of phosphorescent phosphorus influenced the durability and surface characteristics of the road marking materials under standardized testing conditions.

2.5 Sample preparation and formulation

Four different formulations were prepared with phosphorus powder concentrations of 0%, 10%, 20%, and 30% by weight, maintaining a constant thermoplastic paint weight of 400g for each sample. These formulations allowed for direct comparison between the control (0%) and phosphorus-enhanced samples. Samples were prepared by thoroughly mixing the thermoplastic paint and phosphorus powder in a container, followed by heating for 4 hours at 218 ± 25°C. After the heating, the mixture was stirred rapidly with a spatula for 10 seconds and poured onto tin plates (75 mm diameter) to form test specimens. The specimens were then cooled to room temperature before testing. Specimen distribution is shown in Table 1.

Specimen preparation began by mixing the thermoplastic paint with phosphorus powder according to the specified percentages. The mixture was placed in a container and heated for 4 hours at 218 ± 25 °C. After the heating, the mixture was quickly stirred with a spatula for 10 seconds and poured onto a tin plate (75 mm diameter), then cooled to room temperature.

2.6 Visibility and safety performance testing

Three primary performance tests were conducted to evaluate the practical safety benefits of phosphorus addition:

1. Luminance intensity measurement
   Luminance measurements assessed phosphorescent performance under both clear and rainy conditions. Measurements were conducted between 18:30 and 19:30 at 15-minute intervals using a calibrated lux meter positioned perpendicularly above the sample surface at a fixed distance in a completely dark room. All the samples were pre-exposed to natural sunlight to activate phosphorescence before testing. Control samples were included for comparative analysis.
2. Skid resistance test
   Skid resistance was evaluated under both dry and wet conditions using a British Pendulum Tester. Wet conditions were simulated by uniformly spraying water onto the sample surfaces. The British Pendulum Number (BPN) was recorded for each condition to assess slip resistance and surface safety characteristics, following standard procedures [22].

***Table 2** Physical properties of thermoplastic paint*

No.	Tested parameter	Unit	Test Result	SKh-1.M-03 Standard
1.	Specific gravity	-	2.02	Max. 2.15
2.	Drying time	Min	5	Max. 10
3.	Softening point	°C	101	102.5 ± 9.5
4.	Low-Temp crack resistance	-	No cracks	No cracks
5.	Flow resistance	%res	7.36	Max. 18
6.	Flow resistance with overheating	%res	11.54	Max. 28

***Table 3** Physical properties with phosphorus addition (10%, 20%, 30%)*

No.	Tested parameter	Unit	Test Results			SKh-1.M-03 Standard
			10%	20%	30%	
1.	Spesific gravity	-	2.08	2.10	2.13	Max. 2.15
2.	Drying time	min	5	5	5	Max. 10
3.	Softening point	°C	101	105	107	102.5 ± 9.5
4.	Low-Temp crack resistance	-	No cracks	No cracks	No cracks	No cracks
5.	Flow resistance	% res	9.11	11.63	14.42	Max. 18
6.	Flow resistance after overheating	% res	14.42	15.96	19.21	Max. 28

3. Retroreflectivity test
   Retroreflectivity measurements assessed the effectiveness of markings under the nighttime driving conditions. Tests were performed using a lux meter with vehicle headlights as the illumination source, directed at a 30°-45° incidence angle to simulate real driving scenarios. Wet conditions were simulated by spraying water over the sample surfaces for 30 seconds before measurement. According to SNI 06-486-1998 and SKh-1.M.03, the minimum retroreflectivity requirements are ≥ 200 mcd/m² for dry surfaces and 100-150 mcd/m² for wet surfaces.

2.7 Data analysis technique

In this study, the effect of phosphorus concentration on the performance of thermoplastic road markings utilizing a rosin ester binder derived from natural pine resin was investigated. The experimental design includes two primary variables: the independent variable is the phosphorus concentration, varied at 0%, 10%, 20%, and 30%; and the dependent variable is the overall performance of the thermoplastic road marking material. Performance evaluation focuses on three key parameters: luminance, reflectivity, and skid resistance. Those indicators were quantitatively measured to determine how the addition of phosphorus influences the visibility and safety characteristics of the road marking under both dry and wet conditions. The findings aim to support the development of improved road marking materials, particularly suited for tropical climates that experience high rainfall and limited night-time illumination. Moreover, this research contributed to the sustainable use of natural resources by promoting rosin ester, a renewable binder derived from pine resin, as a key component in the thermoplastic formulation.

3 Results and discussion

In this section are presented and discussed the results obtained from the experimental evaluation of thermoplastic road marking paints formulated with varying phosphorus additive concentrations. The analysis covers their physical properties, visibility performance under different weather conditions, and safety-related characteristics, aiming to determine compliance with national standards and to assess their potential benefits for road safety applications.

3.1 Physical properties of thermoplastic paint

Tests included specific gravity, drying time, low-temperature crack resistance, softening point, flow resistance, and flow resistance after overheating. Table 2 shows that all the tested parameters met the SKh-1.M-03 standard.

3.2 Physical properties with phosphorus addition

Tests with 10%, 20%, and 30% phosphorus showed compliance with SKh-1.M-03 standards. Results are detailed in Table 3.

The test results showed an increase in specific gravity from 2.02 (without phosphorus) to 2.11 (with

__Table 4__ Regression summary (clear and rainy conditions)

Condition	Time	Intercept	Slope (per %)	R²	p-value (slope)	F-statistic
Rainy	18:30	2.5	12.35	0.9929	0.00354	280.6302
	18:45	-1.9	11.41	0.9944	0.00279	356.9731
	19:00	-9.4	10.66	0.9946	0.00273	365.1530
	19:15	-13.9	9.26	0.9820	0.00902	109.3440
	19:30	-14	7.4	0.9722	0.01402	69.8469
Sunny	18:30	2.6	17.91	0.9999	0.00007	14130.7533
	18:45	0.9	16.79	0.9985	0.00077	1288.9991
	19:00	-2.1	15.59	0.9981	0.00095	1053.5245
	19:15	-15.9	14.66	0.9921	0.00396	251.0110
	19:30	-11.2	11.88	0.9868	0.00660	150.01531

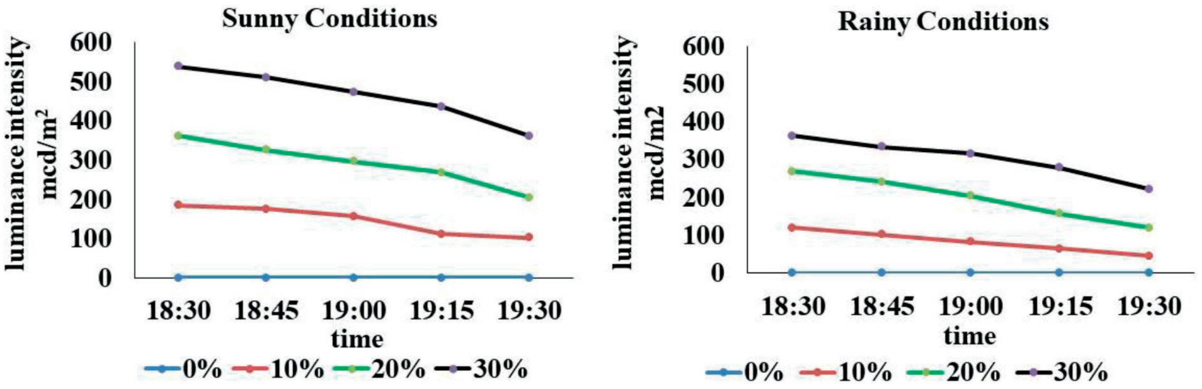

***Figure 3** Phosphorus content versus luminance intensity*

30% phosphorus), remaining below the maximum limit. Drying time remained consistent at 5 minutes. Softening point increased, from 101°C to 107°C, but stayed within the acceptable range. All the variations showed good low-temperature crack resistance. The flow resistance residue rose from 7.36% to 14.42%, and after overheating, from 11.54% to 19.21%, both remaining within limits. These results confirm that phosphorus can be added up to 30% without compromising paint quality.

3.3 Road marking performance

In this section, the performance evaluation of road markings enhanced with phosphorus additives is presented. The tests focused on two key parameters affecting the visibility of road markings, namely luminance and retroreflectivity, under various weather conditions. The detailed results for each parameter are described below.

3.3.1 Luminance of road markings

This experiment was aimed at assessing the influence of phosphorus additive concentration on the luminous intensity of thermoplastic road markings under two distinct weather conditions: clear (sunny) and rainy. Measurements were conducted periodically using a lux meter to compare the luminance of samples with varying phosphorus concentrations. The measurement results are presented in Figure 3.

Based on measurements using a lux meter, it was observed that the addition of phosphorus significantly increased the luminance intensity. On clear days, the luminance increased with higher phosphorus content, from 185 mcd/m^2 (10%) to 538 mcd/m^2 (30%). On rainy days, although the overall luminance intensity was lower, a similar upward trend was observed, with luminance rising from 120 mcd/m^2 (10%) to 362 mcd/m^2 (30%). This indicates that phosphorus possesses strong light-emitting properties, particularly under clear conditions, and can retain a substantial portion of its luminance even under less favorable conditions (rain).

On clear days, the peak luminance was recorded between 18:30 and 19:00, after which it tended to decline. Higher phosphorus content (30%) consistently produced greater luminance intensity compared to lower concentrations (0% and 10%) until 19:30. A similar trend was observed on rainy days, despite the lower overall light levels compared to clear weather, the decline in luminance was more pronounced in samples with lower phosphorus concentrations.

To validate these observations, statistical regression analyses were conducted separately for clear and

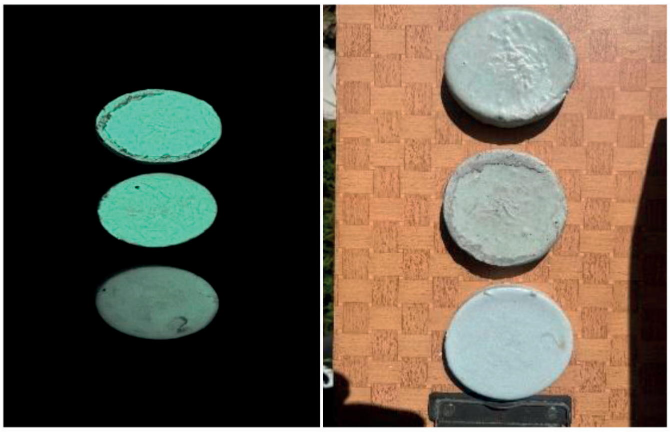

Figure 4 *Phosphorescence intensity of phosphorus*

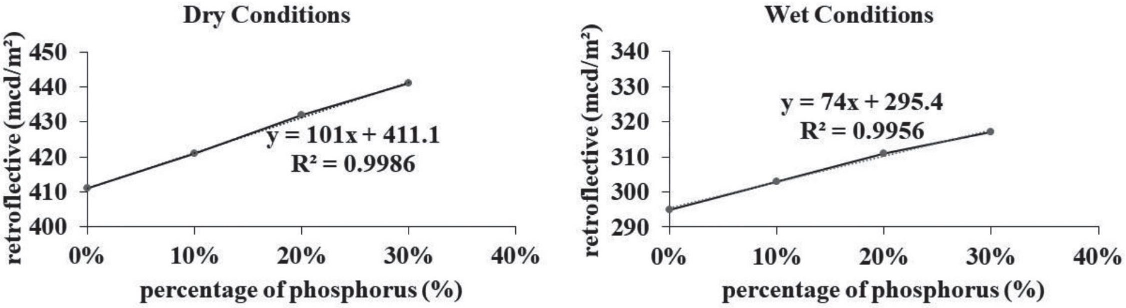

Figure 5 *Effect of phosphorus content on reflectivity*

rainy conditions, as well as using a pooled model with interaction terms. The results confirmed a strong linear relationship between the phosphorus concentration and a luminance intensity. The statistical outcomes of these regression analyses are summarized in Table 4.

The regression analysis confirmed a strong and statistically significant linear relationship between the phosphorus concentration and a luminance intensity under clear and rainy conditions. Under rainy conditions, the slopes ranged from 12.35 mcd/m^2 per % at 18:30 to 7.4 mcd/m^2 per % at 19:30, with R^2 values between 0.9722 and 0.9946, indicating that phosphorus concentration explains more than 97% of the luminance variability at all observation times. All slopes were statistically significant ($p < 0.05$), and F-statistics ranged from approximately 69.8 to 365.2, confirming the robustness of the linear relationships. The progressive decrease in slope across time reflects the gradual decline of luminance intensity as the evening progressed, though the phosphorus-induced enhancement remained evident throughout the wet surface condition.

Under sunny conditions, the relationship was even stronger. The slopes started at 17.91 mcd/m^2 per % at 18:30 and gradually decreased to 11.88 mcd/m^2 per % at 19:30. All the regressions exhibited very high R^2 values (0.9868 - 0.9999), with F-statistics ranging from 150.0 to 14,130.8 and p-values well below 0.01, indicating highly significant effects. The higher slopes under sunny conditions compared to rainy conditions highlight the superior luminance performance of phosphorus-enhanced markings in dry environments, particularly during the earlier evening hours when ambient light is still present.

Overall, these results demonstrate that phosphorus concentration is a dominant predictor of luminance in both weather scenarios, with consistently strong linear fits. However, the magnitude of the effect (slope) is notably greater under sunny conditions, suggesting that the reflective and luminance-enhancing properties of phosphorus are maximized on dry surfaces. This finding supports the potential application of phosphorus-enhanced thermoplastic markings to improve the night-time visibility, especially in dry weather.

The addition of phosphorus to road markings, particularly at a concentration of 30%, significantly improves lighting and illumination performance under both clear and rainy conditions. This confirms that phosphorus is a highly promising material for enhancing the visibility and effectiveness of road markings in accordance with established standards. The luminance intensity of the samples is presented in Figure 4.

3.3.2 Retroreflectivity of the road markings

The results of the road marking reflectivity test, or light reflectance of the markings, with phosphorus additions of 10%, 20%, and 30% are shown in Figure 5.

Table 5 *Regression summary (dry vs wet conditions with interaction)*

Condition	Intercept	Slope (per %)	R^2	F-statistic	p-value (slope)
Dry	411.10	101.00	0.999	1457.0	0.001
Wet	295.40	74.00	0.996	456.3	0.002

Table 6 *Regression summary - skid resistance (dry vs wet)*

Condition	Intercept	Slope (per %)	R^2	F-statistic	p-value (slope)
Dry	50.90	0.290	0.984	120.1	0.008
Wet	47.10	0.210	0.969	63.0	0.016

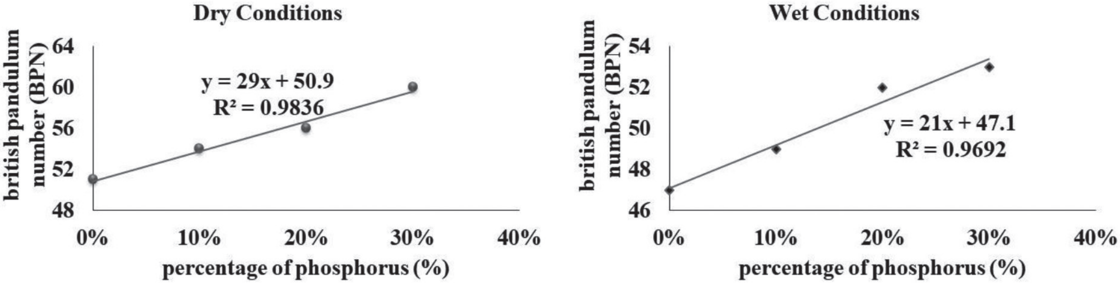

Figure 6 *Effect of phosphorus content on skid resistance*

The test results graph shows the effect of phosphorus addition on the reflectivity of road markings. Under the dry conditions, reflectivity tests revealed that increasing phosphorus content led to higher retroreflective values. Without phosphorus (0%), the retroreflectivity was 411 mcd/m², while the addition of 30% phosphorus raised it to 441 mcd/m². All the values exceeded the minimum standard for road marking retroreflectivity (200 mcd/m²), indicating that phosphorus-enhanced markings have excellent reflectivity under dry conditions.

Under the wet conditions, phosphorus addition continued to improve retroreflectivity, though values were lower than those under dry conditions. At 0% phosphorus, retroreflectivity measured 295 mcd/m², increasing to 317 mcd/m² with 30% phosphorus. All the measurements remained above the minimum requirement (200 mcd/m²), proving that phosphorus-enhanced markings remain effective even in rainy conditions.

The incorporation of phosphorus in road marking materials significantly enhances the light reflectance under both dry and wet conditions. This demonstrates that phosphorus improves visibility, which is essential for driving safety, particularly at night or during the rain. Although the retroreflectivity values are lower under the wet conditions, all samples met the minimum standard, which is reasonable since water typically reduces light reflection. Thus, all phosphorus variations tested fulfill the required retroreflectivity standards, making them suitable for road marking applications.

The statistical regression analysis further confirmed the consistency of these trends, as summarized in Table 5.

The regression analysis confirmed a strong linear relationship between the phosphorus concentration and retroreflectivity under both dry and wet conditions. In dry conditions, retroreflectivity increased sharply with phosphorus addition (slope ≈ 101 mcd/m² per 1%, $R^2 = 0.999$), whereas under wet conditions the slope was lower (≈ 74 mcd/m² per 1%, $R^2 = 0.996$) but remained highly significant. The interaction term further demonstrated a statistically significant difference between the two conditions, indicating that the positive effect of phosphorus on retroreflectivity was attenuated under wet surfaces. All measured values were well above the international minimum standard of 200 mcd/m², demonstrating that phosphorus-enhanced thermoplastic road markings are highly effective for ensuring visibility and road safety, even under adverse weather conditions.

3.4 Skid resistance performance of road markings

The results of the skid resistance test, conducted using a Skid Resistance Tester with phosphorus additions of 10%, 20%, and 30%, are shown in Figure 6.

The skid resistance testing was carried out under two surface conditions: dry and wet, with phosphorus addition variations of 0%, 10%, 20%, and 30%. The test result table shows the effect of phosphorus addition on the skid resistance values of the road markings, all of which exceed the minimum standard for road marking skid resistance (Min. 45). The increase in values indicates that the addition of phosphorus significantly contributes to the improvement of the road marking's grip performance. Under the dry conditions, the increase in skid resistance is more significant compared to wet conditions. This may be due to differences in interaction between the marking material and water, which tends to reduce friction. Nevertheless, the skid resistance values under the wet conditions remained above the required minimum threshold.

Table 6 presents the regression summary of skid resistance responses to phosphorus concentration under both dry and wet surface conditions. The regression analysis indicates that the skid resistance increases with phosphorus concentration under both dry and wet conditions. In dry surfaces, the slope was approximately 0.290 SRT per 1% phosphorus (R^2 = 0.984), while in wet surfaces the slope was about 0.210 SRT per 1% phosphorus (R^2 = 0.969). The interaction term (Concentration×Wet) was -0.080 with p = 0.099, suggesting that the difference in slopes between dry and wet conditions is not statistically significant at the 5% level (marginal at the 10% level).

4 Discussion

The findings of this study demonstrate that incorporating up to 30% phosphorus into thermoplastic road marking paint with rosin ester binder significantly enhanced marking visibility, particularly under low-light conditions. Visibility parameters tested luminance intensity, retroreflectivity, and skid resistance, all improved consistently with increasing phosphorus content. Regression and interaction analyses further confirmed that these improvements were statistically significant under both dry and wet conditions, with slightly lower effects observed in wet conditions.

This study results supported the findings of Ismail and Nazri [10], who reported that glow-in-the-dark phosphorus could produce luminance up to 6 cd/m² in dry conditions, with skid resistance and reflectivity meeting international standards. The maximum reflectivity in this study reached 441 mcd/m² (dry) and 317 mcd/m² (wet), surpassing the global minimum threshold of 200 mcd/m². These results are consistent with earlier research [4], which confirmed that phosphorus is a more effective additive than conventional glass beads.

Previous studies [12] reported that the phosphorus-based resins exhibit high reflectivity performance across various light wavelengths relevant to nighttime visibility. Similarly, research [15] developed polyurethane-based road marking paint with phosphorus that showed the improved weather resistance and stable luminance throughout the observation period. Another study [5] reported that phosphorus enhances the mechanical durability of road markings under extreme weather conditions such as rain and cold.

Moreover, integration of the current findings with recent studies [14] highlights that aluminate-based luminescent materials such as strontium aluminate ($SrAl_2O_4:Eu^{2+},Dy^{3+}$) have significant potential for road marking due to their long-lasting glow capability. Moisture-related degradation challenges were successfully addressed using dual organic-inorganic coating techniques that enhance hydrothermal durability.

The study [23] authorsexamined active luminescent phosphorus-based road marking paint and found that a layer thickness of 500 µm resulted in an initial luminance of 4.38 cd/m² with optimal abrasion resistance, even under high temperatures. This strengthens the experimental rationale that controlling the composition and thickness of the coating directly impacts its optical and functional performance.

The improvement in luminance and surface performance can be attributed to the physicochemical interactions between the phosphorescent phosphorus compound and the rosin ester binder. The rosin ester, primarily composed of abietic acid derivatives, forms a hydrophobic polymeric network that encapsulates $SrAl_2O_4:Eu^{2+},Dy^{3+}$ particles. This structure prevents excessive moisture penetration and protects the phosphor particles from hydrolysis, which is a major factor reducing luminescence stability. During the thermoplastic melting and mixing process, partial interfacial bonding occurs between ester functional groups and the phosphor particle surfaces, enhancing particle dispersion within the binder matrix. This uniform dispersion improves the photon absorption and energy release, leading to a more stable and prolonged afterglow performance under the dark conditions. Furthermore, the viscoelastic property of rosin ester supports mechanical flexibility and microtexture retention on the pavement surface, which maintains sufficient skid resistance while improving optical brightness. These combined mechanisms explain how the phosphorus rosin ester system effectively enhances both luminance and surface performance, confirming the synergistic interaction between optical and structural properties of the composite material.

Thus, these research results are not only consistent with previous studies but also align with the latest global findings. The main contribution of this study lies in its innovative combination of phosphorus and natural rosin ester binder, an area rarely explored systematically. This formulation significantly enhances visibility and addresses sustainability by utilizing environmentally friendly materials. Therefore, the approach offers strong potential as a technical solution for improving traffic safety, especially in poorly lit or tropical rainy environments. The role of road markings in reducing the crash frequency has been further supported by recent field safety audits and predictive safety studies. Inadequate road markings and the absence of reflective devices have been identified as dominant contributors to blackspot formation on highways, while improved visibility and surface markings have been shown to effectively reduce accident rates. Hence, enhancing the luminance and durability of thermoplastic road markings, as confirmed in this study, aligns with global efforts to reduce visibility-related traffic crashes and supports evidence from recent safety audits and predictive analyses worldwide [24-25].

In practical terms, the adoption of higher phosphorus concentrations has not yet been standardized in current road marking specifications. Most commercial products still rely on conventional glass beads for cost efficiency and regulatory acceptance [26]. From an economic perspective, the introduction of phosphorus-based thermoplastic paint may increase initial production costs compared with conventional markings, primarily due to the higher price of phosphorescent pigments. However, these additional expenses could be offset by performance benefits, such as improved nighttime visibility, extended service life, and reduced repainting frequency, which ultimately contribute to more favorable long-term life-cycle costs [27]. These findings align with broader evidence on sustainability from previous studies. As reported in [28], advanced road marking systems reduced glass bead consumption by approximately 54%, paint usage by 63%, and organic solvent emissions by 97% over a 10-year life cycle. This supports the economic and environmental arguments presented in this study, confirming that the high-performance materials, such as phosphorus-based thermoplastic markings, can simultaneously enhance safety and resource efficiency. The economic and environmental discussions in this paper are based on theoretical assessments and literature evidence; further experimental validation is recommended.

In terms of environmental aspects, the phosphorescent additive $SrAl_2O_4$:Eu^{2+},Dy^{3+} is generally considered chemically stable and largely insoluble in water, which minimizes the risk of leaching and offers a safer profile compared to the conventional heavy-metal-based phosphors. However, previous studies have shown that prolonged exposure to moisture may induce partial hydrolysis, thereby reducing luminescent performance [29]. To address this issue, surface coating and modification techniques, such as silica or fluoride layers, have been reported to significantly improve water resistance and long-term stability [30-31]. These findings suggest that while the environmental risks of leaching are relatively low under normal conditions, further long-term durability and environmental impact studies are necessary to ensure sustainable use of road-marking materials.

Overall, those results confirm that the phosphorus additives enhance luminance, retroreflectivity, and skid resistance of thermoplastic road markings under both dry and wet conditions. Nevertheless, one limitation of this study is the absence of the long-term durability data and field validation. Future research should therefore include expanded testing, such as extended durability evaluation under real traffic and weather conditions, to validate and strengthen the laboratory findings.

5 Conclusion

Based on the findings, adding phosphorescent phosphorus to thermoplastic road marking paint with rosin ester binder significantly improves both visibility and surface safety performance. A concentration of 30% yielded the highest light emission intensity (538 mcd/m^2 under clear conditions), enhancing nighttime and rainy-weather visibility for drivers. All the modified samples met the SKh-1.M.03 technical specifications and maintained safe skid resistance values on both dry and wet surfaces, with maximum readings of 60 and 53, respectively. Therefore, incorporating up to 30% phosphorus is recommended as an effective safety improvement strategy to reduce accident risks by ensuring clearer and safer road markings under low-light or adverse weather conditions, without compromising paint quality.

Acknowledgment

The authors received no financial support for the research, authorship and/or publication of this article.

Conflicts of interest

The authors declare that they have no known competing financial interests or personal relationships that could have appeared to influence the work reported in this paper.

References

[1] Ministry of Public Works and Housing (PUPR). Special Specification SKh-1.9.21: Road markings. Jakarta: Directorate General of Highways, 2024.

[2] LYU, L., CHEN, Y., YU, L., LI, R., ZHANG, L., PEI, J. The improvement of moisture resistance and organic compatibility of $SrAl_2O_4$:Eu^{2+},Dy^{3+} persistent phosphors coated with silica-polymer hybrid shell. *Materials* [online]. 2020, **13**(426), 426. eISSN 1996-1944. Available from: https://doi.org/10.3390/ma13020426

[3] MUNIKANAN, V., PENG, N. C., YAHYAA, M. A., YUSOF, M. A. Strontium aluminate compound as road line materials application. *Jurnal Kejuruteraan/Engineering Journal* [online]. 2021, **4**(2), p. 17-21. eISSN 2289-7526. Available from: https://doi.org/10.17576/jkukm-2021-si4(2)-03

[4] POULOSE, A. M., ANIS, A., SHAIKH, H., ALHAMIDI, A., SIVA KUMAR, N., ELNOUR, A. Y., AL-ZAHRANI,

S. M. Strontium aluminate-based long afterglow PP composites: phosphorescence, thermal, and mechanical characteristics. *Polymers* [online]. 2021, **13**(1373), 1373. eISSN 2073-4360. Available from: https://doi.org/10.3390/polym13091373

[5] LIU, H., SUN, M., SU, Y., DENG, D., HUA, J., LV, Y. Chemiluminescence of black phosphorus quantum dots induced by hypochlorite and peroxide. *Chemical Communications* [online]. 2018, **54**, p. 7987-7990. ISSN 1359-7345. Available from: https://doi.org/10.1039/C8CC04513E

[6] MUVAZIZ, O. Understanding thermoplastic road markings and their functions. Solidline (in Indonesian) [online]. 2024. Available from: https://solidline.id/marka-jalan-thermoplsatic

[7] YILMAZ, B., DENIZ, I., FAZLI, H., BEKIRCAN, O., PRANOVICH, A., KARAOGUL, E. Sustainable thermoplastic road marking paint production from natural modified rosins. *Bioresources* [online]. 2024, **19**(2), p. 2160-2178. ISSN 1930-2126. Available from: https://doi.org/10.15376/biores.19.2.2160-2178

[8] DHAPODKAR, T. S., KADAM, A. R., DURAGKAR, A., DHOBLE, N. S., DHOBLE, S. J. Recent progress in phosphate based luminescent materials: a case study. *Journal of Physics: Conference Series* [online]. 2021, **1913**(1), 012024. eISSN 1742-6596. Available from: https://doi.org/10.1088/1742-6596/1913/1/012024

[9] XU, L., CHEN, Z., LI, X., XIAO, F. Performance, environmental impact and cost analysis of marking materials in pavement engineering: the state-of-the-art. *Journal of Cleaner Production* [online]. 2021, **294**(126302), 126302. ISSN 0959-6526, eISSN 1879-1786. Available from: https://doi.org/10.1016/j.jclepro.2021.126302

[10] ISMAIL, N., NAZRI, S. N. Performance of the glow in the dark thermoplastic road marking in Uniten. *International Journal of Civil Engineering and Technology (IJCIET)* [online]. 2019, **10**(11), p. 235-242. ISSN 0976-6308, eISSN 0976-6316. Available from: https://iaeme.com/Home/article_id/IJCIET_10_11_024

[11] NANCE, J., SPARKS, T. D. Comparison of coatings for $SrAl_2O_4$:Eu^{2+},Dy^{3+} powder in waterborne road striping paint under wet conditions. *Progress in Organic Coatings* [online]. 2020, **144**, 105637. ISSN 0300-9440, eISSN 1873-331X. Available from: https://doi.org/10.1016/j.porgcoat.2020.105637

[12] LI, G., LI, N., ZHANG, Y., HAN, J., YAO, T., FENG, X. Preparation of long afterglow luminescent road marking coatings and its applicability simulation. *PLOS One* [online]. 2025, **20**(9), e0330387. eISSN 1932-6203. Available from: https://doi.org/10.1371/journal.pone.0330387

[13] KIZIL, R., IRUDAYARAJ, J., SEETHARAMAN, K. Characterization of irradiated starches by using FT-raman and FTIR spectroscopy. *Journal of Agricultural and Food Chemistry* [online]. 2002, **50**(14), p. 3912-3918. ISSN 0021-8561, eISSN 1520-5118. Available from: https://doi.org/10.1021/JF011652P

[14] ZHANG, F., XIE, Y., ZHAO, X., HE, Y., PEI, J., XING, Y., WANG, S., ZHANKG, J. Aluminate long afterglow luminescent materials in road marking field: research progress and development a review. *Buildings* [online]. 2024, **14**(7), 2152. 2152. eISSN 2075-5309. Available from: https://doi.org/10.3390/buildings14072152

[15] YANG, X., FAN, Z., YULIN, H., CUI, K., WEI, L., ZHANG, H., LI, J. Mechanical properties, luminescent properties, and durability of solvent-free polyurethane-based phosphorescent road markings on asphalt pavements. *Construction and Building Materials* [online]. 2024, **414**, 135053. ISSN 0950-0618, eISSN 1879-0526. Available from: https://doi.org/10.1016/j.conbuildmat.2024.135053

[16] VILLA, C., EYMOND, F., MARQUET, P. L., BREMOND, R., SAINT-JACQUES, E. Method to predict the performance of luminescent road markings over a year. *Results in Engineering* [online]. 2024, **24**, 103388. eISSN 2590-1230. Available from: https://doi.org/10.1016/j.rineng.2024.103388

[17] AQSHA, A., WINOTO, H. P., ADHI, T. P., ET AL. Sequential esterification-Diels-Alder reactions for improving pine rosin durability within road marking paint. *Molecules*. 2023, **28**(13), 5236. ISSN 1420-3049. Available from: https://doi.org/10.3390/molecules28135236

[18] NOTOATMODJO, S. *Health research methodology*. Jakarta: Rineka Cipta, 2018. ISBN 978-979-518-984-8.

[19] ALFATIH, A. *Social research methodology*. Jakarta: Unsri Press, 2023. ISBN 978-979-587-758-5.

[20] National Standardization Agency of Indonesia. SNI 06-4826-1998: Specification for reflective thermoplastic road marking paint. Jakarta, Indonesia, 1998.

[21] Ministry of Public Works and Housing (PUPR). Interim special specification SKh-1.M-03: Thermoplastic road marking paint with Rosin Ester binder. Jakarta: Directorate General of Highways, 2024.

[22] AJI, S. Evaluation of surface skid resistance of asphalt concrete wearing course (AC-WC) pen 60/70 and buton natural asphalt (BNA) blend 75/25 under wet conditions with temperature variations. Undergraduate thesis. Indonesia: University of Indonesia, 2011. Available from: https://lib.ui.ac.id/detail?id=20290564&lokasi=lokal&utm

[23] WANG, K., LU, Z., ZOU, Y., ZHU, Y., YU, J. Preparation and performance characterization of an active luminous coating for asphalt pavement marking. *Coatings* [online]. 2023, **13**(6), 1108. eISSN 2079-6412. Available from: https://doi.org/10.3390/coatings13061108

[24] KHAN, M. N., SABIR, DASS, S., SINGH, G., JAGLAN, S. Road accident analysis and safety audit: a case study of MDR 132. *Communications - Scientific Letters of the University of Zilina* [online]. 2023, **25**(2), p. F26-F38. ISSN 1335-4205, eISSN 2585-7878. Available from: https://doi.org/10.26552/com.C.2023.026

[25] GORZELANCZYK, P., GROBELNY, M. An estimate of the number of accidents on polish highways based on the kind of road. *Communications - Scientific Letters of the University of Zilina* [online]. 2024, **26**(1), p. F13-F22. ISSN 1335-4205, eISSN 2585-7878. Available from: https://doi.org/10.26552/com.C.2024.012

[26] XU, L., SHI, Y., YANG, W. Performance, environmental impact and cost analysis of marking materials in pavement engineering: the state of the art. *Journal of Cleaner Production* [online]. 2021, **294**, 126302. ISSN 0959-6526, eISSN 1879-1786. Available from: https://doi.org/10.1016/j.jclepro.2021.126302

[27] PICARDO, A., GALVAN, M. J., SOLTERO, V. M., PERALTA, E. A comparative life cycle assessment and costing of lighting systems for environmental design and construction of sustainable roads. *Buildings* [online]. 2023, **13**(4), 983. eISSN 2075-5309. Available from: https://doi.org/10.3390/buildings13040983

[28] BURGHARDT, T. E., PASHKEVICH, A. Materials selection for structured horizontal road markings: financial and environmental case studies. *European Transport Research Review* [online]. 2020, **12**, 11. eISSN 1866-8887. Available from: https://doi.org/10.1186/s12544-020-0397-x

[29] GUO, C., LUAN, L., HUANG, D., SU, Q., LV, Y. Study on the stability of phosphor $SrAl_2O_4:Eu^{2+},Dy^{3+}$ in water and method to improve its moisture resistance. *Materials Chemistry and Physics* [online]. 2007, **106**(2-3), p. 268-272. ISSN 0254-0584, eISSN 1879-3312. Available from: https://doi.org/10.1016/j.matchemphys.2007.05.052

[30] QI, T., XIA, H., ZHANG, Z., KONG, S., PENG, W., ZHAO, Q., HUANG, Z. Improved water resistance of $SrAl_2O_4$: Eu^{2+}, Dy^{3+} phosphor directly achieved in a water-containing medium. *Solid State Sciences* [online]. 2017, **65**, p. 88-94. ISSN 1293-2558, eISSN 1873-3085. Available from: https://doi.org/10.1016/j.solidstatesciences.2017.01.006

[31] ACHARI, A. M., PERUMALSAMY, V., SWATI, G., KHARE, A. $SrAl_2O_4:Eu^{2+},Dy^{3+}$ long afterglow phosphor and its flexible film for optomechanical sensing application. *ACS Omega* [online]. 2023, **8**(48), p. 45483-45494. eISSN 2470-1343. Available from: https://doi.org/10.1021/acsomega.3c05222

DYNAMIC ROUTING WITH STATIC DELIVERY TIME WINDOWS IN URBAN LAST-MILE TRANSPORT LOGISTICS

Viktor Danchuk[1], Oleksandr Hutarevych[1], Stanislav, Popov[2,*], José Vicente Busquets-Mataix[3]

[1]Department of Information Analysis and Information Security, Faculty of Transport and Information Technologies, National Transport University, Kyiv, Ukraine
[2]Department of Transport Systems and Road Safety, Faculty of Transport and Information Technologies, National Transport University, Kyiv, Ukraine
[3]Department of Computer Engineering (DISCA), Polytechnic University of Valencia, Valencia, Spain

*E-mail of corresponding author: popov@ntu.edu.ua

Viktor Danchuk 0000-0003-4282-2400,
Stanislav Popov 0000-0002-9373-2934,
Oleksandr Hutarevych 0009-0003-7355-8160,
José Vicente Busquets-Mataix 0000-0003-2949-502X

Resume

To address the challenges of dynamic routing in the last-mile transport logistics, an adaptive method has been developed for solving a multi-criteria dynamic vehicle routing problem with static time windows, taking into account the actual configuration of the urban road network and the non-stationary traffic dynamics on its sections. At the same time, the method enables the use of consolidated real-time data on the dynamic characteristics of traffic flow on sections of the transport network from any sources available at the time of optimization (e.g., GIS, road sensors, mobile devices, etc.). The results of simulation studies using the ant colony optimization method indicate the promising potential of the proposed approach.

Available online: https://doi.org/10.26552/com.C.2026.001

Article info

Received 19 June 2025
Accepted 12 October 2025
Online 29 October 2025

Keywords:

last-mile transport logistics
intelligent transport systems
dynamic routing
optimization methods
artificial intelligence
sustainable transport

ISSN 1335-4205 (print version)
ISSN 2585-7878 (online version)

1 Introduction

One of the key approaches to improving the efficiency of urban last-mile transport logistics is enhancing delivery performance through the effective organization of supply processes and route optimization. Given the dynamic nature of urban road networks, practical solutions require the implementation of dynamic routing technologies that utilise the real-time data collection on urban road network conditions and advanced methods of discrete route optimization.

While the primary objective of general dynamic routing is to optimize overall costs and travel time, in last-mile e-commerce logistics, meeting delivery within a specified time window is a critical factor. Therefore, solving the Dynamic Vehicle Routing Problem with Time Windows (DVRPTW) is particularly important for the development of efficient, environmentally sustainable, and customer-oriented logistics in the context of the digital economy, as it enables a balance between the delivery optimality and customer requirements. The effective implementation of DVRPTW should contribute to the sustainable development of cities, the reduction of carbon footprint, and the improvement of accessibility and quality of delivery services in e-commerce.

Indeed, urbanization and the growing volume of e-commerce deliveries lead to increased traffic congestion and higher emissions of harmful substances. A systematic approach to analyzing the challenges of sustainable urban last-mile transport (ULMT) logistics involves the use of innovative operational and organizational solutions, including, in particular, the deployment of urban micro-consolidation centers (UMCCs), which reduce delivery distances, optimize routes, lower transport costs, and enhance accessibility for customers. In addition to traditional vehicles, this requires the adoption of alternative modes of transport to enhance efficiency and sustainability - such as cargo bikes and scooters, autonomous delivery robots, and unmanned aerial vehicles - which help to reduce congestion and are suitable for diverse urban environments. Accordingly, solving the DVRPTW problem enables not only the optimization of overall delivery routes, while accounting for traffic dynamics on sections of urban road network, but the efficient allocation of courier resources as well, by minimizing idle times and empty trips, as well as synchronizing operations with other services such as food, medicine, and bulky item deliveries.

Despite the significant progress, the development of effective dynamic routing systems remains a complex and challenging task. Although modern motion sensors and GPS/Galileo systems have significantly improved the real-time collection of road network data, the implementation of intelligent optimization methods - particularly for complex delivery configurations such as the dynamic traveling salesman problem - remains largely confined to simulation studies without full integration of actual traffic dynamics. Existing approaches address individual aspects of the last-mile delivery, such as route planning, scheduling, and fleet allocation. At present, there are no advanced online routing methods that simultaneously integrate delivery time windows and adapt to real-time traffic conditions. This problem can be addressed through adaptive dynamic routing systems capable of responding to demand fluctuations, optimizing transport efficiency, accounting for delivery time windows, and accommodating newly emerging orders. The development of such systems is the focus of this study.

2 Literature review

Urban last-mile freight transport logistics plays a key role in the functioning of modern urban ecosystems. With the rapid growth of e-commerce, increasing order volumes, and rising consumer expectations regarding delivery speed and timeliness, last-mile logistics processes are facing unprecedented challenges. These challenges include road congestion and traffic jams, high levels of pollution, low delivery efficiency, unpredictable shifts in consumer expectations and order patterns, and limited urban space for unloading and parking. This situation, in particular, results in the last link of the e-commerce supply chain accounting for 50% or more of total logistics costs, along with substantial greenhouse gas emissions and energy consumption [1]. Thus, addressing the challenges of urban last-mile transport logistics is crucial not only for ensuring economic efficiency and customer satisfaction but also for environmental sustainability.

The application of a systems approach to analyzing the identified challenges necessitates the development of appropriate pathways for achieving sustainable urban last-mile transport logistics, which are linked to the implementation of innovative organizational, transport, and operational solutions [2]. In recent years, the key directions for implementing organizational innovations have included the deployment of urban micro-consolidation centers, decentralized logistics hubs, robotic warehouses, and the use of shared logistics platforms that enable different companies to share infrastructure and delivery routes. The integration of such distribution logistics centers, automated parcel lockers, and various crowdsourced delivery models provides a strategic advantage by minimizing travel distances, thereby increasing operational efficiency [2]. These innovations are essential for ensuring fast and convenient delivery to recipients while simultaneously reducing the carbon footprint associated with long travel distances ([3] Mutavdzija et al., 2024). Simulation models, such as LOCAMM (Logistics and City Architecture Multilevel Model), demonstrate their effectiveness in urban freight management. Studies conducted in Dresden show that micro-hubs reduce the load on the road network while maintaining the efficiency of last-mile delivery operations [4].

The implementation of multi-echelon logistics systems, intermodal transport solutions, and advanced monitoring systems is also one of the key approaches to achieving sustainable urban last-mile transport logistics [5]. Particular importance is attached to the ongoing digitalization of transport and logistics processes, which has become increasingly evident in recent years. Studies show that digitalization affects logistics infrastructure, vehicle routing, and inventory management, enhancing both efficiency and resilience [6-7]. Digital logistics systems support the implementation of ESG principles (Environmental, Social, and Governance) by integrating logistics operations with clean technologies and the sustainable development goals of cities [6]. The use of digital twins for modeling urban logistics systems enables more effective decision-making [8]. The use of IoT, real-time GPS/Galileo data, predictive analytics, and artificial intelligence in planning leads to increased efficiency of transport operations, reduced load in the urban road network, improved environmental performance, and lower operational costs [9].

In addressing the last-mile delivery challenges, a variety of solutions are employed concerning the selection of different types of vehicles for executing deliveries. Here, the potential use of innovative transport modes - such as electric vehicles, cargo bikes, ground and aerial drones - is significant for reducing energy demand and mitigating the environmental impact associated with last-mile delivery [10-13].

However, the implementation of environmentally friendly transport modes faces a number of challenges. In particular, for electric vehicles, these challenges include operational limitations (such as limited driving range), battery-related issues (such as long charging times), and both infrastructural and financial difficulties in replacing existing fleets with more sustainable alternatives due to the need for charging stations and the high cost of vehicle acquisition (see, for example, [2]). Accordingly, the limited speed and load capacity of cargo bikes (CBs), along with the need for a new road infrastructure, represent major drawbacks for their use. Drone-based delivery also requires additional investments, such as the development of landing stations (see, for example, [2]). As a result, in most countries - particularly in less developed ones - the last-mile delivery is carried out within the framework of multimodal transport, using conventional vehicles at least during the initial stages of the supply chain [10].

The implementation of modern innovative operational solutions in sustainable urban last-mile transport logistics is linked to the optimization of dynamic routing processes, delivery time windows, the location of distribution centers, environmental impact, crowdsourcing, and business models based on collaboration between the private enterprises and public authorities. As the analysis shows, this set of operational challenges can be effectively addressed within the framework of the generalized DVRPTW model [14-15]. Indeed, such a model makes it possible to account for traffic dynamics on sections of the urban road network, the stochastic nature of customer orders, optimize courier resource allocation by minimizing idle times and empty runs, and synchronize goods delivery across different transport modes within multimodal systems. The implementation of such a real-time dynamic routing, while considering static delivery time windows, is crucial for reducing environmental impact, enhancing operational efficiency, and supporting the integration with urban sustainability initiatives.

However, it should be noted that existing approaches currently address only individual aspects of urban last-mile transport logistics, optimizing specific logistics tasks, such as route planning, scheduling and allocation of vehicles, handling the stochastic nature of customer orders, minimizing emissions, and improving vehicle utilization. This is due to the complexity of developing adaptive multi-factor mathematical models for the DVRPTW optimization, particularly for complex delivery configurations that could, in real time, simultaneously minimize delivery costs and maximize customer satisfaction. It is necessary to account for a large number of parameters, including traffic dynamics, delivery time, shipment volume, fleet size and composition, as well as the uncertainty and variability of customer requests during vehicle movement. Accordingly, [16] presents a DVRPTW variant that incorporates dynamic customer requests and variable time windows. In this case, a multiple ant colony algorithm combined with powerful local search procedures is proposed to solve the DVRPTW. In [17], a literature review is presented on shortest path optimization for courier services using heuristic and metaheuristic algorithms. In [18], the vehicle routing problem, involving multiple vehicles, time windows, and heterogeneous fleets, was addressed using ant colony optimization. To integrate the dynamic routing with urban micro-consolidation centers, where customer requests are directed to alternative third-party transshipment points in accordance with existing time window allocations, Adaptive Large Neighborhood Search algorithms are applied [19].

Recent research on DVRPTW solution methodologies indicates a trend towards the integration of heuristic and metaheuristic optimization algorithms with AI-based machine learning methods [15]. For example, hybrid models, combining deep reinforcement learning and simulated annealing-based optimization heuristics, are applied to vehicle routing problems that take into account time windows, as well as both known and stochastic customer behavior [20]. This enables the use of machine learning potential to search for adaptive routing solutions. Such models improve real-time route optimization by analyzing historical traffic patterns and fluctuations in delivery demand [21], enabling highly efficient management of the delivery process [22]. In [23], the application of metaheuristic and traditional algorithms to intelligent logistics planning is examined. It is shown that the highest performance and accuracy are achieved using ant colony optimization (ACO) algorithms. In [24], an analysis is provided on the prospects of integrating the neural network-based predictive analytics, route optimization algorithms, real-time tracking systems, and sustainable practices to address last-mile delivery challenges. In [25], to enhance the effectiveness of forecasting based on deep learning neural networks, the use of social media data is proposed. The proposed traffic forecasting framework, based on historical data, allows for the integration of additional analytical methods to further improve vehicle routing. These include modelling tools such as agent-based simulation, discrete-event simulation, and system dynamics modelling. The approaches presented in [15, 19, 21-22, 25] have the potential to reduce the delivery costs through fuel savings and increased efficiency; however, they do not resolve the challenge of real-time routing.

Thus, the conducted analysis reveals that the literature lacks comprehensive solutions to DVRPTW problems for urban last-mile transport logistics that simultaneously account, in real time, for the actual configuration and non-stationary traffic dynamics of the urban road network. Recent studies on dynamic vehicle routing within the traveling salesman problem (TSP) framework, conducted in [26-28] without consideration of time windows, indicate the promising potential of the approaches developed in these works for addressing DVRPTW problems.

Building upon [26-28], the results of developing a method for solving multi-criteria DVRPTW that accounts, in real time, for non-stationary traffic dynamics on the sections of the urban road network, are presented in this paper. The optimization criteria in this case are the minimization of total transport costs (in terms of route time) and the maximization of overall customer satisfaction. The solution strategy is based on the use of a modified AI method for the ant colony optimization (ACO_{mod}), which contains the concept of Pareto optimality for multi-objective optimization. Based on the developed method, an adaptable information system for dynamic vehicle routing with time windows is proposed for use in urban last-mile transport logistics. Within the adaptable information system DVRPTW framework, it is possible to take into account the actual configuration of the urban road network and utilise consolidated data on the dynamic characteristics of traffic flows on sections of this network from any sources available at the time of operation (e.g., GIS, road sensors, mobile devices) during the optimization process.

3 Research methodology

In this article are presented the results of developing a real-time DVRPTW solution method for urban last-mile transport logistics, based on solving an asymmetric Dynamic Traveling Salesman Problem with Time Windows, taking into account the actual configuration of the urban road network and traffic flow dynamics on its sections. Following [26], the urban road network is represented as a bidirectionally oriented weighted graph, where the nodes correspond to delivery points with time windows and depots. The arcs contain a sequence of urban road network sections, the traversal of which defines the optimal route between the corresponding pair of delivery points at specific times of the day. The solution of the DVRPTW in urban last-mile transport logistics is based on the following assumptions.

Delivery points may include customers, hubs, and parcel lockers. Parcel lockers are located in easily accessible areas for both couriers and customers, such as large residential neighborhoods or near public transport hubs.

The dynamic nature of the problem is due to the fact that routes may change in real time as a result of new orders or unforeseen events (e.g., changes in traffic flow dynamics on the urban road network sections, road congestion, weather conditions, etc.).

The delivery time windows (slots) generally differ for each delivery point, depending on factors such as order priority; however, the overall delivery timeframe is defined within the limits of a single day (e.g., night to morning, morning to noon, noon to evening, etc.).

For hubs and parcel lockers, the volume of goods and the number of delivery points are sufficiently large, and the delivery points are spaced far apart, making the use of pedestrian couriers and couriers on “green” transport modes inefficient in Dynamic Traveling Salesman Problem with Time Windows solutions. The use of bicycles, drones, or electric scooters is applied for short distances - from hubs to parcel lockers and from parcel lockers to customers - which aligns with the concept of sustainable development.

In urban settings, dynamic routing for deliveries from hubs to parcel lockers and from parcel lockers to customers is generally not relevant, as the movement is largely unaffected by traffic dynamics (couriers travel on foot, by bicycle, or scooter over relatively short distances).

The distribution of time windows at the delivery points allows all deliveries in the dynamic problem under consideration to be performed by a single vehicle.

To solve a Dynamic Traveling Salesman Problem with Time Windows, the use of a modified ant colony optimization algorithm, $\mathrm{ACO}_{\mathrm{mod}}$, is proposed. The choice of the ant colony optimization algorithm, as an AI optimization method for solving the last-mile urban transport logistics problems, is motivated by several factors. First, the ACO and its modifications are more versatile compared to most other heuristic optimization methods (see, for example, [28]), allowing for the solution of routing problems in urban road networks of the required scale. In addition, the ACO and its modifications often demonstrate higher performance [28]. Moreover, due to their synergetic nature, the optimization mechanisms of ACO and its modifications resemble the dynamics of traffic flow, particularly in high-density areas [28]. It should be noted that such synergetic effects are observed in nonlinear, nonequilibrium, dissipative systems of various physical natures (see, for example, [29-30]).

The modification of the classical ACO algorithm [31], to account for the time windows, which is used in this paper, is described in [32]. Here, the original transition rule of the classical ACO algorithm, which governs the movement of an ant from node i to node j, takes the following form in the modified algorithm $\mathrm{ACO}_{\mathrm{mod}}$:

$$j = \begin{cases} \underset{z \in N_i}{\operatorname{argmax}} \ (\tau_{iz})^{\alpha} (\eta_{iz})^{\beta} (g_{iz})^{\theta} (h_{iz})^{\gamma} & if\ q \leq q_0 \\ S, & otherwise \end{cases}, \quad (1)$$

where: τ_{iz} is represents the current amount of pheromone on the path from node i to node z; η_{iz} is denotes visibility, which in the classical algorithm is defined as the inverse of the distance $(\eta_{iz} = 1/d_{iz})$; g_{iz} is a heuristic that ensures prioritization of transitions to nodes whose upper time window bounds are closer to the ant’s expected arrival time at the node z; h_{iz} is a heuristic that aimed at minimizing the ant’s waiting time in cases where it arrives at a node before the lower bound of the time window; q_0 $(0 \leq q_0 \leq 1)$ is a user-defined parameter that determines the probability of selecting the most attractive node for the next move; q is a random number drawn from a uniform distribution over the interval [0, 1]; N_i is the set of nodes not yet visited by the ant; $\alpha, \beta, \theta, \gamma$ are user-defined parameters that control the influence of $\tau_{iz}, \eta_{iz}, g_{iz}$ and h_{iz} respectively; S is a probabilistic transition rule that defines the probability P_{ij} of an ant moving from node i to node j.

In presented case, in the modified ant colony optimization algorithm $\mathrm{ACO}_{\mathrm{mod}}$, unlike the classical ACO, two additional local heuristics g_{iz} and h_{iz} are used in Equation (1). In addition, according to the delivery time minimization criterion in DTSPTW, the visibility $\eta_{iz} = 1/t_{iz}$, where t_{iz} - is the expected travel time from node i to node z. Then, taking into account the heuristics g_{iz} and h_{iz}, the transition probability P_{ij} is determined as follows:

$$P_{ij} = \begin{cases} \dfrac{(\tau_{ij})^{\alpha}(\eta_{ij})^{\beta}(g_{ij})^{\theta}(h_{ij})^{\gamma}}{\Sigma_{z \in N_i}(\tau_{iz})^{\alpha}(\eta_{iz})^{\beta}(g_{iz})^{\theta}(h_{iz})^{\gamma}}, & if\ j \in N_i \\ 0. & otherwise, \end{cases} \quad (2)$$

where the heuristic g_{iz} is calculated according to [32] as follows:

$$g_{iz} = \begin{cases} \dfrac{1}{1+\exp(\delta(G_{iz}-G_{avg}))} & G_{iz} \geq 0 \\ 0, & otherwise. \end{cases} \quad (3)$$

Here $G_{iz} = b_z - t_{iz}$, where b_z is the upper bound of the time window at node z, and t_{iz} is the estimated arrival time of the ant traveling from node i to node z; δ is user-defined parameter, which controls the slope of the function; G_{avg} is average of all G_{ij} where $G_{ij} \geq 0$, $j \in N_i$ [32]. It is worth noting that although Equation (3) formally allows $g_{iz} = 0$, in the algorithm implementation, it is advisable to replace zero with a sufficiently small non-zero value to avoid zero transition probabilities in Equation (2).

According to [32], the heuristic h_{iz} in Equations (1) and (2) is calculated as follows:

$$h_{iz} = \begin{cases} \dfrac{1}{1+\exp(\lambda(H_{iz}-H_{avg}))} & H_{iz} \geq 0 \\ 0, & otherwise. \end{cases} \quad (4)$$

Here $H_{iz} = a_z - t_{iz}$, where a_z is the lower bound of the time window at node z, and t_{iz} is the arrival time of the ant currently at node i, traveling to node z; λ is user-defined parameter, which controls the slope of the function; H_{ava} is average of all H_{ij} ,where $H_{ij} > 0, j \in N_i$ [32].

In the classical ant colony algorithm [31] ants are uniformly distributed across all the nodes at the start of each iteration to enhance exploration. In contrast to [31], the present approach requires placing all ants at the same node to correctly account for the time window constraints, as time window feasibility necessitates a consistent temporal reference across all the ants within a single iteration. Thus, in the proposed modification of the Ant Colony Optimization model, the artificial ants start each iteration from a single location - either from the current position of the vehicle in the dynamic version of the Travelling Salesman Problem with Time Windows or from the starting depot in its static version. Although this approach somewhat reduces the algorithm‘s exploration capabilities, this limitation can be mitigated by appropriately decreasing the value of the parameter q_0 in Equation (1).

Thus, the main advantages of using the proposed ACO_{mod} algorithm for solving the Dynamic Travelling Salesman Problem with Time Windows include its relatively high performance, configurational flexibility to meet user-specific needs, and the minimization of vehicle idle time at delivery points. At the same time, the optimization criterion can be defined by redefining η, while the degree of influence of the time windows is controlled through the user-defined parameters. For example, in the cases where the strict adherence to time windows is required, higher values can be assigned to the parameters θ, and γ. Conversely, if the priority is to minimize delivery time t_{min}, it is recommended to use $\eta_{iz} = 1/d_{iz}$ instead of $\eta = 1/t$ and to assign a higher value to the parameter β. Thus, the proposed method enables the implementation of the Pareto optimality concept for multi-objective optimization.

Based on the developed method, the adaptable information system DVRPTW system has been proposed for use in urban last-mile transport logistics. The model of this system is schematically illustrated in Figure 1. Adaptable information system DVRPTW performs two main functions: it monitors the state of the urban road network based on section characteristics obtained from various data collection sources, and it supports the dynamic online optimization of routes using current or historical urban road network condition data.

To address the urban road network state monitoring task, it is necessary to collect and process data from all the available sources of information regarding the dynamic and sections static characteristics of this network. In this context, a key role is played by the monitoring of dynamic characteristics of urban road network sections, such as traffic flow parameters (average speed, density and intensity), environmental indicators (emissions of carbon dioxide (CO_2), particulate matter (PM), nitrogen oxides (NO_x), sulfur oxides (SO_x), volatile organic compounds (VOCs), etc.), noise pollution and others. Particular attention should be given to monitoring of environmental indicators, which play a significant role in the implementation of modern urban transport logistics methods aimed at realizing the concept of sustainable development.

In the absence of current values for certain dynamic characteristics of an urban road network section, they can be estimated based on the available current values of other characteristics and historical data. For example, in [27], the average traffic flow speed is calculated through an approximation using the current data on traffic intensity at the section under study and historical data on traffic density from a representative section within the homogeneous cluster of urban road network to which the section belongs.

To collect and store data on the characteristics of sections for the purpose of generating consolidated information on urban road network conditions, the proposed adaptable information system DVRPTW includes a dedicated subsystem called the “Urban Road Network State Monitoring Subsystem” (see Figure 1). This subsystem contains modules for processing and storing information on the condition of sections from various sources, such as GIS platforms, traffic sensors, air pollution detectors, VANET, MANET systems, and others. The system administrator configures access to available data sources and sets up update triggers

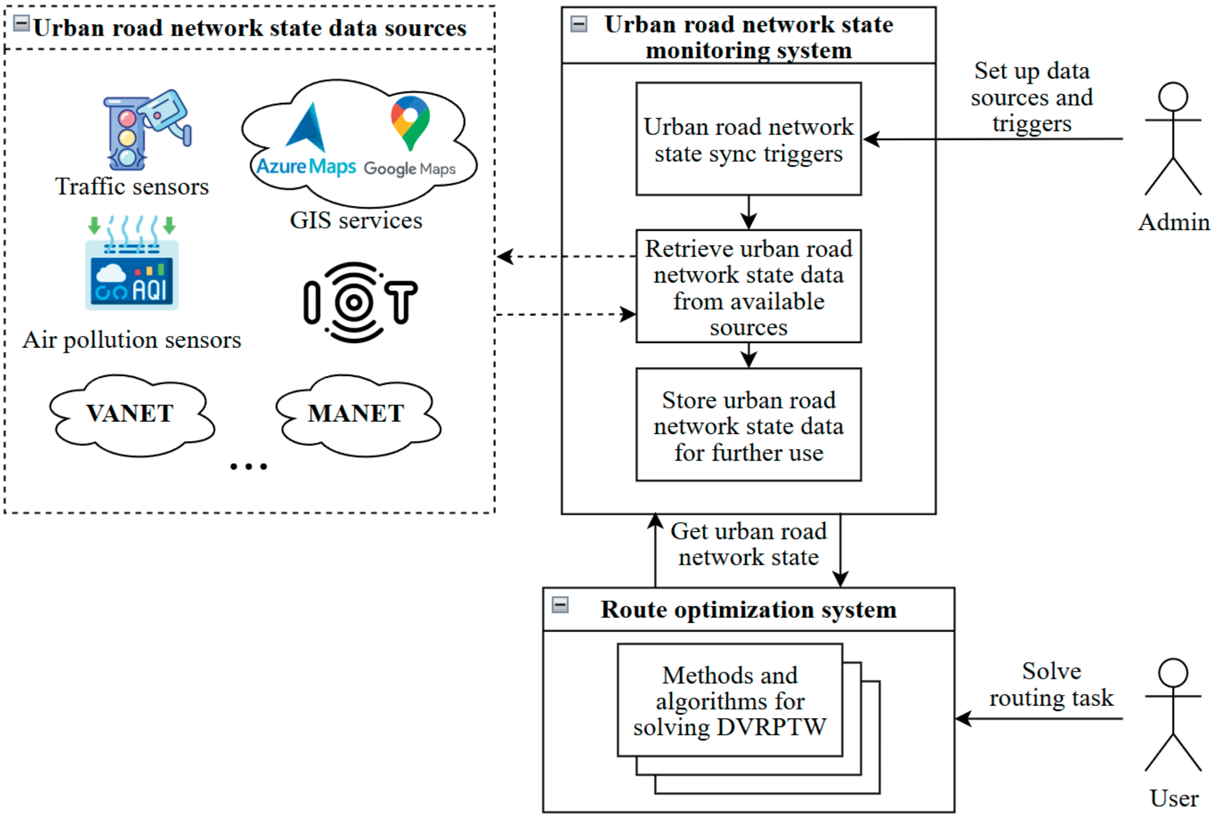

Figure 1 *Model of the adaptable information system for solving the DVRPTW with consideration of real-time urban road network conditions*

according to user requirements. The subsystem retrieves data on urban road network section conditions based on these predefined triggers and stores it for subsequent use in dynamic routing processes.

In the proposed adaptable information system DVRPTW, the task of dynamic user routing is handled by the "Route Optimization Subsystem" (see Figure 1). This subsystem incorporates various optimization methods and algorithms to solve different types of dynamic routing problems. It is important to emphasize that the optimization methods included in the system must be sufficiently versatile to address problems involving complex, multi-factor optimization criteria, while also being flexible and responsive to dynamic changes in the urban road network state. In this study, the ACO_{mod} algorithm is employed, with its application justified in the preceding sections.

At the start of the journey from the depot, the user submits a request to the system, including all the necessary input data according to the specific VRP type, such as the route optimization criterion, the locations of delivery points, their respective time windows, and/or other constraints. The Route Optimization Subsystem retrieves current data on the state of the urban road network in the required representation based on the problem type, determines the optimal solution using the most appropriate method for the given task, and sends the optimized solution back to the user. Dynamic re-optimization of the route occurs during the execution of the optimized path, depending on changes in current traffic characteristics on urban road network sections, the appearance of new orders, and other factors.

The operation of each subsystem is closely linked to the specifics of accessing information sources regarding the urban road network characteristics. To store historical data and enable its subsequent analysis, the system includes a dedicated data warehouse. For deploying such a system, the use of modern cloud technologies is recommended.

In authors' prior work [33] the architectural implementation of adptable intelligent transport system for dynamic routing is presented. The system's technical implementation leverages Amazon Web Services (AWS), which provides high level of cybersecurity, reliability, and system performance. The urban road network monitoring subsystem is built on a serverless architecture, enabling the robust scalability and efficient resource utilization when processing large volumes of real-time data from diverse sources. A dedicated data synchronization process leverages the AWS services such as Lambda, SQS, and DynamoDB to collect and store current urban road network characteristics. This real-time data is then consumed by the route optimization subsystem to support dynamic re-optimization. The re-optimization process is automatically triggered during route execution according to user-defined configurations, ensuring that the system remains both responsive and reliable.

***Table 1** Warehouse and shops (delivery points) with time windows*

Point ID	Address	Time Window
0	82 Kyrylivska Street	
1	24 Beresteiskyi Avenue	9:30 - 13:00
2	40 Mytropolyta Vasylia Lypkivskoho Street	9:30 - 11:30
3	50 Antonovycha Street	9:00 - 12:30
4	2 Vasylkivska Street	9:30 - 11:30
5	24 Lesi Ukrainky Boulevard	8:30 - 11:00
6	3A Mykhaila Hryshka Street	8:30 - 10:30
7	22/20 Petra Hryhorenka Avenue	8:00 - 11:00
8	2A Kharkivske Highway	8:00 - 10:30
9	12V Voskresenska Street	6:30 - 9:30
10	7/11 Khreshchatyk Street	6:00 - 9:00

4 Result and discussion

To evaluate the proposed DVRPTW method within the context of urban last-mile transport logistics, a series of simulation studies were conducted. The selected case involved the distribution of goods to retail outlets in Kyiv. During the simulation, a Dynamic Traveling Salesman Problem with Time Windows was solved in which a delivery vehicle transported customer orders from a warehouse (depot) to 10 designated delivery points and then returned to the depot. Those delivery points corresponded to branches of the well-known e-commerce retailer „Rozetka,“ which possesses a developed logistics infrastructure including stores, pickup points, and parcel lockers [34].

The addresses of the stores (delivery points) and the corresponding time windows for receiving the goods are summarized in Table 1. The column “Point ID” contains the identifiers of the points (the depot is assigned ID 0, and delivery points are numbered 1-10); the column “Address” specifies the address of each point; and the column “Time Window” indicates the time interval during the day which the respective delivery point can accept goods from the depot.

A graphical representation of the delivery point locations is shown in Figure 2.

The simulation studies were conducted under the following conditions:

- A truck loaded with customer orders departs at 7:30 AM from the warehouse (depot) - Point 0 (82 Kyrylivska Street).
- Due to the specific organization of store operations (e.g., workload balancing, urgent orders, etc.), each store has its own delivery schedule, meaning a static time window during which the delivery point is able to accept goods (see Table 1).
- The optimization criterion is the minimization of the total time spent on delivering goods to the specified stores in strict compliance with the defined time windows, followed by a return to the warehouse (depot). The optimization was carried out using the proposed method described in Section 3, with the following parameter values: $q_0 = 0.9$, $\alpha = 1$, $\beta = 5$, $\theta = 0.5$, $\gamma = 3$, $\delta = \lambda = 0.05$, $\rho = 0.1$, $m = 10$. This parameter configuration, except q_0, was adopted from [32]. The value of q_0 was reduced to enhance $\mathrm{ACO}_{\mathrm{mod}}$ exploration, which refers to the algorithm’s ability to search a broader range of potential solutions rather than prematurely converging. Such exploration is particularly important for the re-optimization process in dynamic scenarios.
- Unloading of goods at each store takes 15 minutes.
- Route re-optimization is performed after the goods are unloaded at a delivery point, and before the vehicle departs for the next destination.
- In the course of the simulation studies based on the proposed method, dynamic routing is carried out using the real-world data on the state of the urban road network, including GIS-based traffic data for sections (obtained from the Azure Maps service [35]) and data from road sensors located on selected sections.
- After completing deliveries to all the stores, the truck must return to the warehouse (depot).

The results of the simulation study on dynamic routing of goods deliveries to the specified “Rozetka” stores, taking into account time windows, are presented in Table 2. The symbol * marks the delivery point at which re-optimization is performed. The column “Current Time” indicates the time of day when the route was re-optimized. The column “Optimal Route” lists the optimal sequence of delivery points obtained as a result of re-optimization at the respective delivery point. The column “Current” provides the expected time (in seconds) for the optimal route obtained through re-optimization at that delivery point. The column “Previous” shows the expected time of the optimal route obtained from the previous re-optimization but recalculated for the current dynamic state of the network. The column “Initial” gives the expected time for the optimal route obtained from the initial optimization (at the time of departure from

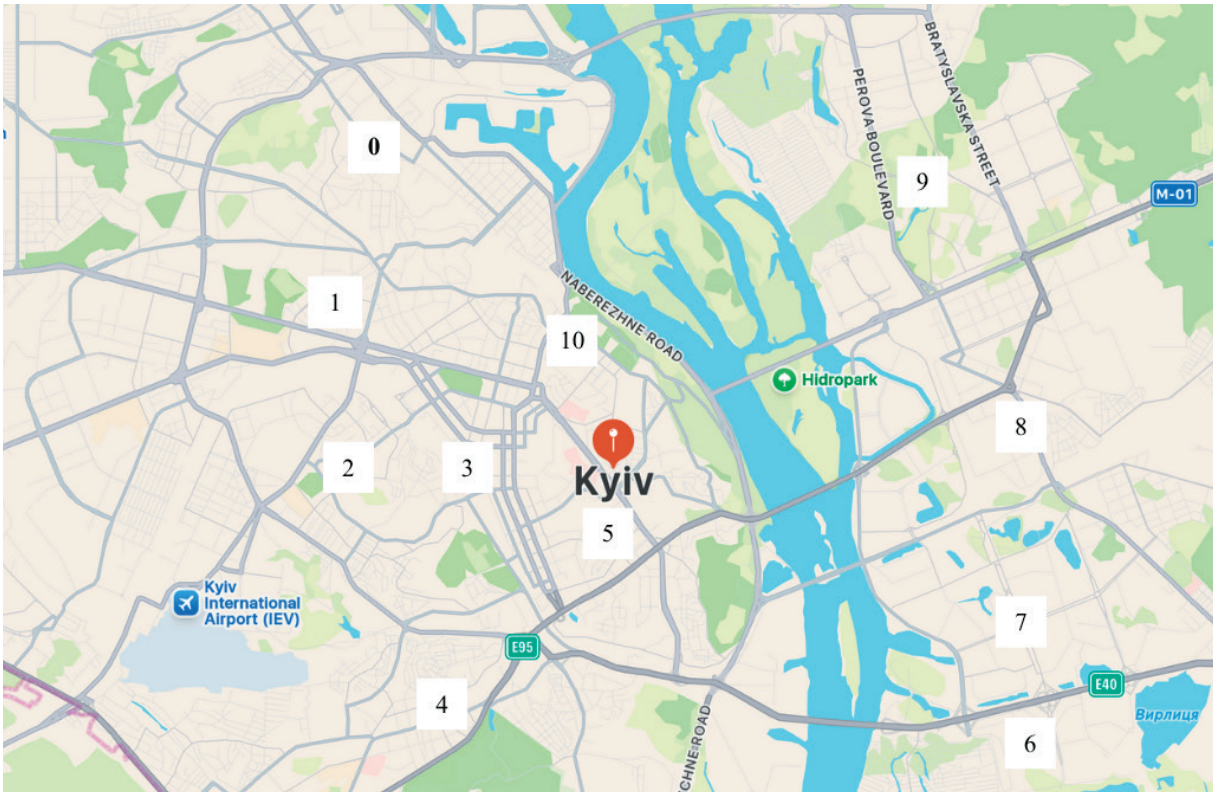

***Figure 2** Locations of the warehouse (0) and delivery points (1, …, 10) on the map of Kyiv*

***Table 2** Results of dynamic freight delivery routing with time windows in the* urban road network *of Kyiv*

Current time	Optimal route	Optimal route expected time, s		
		Current	Previous	Initial
07:30:00	0*10-9-8-7-6-5-4-3-2-1-0	15792	-	-
07:57:15	0-10*9-8-7-6-5-4-3-2-1-0	15755	15755	15755
08:24:26	0-10-9*8-7-6-5-4-(2-3)-1-0	18247	17974	17974
08:48:53	0-10-9-8*(5-7-6)-4-2-3-1-0	18420	18625	18248
09:16:05	0-10-9-8-5*(6-7)-4-(3-2)-1-0	17342	18469	17517
09:42:30	0-10-9-8-5-6*7-4-3-2-1-0	16645	16645	16766
10:01:12	0-10-9-8-5-6-7*4-3-2-1-0	16335	16335	16438
10:29:03	0-10-9-8-5-6-7-4*3-2-1-0	16237	16237	16359
10:53:36	0-10-9-8-5-6-7-4-3*2-1-0	16168	16168	16283
11:15:42	0-10-9-8-5-6-7-4-3-2*1-0	16197	16197	16331
11:36:35	0-10-9-8-5-6-7-4-3-2-1*0	16184	16184	16324
11:59:44	0-10-9-8-5-6-7-4-3-2-1-0*	-	16184	16324

* the current delivery point where re-optimization is being performed

the depot), but recalculated for the current dynamic state of the network, as well. In parentheses is shown the section of the route that is modified as a result of the re-optimization.

As evident from Table 2, the simulation studies, conducted using the proposed DVRPTW method in urban last-mile transport logistics, revealed several effects associated with the restructuring of the optimal route. For example, at specific times of day - 08:24:26, 08:48:53, and 09:16:05 - the optimal route is rebuilt (see Table 2) due to changes in traffic flow load distribution across the urban road network sections and the failure of some delivery time windows to align with the arrival times generated by the previously optimized route configurations, based on earlier (previous) states of traffic dynamics.

For instance, at 08:24:26, the optimal route was adjusted: the section 4-3-2-1 was restructured to 4-2-3-1. In this case, the travel time of the newly optimized route (18247 s ≈ 304 min) became longer than that of the previously determined optimal route (17974 s ≈ 300 min) due to an increase in traffic density - and consequently, a decrease in average speed - on certain sections of the urban road network. At the same time, an interesting observation is made (see Table 2). Route optimization at Point 9 at 08:24:26 reveals that the previously determined optimal route at Point 10 at 07:57:15 (0-10*-9-8-7-6-5-4-3-2-1-0) fails to ensure compliance with the delivery time windows at some of the subsequent points according to the specified optimal route configuration. Specifically, according to this route, arrival and completion of unloading at Point 2 is scheduled for 11:36:52 (see Table 2), whereas the time window for Point 2 is 09:30 - 11:30 (see Table 1). In contrast, for the updated optimal route generated at Point 9 at 08:24:26 - taking into account the current urban road network states - arrival and completion of unloading at Point 2 occurs at 11:12:49, which ensures compliance with the established delivery time window.

Next, at Point 8 at 08:48:53, the optimal route is further rebuilt - based on updated trafic data - to the configuration (0-10-9-8*-5-7-6-4-2-3-1-0), resulting in a reduction of the expected total delivery time from 18,625 s (≈ 310 min) to 18,420 s (≈ 307 min) (see Table 2). Accordingly, at Point 5 at 09:16:05, re-optimization also results in a rebuilding of the optimal route to the configuration (0-10-9-8-5*-6-7-4-(3-2)-1-0), which reduces the expected total route time by 6.1% (1,127 s ≈ 19 min) - from 18,469 s (≈ 308 min) to 17,342 s (≈ 289 min) (see Table 2). Interestingly, the rebuilding of the optimal route at Point 5 resulted in a reverse inversion of the sequence (3-2) to (2-3), which had previously occurred during the re-optimization at Point 9. Such a change in route configuration, resulting from decreased traffic intensity on urban road network sections, not only shortened the total route duration, but restored compliance with the time windows that had been violated at Point 9 at 08:24:26, as well. Now, the completion of delivery and unloading at Point 2 is scheduled within the designated time window of 09:30 - 11:30, specifically at 11:26:13.

Thus, the results of the simulation studies demonstrate the sufficient effectiveness and adaptability of the developed dynamic routing method with static time windows for urban last-mile transport logistics.

5 Conclusion

This study addressed the dynamic routing problems in urban last-mile transport logistics by developing a multi-criteria DVRPTW method that accounts non-stationary traffic dynamics on urban road network sections in real time.

The optimization criteria in this case are the minimization of total transport costs (in terms of route time) and the maximization of overall customer satisfaction. The solution strategy is based on a modified AI optimization method using the ant colony system, ACO_{mod}, which incorporates the concept of Pareto optimality for multi-objective optimization. Based on the developed method, an adaptable information system for dynamic vehicle routing with static delivery time windows has been proposed. The presented system is a universal solution for addressing the dynamic routing problems in transport logistics, as it incorporates capabilities for accounting for the actual configuration of the urban road network and enables the real-time use of consolidated data on dynamic traffic characteristics across network sections from any available sources at the time of operation (e.g., GIS, road sensors, mobile devices, etc.).

To validate the proposed method, simulation studies were conducted to determine the optimal route within the framework of an asymmetric Dynamic Traveling Salesman Problem with Time Windows, using travel time as the optimization criterion. These studies conducted in the urban road network of Kyiv, with deliveries to e-commerce retailer Rozetka pickup points, demonstrated the method's effectiveness and adaptability. The results showed that the optimal route is dynamically restructured in response to changing traffic load, ensuring that the deliveries remain within designated time windows. For example, some deliveries that would have violated their time windows under previously determined routes were successfully rebuilt through real-time optimization, and total travel time reductions of up to 6% were observed due to improved route sequence. These findings highlight the method's capability to adjust to traffic fluctuations, restore compliance with delivery schedules, and reduce overall route durations, confirming its practical value for urban last-mile logistics.

Despite these positive results, some limitations should be noted. The method was tested in a medium-sized urban segment with a single-vehicle case, and scaling to very large metropolitan networks may significantly increase computational requirements. While the architecture of the proposed system theoretically does not impose strict limitations on computing capacity, in practice its performance and stability are strongly influenced by the hosting environment, including the cloud infrastructure configuration and resource allocation. In addition, the approach assumes reliable and continuous access to traffic and environmental data; in the real-world conditions, incomplete or inconsistent data streams may reduce solution accuracy. Finally, the applicability of the method in other contexts - such as multimodal logistics systems, suburban areas, or cross-border transport corridors - remains to be further investigated. These limitations outline promising directions for future research.

Overall, the study demonstrates that developed method and information system DVRPTW propose a practical and adaptable approach to dynamic routing in urban logistics, effectively balancing operational efficiency and delivery reliability.

Acknowledgment

The authors received no financial support for the research, authorship and/or publication of this article.

Conflicts of interest

The authors declare that they have no known competing financial interests or personal relationships that could have appeared to influence the work reported in this paper.

References

[1] CUSHMAN and WAKEFIELD. Last link: quantifying the cost. Last link of e-commerce accounts for half of total supply chain costs [online] [accessed 2025-06-16]. Available from: https://industrial.pl/en/news/reports/266-what-is-an-expensive-link-in-the-supply-chain-last-link-report

[2] SILVA, V., AMARAL, A., FONTES, T. Sustainable urban last-mile logistics: a systematic literature review. *Sustainability* [online]. 2023, **15**(3), 2285. eISSN 2071-1050. Available from: https://doi.org/10.3390/su15032285

[3] MUTAVDZIJA, M., KOVACIC, M., BUNTAK, K. Moving towards sustainable mobility: a comparative analysis of smart urban mobility in Croatian cities. *Sustainability* [online]. 2024, **16**(5), 2004. eISSN 2071-1050. Available from: https://doi.org/10.3390/su16052004

[4] RIBESMEIER, M. Impacts of inner-city consolidation centres on route distances, delivery times and delivery costs. In: 12th International Scientific Conference on Mobility and Transport. Lecture Notes in Mobility: proceedings [online]. ANTONIOU, C., BUSCH, F., RAU, A., HARIHARAN, M. (Eds.). Singapore: Springer, 2023. ISBN 978-981-19-8360-3, eISBN 978-981-19-8361-0, p. 157-173. Available from: https://doi.org/10.1007/978-981-19-8361-0_11

[5] LAUENSTEIN, S., SCHANK, C. Design of a sustainable last mile in urban logistics - a systematic literature review. *Sustainability* [online]. 2022, **14**(9), 5501. eISSN 2071-1050. Available from: https://doi.org/10.3390/su14095501

[6] POURMOHAMMADREZA, N., JOKAR, M. R. A. A novel two-phase approach for optimization of the last-mile delivery problem with service options. *Sustainability* [online]. 2023. **15**(10), 8098. eISSN 2071-1050. Available from: https://doi.org/10.3390/su15108098

[7] BARYKIN, S. E., STRIMOVSKAYA, A. V., SERGEEV, S. M., BORISOGLEBSKAYA, L. N., DEDYUKHINA, N., SKLYAROV, I., SKLYAROVA, J., SAYCHENKO, L. Smart city logistics on the basis of digital tools for ESG goals achievement. *Sustainability* [online]. 2023, **15**(6), 5507. eISSN 2071-1050. Available from: https://doi.org/10.3390/su15065507

[8] BELFADEL, A., HORL, S., TAPIA, R., POLITAKI, D., PUCHINGER, J., TAVASSZY, L., PUCHINGER, J. A conceptual digital twin framework for city logistics. *Computers, Environment and Urban Systems* [online]. 2023, **103**, 101989. ISSN 0198-9715, eISSN 1873-7587. Available from: https://doi.org/10.1016/j.compenvurbsys.2023.101989

[9] HADIYANA, T., JI-HOON, S. AI-driven urban planning: enhancing efficiency and sustainability in smart cities. *ITEJ Information Technology Engineering Journals* [online]. 2024, **9**(1), p. 23-35. ISSN 2548-2130, eISSN 2548-2157. Available from: https://doi.org/10.24235/itej.v9i2.124

[10] GIRET, A. Smart and sustainable urban logistic applications aided by intelligent techniques. *Service Oriented Computing and Applications* [online]. 2019, **13**, p. 185-186. eISSN 1863-2394. Available from: https://doi.org/10.1007/s11761-019-00271-z

[11] VASIUTINA, H., SZARATA, A., RYBICKI, S. Evaluating the environmental impact of using cargo bikes in cities: a comprehensive review of existing approaches. *Energies* [online]. 2021, **14**(20), 6462. eISSN 1996-1073. Available from: https://doi.org/10.3390/en14206462

[12] HOSSAIN, M. Autonomous delivery robots: a literature review. *IEEE Engineering Management Review* [online]. 2023, **51**(4), p. 77-89. ISSN 0360-8581, eISSN 1937-4178. Available from: https://doi.org/10.1109/emr.2023.3304848

[13] LEMARDELE, C., ESTRADA, M., PAGES, L., BACHOFNER, M. Potentialities of drones and ground autonomous delivery devices for last-mile logistics. *Transportation Research Part E: Logistics and Transportation Review* [online]. 2021, **149**, 102325. ISSN 1366-5545, eISSN 1878-5794. Available from: https://doi.org/10.1016/j.tre.2021.102325

[14] PAVONE, M., BISNIK, N., FRAZZOLI, E., ISLER, V. A stochastic and dynamic vehicle routing problem with time windows and customer impatience. *Mobile Networks and Applications* [online]. 2009, **14**(3), p. 350-364. ISSN 1383-469X, eISSN 1572-8153. Available from: https://doi.org/10.1007/s11036-008-0101-1

[15] GIUFFRIDA, N., FAJARDO-CALDERIN, J., MASEGOSA, A. D., WERNER, F., STEUDTER, M., PILLA, F. Optimization and machine learning applied to last-mile logistics: a review. *Sustainability* [online]. 2022, **14**(9), 5329. eISSN 2071-1050. Available from: https://doi.org/10.3390/su14095329

[16] YANG, Z., VAN OSTA, J.-P., VAN VEEN, B., VAN KREVELEN, R., VAN KLAVEREN, R., STAM, A., KOK, A., BACK, T., EMMERICH, M. Dynamic vehicle routing with time windows in theory and practice. *Natural Computing* [online]. 2017, **16**, p. 119-134. ISSN 1567-7818, eISSN 1572-9796. Available from: https://doi.org/10.1007/s11047-016-9550-9

[17] PURNAMASARI, C. D., SANTOSO, A. Vehicle routing problem (VRP) for courier service: a review. *MATEC Web of Conferences* [online]. 2018, **204**, 07007. eISSN 2261-236X. Available from: https://doi.org/10.1051/matecconf/201820407007

[18] PHUC, P. N. K., THAO, L. P. Vehicle routing problem with time window and heterogeneous fleets. *Logistics* [online]. 2021, **5**(2), 28. eISSN 2305-6290. Available from: https://doi.org/10.3390/logistics5020028

[19] FRIEDRICH, C., ELBERT, R. Adaptive large neighborhood search for vehicle routing problems with transshipment facilities arising in city logistics. *Computers and Operations Research* [online]. 2022, **137**, 105491. ISSN 0305-0548, eISSN 1873-765X. Available from: https://doi.org/10.1016/j.cor.2021.105491

[20] JOE, W., LAU, H. C. Deep reinforcement learning approach to solve dynamic vehicle routing problem with stochastic customers. In: International Conference on Automated Planning and Scheduling: proceedings [online]. Vol. 30(1). 2020. ISSN 2334-0835, eISSN 2334-0843, ISBN 978-1-57735-903-6, p. 394-402. Available from: https://doi.org/10.1609/icaps.v30i1.6685

[21] LI, Y., GUAN, Q., GU, J., JIANG, X. A deep reinforcement learning with dynamic spatio-temporal graph model for solving urban logistics delivery planning problems. *International Journal of Digital Earth* [online]. 2024, **17**(1). ISSN 1753-8947, eISSN 1753-8955. Available from: https://doi.org/10.1080/17538947.2024.2376273

[22] YAN, L., TANG, Y., CHAN, P., YU, C. Y., ZHANG, W., WANG, J. Ecological and real-time route selection method for multiple vehicles in urban road network. *Journal of Advanced Transportation* [online]. 2023, 770800. eISSN 2042-3195. Available from: https://doi.org/10.1155/2023/3770800

[23] JIN, X. Application of metaheuristic algorithm in intelligent logistics scheduling and environmental sustainability. *Intelligent Decision Technologies* [online]. 2024, **18**(3). ISSN 1872-4981, eISSN 1875-8843. Available from: https://doi.org/10.3233/IDT-240280

[24] ZOSU, S., AMAGHIONYEODIWEM, C., OYETUNJI, E., YUSSUF, A. Last-mile delivery optimization: balancing cost efficiency and environmental sustainability. *International Journal of Emerging Trends in Engineering Research* [online]. 2024, **12**(11), p. 153-166. ISSN 2347-3983. Available from: https://doi.org/10.30534/ijeter/2024/0112112024

[25] LAYNES-FIASCUNARI, V., GUTIERREZ-FRANCO, E., RABELO, L., SARMIENTO, A. T., LEE, G. A framework for urban last-mile delivery traffic forecasting: an in-depth review of social media analytics and deep learning techniques. *Applied Sciences* [online]. 2023, **13**, 5888. eISSN 2076-3417. Available from: https://doi.org/10.3390/app13105888

[26] DANCHUK, V., HUTAREVYCH, O. Adaptable dynamic routing system in urban transport logistics problems using GIS data. *Scientific Journal of Silesian University of Technology. Series Transport* [online]. 2024, **125**, p. 19-31. ISSN 0209-3324, eISSN 2450-1549. Available from: https://doi.org/10.20858/sjsutst.2024.125.2

[27] DANCHUK, V., HUTAREVYCH, O., TARABAN, S. Dynamic routing in urban transport logistics under limited traffic information. *Communications - Scientific Letters of the University of Zilina* [online]. 2025, **27**(2), p. E21-E34. ISSN 1335-4205, eISSN 2585-7878. Available from: https://doi.org/10.26552/com.C.2025.021

[28] DANCHUK, V., COMI, A., WEISS, C., SVATKO, V. The optimization of cargo delivery processes with dynamic route updates in smart logistics. *Eastern - European Journal of Enterprise Technologies* [online]. 2023, **2**(3/122), p. 64-73. ISSN 1729-3774, eISSN 1729-4061. Available from: https://doi.org/10.15587/1729-4061.2023.277583

[29] PUCHKOVSKA, G. O., MAKARENKO, S. P., DANCHUK, V. D., KRAVCHUK, A. P., BARAN, J., KOTELNIKOVA, E. N., FILATOV, S. K. Dynamics of molecules and phase transitions in the crystals of pure and binary mixtures of n-paraffins. *Journal of Molecular Structure* [online]. 2002, **614**(1-3), p. 159-166. ISSN 0022-2860, eISSN 1872-8014. Available from: https://doi.org/10.1016/s0022-2860(02)00237-5

[30] DANCHUK, M. V., KRAVCHUK, A. P. Features of value-at-risk methodology application for business risks estimation under nonlinear dynamics of economic development. *Actual Problems of Economics* [online]. 2013, **148**(10), p. 207-213. ISSN 1993-6788. Available from: https://www.scopus.com/record/display.uri?eid=2-s2.0-84929995264&origin=recordpage

[31] DORIGO, M., GAMBARDELLA, L. M. Ant colony system: a cooperative learning approach to the traveling salesman problem. *IEEE Transactions on Evolutionary Computation* [online]. 1997, **1**(1), p. 53-66. ISSN 1089-778X, eISSN 1941-0026. Available from: https://doi.org/10.1109/4235.585892

[32] CHENG, C.-B., MAO, C.-P. A modified ant colony system for solving the travelling salesman problem with time windows. *Mathematical and Computer Modelling* [online]. 2007, **46**(9-10), p. 1225-1235. ISSN 0895-7177. Available from: https://doi.org/10.1016/j.mcm.2006.11.035

[33] DANCHUK, V., HUTAREVYCH, O. Dynamic routing in urban transport logistics in wartime conditions. In: *Intelligent transport systems: ecology, safety, quality, comfort. Proceedings of ITS ESQC 2024. Lecture notes in networks and systems (LNNS, volume 1335) Vol. 1* [online]. SLAVINSKA, O., DANCHUK, V., KUNYTSKA, O., HULCHAK, O. (Eds.). Cham: Springer, 2025. ISSN 2367-3370, eISSN 2367-3389, ISBN 978-3-031-87375-1, eISBN 978-3-031-87376-8, p. 339-349. Available from: https://doi.org/10.1007/978-3-031-87376-8_30

[34] ROZETKA shops - Kyiv (in Ukrainian) [online] [accessed 2025-04-16]. Available from: https://rozetka.com.ua/ua/retail/kyiv/

[35] Azure Maps - Geospatial Mapping APIs [online] [accessed 2025-04-19]. Available from: https://azure.microsoft.com/en-us/products/azure-maps

OPTIMIZING PATIENT TRANSPORT UNDER INFECTION CONTROL CONSTRAINTS: A MILP-BASED DIAL-A-RIDE APPROACH

Martin Tóth[1], **Adrián Horváth**[2,*], **Tamás Hajba**[3]

[1]Toma Logistics Kft, Sopron, Hungary
[2]Faculty of Architecture, Civil Engineering and Transport Sciences, Szechenyi Istvan University, Gyor, Hungary
[3]Faculty of Informatics and Electrical Engineering, Szechenyi Istvan University, Gyor, Hungary

*E-mail of corresponding author: hadrian@sze.hu

Martin Tóth 0009-0006-7252-1448, Adrián Horváth 0000-0002-1563-583X,
Tamás Hajba 0000-0003-0970-7267

Resume

With aging populations and rising healthcare demands, efficient patient transportation has become a critical challenge, particularly in the context of infection control. In this paper an extended mixed-integer linear programming (MILP) model for optimizing patient transport in urban environments is presented, with a focus on the separate transportation of infectious and non-infectious individuals. The model incorporates time windows, maximum allowable ride durations, and mandatory vehicle disinfection requirements. Experimental results obtained using CPLEX demonstrate that incorporating infection control measures significantly influences both route planning and computational complexity. The proposed approach provides a scalable foundation for future multi-vehicle extensions and cost-based optimization strategies.

Article info

Received 3 October 2025
Accepted 18 November 2025
Online 16 January 2026

Keywords:

Dial-a-Ride problem
patient transportation
mathematical modeling
mixed-integer linear programming

Available online: https://doi.org/10.26552/com.C.2026.008

ISSN 1335-4205 (print version)
ISSN 2585-7878 (online version)

1 Introduction

Modern transportation systems have undergone the rapid transformation over past decade, primarily driven by the spread of digital platforms and the rise of real-time service coordination. In both passenger and freight sectors, technological advancements have enabled unprecedented levels of flexibility, speed, and user-centered customization. Same-day delivery services, app-based ride-hailing platforms, and real-time tracking have become standard features across much of the logistics landscape. These developments have not only improved operational efficiency but have also reshaped customer expectations regarding accessibility and responsiveness.

While many aspects of transportation have advanced significantly, the mobility of nonemergency patients, particularly in urban healthcare environments remains a complex, evolving area with ongoing challenges. While the ambulances and specialized vehicles are available for critical or long-distance cases, patients attending routine appointments often rely on public transport or private vehicles. However, these alternatives are frequently unsuitable for elderly individuals or those with reduced mobility, as they may involve multiple transfers and long walking distances. Furthermore, private vehicle use is not always a viable option for older adults due to physical or cognitive limitations, and services such as taxis or ride-hailing platforms (e.g., Uber) can be prohibitively expensive for regular use.

In this study a door-to-door, ride-sharing-based patient transportation model that operates with a single vehicle is introduced. The model builds upon the well-established Dial-a-Ride Problem (DARP) framework, which is widely used in demand-responsive transportation systems [1]. It is designed to coordinate multiple patient pickups and drop-offs, while respecting strict time windows and compatibility constraints. The objective was to minimize the total distance traveled by a vehicle, while maximizing its utilization [2].

In the previous work [3] authors studied a problem in which patients are transported to the same hospital by a single vehicle. Each patient specifies their desired arrival time, earliest possible pickup time, and a realistically acceptable maximum travel duration. The model also takes into account the number of passengers at each pickup location, as well as their specific mobility-related requirements.

Four MILP models of the problem were proposed and tested on 5 different sized problems. The largest problem contained 30 pickup points and 60 patients. The best model was able to find the optimal solution in all of the problems in less than 60 seconds.

In this article, the previously examined patient transportation problem is extended by incorporating two real-world features that are essential for practical implementation: (1) the incompatibility between infectious and noninfectious passengers, who must not share the same route segment; and (2) mandatory vehicle disinfection after the transportation of infectious patients, which requires the vehicle to return to the depot before continuing its route. These additional constraints are motivated by infection prevention protocols, particularly those introduced during the COVID-19 pandemic, and they are critical for designing safe and regulation-compliant patient logistics systems.

To address the extended problem, a mixed-integer linear programming (MILP) model is proposed that incorporates infection-aware constraints, such as passenger incompatibility and mandatory vehicle disinfection. The model is tested on various infection scenarios to evaluate its efficiency and scalability. By embedding these constraints into an exact optimization framework, this study contributes both to the theoretical advancement of compatibility-sensitive DARP models and to the practical development of patient transportation systems that comply with modern public health standards.

2 Literature overview

The Dial-a-Ride Problem (DARP) is a well-established framework in transportation research, particularly suited for modelling the demand-responsive services where users specify pickup and drop-off locations, time windows, and service preferences. In its classical form, a fleet of vehicles departs from a depot to fulfill transport requests while minimizing total travel costs or distance, subject to vehicle capacities and temporal constraints [4].

Over the past decade, DARP has been adapted for a variety of real-world applications. Bongiovanni et al. [5] addressed an electric autonomous DARP variant, taking into account energy constraints and recharging infrastructure, by applying a branch-and-cut algorithm. Similarly, Agra et al. [6] explored the use of a new branching algorithm to solve a continuous-time inventory routing problem involving both pickups and deliveries, showcasing the flexibility of the DARP model in logistics domains.

Within the healthcare sector, patient transportation presents additional challenges, including medical requirements, service reliability, and personnel scheduling. Lim et al. [7] proposed a methaheuristic to solve a patient transportation problem in Hong Kong that includes staff scheduling as well. Luo et al. [8] further extended this work by including constraints for the staff breaks and rest periods, and developed a two-phase branch-and-price-and-cut algorithm. In rural Austrian contexts, Armbrust et al. [9] investigated a dynamic deterministic DARP in which the goal was to minimize a linear combination of the total kilometer travelled by the vehicles, the number of the vehicles and the number of the unmet requests. Their hybrid approach combined MILP and large neighborhood search techniques.

One of the most relevant themes for this study is passenger compatibility, especially in the context of infection risk. Molenbruch et al. [10] proposed a bi-objective DARP formulation in which the compatible patients were grouped based on medical needs. Schulz [11] introduced a more refined compatibility model, defining customer types based on their ability or willingness to share a vehicle. Their branch-and-cut algorithm ensured that mutually incompatible passengers would not be transported together. Further advancements were made by Lokhandwala et al. [12], who introduced a graded preference scale for ride-sharing, ranging from those who prefer to ride alone to those who prefer shared travel. The authors applied a column generation approach to address the problem.

The issue of incompatibility also arises in freight and postal delivery contexts. Colombi et al. [13] studied the rural postman problem with incompatible deliveries, modelling route penalties based on pairing constraints. Bernardino et al. [14] applied iterated local search to solve the family Travelling Salesman Problem (TSP) with incompatibility constraints. In the freight sector, Manerba et al. [15] and Gendreau et al. [16] developed multivehicle models to address pairwise incompatibility between transported products, leveraging exact methods including branch-and-cut and hybrid column generation. Factorovich et al. [17] studied the pickup and delivery problem with incompatibilities. In their work, a single vehicle is used to transport the goods, but the problem does not contain time windows or maximum riding times.

Despite the breadth of research on compatibility-aware routing, this literature review found no prior studies that explicitly integrate the infection-based patient incompatibility and mandatory vehicle disinfection procedures into a MILP-based DARP model. This represents a significant research gap, especially in the post-pandemic context where infection control measures are crucial in public health transportation. The present study addresses this gap by developing a model that combines infection-aware constraints with exact optimization techniques, making it directly applicable to real-world healthcare logistics planning.

3 Problem description

Let $G = (V, E)$ be a directed graph whose vertices are labeled from 0 to $N + 1$, where N is the number of the pickup places. The depot is represented by point 0, the hospital is represented by point $N + 1$, and the pickup points are represented by the vertices 1, 2, … N. Every arc (i, j) of the graph has two nonnegative weights: the traveling distance between points i and j and the traveling time from point i to point j. Starting from a depot a single vehicle visits the pickup points and transports the patients to the hospital. After all the patients are transported to the hospital, the vehicle returns to the depot. There is a predefined time window during which the vehicle must start and complete its tour. In the examined scenarios, the operating company allows vehicle operations only between 6:00 AM and 6:00 PM. This constraint limits both the earliest departure from the depot and the latest return, ensuring that all the patient transport activities occur within standard working hours. Furthermore, the vehicle has two different capacities, one for the number of the patients, and another one for the number of the mobility-impaired patients that can be transported by a vehicle. For each pickup point i a list containing the following key parameters is known:

- The number of patients at point i,
- The number of mobility-impaired patients at point i,
- The earliest time the vehicle can pick up the passengers at point i,
- An upper bound on the riding time of the passengers at point i,
- A due date at which the passengers at point i have to arrive at the hospital,
- The boarding time of the patients at point i on the vehicle, and
- The possible presence of infectious patients among the passengers at point i.

The vehicle has to visit each pickup point exactly once, which implies that for each pickup point, neither the number of the patients nor the number of the mobility-impaired patients exceeds the corresponding capacity of the vehicle. Since the goal is to protect patients from infection, infectious and noninfectious patients cannot be transported together. Furthermore, after the vehicle arrives at the hospital with infectious patients, it has to go back to the depot and undergo a disinfection procedure before continuing its tour. Finally, once the vehicle arrives at the hospital all the patients must get off the vehicle. The goal is to find the optimal route for a vehicle, which satisfies all of the constraints and minimizes the total distance run by the vehicle.

4 Mathematical formulation

To formulate the problem as a MILP model, the problem is first transformed into a Traveling Salesman Problem (TSP) with additional constraints.

To model the hospital connections, we define an extended graph $G' = (V', E')$, where each pickup point i has a corresponding hospital point $i + N$. The G' is a directed graph whose vertices are numbered from 0 to $2N + 1$. Vertex 0 is the depot, the vertices labeled as 1, 2, … N are representing the pickup points. For each pickup point i there is a corresponding 'hospital point in G' denoted by $i + N$. For each pickup point i patients at point i have to be transported to the corresponding hospital point $i + N$. Thus, the new graph G' has N hospital points. In G', the traveling time and the distance between points i and j are defined as follows:

- if i is a pickup point or the depot, and j is a pickup point, then the traveling time and the distance between points i and j in G' are the same as in G;
- if i is a pickup point or the depot, and j is a hospital point (i.e., $N + 1 < = j <= 2N + 1$), then the traveling time and the distance between points i and j in G' are the traveling time and the traveling distance between i and the hospital in G;
- if i and j are both hospital points, then the traveling time and the distance between points i and j are 0 in G';
- if i is a hospital point, then the traveling time and the distance between point i and point 0 (i.e. the depot) in G' is the traveling time and the distance between the hospital and the depot in G;
- if i is a hospital point corresponding to a pickup point with noninfectious patients and j is a pickup point, then the traveling time and the distance between points i and j in G' are the traveling time and the distance between the hospital and j in G;
- if i is a hospital point corresponding to a pickup point with infectious patients and j is a pickup point, then the distance between i and j in G' is the sum of the distance between the hospital and the depot in G and the distance between the depot and j in G (i.e., $D_{ij} = D_{i0} + D_{0j}$);
- finally, if i is a hospital point corresponding to a pickup point with infectious patients and j is a pickup point, then the traveling time from i to j in G' is set to the sum of the traveling time from the hospital to the depot in G, the traveling time from the depot to j in G and the time of the disinfection procedure at the depot (i.e., $T_{ij} = T_{i0} + T_{0j} + disinf$).

It can be easily seen that a tour in G' yields a tour in G. However, a tour in G' may not yield a feasible solution of the original problem. To show this, a problem with 4 pickup points is considered. In this case, vertex 0 is the depot, vertices 1/2/3/4 are the pickup points and vertices 5/6/7/8 are the hospital points in G'. The tour 0-1-6-4-3-2-5-7-8-0 is not a feasible tour since the patients at a pickup point 2 are picked up after that vehicle visited the corresponding hospital point 6. Furthermore, the tour 0-1-2-3-5-6-4-8-7-0 is not a feasible tour either, because patients at pickup point 3 are transported to the hospital but they do not get off the vehicle there (the vehicle visits pickup point 3, then it travels to hospital points 5 and 6, but before reaching hospital point 7 (the delivery point of pickup point 3) it visits pickup point 4). So, in order that the solution of the TSP in *G'* yields the optimal solution of the original problem, the model has to ensure that:

- the constraints associated with the vehicle (capacities of the vehicle (patients, mobility-impaired patients) and the passengers (maximum riding time, earliest pickup time, maximal arrival time, incompatibility restrictions) are satisfied;
- each pickup point i has to be visited earlier by the vehicle than the corresponding hospital point $i+N$;
- if the vehicle visits the pickup points i_1, i_2, ...i_k before traveling to a hospital point, then the vehicle has to continue its tour by visiting the hospital points $i_1 + N$, $i_2 + N$, ..., $i_k + N$ in the same order.

The following notations are used in the model:

Parameters:

- N: total number of pickup points,
- $D_{i,j}$: distance between points i and j where $0 \le i, j \le 2N$,
- $T_{i,j}$: time required to travel from point i to j, where $0 \le i, j \le 2N$,
- C_1: maximum capacity of the vehicle for regular patients,
- C_2: maximum capacity of the vehicle for mobility-impaired patients,
- p_i: number of regular patients at pickup point i; $1 \le i \le N$,
- dp_i: number of mobility-impaired patients at pickup point i; $1 \le i \le N$,
- ip_i: indicator of the presence of an infectious patient at point i.; $i_{pi} = 1$ if infectious, otherwise 0,
- I_i: maximum allowable travel time for patients at point i; $1 \le i \le N$,
- a_i: time required for boarding patients at point i; $1 \le i \le N$,
- tr_i: earliest time patients can be picked up at point i; $1 \le i \le N$,
- ta_i: latest allowable arrival time at the hospital for patients from point i; $1 \le i \le N$,
- A_0: opening time of the depot,
- B_0: closing time of the depot.

Continuous variables:

- pn_i: number of regular patients on the vehicle after visiting point i; $0 \le i \le 2N$,
- dpn_i: number of mobility-impaired patients in the vehicle after visiting point i; $0 \le i \le 2N$,
- m_i: arrival time of the vehicle at point i; $0 \le i \le 2N$.
- Integer variables
- u_i; $0 \le i \le 2N$.

The integer variable u_i is an auxiliary variable used in the Miller–Tucker–Zemlin (MTZ) formulation to eliminate subtours [18]. It represents the order or position of vertex i in the route, ensuring that the solution forms a single continuous tour visiting all nodes exactly once. For the depot, $u_0 = 0$.

Binary variables:

- $x_{i,j}$: equals 1 if the vehicle travels from point i to point j; $0 \le i, j \le 2N$.

5 Constraints of the model

The mathematical formulation of the problem includes several constraints, which define the structure of the vehicle's route and the conditions for transporting patients. These constraints ensure the feasibility and efficiency of the solution.

$$\sum_{i=0}^{2N} x_{i,j} = 1, 0 \le j \le 2N, \tag{1}$$

$$\sum_{j=0}^{2N} x_{i,j} = 1, 0 \le i \le 2N, \tag{2}$$

$$u_0 = 1, \tag{3}$$

$$2 \le u_i \quad 1 \le i \le 2N, \tag{4}$$

$$u_i \le 2N + 1, 1 \le i \le 2N, \tag{5}$$

$$u_i + 1 \le u_j + 2N^*(1 - x_{i,j}), 1 \le i, j \le 2N, \tag{6}$$

$$u_i + 1 \le u_{i+N}, 1 \le i \le N, \tag{7}$$

$$x_{i,j} = x_{j+N,i+N}, 1 \le i, j \le N, \tag{8}$$

$$pn_0 = 0, N + 1 \le i \le 2N, \tag{9}$$

$$pn_i = 0, N + 1 \le i \le 2N, \tag{10}$$

$$dpn_0 = 0 \quad N + 1 \le i \le 2N, \tag{11}$$

$$dpn_i = 0, N + 1 \le i \le 2N, \tag{12}$$

$$pn_i \le Cp, 1 \le i \le 2N, \tag{13}$$

$$dpn_i \le Cdp, 1 \le i \le 2N, \tag{14}$$

$$pn_i + p_j + 2 * Cp * (x_{i,j} - 1) \le pn_j, \\ 0 \le i \le 2N; 1 \le j \le N, \tag{15}$$

$$dpn_i + dp_j + 2 * Cdp * (x_{i,j} - 1) \le dpn_j, \\ 0 \le i \le 2N; 1 \le j \le N, \tag{16}$$

$$m_0 + T_{0,i} + M^*(x_{0,1} - 1) \le m_i, \ 0 \le i \le N, \tag{17}$$

$$m_i + T_{i,j} + a_i + M^*(x_{i,j} - 1) \le m_j, \\ 1 \le i \le N; 1 \le j \le 2N, \tag{18}$$

$$m_i + T_{i,j} + M^*(x_{i,j} - 1) \le m_j, \\ N + 1 \le i \le 2N; 1 \le j \le 2N, \tag{19}$$

$$tr_i \leq m_i, 1 \leq i \leq N, \tag{20}$$

$$m_{i+N} - m_i \leq I_i \quad 1 \leq i \leq N, \tag{21}$$

$$m_{i+N} \leq ta_i, 1 \leq i \leq N, \tag{22}$$

$$A_0 \leq m_0, \tag{23}$$

$$m_{i+N} + T_{i+N,0} \leq B_0, 1 \leq i \leq N, \tag{24}$$

$$x_{i,j} = 0 \text{ and } x_{j,i} = 0\,,\ 1 \leq i, j \leq N, ta_i \leq tr_j, \tag{25}$$

$$x_{i,i} = 0, 0 \leq i \leq 2N, \tag{26}$$

$$u_i + 2 \leq u_j\,,\ 1 \leq i, j \leq N, ta_i \leq tr_j, \tag{27}$$

$$x_{i,j} = 0 \text{ and } x_{j,i} = 0, 1 \leq i; j \leq N; ip_i \neq ip_j, \tag{28}$$

$$\sum_{i=0}^{2N} \sum_{j=0}^{2N} x_{i,j} * D_{i,j} \rightarrow \min. \tag{29}$$

Equations (1) and (2) ensure that each point of G' is visited by the vehicle exactly once. Constraints in Equations (3) to (6) are the subtour elimination constraints of the MTZ model of the TSP problem. Constraint in Equation (7) states that each pickup point is visited earlier by the vehicle than the corresponding hospital point. Equation (8) states that the vehicle travels from a pickup point i to a pickup point j if the vehicle travels from hospital point $j + N$ (corresponding to a pickup point j) to hospital point $i + N$ (corresponding to a pickup point i). This implies that if the vehicle visits pickup points i_1, i_2 … i_l, before going to a hospital point, the vehicle visits the corresponding hospital points in the reverse order, i.e., after i_1 the vehicle visits the hospital points i_{l+N}, i_{l-1+N}, … i_{1+N}. Constraints in Equations (9) to (12) ensure that after leaving the depot or a hospital point, there is no patient or mobility-impaired patient in the vehicle. Constraints in Equations (13) and (14) state that the number of patients or mobility-impaired patients cannot exceed the capacity of the vehicle. Constraints in Equations (15) and (16) ensure, that if the vehicle travels from point i to point j, the number of patients (mobility-impaired patients) in the vehicle after leaving point j cannot be less, than the number of patients (mobility-impaired patients) in the vehicle after leaving point i plus the number patients (mobility-impaired patients) at point j. Constraints in Equations (17) to (19) imply that if the vehicle visits point j after points i, the arriving time at point j cannot be less than the arriving time at point i plus the traveling time from point i to point j plus the boarding time of the patients (if there are any patient) at point i. Constraint in Equation (20) states that the vehicle cannot arrive earlier at a pickup point than the earliest pickup time of the patients at that pickup point. Inequality in Equation (21) ensures that the maximal riding time constraints of the passengers are satisfied. Constraint in Equation (22) states that all of the patients arrive at the hospital before their due date. Constraints in Equations (23) and (24) state that the vehicle starts and finishes its tour in the opening time of the depot. Constraints in Equations (25) and (27) imply that if the latest arrival time at the hospital for patients at pickup point i is less or equal than the earliest pickup time of patients at point i, the vehicle can travel neither from i to j nor from j to i. Constraint in Equation (26) states that the vehicle has to move from a point to another point. Constraint in Equation (28) ensures that patients and infectious patients cannot be transported together. Finally, Equation (29) states the total distance travelled by the vehicle has to be minimized.

6 Computational results

To evaluate the performance and scalability of the proposed MILP model, a series of computational experiments were conducted using IBM ILOG CPLEX Optimization Studio (version 22.1.0). The tests were performed on a personal computer equipped with an Intel Core i7-7700HQ CPU, 8 GB of RAM, and a 1 TB SSD. Each test run was subject to a maximum time limit of 3,600 seconds. Except for enabling the strong branching strategy for variable selection, all the other solver parameters were kept at their default settings.

The test instances were generated based on a real-world urban environment in the city of Sopron, Hungary. All the travel distances and travel times between pickups, hospital, and depot locations were determined using Google Maps data under typical traffic conditions. The desired arrival times of patients from each pickup point to the hospital were generated using random number functions in Microsoft Excel to reflect realistic time window constraints. This dataset served as a basis for all computational experiments conducted in this study.

The experimental design included five test groups, categorized by the number of pickup points: 10, 15, 20, 25, and 30. For each group, four infection-related scenarios were examined, varying the proportion of infectious patients across all pickup locations. These scenarios ranged from 0% (no infectious patients) to one-third, two-thirds, and 100% of patients being infectious.

For each scenario, the objective was to minimize the total distance traveled, while satisfying all the constraints related to time windows, vehicle capacity, infection-based compatibility, and mandatory disinfection procedures. The results are summarized in Table 1.

Out of the 20 generated test instances, the MILP model was able to find the optimal solution in all the cases involving 10, 15, and 20 pickup points, typically within just a few seconds of computation time. For the 25-pickup-point cases, the optimal solution was obtained for all four infection scenarios; however, the required runtime was much higher than for the 10–20-point instances, which were solved within seconds. In terms of computation time, for problems with 25 pickup points, the mixed scenarios were easier for CPLEX to solve than the homogeneous ones. The optimal solution was found in 620.2 seconds when one-third of the patients were infectious, and in 392 seconds when two-thirds of the patients were infectious. By contrast, the homogeneous scenarios took considerably longer: 963.04 seconds with no infectious patients and 1001.84 seconds when all patients were infectious.

As expected, the presence of infectious patients resulted in longer total route distances due to additional constraints and the requirement to return to the depot for disinfection. For the 10-pickup point case, the scenario in which all patients were infectious (100%) yielded shorter optimal route lengths than those with mixed groups (e.g., 33% or 66% infectious). For the 25-pickup point case, the scenario in which all patients were infectious also produced shorter optimal route lengths than the mixed case with two-thirds infectious patients. Furthermore, in the 25-pickup point case, this homogeneous scenario converged faster. This is not surprising: when all the patients are infectious, the vehicle must always return to the depot after visiting the hospital, but it can freely travel between any pickup points without compatibility restrictions. In contrast, with mixed groups, transitions are restricted, infectious pickup points can only be followed by another infectious pickup, and similarly for non-infectious points, which significantly reduces the number of feasible routing options, often resulting in longer total distances despite fewer depot returns.

For the largest test group with 30 pickup points, different outcomes were observed depending on the infection composition. In the case without infectious patients, the program was unable to prove optimality within the 3,600-second time limit, but it returned a feasible solution with an objective value of 111.09. At termination, the best lower bound was 93.60, indicating that the reported solution may still be improved. This highlights the substantial computational challenges associated with large-scale instances, even in the absence of infection-related constraints.

By contrast, when infectious patients were included, the problem became unfeasible due to the combined effect of vehicle capacity restrictions, mandatory disinfection times, and tight arrival time windows. In these cases, CPLEX was unable to prove infeasibility within the 3,600-second time limit.

Table 1 summarizes the computational results across all generated test instances. Time values are reported in seconds. Entries marked with „–” denote cases where no feasible solution was found, while „>3600” indicates that the one-hour time limit was exceeded without proving optimality.

***Table 1** Experimental results*

Initial data		Results	
Pick up points	Infectious Points	Time to find Optimum [s]	Total distance of delivery tasks [km]
10	0	1.45	51.9
10	3	1.51	70.3
10	6	1.47	71.1
10	10	1.57	68.9
15	0	1.76	74.4
15	5	1.56	83.2
15	10	1.50	92.2
15	15	1.67	96.1
20	0	3.16	93.3
20	7	4.34	96.2
20	14	8.11	102.1
20	20	6.37	109.1
25	0	963.04	104.6
25	8	620.20	118.35
25	16	392	135.6
25	25	1001.84	125.6
30	0	>3600	111.09 (not proven opt.)
30	10	(n/f)	-
30	20	(n/f)	-
30	30	(n/f)	-

7 Conclusion

In this paper a mathematical optimization model for patient transportation that explicitly incorporates infection control constraints is presented. Building on the classical Dial-a-Ride Problem (DARP) framework, an existing MILP formulation is extended by introducing two critical real-world features: (1) compatibility constraints that prohibit the joint transport of infectious and noninfectious patients, and (2) mandatory vehicle disinfection following the transport of infectious individuals.

The model accommodates a wide range of operational constraints, including passenger-specific pickup and drop-off time windows, maximum allowable ride durations, and vehicle capacity limits differentiated by passenger type (e.g., standard vs. mobility-impaired). To solve the problem, a modified MTZ-based formulation was employed and used IBM ILOG CPLEX to evaluate the model's performance on across multiple scenarios involving varying numbers of pickup locations and different proportions of infectious patients.

The obtained computational results demonstrate that incorporating infection control constraints significantly increases the complexity of route planning, particularly in mixed-infection scenarios. At 25 pickup points, homogeneous scenarios, where either all or none of the patients are infectious, converged slower than mixed scenarios, while for the smaller instances (10, 15, and 20 points) every case was solved within seconds, and for 30 points no feasible solution was returned within the time limit. This suggests that compatibility constraints, while restrictive, can sometimes reduce the solution space in a way that accelerates optimization. Furthermore, the experimental results highlight the limitations of a single-vehicle model when scaling beyond 25 pickup points, thereby motivating the need for more scalable, multivehicle approaches.

The proposed model contributes not only to the theoretical advancement of compatibility-aware DARP formulations but provides practical insights for designing safe, efficient, and regulation-compliant patient transportation systems in urban healthcare settings, as well.

Future work should focus on extending the model to a multivehicle setting, incorporating cost-based objectives, including fuel consumption, labor costs, and addressing return-trip scenarios for patients.

Acknowledgment

The authors received no financial support for the research, authorship and/or publication of this article.

Conflicts of interest

The authors declare that they have no known competing financial interests or personal relationships that could have appeared to influence the work reported in this paper.

References

[1] DAGANZO, C. F., OUYANG, Y. A general model of demand-responsive transportation services: from taxi to ridesharing to dial-a-ride. *Transportation Research Part B: Methodological* [online]. 2019, **126**, p. 213-224. ISSN 0191-2615, eISSN 1879-2367. Available from: https://doi.org/10.1016/j.trb.2019.06.001

[2] TOTH, M., HAJBA, T., HORVATH, A. MILP models of a patient transportation problem. *Central European Journal of Operations Research* [online]. 2024, **32**(4), p. 903-922. ISSN 1435-246X, eISSN 1613-9178. Available from: https://doi.org/10.1007/s10100-023-00902-z

[3] TOTH, M., HAJBA, T., HORVATH, A. Solving a dynamic route planning problem in the area of patient transport with mixed integer linear programming. In: 9th VOCAL Optimization Conference: Advanced Algorithms: proceedings. 2022. ISBN 978-615-01-5987-4, p. 60-67.

[4] CORDEAU, J.-F., LAPORTE, G. The dial-a-ride problem: models and algorithms. *Annals of Operations Research* [online]. 2007, **153**, p. 29-46. ISSN 0254-5330, eISSN 1572-9338. Available from: https://doi.org/10.1007/s10479-007-0170-8

[5] BONGIOVANNI, C., KASPI, M., GEROLIMINIS, N. The electric autonomous dial-a-ride problem. *Transportation Research Part B: Methodological* [online]. 2019, **122**, p. 436-456. ISSN 0191-2615, eISSN 1879-2367. Available from: https://doi.org/10.1016/j.trb.2019.03.004

[6] AGRA, A., CHRISTIANSEN, M., WOLSEY, L. Improved models for a single vehicle continuous-time inventory routing problem with pickups and deliveries. *European Journal of Operational Research* [online]. 2022, **297**(1), p. 164-179. ISSN 0377-2217, eISSN 1872-6860. Available from: https://doi.org/10.1016/j.ejor.2021.04.027

[7] LIM, A., ZHANG, Z., QIN, H. Pickup and delivery service with manpower planning in Hong Kong public hospitals. *Transportation Science* [online]. 2017, **51**(2), p. 688-705. ISSN 0041-1655, eISSN 1526-5447. Available from: https://doi.org/10.1287/trsc.2015.0611

[8] LUO, Z., LIU, M., LIM, A. A two-phase branch-and-price-and-cut for a dial-a-ride problem in patient transportation. *Transportation Science* [online]. 2019, **53**(1), p. 113-130. ISSN 0041-1655, eISSN 1526-5447. Available from: https://doi.org/10.1287/trsc.2017.0772

[9] ARMBRUST, P., HUNGERLANDER, P., MAIER, K., PACHATZ, V. Case study of dial-a-ride problems arising in Austrian rural regions. *Transportation Research Procedia* [online]. 2022, **62**, p. 197-204. Available from: https://doi.org/10.1016/j.trpro.2022.02.025

[10] MOLENBRUCH, Y., BRAEKERS, K., CARIS, A., VANDEN BERGHE. G. Multi-directional local search for a bi-objective dial-a-ride problem in patient transportation. *Computers and Operations Research* [online]. 2017, **77**, p. 58-71. ISSN 0305-0548, eISSN 1873-765X. Available from: https://doi.org/10.1016/j.cor.2016.07.020

[11] SCHULZ, A., PFEIFFER, CH. A branch-and-cut algorithm for the dial-a-ride problem with incompatible customer types. *Transportation Research Part E: Logistics and Transportation Review* [online]. 2024, **181**, 103394. ISSN 1366-5545, eISSN 1878-5794. Available from: https://doi.org/10.1016/j.tre.2023.103394

[12] LOKHANDWALA, M., CAI, H. Understanding the impact of heterogeneous rider preferences on a shared autonomous vehicle system. *Transportation Research Part F: Traffic Psychology and Behaviour* [online]. 2020, **75**, p. 120-133. ISSN 1369-8478, eISSN 1873-5517. Available from: https://doi.org/10.1016/j.trf.2020.09.017

[13] COLOMBI, M., CORBERAN, A., MANSINI, R., PLANA, I., SANCHIS, J. M. The directed profitable rural postman problem with incompatibility constraints. *European Journal of Operational Research* [online]. 2017, **261**(2), p. 549-562. ISSN 0377-2217, eISSN 1872-6860. Available from: https://doi.org/10.1016/j.ejor.2017.02.002

[14] BERNARDINO, R., PAIAS, A. The family traveling salesman problem with incompatibility constraints. *Networks* [online]. 2022, **79**(1), p. 47-82. ISSN 0028-3045, eISSN 1097-0037. Available from: https://doi.org/10.1002%2Fnet.22036

[15] MANERBA, D., MANSINI, R. A branch-and-cut algorithm for the multi-vehicle traveling purchaser problem with pairwise incompatibility constraints. *Networks* [online]. 2015, **65**(2), p. 139-154. ISSN 0028-3045, eISSN 1097-0037. Available from: https://doi.org/10.1002/net.21588

[16] GENDREAU, M., MANERBA, D., MANSINI, R. The multi-vehicle traveling purchaser problem with pairwise incompatibility constraints and unitary demands: a branch-and-price approach. *European Journal of Operational Research* [online]. 2016, **248**(1), p. 59-71. ISSN 0377-2217, eISSN 1872-6860. Available from: https://doi.org/10.1016/j.ejor.2015.06.073

[17] FACTOROVICH, P., MENDEZ-DIAZ, I., ZABALA, P. Pickup and delivery problem with incompatibility constraints. *Computers and Operations Research* [online]. 2020, **113**, 104805. ISSN 0305-0548, eISSN 1873-765X. Available from: https://doi.org/10.1016/j.cor.2019.104805

[18] MILLER, C. E., TUCKER, A. W., ZEMLIN, R. A. Integer programming formulation of traveling salesman problems. *Journal of the ACM (JACM)* [online]. 1960, **7**(4), p. 326-329. ISSN 0004-5411, eISSN 1557-735X. Available from: https://doi.org/10.1145/321043.321046

COMPARISON OF BRAKING DYNAMICS AT HIGH SPEEDS OF FIREFIGHTING VEHICLES ON TATRA CHASSIS WITH DIFFERENT BRAKING SYSTEMS

Ladislav Jánošík[1,*], Ivana Jánošíková[2], Tomáš Konečný[1], Izabela Šudrychová[1]

[1]Faculty of Safety Engineering, VSB - Technical University of Ostrava, Ostrava-Vyskovice, Czech Republic
[2]Faculty of Economics, VSB - Technical University of Ostrava, Ostrava-Poruba, Czech Republic

*E-mail of corresponding author: ladislav.janosik@vsb.cz

Ladislav Janosik 0000-0002-5207-7718, Ivana Janosikova 0000-0002-5665-8210,
Izabela Sudrychova 0000-0003-0520-4152

Resume

In this paper are summarized the results of measurements of the driving characteristics of fire-fighting vehicles during the braking from high speeds. Two water tender vehicles manufactured by TATRA, used by the Fire Rescue Service of the Czech Republic, were compared. The tested vehicles differ in their braking systems. In the study are monitored the braking distance and deceleration, which were compared with previous tests focusing on tire type, test track surface, and weather conditions. When braking from a speed of 80 km/h, the worst results of the braking distance were recorded for SCANIA of 64 m and TATRA TerrNo1 (9T5 2243), of 73 m. These vehicles were equipped with drum brakes. In the case of the SCANIA vehicle, the cause was the heating of the drum brakes. For the TATRA TerrNo1, the reduced braking efficiency was likely due to the brake wear and thermal effects on the drum brakes.

Article info

Received 6 August 2025
Accepted 4 November 2025
Online16 December 2025

Keywords:

firefighting vehicle
braking distance
longitudinal acceleration

Available online: https://doi.org/10.26552/com.C.2026.005

ISSN 1335-4205 (print version)
ISSN 2585-7878 (online version)

1 Introduction

This paper builds upon previous research conducted by the authors [1-2], which presented results of braking distance measurements of firefighting vehicles at higher speeds. The experiments were performed for initial velocities of v_0 = 70, 80, and 90 km/h.

The first series of measurements was carried out on a dry concrete surface at the non-public Prerov-Bochor airfield [1]. The tested vehicles included two fire trucks with TATRA chassis - one equipped with drum brakes and the other with disc brakes, and one SCANIA 4x4 vehicle with drum brakes. The second series of tests was conducted on a wet asphalt road (following overnight rainfall) in the municipality of Hlucin [2]. This phase involved a TATRA vehicle with disc brakes and a SCANIA 4x2 vehicle with drum brakes.

The long-term focus on the fundamental dynamic driving characteristics of firefighting vehicles, specifically braking distances and longitudinal acceleration at higher initial speeds v_0 = 70, 80, and 90 km/h, is motivated by accident statistics, previously analysed by the authors [3] and subsequently updated [4]. Between 2011 and 2022, excessive speed was identified as the primary cause in only 68 at-fault traffic accidents (15%) involving firefighting vehicles responding to emergency calls. However, those incidents accounted for as much as 79% of the total material damage to firefighting vehicles during the analysed period, amounting to EUR 3,290,200.

2 Tested firefighting vehicles

The measurements were conducted on two TATRA firefighting vehicles with different braking systems and of different ages. These vehicles are designed for operation on paved roads with rear-wheel drive, with the option to engage front-wheel drive for off-road use on unpaved surfaces. This corresponds to the chassis design, which features a central load-bearing tube and swinging half-axles. An overview of the basic characteristics of the tested vehicles is provided in Table 1.

***Table 1** Overview of the basic characteristics of the tested vehicles*

Firefighting vehicle	TATRA TerrNo1 (9T5 2243)	TATRA Terra (1TH 0621)
Fire marking	CAS 20/4000/240-S2T	CAS 20/4000/240-S2T
Registration number	9T5 2243	1TH 0621
Location	HS Novy Jicin	HS Koprivnice
Extinguishing agent volume - Water (l)	4000	4000
- Foaming agent (l)	240	240
Crew during testing	1+3	1+5
Dimensions (L/W/H) (mm)	8070/2550/3150	8355/2550/3245
Operating weight (kg)	12600	13300
Maximum weight (kg)	18000	20000
Engine power (kW)	325	325
Tires - Front axle	Michelin XZY 3	Michelin XZY 3
- Rear axle	Michelin X Multi HD	Michelin X Multi HD
Date of manufacture of tires	Week 5, 2020	Week 35, 2022
Transmission	Semi-automatic Norgren	Automatic Allison
Brake system	Drum brakes	Disc brakes
Assistance systems	ABS	ABS
Date of purchase	28/05/2015	15/12/2020

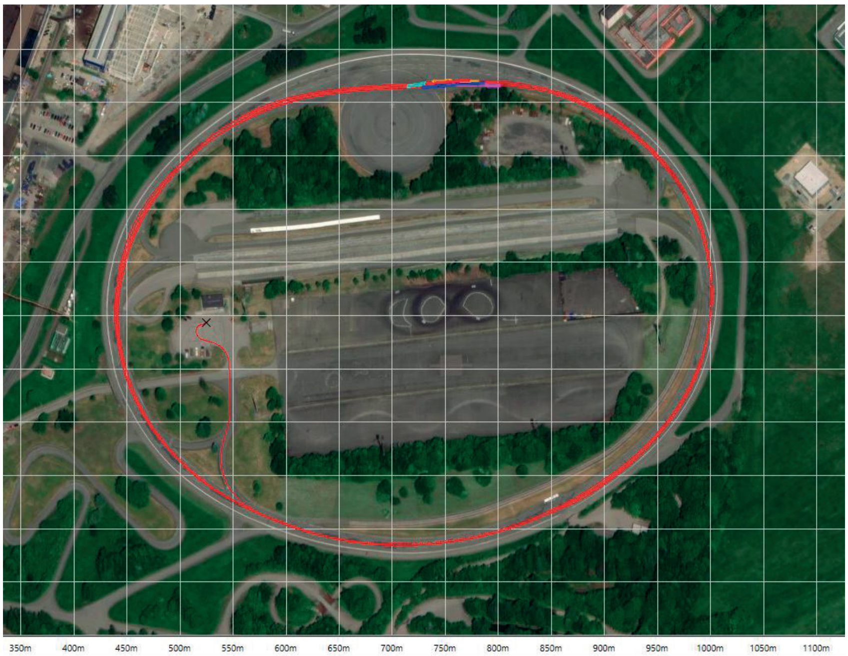

***Figure 1** Recording of the position of the TATRA TerrNo1 firefighting vehicle during testing from an initial speed of 70 km/h*

The first tested firefighting vehicle is the TATRA 815-231R55 4x4.2, commercially designated as TerrNo1 (hereinafter referred to as TATRA TerrNo1), registration number 9T5 2243. A detailed description is available on the website [5].

The second tested firefighting vehicle is the TATRA 815-2T5RA3 4x4.1, commercially designated as Terra (hereinafter referred to as TATRA Terra), registration number 1TH 0621. A detailed description is available on the website [6].

3 Measuring equipment

Two Performance Box devices, manufactured by Racelogic Ltd, Buckingham, United Kingdom, were used to measure the driving characteristics. A detailed specification of the devices is available on the manufacturer's website [7]. The measuring devices were mounted inside the cabin on the windshield along the longitudinal axis of the vehicle. The device determines the absolute position of the vehicle in real time using signals from the GPS and GLONASS systems. Based on position and time, it calculates the travelled distance, instantaneous speed, acceleration, and a range of other parameters. The recording frequency is 10 Hz. The device has been equipped with an SD card on which the recorded data were stored. These data were subsequently transferred to a computer and processed using the VBOX Test Suite software (hereinafter referred to as VTS), version 2.1.6.5877 [8].

The theoretical basis for evaluating the measured data was described in detail in previous studies by the authors [9]. It is based on general principles of physics [10] and relevant technical literature [11-12].

4 Test location

The experimental measurements were conducted at the TATRA TRUCKS company test track in Koprivnice on November 2, 2024. The testing began at 9:00 a.m., with an ambient temperature of 9 °C. The weather was overcast, and light drizzle occurred intermittently during the testing. The asphalt surface of the track remained wet throughout the entire measurement period. An example of the recorded driving path of the TATRA TerrNo1 vehicle (red trace) and its braking phases (multi-coloured traces) overlaid on a map background during evaluation in the VTS software is shown in Figure 1.

5 Measurement procedure

Braking and acceleration tests were conducted with fully loaded firefighting vehicles, including filled extinguishing agent tanks and complete operational equipment. It was determined that for each initial speed of 70, 80, and 90 km/h, seven experimental runs would be performed to eliminate the possibility of invalid trials, such as failure to reach the prescribed initial speed. The objective was to obtain at least five valid runs for further evaluation. Each test run began with departure from the parking area, followed by acceleration on the test track loop to the required initial speed for braking. The driver maintained this speed until reaching the designated braking zone, where the intensive braking was initiated using the service brake until the vehicle came to a complete stop. After stopping, the driver continued to apply pressure to the brake pedal for approximately three seconds to secure the vehicle in place following the rebound of the suspended cabin. No auxiliary braking systems were used during the measurements.

6 Evaluation of measured data

The primary evaluation of the measured data was carried out using the VTS software. Boundary conditions for each tested task were gradually configured within the software. The resulting evaluated values were exported in “csv“ format and subsequently processed further in the MS Excel environment. The evaluated data from the braking distance measurements of both tested vehicles are summarized in the graphs shown in Figures 2 to 4, according to the initial speed.

For evaluation of the longitudinal deceleration during braking, a correction based on Regulation ECE No. 13 [13] was applied. According to this regulation, longitudinal acceleration is evaluated within the interval from 80% to 10% of the initial braking speed. This approach eliminates nonlinearities at the beginning of the braking process, related to brake system engagement, and at the end, where vehicle oscillation may occur during complete stop. Due to the scope of the evaluated data, only the calculated average values are presented in Figure 5. Since the VTS software uses gravitational acceleration (g = 9.81 m/s^2) as the unit for acceleration, the reported values can be interpreted as the coefficient of adhesion.

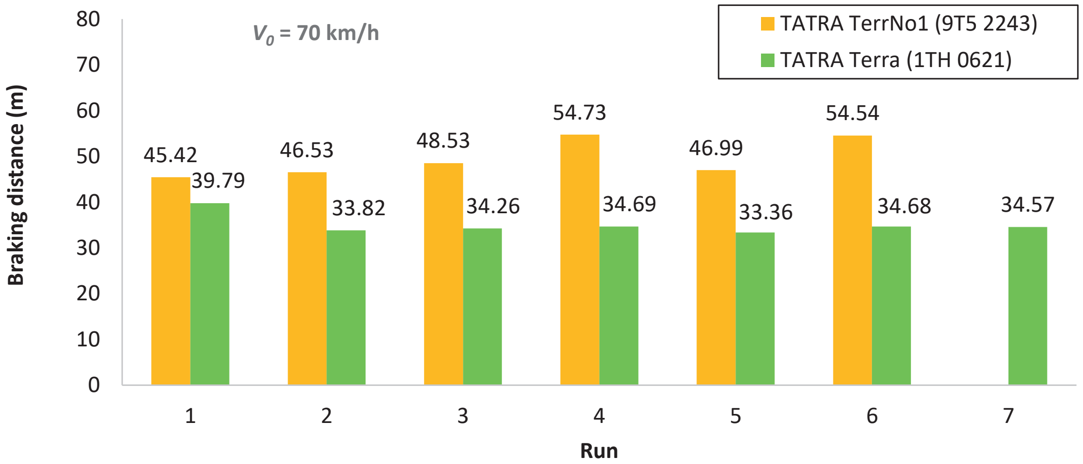

***Figure 2** Braking distances of tested vehicles for initial speed v_0 = 70 km/h*

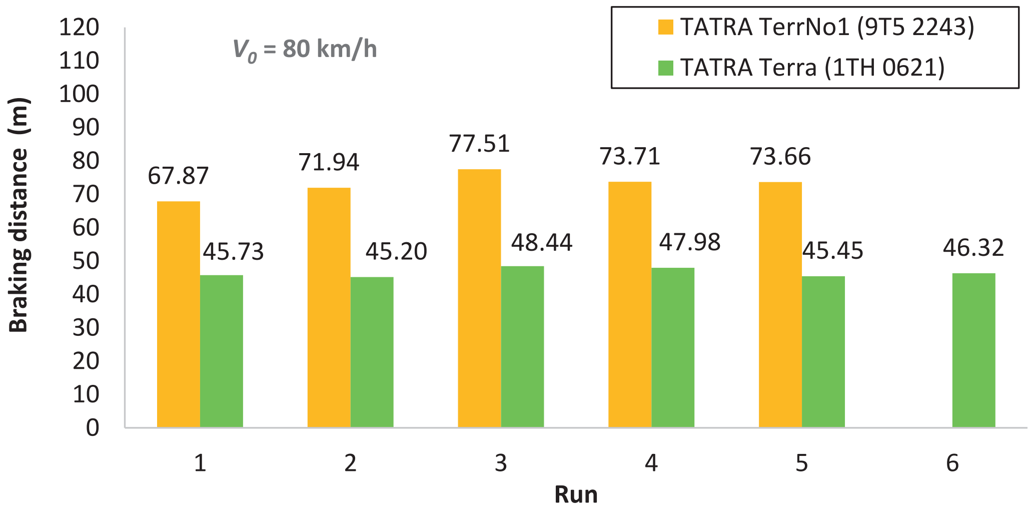

Figure 3 *Braking distances of tested vehicles for initial speed* v_0 *= 80 km/h*

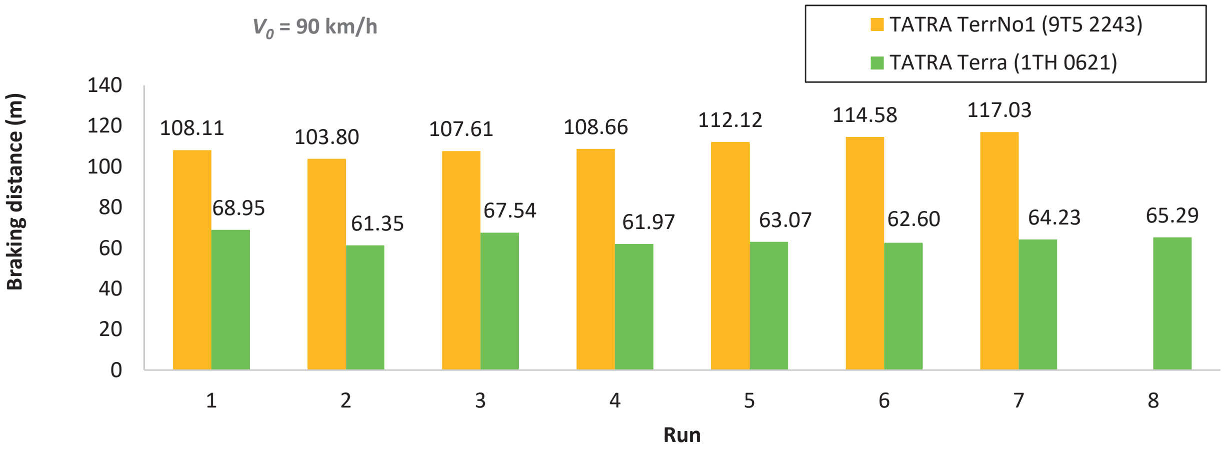

Figure 4 *Braking distances of tested vehicles for initial speed* v_0 *= 90 km/h*

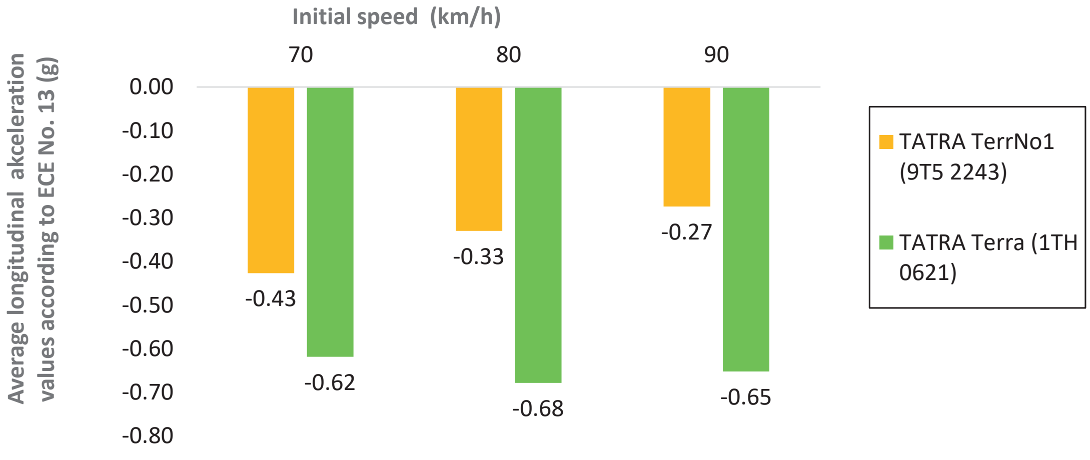

Figure 5 *Average longitudinal acceleration values according to ECE No. 13 during braking*

***Table 2** Wheel disc temperatures during testing*

Firefighting vehicle	TATRA TerrNo1 (9T5 2243)	TATRA Terra (1TH 0621)
Wheel disc temperature at the end of braking from v_0 = 80 km/h (°C)		
- left front wheel	250	310
- left rear wheel	190	140
Wheel disc temperature at the end of braking from v_0 = 90 km/h (°C)		
- left front wheel	295	321
- left rear wheel	240	180

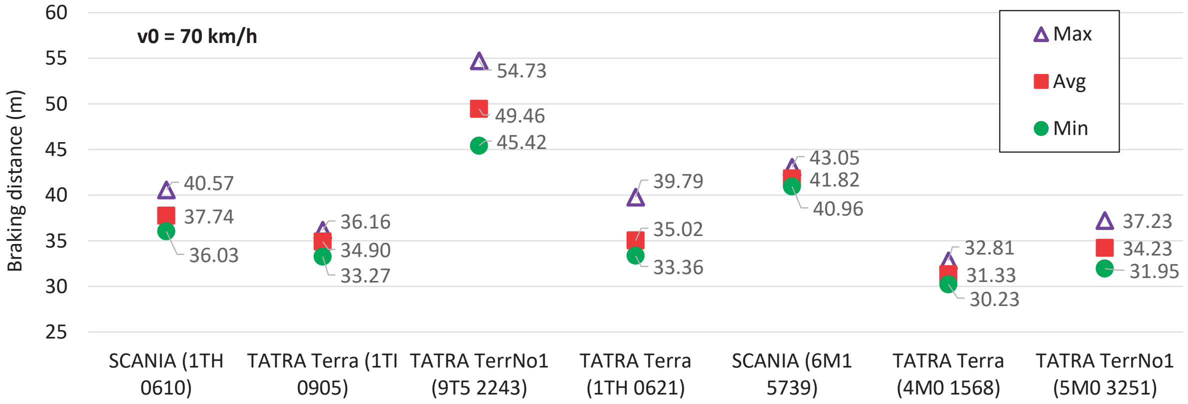

***Figure 6** Braking distance (m) for an initial speed of v_0 = 70 km/h*

The TATRA TerrNo1 vehicle (9T5 2243) equipped with drum brakes exhibited the poorest performance across all the tests. At the defined higher initial speeds, repeated test cycles led to gradual overheating of the drum brakes. This phenomenon had a noticeable impact on the braking distance results. A progressive increase in braking distance was recorded for this vehicle, with differences reaching nearly 10 meters even at speeds of 70 km/h. It was necessary to interrupt the testing several times and allow the brakes to cool down by driving around the test track with occasional light braking.

After completing the braking distance test cycles, from initial speeds of 80 and 90 km/h, an indicative temperature measurement of wheel discs was performed using a Dräger UCF 7000 thermal imaging camera. The measurement was conducted only on the left side of the vehicle, on both the front, and rear wheels. The recorded temperatures are presented in Table 2. The comparison showed that the disc brakes reached higher temperatures, yet their braking performance did not deteriorate.

7 Comparison to previous similar tests

One of the objectives of this paper was to summarize and compare the obtained results with previous tests [1-2]. The graphical representations in Figures 6 to 8 summarize the braking distance measurements' results of the tested vehicles from all three experimental campaigns. The graphs are categorized according to the initial braking speed. The average (Avg), maximum (Max), and minimum (Min) values of the measured braking distances are presented.

The first four tested vehicles shown on the graphs from the left were provided by the Fire Rescue Service of the Moravian-Silesian Region. Their license plates contain the letter "T". The remaining three vehicles were provided by the Fire Rescue Service of the Olomouc Region, with license plates containing the letter "M".

All four vehicles from the Moravian-Silesian Region were tested on a wet asphalt road surface. The three vehicles from the Olomouc Region were tested on a dry concrete surface at an airfield. During the testing of all vehicles, the ambient temperature ranged between 6 and 11 °C.

As the initial speed increased, the differences in braking distances between the worst-performing vehicles - TATRA TerrNo1 (9T5 2243) and SCANIA (6M1 5739) - and the other vehicles became more pronounced. It cannot be conclusively stated that this was solely due to their drum brakes, as three other vehicles in the group also had the drum brakes but performed better in braking.

Figure 9 summarizes the average braking distances depending on the initial speed of the tested vehicles, including the type of front axle tires. The data presented in Figure 9 suggest that the influence of the tires on the TATRA TerrNo1 (9T5 2243) vehicle can likely be excluded. The same tires on the TATRA Terra (1TH 0621) vehicle with disc brakes showed better braking performance on the same road surface.

Figure 10 presents the average values of longitudinal acceleration depending on the initial speed of the tested vehicles, also including the type of front axle tires. These values were obtained using the VTS software after applying the correction according to Regulation [13]. The best results were achieved by all three TATRA Terra vehicles with disc brakes and the SCANIA (1TH 0610) vehicle with drum brakes and a 4x2 road chassis.

8 Conclusion

The objective of the testing was to conduct and evaluate measurements of the basic driving dynamics of firefighting vehicles during braking from high speeds, and to compare the findings with previous tests. The resulting braking distance of a vehicle is influenced by a number of factors. The primary ones include climatic conditions, road surface condition and its type, tires, and the braking system.

All vehicles were tested under similar ambient temperatures. Therefore, the influence of this factor cannot be assessed in the context of this testing.

The conditions and type of road surface had an

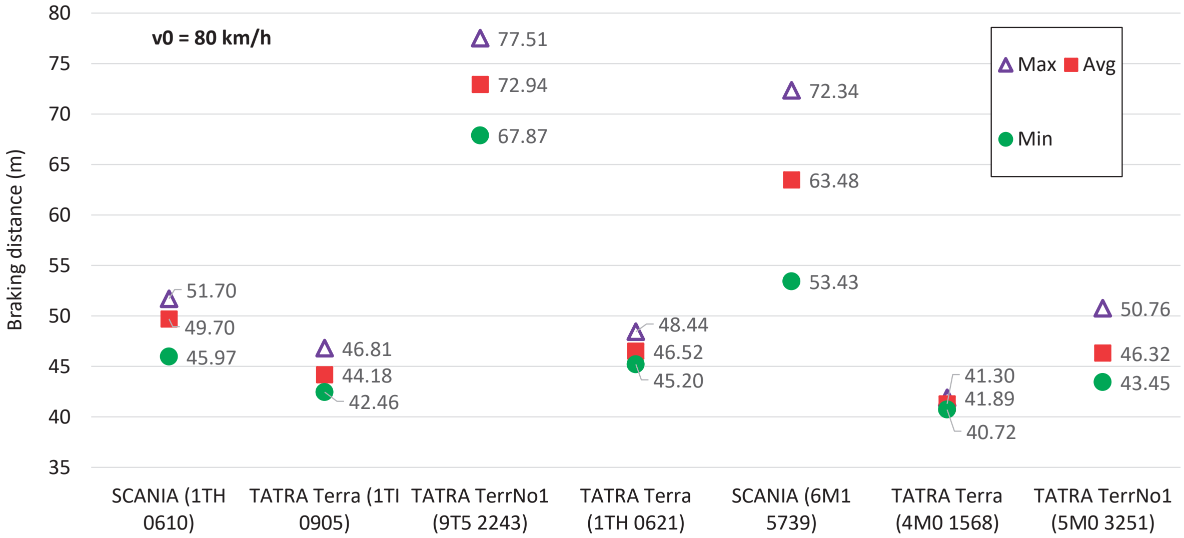

Figure 7 Braking distance (m) for an initial speed of v_0 = 80 km/h

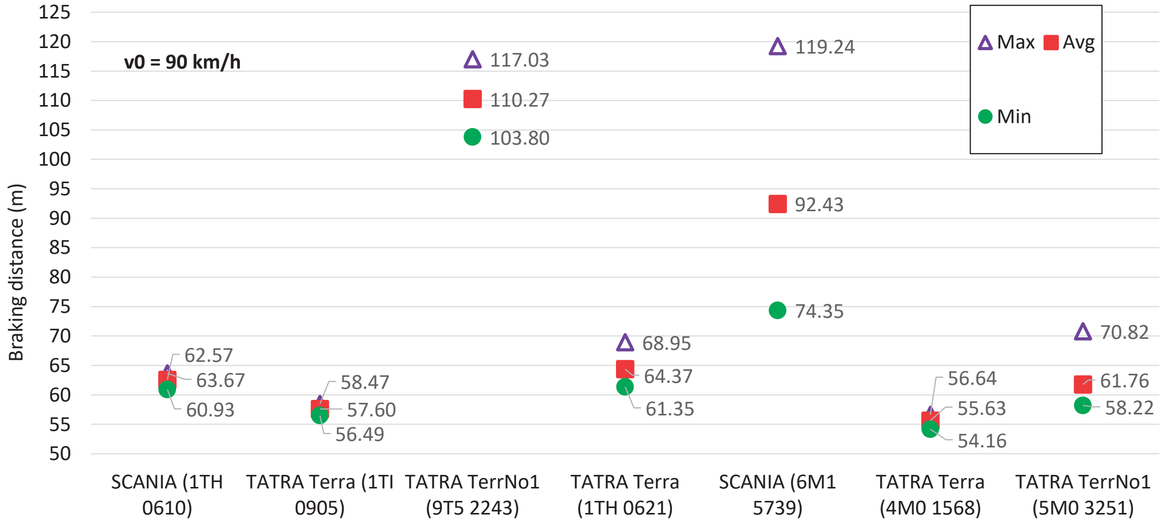

Figure 8 Braking distance (m) for an initial speed of v_0 = 90 km/h

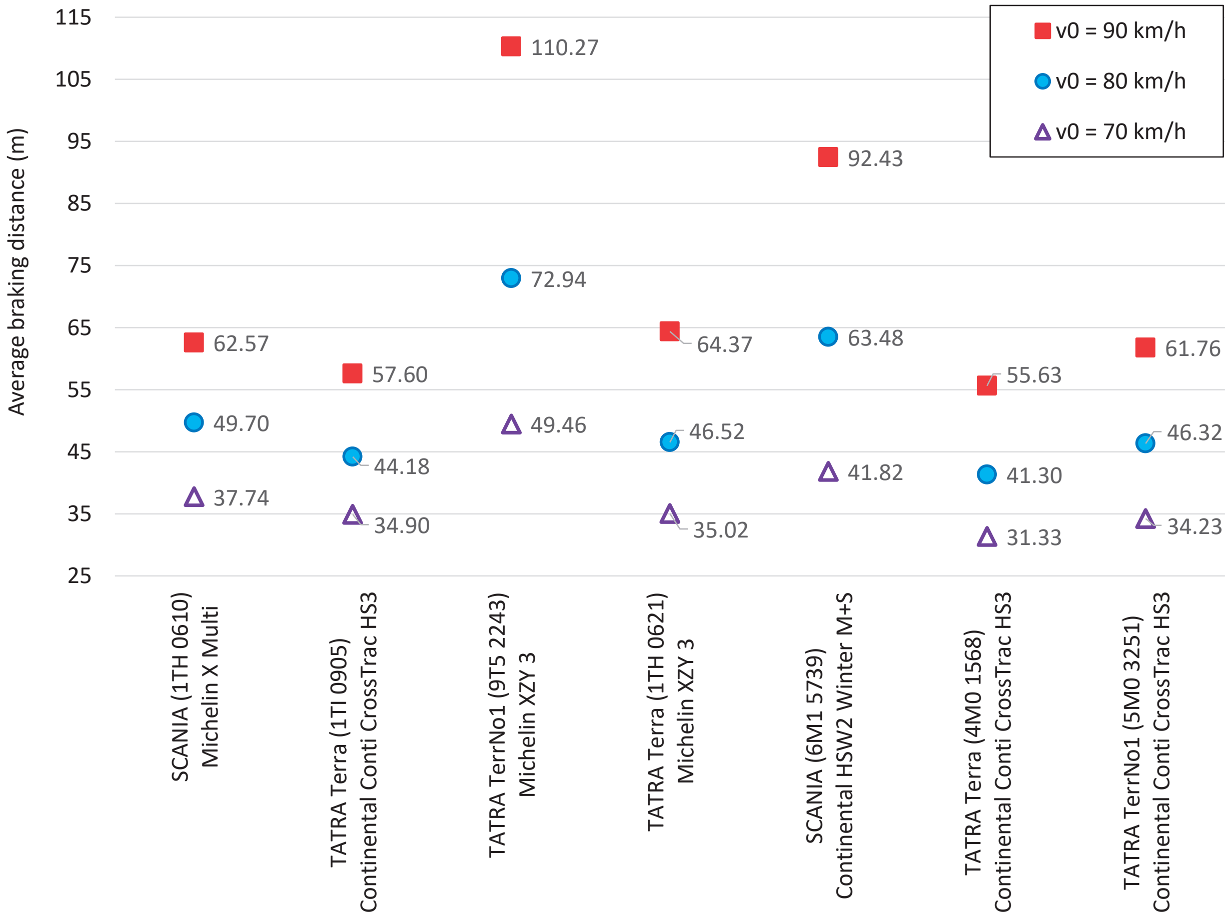

***Figure 9** Effect of tire type on average braking distance (m)*

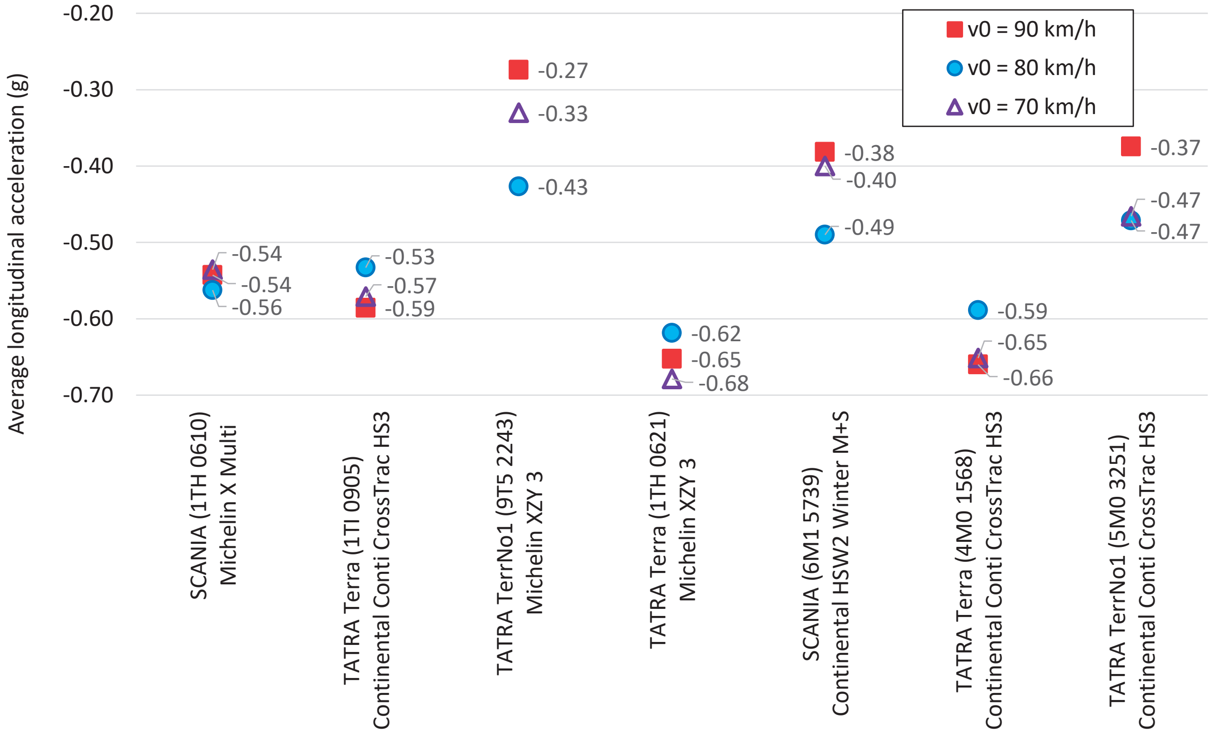

***Figure 10** Effect of tire type on average longitudinal acceleration during braking according to ECE No. 13 (g)*

impact only on both TATRA TerrNo1 vehicles. During testing on a wet asphalt surface, worse braking distances were recorded compared to a dry surface. At an initial speed of 70 km/h, the difference in average braking distance was 15 m; at 80 km/h, it increased to 27 meters; and at 90 km/h, it reached up to 48 m. These significant differences suggest a possible technical issue with the 10-year-old TATRA TerrNo1 (9T5 2243) vehicle equipped with drum brakes. The other vehicles performed comparably well regardless of the road surface. An exception was the SCANIA vehicle (6M1 5739), where the effect of drum brakes overheating became apparent due to frequent braking without regular cooling runs between braking cycles.

The TATRA vehicles were fitted with Continental Conti CrossTrac and Michelin XZY 3 tires. The SCANIA (6M1 5739) vehicle was equipped with Continental HSW2 Winter M+S tires. The influence of this factor cannot be reliably assessed here. TATRA vehicles with Continental Conti CrossTrac tires performed comparably well in braking. The TATRA vehicles with Michelin XZY 3 tires showed significantly different braking performance (see Figure 9). If, however, the cause of the discrepancy lies in the technical condition of the 10-year-old TATRA TerrNo1 (9T5 2243) vehicle, then the Michelin XYZ 3 tires demonstrated the best performance. We would therefore recommend equipping first-response fire vehicles with these tires.

Based on the above results, the best braking performance was achieved by the TATRA Terra vehicles with disc brakes. The worst braking performance was recorded for the TATRA TerrNo1 (9T5 2243) vehicle with drum brakes.

Given the increasing number of fire trucks being purchased on SCANIA chassis in the Czech Republic, authors recommend that the driver training for these vehicles include a focus on the issue of drum brake overheating at higher speeds during the frequent intensive braking. This phenomenon was particularly evident during the braking from an initial speed of 80 km/h. After the fifth braking cycle, it was necessary to cool the brakes by driving along the test track without braking [1].

The type of brake material used has a significant impact on the braking distance. During the testing the specific brake materials used on the tested vehicles were unknown. The issue of brake materials was addressed in a paper [14], which briefly presented the results of the project “Safe Response Driving of Firefighting Vehicles to Emergency Sites” (project number VH20182021035). Laboratory measurements of the friction coefficients of brake materials showed that the original brake material used in the SCANIA 4x4 vehicle performed the worst.

Acknowledgements

This paper was created within the research on the projects of specific research ”Verification of driving characteristics of firefighting water tenders“ (project registration number SP2021/58), but primarily with the support of the management of the Fire Rescue Service of the Moravian-Silesian Region. The author team of this paper would like to express their gratitude to all collaborators, firefighters, and their commanders, especially from the fire stations in Novy Jicin and Koprivnice.

Conflicts of interest

The authors declare that they have no known competing financial interests or personal relationships that could have appeared to influence the work reported in this paper.

References

[1] JANOSIK, L., SUDRYCHOVA, I., JANOSIKOVA, I., JERABKOVA, M. Comparison of driving dynamics of selected firefighting vehicles on TATRA and SCANIA chassis at high speeds (in Slovak). *Krizovy Manazment / Crisis Management* [online]. 2024, **23**(2), p. 5-14. ISSN 1336-0019, eISSN 2730-0544. Available from: https://doi.org/10.26552/krm.C.2024.2.5-14

[2] JANOSIK, L., SUDRYCHOVA, I., JANOSIKOVA, I., GOLD, P. Firefighting vehicles’ driving dynamics under extreme load. *Journal of Loss Prevention in the Process Industries* [online]. 2025, **2025**(94), 105559. ISSN 0950-4230, eISSN 1873-3352. Available from: https://doi.org/10.1016/j.jlp.2025.105559

[3] JANOSIK, L., JANOSIKOVA, I., COCHLAR, M., POLEDNAK, P., SUDRYCHOVA, I. Economic consequences of firefighting trucks risky emergency driving. In: 5th International Conference on European Integration 2020: proceedings [online]. 2020. ISBN 978-80-248-4455-8, eISBN 978-80-248-4456-5, ISSN 2571-029X, p. 330-337. Available from: https://doi.org/10.31490/9788024844565

[4] JANOSIK, L., SUDRYCHOVA, I., JANOSIKOVA, I., COCHLAR, M., TOMASEK, M. Trends in traffic accidents of firefighting vehicles and their evaluation. *Communications - Scientific Letters of the University of Zilina* [online]. 2023, **25**(4). p. F96-F107. ISSN 1335-4205, eISSN 2585-7878. Available from: https://doi.org/10.26552/com.C.2023.075

[5] Fires - Technology 2013 / Pozary - Technika 2013 (in Czech) [online] [accessed 2024-08-19]. Available from: https://www.pozary.cz/clanek/68035-cisterny-cas-20-tatra-815-terrno-dodal-nastavbar-wawrzaszek-iss-spolufinancovala-je-evropska-unie/

[6] Fires - Technology 2023 / Pozary - Technika 2023 (in Czech) [online] [accessed 2024-08-19]. Available from: https://www.pozary.cz/clanek/264131-tht-policka-zacala-s-dodavkou-cisteren-tatra-terra-pro-profesionalni-hasice-ramcova-smlouva-muze-presahnout-jednu-miliardu-korun/

[7] Performance Box - VBOX Motorsport [online] [accessed 2024-01-06]. Available form: https://vboxmotorsport.co.uk/index.php/en/performancebox

[8] Software VBOX Test Suite - Racelogic Support Centre [online] [accessed 2024-01-06]. Available from: https://en.racelogic.support/01VBOX_Automotive/03Software_applications/VBOX_Test_Suite

[9] JANOSIK, L., JANOSIKOVA, I., POLEDNAK, P., SUDRYCHOVA, I., TOMASEK, M., VLCEK, J., KUCZAJ, J. Measuring of braking distances of firefighting trucks. *Communications - Scientific Letters of the University of Zilina* [online]. 2022, **24**(2). p. F1-F13. ISSN 1335-4205, eISSN 2585-7878. Available from: 10.26552/com.C.2022.2.F1-F13

[10] HALLIDAY, D., RESNICK, R., WALKER, J. *Fundamentals of physics*. 5. ed. Hoboken: John Wiley and Sons, 1997. ISBN 1119773512.

[11] VLK, F. *Dynamics of motor vehicles* (in Czech). 2. ed. Brno: Vlk Publishing, 2003. ISBN 80-239-0024-2.

[12] BRADAC, A., KREJCIR, P., LUKASIK, L., OSLEJSEK, J., PLCH, J., KLEDUS, M., VEMOLA, A. *Forensic engineering* (in Czech). Brno: Academic publishing CERM, 1997. ISBN 80-7204-057-X.

[13] Regulation No. 13 of the Economic Commission for Europe of the United Nations (UN/ECE) - Uniform provisions concerning the approval of vehicles of categories M, N and O with regard to braking [online]. 2016. Available from: https://eur-lex.europa.eu/eli/reg/2016/194/oj

[14] JANOSIK, L., POLEDNAK, P., SUDRYCHOVA, I., FUSEK, M., FAMFULIK, J., VACULIK, M., RASKA, P, KARES, D., COCHLAR, M. Project objectives, solution procedures and results “Safe driving of emergency fire equipment”. In: 25th Scientific Conference with International Participation Crisis management in Specific Environments: proceedings. 2022. p. 190-199. ISBN 978-80-554-1872-8.

KOMUNIKÁCIE
COMMUNICATIONS

VEDECKÉ LISTY ŽILINSKEJ UNIVERZITY
SCIENTIFIC LETTERS OF THE UNIVERSITY OF ZILINA
multidisciplinary journal for sciences in transport

VOLUME 28 Number 1

January 2026

Editor-in-chief:
Gabriel GASPAR - SK

Associate editor:
Branislav HADZIMA - SK

Executive editor:
Sylvia DUNDEKOVA - SK

Language editors:
Ruzica NIKOLIC - SK
Marica MAZUREKOVA - SK

Honorary members:
Otakar BOKUVKA - SK
Jan COREJ - SK (in memoriam)
Milan DADO - SK
Pavel POLEDNAK - CZ

Scientific editorial board:
S. M. ANAS - IN
Greg BAKER - NZ
Abdelhamid BOUCHAIR - FR
Pavel BRANDSTETTER - CZ
Mario CACCIATO - IT
Jan CELKO - SK
Andrew COLLINS - GB
Samo DROBNE - SI
Erdogan H. EKIZ - UZ
Michal FRIVALDSKY - SK
Juraj GERLICI - SK
Vladimir N. GLAZKOV - RU
Ivan GLESK - GB
Marian GRUPAC - SK
Mario GUAGLIANO - IT
Mohamed HAMDAOUI - FR
Andrzej CHUDZIKIEWICZ - PL
Jaroslav JANACEK - SK
Zdenek KALA - CZ
Antonin KAZDA - SK
Michal KOHANI - SK
Tomasz N. KOLTUNOWICZ - PL
Jozef KOMACKA - SK
Matyas KONIORCZYK - HU
Matus KOVAC - SK
Gang LIU - CN
Tomas LOVECEK - SK
Frank MARKERT - DK
Pavlo MARUSCHAK - UK
Jaroslav MAZUREK - SK
Marica MAZUREKOVA - SK
Vladimir MOZER - CZ
Jorge Carvalho PAIS - PT
Peter POCTA - SK
Maria A. M. PRATS - ES
Pavol RAFAJDUS - SK
Giacomo SCELBA - IT
Martin SOLIK - SK
Jakub SOVIAR - SK
Blaza STOJANOVIC - RS
Che-Jen SU - TW
Eva SVENTEKOVA - SK
Eva TILLOVA - SK
Anna TOMOVA - SK
Audrius VAITKUS - LT
Neven VRCEK - HR
Yue XIAO - CN
Franco Bernelli ZAZZERA - IT

Executive editorial board
Michal BALLAY - SK
Pavol BELANY - SK
Martin BOROS - SK
Marek BRUNA - SK
Roman BUDJAC - SK
Nikola CAJOVA KANTOVA - SK
Kristian CULIK - SK
Jan DIZO - SK
Lukas FALAT - SK
Filip GAGO - SK
Lubica GAJANOVA - SK
Patrik GRZNAR - SK
Marian HANDRIK - SK
Stefan HARDON - SK
Martin HOLUBCIK - SK
Maros JANOVEC - SK
Daniela JURASOVA - SK
Daniel KAJANEK - SK
Matus KOZEL - SK
Lenka KUCHARIKOVA - SK
Richard LENHARD - SK
Michal LOMAN - SK
Matus MATERNA - SK
Eva NEDELIAKOVA – SK
Radovan NOSEK - SK
Daniel PAPAN - SK
Filip PASTOREK - SK
Pavol PECHO - SK
Slavka PITONAKOVA - SK
Jozef PROKOP - SK
Michal SAJGALIK - SK
Anna SIEKELOVA - SK
Jakub SVEC - SK
Michal TITKO - SK
Milan VASKO - SK
Vladislav ZITRICKY - SK

This is an open access article distributed under the terms of the Creative Commons Attribution 4.0 International License (CC BY 4.0), which permits use, distribution, and reproduction in any medium, provided the original publication is properly cited. No use, distribution or reproduction is permitted which does not comply with these terms.

KOMUNIKÁCIE
COMMUNICATIONS

VEDECKÉ LISTY ŽILINSKEJ UNIVERZITY
SCIENTIFIC LETTERS OF THE UNIVERSITY OF ZILINA
multidisciplinary journal for sciences in transport

VOLUME 28 Number 1

January 2026

Each paper is reviewed by at least two reviewers.
Individual issues of the journal are available at: http://komunikacie.uniza.sk
The full author guidelines are available at: https://komunikacie.uniza.sk/artkey/inf-990000-0400_Author-guidelines.php
Published quarterly by the University of Žilina via EDIS - Publishing House of the University of Žilina
Multidisciplinary journal for sciences in transport Komunikácie / Communications is currently indexed, abstracted and accepted by CEEOL, CLOCKSS, COPE (Committee on Publication Ethics), Crossref (DOI), digitálne pramene, DOAJ, EBSCO Host, Electronic Journals Library (EZB), ERIH Plus, Google Scholar, Index Copernicus International Journals Master list, iThenticate, JournalGuide, Jouroscope, Norwegian Register for Scientific Journals Series and Publishers, Portico, ROAD, ScienceGate, SCImago Journal & Country Rank, SciRev, SCOPUS, Ulrich´s, Web of Science database, WorldCat (OCLC).

Multidisciplinary journal for sciences in transport Komunikácie - vedecké listy Žilinskej univerzity v Žiline / Communications - Scientific Letters of the University of Žilina has been selected for inclusion in the Web of Science™.

Contact:

Komunikácie - vedecké listy Žilinskej univerzity v Žiline
Communications - Scientific Letters of the University of Žilina
University of Žilina, Univerzitná 8215/1
010 26 Žilina, Slovakia

E-mail: komunikacie@uniza.sk
Web: https://komunikacie.uniza.sk

ISSN (print version): 1335-4205
ISSN (online version): 2585-7878

Registered No. (print version): EV 3672/09
Registered No. (online version): EV 3/22/EPP
Publisher, owner and distribution:
University of Žilina, Univerzitná 8215/1,
010 26 Žilina, Slovakia

Company identification number IČO: 00 397 563
Frequency of publishing: four times a year
Circulation: 30 printed copies per issue
Print edition price: 100 Euro (price without VAT)
Article Processing Charge (APC): 400 Euro (price without VAT)

Publishing has been approved by:
Ministry of Culture, Slovak Republic

COPE
Member since 2025
JM18002

UNIVERSITY
OF ŽILINA

In its over 70 years of successful existence, the University of Žilina (UNIZA) has become one of the top universities in Slovakia.

Scientific conferences

organized by University of Žilina

29th International Seminar of Ph.D. Students SEMDOK 2026
Date and venue: 4 - 6 February 2026, Zuberec (SK)
Contact: lenka.kucharikova@fstroj.uniza.sk
Web: http://kmi2.uniza.sk/

Advanced Industrial Engineering Seminar
Date and venue: February - April 2026, Žilina (SK)
Contact: luboslav.dulina@fstroj.uniza.sk
Web: https://www.priemyselneinzinierstvo.sk/

Conference for FPEDAS Students
Date and venue: 11 March 2026, Žilina (SK)
Contact: eva.nedeliakova@uniza.sk
Web: https://fpedas.uniza.sk/sk/

Netmarketer Workshop
Date and venue: 17 March 2026, Žilina (SK)
Contact: marian.grupac@umkd.uniza.sk
beata.postekova@umkd.uniza.sk
Web: https://umkd.uniza.sk/

2nd Conference Cybersecurity in the Regions - Žilina
Date and venue: 18 March 2026, Žilina (SK)
Contact: ales.janota@uniza.sk
Web: https://iresa-cz.cz/konference/

3rd Conference Sports Management in Central and Easten Europe
Date and venue: 13 – 15 April 2026, Rajecké Teplice (SK)
Contact: michal.varmus@fri.uniza.sk
Web: www.smicee.org

2nd EDUDOS Project Training
Date and venue: 17 April 2026, Žilina (SK)
Contact: peter.danisovic@uniza.sk
Web: https://svf.uniza.sk/

UNIVERSITY OF ŽILINA
Science & Research Department

Univerzitná 8215/1,
010 26 Žilina,
Slovakia

Ing. Janka Macurová
tel.: +421 41 513 5143
e-mail: janka.macurova@uniza.sk